UNIVERSITY OF SOUTHAMPTON

FACULTY OF ENGINEERING, SCIENCE & MATHEMATICS

School of Ocean and Earth Science

The application of adaptive mesh modelling techniques to the study of open ocean deep convection

by

Zoe Louise Roberts

This dissertation is submitted for the degree of

Doctor of Philosophy

May 2008

DECLARATION OF AUTHORSHIP

I, **Zoe Louise Roberts**, declare that the thesis entitled **The application of adaptive mesh modelling techniques in the study of open ocean deep convection** and the work presented in it are my own. I confirm that:

- this work was done wholly or mainly while in candidature for a research degree at this University;
- where any part of this thesis has previously been submitted for a degree of any other qualification at this University or any other institution, this has been clearly stated;
- where I have consulted the published work of others, this is always clearly attributed;
- where I have quoted from the work of others, the source is always given. With the exception of such quotations, this thesis is entirely my own work;
- I have acknowledged all main sources of help;
- where the thesis is based on work done by myself jointly with others, I have made clear exactly what was done by others and what I have contributed myself;
- none of this work have been published before submission.

Signed:

Date:

Graduate School of the National Oceanography Centre, Southampton

This PhD dissertation by **Zoe Louise Roberts** has been produced under the supervision of the following persons:

Supervisors

Prof. Peter D. Killworth

Dr. George Nurser

Prof. Harry Bryden

Chair of Advisory Panel

Mr. Peter Challenor

To Peter Killworth

Acknowledgements

Numerous people have contributed to the successful completion of this thesis. My particular thanks go to Peter Killworth for the support, friendship and guidance given throughout this project, who sadly passed away before this thesis finally materialised. Special thanks to George Nurser for his support and direction during the final stages of the project. Thanks to Jeff Blundell, Kate Stansfield, Harry Bryden, David Smeed and Peter Challenor for their continuous encouragement and feedback, Yves Soufflet and Luke West for their ICOM support at NOCS and Lucas Merckelbach for help with the MITgcm.

Thank you to everyone at Imperial College Applied Mathematical and Computation Group - Matt, Colin, Chris, David, Tim, Adrian, Stephan, Patrick and all those in the AMCG chatroom who kept me company late at night. Special thanks to Lucy Bricheno for her ongoing help and friendship.

Jeremy Wilkinson at SAMS for the advice and opportunity to participate on a research cruise to the Greenland Sea, and Bob Pickart at WHOI for allowing me to study there for three months on the WHOI-NOCS exchange.

BMT Cordah, for their flexibility to allow this work to be completed and specifically Allan McVeigh for his mathematical guidance.

Personal thanks to Mum, Dad and Julia for their love and encouragement throughout all my endeavours. Pete - who deserves a medal for supplying tea and biscuits at regular intervals during the writing up process. Thanks to the office mates, friends and colleagues at NOCS who have ensured that undertaking a PhD project is not all work and no play. In particular Anna Maxey, Rachel Hadfield, Emma Guirey and Lizzie Jolley whose friendships have made life that extra bit more colourful.

Finally, thanks to NERC and the RAPID Programme for funding the project.

Abstract

The rapid cooling of the waters at high latitudes creates an unstable stratification which in turn leads to localised overturning (sinking) of the water column. This process is called open ocean deep convection (OODC). The process of OODC occurs in stages. Initially, individual convective elements known as plumes form and cold, dense water descends from the surface. Over time these plumes build up to produce a well-mixed 'chimney' of cold dense fluid. This chimney then slumps and sinks, and restratification (the return to a stable state throughout the water column) occurs.

It is widely accepted that OODC plays a main role in driving the thermohaline circulation (THC) and hence has a potentially major role in climate. However, the mechanisms of OODC itself are not fully understood, and there is much debate surrounding how it contributes to THC. One difficulty is that OODC tends to occur sporadically in only a few isolated regions around the globe, making direct observations difficult. As a result, theoretical and numerical investigations have become key to the development of our understanding of OODC. The scale on which OODC occurs presents a further issue, with traditional numerical representations (parameterisations) of OODC in global circulation models (GCMs) omitting convective detail due to resolution.

Due to the scales on which OODC occurs, it has been difficult to numerically investigate the nature of OODC in the small scale at the same time as resolving basin scale circulation. With the advent of finite element methods and adaptive meshing techniques, it is now possible to study OODC in regional models without the need to parameterise. One such model, the Imperial College Ocean Model (ICOM) is employed in this thesis for these purposes. ICOM is a 3D finite element, non-hydrostatic model with an adaptive, unstructured mesh and non-uniform resolution, allowing modelling of

the gyre circulation and resolution of OODC simultaneously.

As the use of an adaptive, unstructured mesh model is novel in investigating Greenland Sea open ocean deep convection, it is of interest to assess the accuracy of the ICOM model, and the amount of numerical diffusion present. The classical fluid dynamics problem of parallel plate convection provides a simple test problem for this purpose. A series of tests investigating the linear stability of various temperature gradients were performed in order to diagnose the amount of numerical diffusivity associated with hexahedral, tetrahedral and adaptive meshes within ICOM, and ICOM was further compared with a leading GCM (MITgcm). The use of the linear instability problem was found to be a useful case against which to test numerical models in an attempt to diagnose implicit diffusivity and viscosity.

A series of experiments were conducted in order to identify any prevailing differences between model convection in fixed and adaptive mesh configurations, under varying durations of applied cooling, and using varying extents of horizontal cooling. The adaptive mesh proved to be highly suitable for studying the convective problem, it was less computationally expensive and free from the numerical instability observed on the fixed mesh.

The sensitivity of model convection to the introduction of stratification was investigated. Uniform cooling was applied across the surface of a domain initialised with a weak stratification over the surface 1500m and a more strongly stratified region below, and the development of a convective layer was observed within the initial upper layer. Convection was constrained to the upper layer of stratification, and some penetrative convection was identified in the early stages of the model run.

Contents

List of Figures

List of Tables

Chapter 1

Introduction

Climate change has been identified as one of the major challenges facing the world today. Globally, Scientists now agree that the rapid rise in global temperatures over the last quarter of a century is the result of man's continuous neglect of the planet in pursuit of prosperity (IPCC, 2007), including rapid industrial development underpinned by the burning of fossil fuels to meet energy demands. In the western world, attempts are being made to reduce the impact of man's activities on the planet (Kyoto, 1997). Until recently, the USA has remained steadfastly reticent about the warnings of the scientific community, but agreed to a reduction in emissions at the United Nations Climate Change Conference in Bali (UN, 2007). However, large industrialising nations such as China and India continue to emit increasing amounts of 'greenhouse gases' as these countries emerge as industrial superpowers.

Scientists worldwide are working to understand the changes in climate and their consequences - including the development of clean energy sources to replace the worlds depleting resources of 'dirty' fuels, determining the impact of continuing rising global temperatures on the human population, monitoring the rapidity of the change in climate, and finding ways to reverse the predominant warming trend. The economic impact of changing climate has become a major concern, with many businesses now confronting the associated risk of climate change. Climate change may also lead to the mass migration of worldwide populations, and an increase in conflict (already evident in regions of drought and famine, such as Darfur in Sudan).

News headlines provide daily reminders of the impact of human activity

on the planet's landscape and habitats. The Hollywood blockbuster 'The Day after Tomorrow' took the message of the threat of climate change to the masses (in a somewhat sensational way), and recently Al Gore's 'An Inconvenient Truth' won an Academy Award in the Best Documentary category (Oscars, 2007), highlighting the causes and impacts of climate change. Al Gore and the Inter-Governmental Panel on Climate Change (IPCC) were jointly awarded the Nobel Peace Prize in 2007 (Nobel, 2007).

Despite increasing interest in the climate and its components, much about the Earth system is still unknown. Of particular interest is the role of the oceans in climate, as they cover more than two thirds of the surface of the Earth, and act as a reservoir of both heat and carbon. The possibility that a warming planet could impact the ocean circulation due to increased freshwater inputs (for example, increased precipitation at high latitudes and the melting of polar ice and glaciers leading to an enhanced water cycle) is cause for concern, particularly in Northern Europe, which benefits from increased temperatures for its latitude due to the warming effect of the ocean currents (Broecker, 1997). If the ocean currents responsible for this exaggerated warming were interrupted this could spell disaster for the peoples and economies of Northern Europe.

The large scale deep water ocean circulation is known as the thermohaline circulation (THC) (see Figure 1.1). This circulation is driven by gradients in temperature ('thermo') and salinity ('haline') (however, this is also debated within the scientific community, see Wunsch (2002)). The ocean is warmed at the equator by the sun's radiation, and evaporation from the surface of the ocean increases salinity, resulting in very low density (buoyant) water. At the poles, the ocean loses heat to the atmosphere, producing a high density water mass. The dense polar waters sink, and the buoyant low latitude waters rise, driving the meridional overturning circulation observed in the Atlantic. The warm, salty low latitude waters move poleward, and the cold, fresh polar waters move equatorward as the circulation works to iron out the temperature and salinity differences and attain equilibrium. However, the thermohaline circulation is opposed by the water cycle, so the freshening of water at the poles resulting from increasing global temperatures is a major concern.

The rapid cooling and freshening of the waters at high latitudes creates an unstable stratification (i.e. a layer of cold, dense water overlies the warmer,

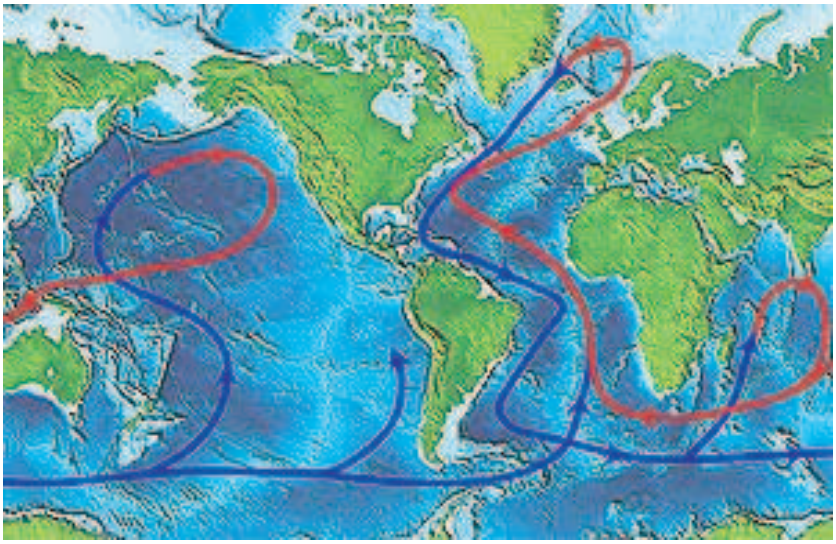

Figure 1.1: The thermohaline circulation of the oceans. Reproduced from NOC (2004).

less dense water below in an unstable equilibrium), which in turn leads to localised overturning (sinking) of the water column. This process is called open ocean deep convection (OODC). The process of OODC occurs in stages. Initially, individual convective elements known as plumes form and cold, dense water descends from the surface. Over time these plumes build up to produce a well-mixed 'chimney' of cold dense fluid. This chimney then slumps and sinks, and restratification (the return to a stable state throughout the water column) occurs.

It is widely accepted that OODC plays a main role in driving the THC (Dickson et al., 1996; Paluskiewicz et al., 1994), and hence a potentially major role in climate. However, the mechanisms of OODC itself are not fully understood, and there is much debate surrounding how it contributes to THC. One difficulty is that OODC tends to occur sporadically in winter in only a few isolated and inhospitable regions around the globe, making direct observations difficult. As a result, theoretical and numerical investigations have become key to the development of our understanding of OODC. The scale on which OODC occurs presents a further issue, with traditional numerical representations (parameterisations) of OODC in global circulation models (GCMs) which omit details of convection due to resolution.

Recent publications concerning the investigation of OODC have focused

on differing modes of convection (Noh et al., 2003; Gascard et al., 2002; Legg, 2004), identifying further convective regions (Bacon et al., 2003; Talley et al., 2003; Pickart et al., 2003), and the debate over which processes of OODC are most important for climate, i.e. plume dynamics versus chimney formation and breakup (Noh et al., 1999; Spall, 2004).

For the purpose of this thesis, we investigate OODC in the Greenland Sea. This region has given cause for concern in recent years as (limited) observations suggest that deep convection has ceased in the region since the late 1970s (Smethie et al., 1986; Schlosser et al., 1991; Alekseev et al., 2001). This reduction in deep water formation in the region has been attributed to a number of factors, including reduction in ice coverage (Wilkinson and Wadhams, 2003; Stossel et al., 2002; Ronski and Budeus, 2005b), and an increase in freshwater inputs (Oka et al., 2006). Historically, OODC in the Greenland Sea seems to have been haline forced as a result of brine rejection associated with the formation of ice. In recent years, however, thermal convection has been predominant, penetrating to intermediate depths only (Backhaus and Kampf, 1999). This has coincided with an erosion of the strong stratification observed in the 1970s (Budeus et al., 1998; Ronski and Budeus, 2005a; Karstensen et al., 2005; ICES, 2008). It has been suggested that the Greenland Sea and Labrador Sea OODC are dependent on the phase of the North Atlantic Oscillation (NAO) index (the index of the pressure gradient between the Azores and Iceland) (Mertens, 2000; Dickson et al., 1996; Broecker et al., 1999), locking the seas into a negative convective correlation (that is, when convection is strong in the Labrador Sea, it is weak in the Greenland Sea, and vice versa). However, studies have proved inconclusive. It is now thought that this see-saw effect is the result of freshwater balances (Oka et al., 2006). Understanding OODC is a key component in understanding the ocean circulation, and hence, climate.

Due to the scales on which OODC occurs, it has been difficult to numerically investigate the nature of OODC in the small scale at the same time as resolving basin scale circulation. Numerical investigations have relied on techniques that make assumptions about small scale turbulence, high resolution small scale regional models (restricted by the scale of the domain), and parameterisation (approximation) in GCMs. With the advent of finite element methods and adaptive meshing techniques, it is now possible to study OODC in regional models without the need to parameterise, because these

methods allow the resolution of both the basin scale circulation and small scale processes simultaneously, by placing resolution only where it is needed. One such model, the Imperial College Ocean Model (ICOM) (Ford et al., 2004a,b), is employed in this thesis for these purposes. ICOM is a 3D finite element, non-hydrostatic model with an adaptive, unstructured mesh and non-uniform resolution, allowing modelling of the gyre circulation and resolution of OODC simultaneously.

1.1 Aims

This thesis contributes to the Rapid Climate Change Programme objective of applying a hierarchy of modelling approaches to understand the processes that connect changes in ocean convection and its atmospheric forcing to the large-scale transports relevant to the modulation of climate. The Rapid Climate Change Programme aims to investigate and understand the causes of rapid climate change, with a main (but not exclusive) focus on the role of the Atlantic THC (Rapid, 2008). The understanding gained will be used to assess the probability and magnitude of future rapid climate change.

This project aims to contribute to the RAPID programme through the development of an idealised model of the Greenland Sea and the conducting of an in-depth study of OODC - its formation, behaviour and sensitivity to, for example, stratification, bathymetry, meteorology and ice, with greater accuracy than possible before, using ICOM. A number of techniques are employed to quantify convective strength observed within the model, including the diagnosis of depth of penetration, variation in vertical velocity and the ability of the model to capture the theoretical convective process. Because the application of adaptive mesh modelling to the convective problem is novel, a secondary aim of investigating the ability of such techniques to capture the convective process also underlies the majority of work presented here. The results of this study will contribute to improvement in parameterisation of OODC in GCMs. To achieve these aims, a thorough understanding of the OODC process and the factors influencing OODC in the Greenland Sea must be gained.

1.2 Chapter content

Chapter 2 of this thesis explores the relevant background material for this project, including a detailed description of the OODC process, and the hydrography, bathymetry, meteorology and presence of sea ice in the Greenland Sea. Chapter 3 contains the methodology of the project, model formulation, boundary conditions and experimental design. Chapter 4 investigates the presence of numerical diffusivity within ocean models, comparing ICOM with the Massachusetts Institute of Technology General Circulation Model (MITgcm) (MIT, 2008). Chapter 5 contains an initial investigation into OODC using simplified, small scale, box models in ICOM. A comparison between convection observed on fixed and adaptive meshes is presented, along with supplementary comparisons of variation in convection resulting from the choice of episodic or continuous duration cooling forcing and the use of disk shaped or uniform cooling. Chapter 6 presents a preliminary study of model convection into a domain with a background stratification similar to that observed in the Greenland Sea, focusing on whether penetrative convection (convection of relatively low density water into layers of higher density stratified water) is observed using ICOM. Chapter 7 draws the main conclusions of this thesis and discusses them, and outlines a number of other avenues and opportunities for studying model convection within ICOM, including the formulation of both progressively more complex idealised and realistic Greenland Sea basins, and further sensitivity tests that may be considered, which were not within the scope of this thesis.

Chapter 2

Background

2.1 Introduction

The first part of this chapter is concerned with what is known about deep convection. While this section seems quite robust, it would be wrong to assume that convection is a process that is fully understood. Because convection occurs in regions that remain inaccessible for much of the year, and is sporadic in nature, observational data are difficult to obtain. This in turn means that laboratory investigations, whilst providing a key insight, are hard to verify in practical terms. Furthermore, without detailed observations of convection, the results of experiments performed using numerical models cannot be confirmed as accurate. However, this does not mean that such techniques are not useful, and do not have a role to play within the investigation of convection.

It is accepted that convection plays a key role in the formation of the deep water that drives the thermohaline circulation. It is also accepted that the convective process occurs in stages: pluming, chimney formation; sinking; and finally, restratification. However, much of the process remains shrouded in mystery, particularly the final stage of chimney break-up, and there is much debate over which stage plays the most significant role in climate.

2.2 Open Ocean Deep Convection

OODC has been identified in only five regions worldwide: the Greenland Sea, the Labrador Sea, the Mediterranean and the Ross and Weddell Seas in Antarctica. It is suspected that it also occurs in a number of other regions. Recent studies, for example Pickart et al. (2003); Bacon et al. (2003), have identified the Irminger Sea as a source of mid-depth North Atlantic water. Deep convection is also believed to occur in the East Japan Sea (Senjyu and Sudo, 1994; Seung and Yoon, 1995). Other yet unmapped regions may also contribute to deep-water production (Broecker et al., 1999).

For a region to be inclined to OODC it must have a combination of features, including: a background cyclonic circulation, some preconditioning processes to create a region of weak static stability, a number of water masses and some surface forcing to induce convection (Killworth, 1983). The process of OODC occurs in stages. Initially, individual convective elements form (plumes) and cold, dense water descends from the surface. Plumes typically have a horizontal scale of approximately 1km. Over time the plumes build up to produce a well-mixed 'chimney' of cold dense fluid, up to 100km wide. This chimney then slumps and sinks, and restratification occurs. Marshall and Schott (1999) have produced a comprehensive review of the convective process in the open ocean, and the reader is referred to their paper for further details including convection in other regions.

2.2.1 Observations of Open Ocean Deep Convection

Observations of deep mixed patches in the Greenland Sea are rare as they occur during the winter months. More frequently, homogeneous chimneys in the spring and summer following convection are observed (Marshall and Schott, 1999). Gascard et al. (2002) present observations of long-lived vortices as a relic of deep convection in the Greenland Sea. Observations are gathered from tracer (for example oxygen), float and hydrographic sections. Evidence from tracer data has shown a reduction in Greenland Sea deep-water formation during the 1980's (Schlosser et al., 1991). The last known convective event reaching 3500m occurred in the 1970s (Smethie et al., 1986). Subsequent events have not reached deeper than 2000m (Rudels et al., 1989). In the same period a reduction in concentration and extent of sea ice cover

has been observed (Wilkinson, 2005; Divine and Dick, 2006).

A number of observational projects have been conducted in other known convective regions. These include the Mediterranean Ocean Convection experiment in the Gulf of Lions (MEDOC-Group, 1969), and the Labrador Sea Deep Convection Experiment (LabSea-Group, 1998). Other studies (Lilley et al., 1999; Lavender et al., 2002; Pickart et al., 1996; Clarke and Gascard, 1983) also produced useful data for the understanding of OODC. Similar studies in the Greenland Sea, for example the Greenland Sea Project (GSP) (GSP-Group, 1990), have failed to observe convection to great depths (Rudels et al., 1989; Schott et al., 1993). The availability of new technologies such as moored ADCPs (Acoustic Doppler Current Profilers) has enabled observations to be carried out during the winter months (Mertens, 2000). The Greenland Sea Project organised the deployment of a number of bottom anchored convection moorings, along with intense CTD (Conductivity, Temperature, Depth) surveys of the region, providing a nearly continuous time series of the central Greenland Sea from 1988-1995 (GSP-Group, 1990).

2.2.2 Theory of Open Ocean Deep Convection

A number of features act to bias a region to OODC (Killworth, 1983). A background cyclonic circulation causes upward doming of isopycnals (lines of constant density) in the centre of the cyclonic gyre and reduces the vertical stability of water columns within the gyre. Preconditioning creates a region of shallow static stability which may convect if the surface forcing is sufficiently intense. The presence of more than one water mass is required, and a sufficiently intense surface forcing for example the passage of a severe mid-latitude cyclone, is needed to induce the violent mixing stage. However, the nature of OODC is temporally sporadic, spatially restricted and therefore difficult to observe and predict, posing a number of difficulties for parameterisation in GCMs.

Each stage in the convective process has a scale associated with it. The preconditioning stage occurs on the large scale, of the order 100km. Individual convective plumes are typically of the order 1km. At the sinking and spreading stage of the resultant homogenised chimney the Rossby deformation radius, L_R (Equation 2.1), sets the scale for the geostrophic eddies observed in the breakup (typically 5-10km). At scales greater than L_R the

Earth's rotation controls the dynamics, and geostrophic balance exists. L_R is given by:

$$L_R = (NH/f) \tag{2.1}$$

where N is the Brunt-Vaisala frequency, H is the depth scale and f is the Coriolis parameter.

The deepening of the oceanic mixed layer is driven by momentum and buoyancy flux variations at the surface associated with the prevailing meteorological conditions. The buoyancy force (b) acting on a fluid parcel in a column is determined by its anomaly in buoyancy:

$$b = -g(\rho - \rho_0)/\rho_0 \tag{2.2}$$

where g is acceleration due to gravity, ρ is the density of the fluid parcel and ρ_0 is a constant reference density. For a linearised equation of state:

$$\rho = \rho_0[1 - \alpha(\theta - \theta_0) + \beta(S - S_0)] \tag{2.3}$$

$$b = g[\alpha(\theta - \theta_0) - \beta(S - S_0)] \tag{2.4}$$

where α and β are the thermal expansion and haline contraction coefficients respectively, θ is the potential temperature, S is the salinity and ρ is the density. θ_0 and S_0 are reference temperature and salinity. Values of α and β typical for the Greenland Sea are given by Mertens (2000). From Equation 2.4, the buoyancy flux at the sea surface can be expressed in terms of heat and fresh water fluxes as follows:

$$B = g[\alpha(Q/\rho_0 c_p) - \beta S_0(E - P)] \tag{2.5}$$

where Q is the surface heat flux (negative values imply flux of heat from the ocean to the atmosphere), $E - P$ represents the net freshwater flux (evaporation minus precipitation), and c_p is the specific heat capacity of water. The surface buoyancy flux B fundamentally drives convection in the ocean.

Cold water shows a stronger density variation with depth than warm water. This is termed the thermobaric effect (Denbo and Skyllingstad, 1996).

If cold, fresh water is displaced downward into relatively warm, salty water it becomes relatively denser. Studies have shown that the correct representation of the thermobaric effect generally increases the depth of convection, and may determine whether OODC will occur (Killworth, 1976; Sander et al., 1995; Garwood et al., 1994). For the purposes of the study presented within this thesis, however, the thermobaric effect is not considered, and is effectively excluded via the use of the linear equation of state.

Marshall and Schott (1999) identify three main convective regimes and present the key scaling ideas associated with each. These regimes and their associated scales are summarised in the following sections.

Convection on short timescales

For a loss of buoyancy associated with some surface flux of magnitude B_0, convection into a homogeneous fluid with depth h, a layer of 3D, buoyancy driven turbulence will deepen as the plumes associated with it evolve over time. The convection will eventually reach depth h. Initially, the plumes are so small they cannot feel the finite depth h, and for timescales $t << 1/f$, rotation is unimportant. The scales associated with the plumes are therefore dependent only on B_0, as follows:

$$l \sim \sqrt{(B_0 t^3)} \tag{2.6}$$

$$u \sim w \sim \sqrt{(B_0 t)} \tag{2.7}$$

$$b' \sim \sqrt{(B_0/t)} \tag{2.8}$$

where l is the scale of the convective elements, and b' is the buoyancy perturbation.

Convection constrained by depth

For timescales $t < 1/f$, the depth h of the fluid becomes important and effectively limits the scales of the plumes as follows:

$$l \sim l_{norot} = h \tag{2.9}$$

$$w \sim w_{norot} = (B_0 h)^{1/3} \tag{2.10}$$

$$b' \sim b'_{norot} = (B_0^2/h)^{1/3} \tag{2.11}$$

where the subscript 'norot' indicates the absence of rotation. The timescale of convective overturning can be estimated as:

$$t* = h/w_{norot} \tag{2.12}$$

Convection constrained by the Earth's rotation

If the depth of the fluid is large enough, plumes will be controlled by geostrophy before reaching h. The transition to rotationally dominated motion will occur as the timescale t approaches $1/f$. The convective scale thus becomes constrained as:

$$l \sim l_{rot} = \sqrt{(B_0/f^3)} \tag{2.13}$$

$$w \sim w_{rot} = \sqrt{(B_0/f)} \tag{2.14}$$

$$b' \sim b'_{rot} = \sqrt{(B_0 f)} \tag{2.15}$$

where the subscript 'rot' indicates the scales at which rotation becomes important. At these scales the plume Rossby number is equal to unity (that is, the vertical velocity within the plume is comparative with the background vorticity due to Coriolis):

$$R_0 = \frac{w}{fl} \sim \frac{w_{rot}}{f l_{rot}} = 1 \tag{2.16}$$

The natural Rossby number, R_o* is a measure of the ratio l_{rot}/h. When R_o* is small, pluming to the bottom is rotationally controlled. R_0* can be interpreted as the fraction of the total depth that a convected parcel reaches or as a measure of the number of vertical cycles the parcel makes in a rotation period. ${R_o*}^2$ implies the strength of the forcing, B_0, and $\sqrt{R_0*}$ is a measure of the radius deformation relative to the depth once convection has ceased.

In the ocean, R_o* typically ranges from 0.01-1. It is therefore concluded by Marshall and Schott (1999) that rotation is important, even at the plume scale. However, Marshall and Schott (1999) identify that the mixing process is of less importance in comparison with horizontal processes i.e. at later stages in the convective process horizontal transport of the transformed water by eddies takes precedence over vertical processes.

2.2.3 Modelling Open Ocean Deep Convection

Oceanic convection has been modelled numerically in a number of studies, for example Jones and Marshall (1993), Coates et al. (1995), Sander et al. (1995), and Maxworthy and Narimousa (1994). The majority of these experiments use non-hydrostatic models (see Section 2.2.4 for an explanation of hydrostacy) and a large eddy simulation (LES) approach.

LES is a method by which all large scale turbulent eddies are calculated explicitly, and small scale turbulent eddies are modelled using a sub-grid scale model (Bakker, 2005). This makes LES suitable for use in OODC modelling, taking into account the effects of a gyre circulation and resolving the necessary dynamics of the convective process. Small scale turbulence is assumed to be isotropic (i.e. the same in all directions) and homogeneous (well mixed) (Garwood et al., 1994).

Numerous studies of OODC have been made in recent years using LES models. Raasch and Etling (1998) compared results from a LES with laboratory experiments showing good agreement between both sets of results. Noh et al. (2003) showed that the evolution of convection depends on the preconditioning and the buoyancy flux incident on the convecting region, inferring two types of OODC exist - 'distributed' and 'localised'. These predictions are, however, unconfirmed by observations. Barbosa and Metais (2000) perform LES based on an elaborate subgrid scale parameterisation of oceanic deep convection resulting from a localised cooling applied at the surface, ascertaining that refined subgrid scale models and greater precision in numerical methods produce better agreement with laboratory experiments (such as Maxworthy and Narimousa (1994)).

The LES method has also been applied to investigations into the occurrence of OODC in the East Japan Sea. Noh et al. (1999) investigate the effects of spatial and temporal variations of surface forcing on penetrative

depth of convection, generation of baroclinic eddies, the volume of deep-water formation and intensity of the rim current. Denbo and Skyllingstad (1996) apply a 3D LES model that simulates the mixing process by generating eddies with scales comparable to the mixing length, with the inclusion of a realistic non-linear equation of state for seawater in order to demonstrate the effect of thermobaricity and rotation on deep convection. They conclude that it is necessary to include such effects in vertical mixing parameterisations in GCMs. Similar conclusions had previously been reached by Sander et al. (1995).

2.2.4 Parameterisation

The use of the hydrostatic approximation and the restriction on resolution due to computational expense in many GCMs means that convective processes must be parameterised (or approximated). The hydrostatic approximation (Equation 2.17) assumes that vertical accelerations are small compared with gravitational acceleration:

$$(\partial p/\partial z) = -\rho g \tag{2.17}$$

where p is pressure, z is depth, ρ is density and g is acceleration due to gravity. Essentially, the use of the hydrostatic approximation disallows the formation of unstable stratification throughout the ocean, that is it assumes that the ocean is stably stratified everywhere.

Attempts have been made since the beginning of ocean modelling in the 1960s to provide a useful, low cost convection parameterisation (Griffies et al., 2000a). The convective adjustment scheme (Cox, 1984) is a series of iterations that act to homogenise vertically adjacent boxes if they are unstable, converging to a gravitationally stable column after an uncertain (or infinite) number of iterations. As vertical resolution improves, an increasing number of iterations are needed to achieve stability, becoming computationally expensive. Killworth (1989) has shown that the number of iterations is directly related to the ability to resolve the large scale ocean circulation.

Marotzke (1991) compares three schemes: the standard convective adjustment scheme (Cox, 1984), an algorithm that guarantees complete vertical stability by treating any previously mixed adjacent boxes as one unit (effec-

tively mixing a column in one time step) (Marotzke, 1989, 1991), and an implicit scheme which treats convective overturning as vertical diffusion which reduces dependence on the vertical grid resolution (Griffies et al., 2000a). The choice of convective scheme is shown to have important implications for the stability of the thermohaline circulation. Rahmstorf (1993) further refines the method of instantaneous column mixing. Klinger et al. (1996) show that the use of an implicit scheme to place a large finite vertical diffusivity in regions of instability, produces results similar to a non-hydrostatic model where convection is explicitly resolved (Griffies et al., 2000a). Thus a mixing model of convection is sufficient to represent gross properties of plumes in a high resolution model (Mertens, 2000). Paluskiewicz and Romea (1997) produce a 'penetrative plume scheme', a one dimensional parameterisation for the violent mixing stage. England and Rahmstorf (1999) have shown the dependence of deep water formation (for example freshening and warming) on the use of different convection parameterisations.

Convection parameterisations have historically focused on the violent mixing stage. However, it has been suggested that the details of convective pluming may not matter for climate, but sinking of newly formed deep water is associated with the geostrophic eddies that occur during the breakup stage (Marshall and Schott, 1999; Spall, 2003). Thus, future convective parameterisations may be required to include horizontal mixing when horizontal resolution is larger than L_R.

2.3 The Greenland Sea

The Greenland Sea, situated between approximately 70 and 80 degrees north and 0 - 20 degrees east, has for many years been hypothesised to play an important role in the formation of North Atlantic Deep Water (NADW) and hence the THC. It is one of only a handful of identified regions in the world where OODC is known to occur. Preconditioning by winter ice, a background cyclonic circulation, the convergence of a number of differing water masses, extreme seasonal variations in meteorology and the isolation of the Greenland Sea basin caused by bottom topography characterise the region, making it a prime site for convective activity.

2.3.1 Hydrography

One of the conditions conducive to convection is the presence of a number of differing water masses exhibiting different properties such as salinity and temperature causing a weak and sometimes unstable background stratification. The Greenland Sea is a region of complex hydrography. The range of currents present in the Greenland Sea (and the Nordic Seas as a whole) can be seen in Figure 2.1. The result of the interaction between the different water masses is a 3 layered stratification including a thin surface layer to 60-100m depth of Arctic Surface Water from the East Greenland Current (typically cold and fresh), a layer of Atlantic Intermediate Water supplied from the south-east to 800m depth and a weakly stratified Greenland Sea Deep Water (GSDW) to sea floor (approximately 3000m) (coldest and least saline), resulting from previous deep convection events.

The Greenland Sea is dominated by the southward flowing East Greenland Current, which produces two eastward flowing branches, the Jan Mayen current flowing along the Jan Mayen ridge, and the East Iceland Current just north of Iceland. The northward flowing Norwegian Atlantic Current sends branches of warm saline Atlantic Water westwards into the interior of the Greenland Sea before continuing into the Arctic Ocean through Fram Strait. Rasmussen et al. (1999) give a detailed summary of estimated transports into and out of the Greenland, Iceland and Norwegian (GIN) Seas from a collection of studies, both from numerical studies and from cruise data (these are quoted in Section 2.3.2). Malmberg (1983) gives a detailed description

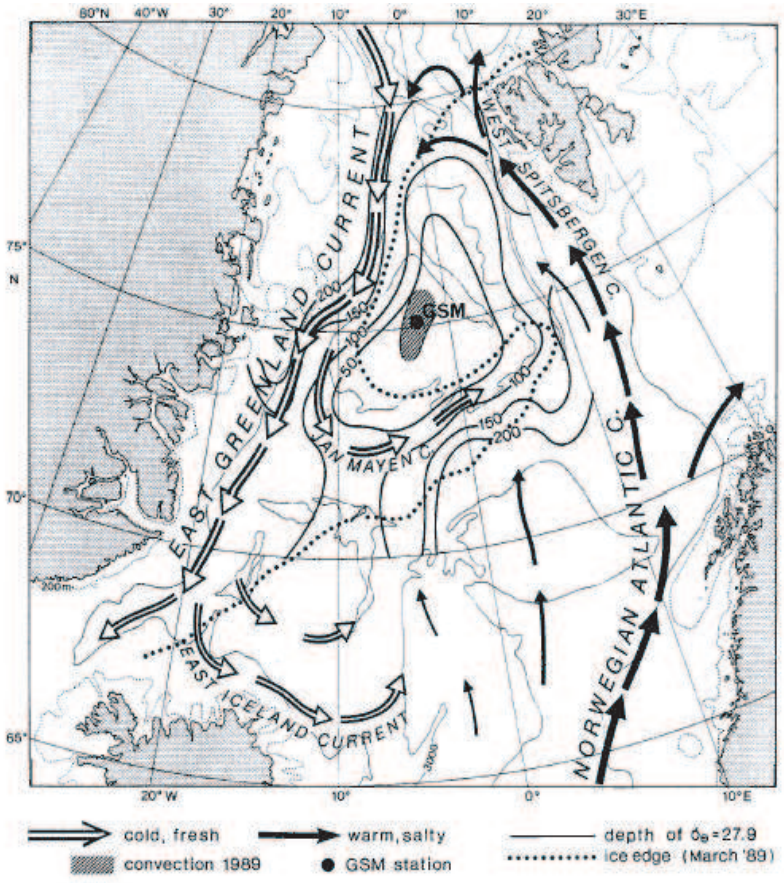

Figure 2.1: Schematic of the circulation of the Greenland Sea showing the warm water flow of the Norwegian Atlantic current and its recirculation, and cold water flows of the East Greenland and Jan Mayen currents that constitute the cyclonic circulation. Doming is indicated by the depth of the isopycnal $\sigma_\theta = 27.5$, and the Is Odden is marked by the position of the ice edge (dotted line) in March 1989. 'GSM' is the location of repeated moored deployments. Reproduced from Marshall and Schott (1999).

of water masses present in the Greenland Sea from observations.

Traditionally, the hydrography of the Greenland Sea has been thought to be dominated by a vertically homogeneous upward dome of cold and fresh GSDW (Ronski and Budeus, 2005b). However, the reduction in occurrence of deep penetrating ventilation events has lead to the gradual erosion of the previously strong stratification observed in the 1980's. Figures 2.2 and 2.3 show the erosion of GSDW layer in the centre of the Greenland Sea over time.

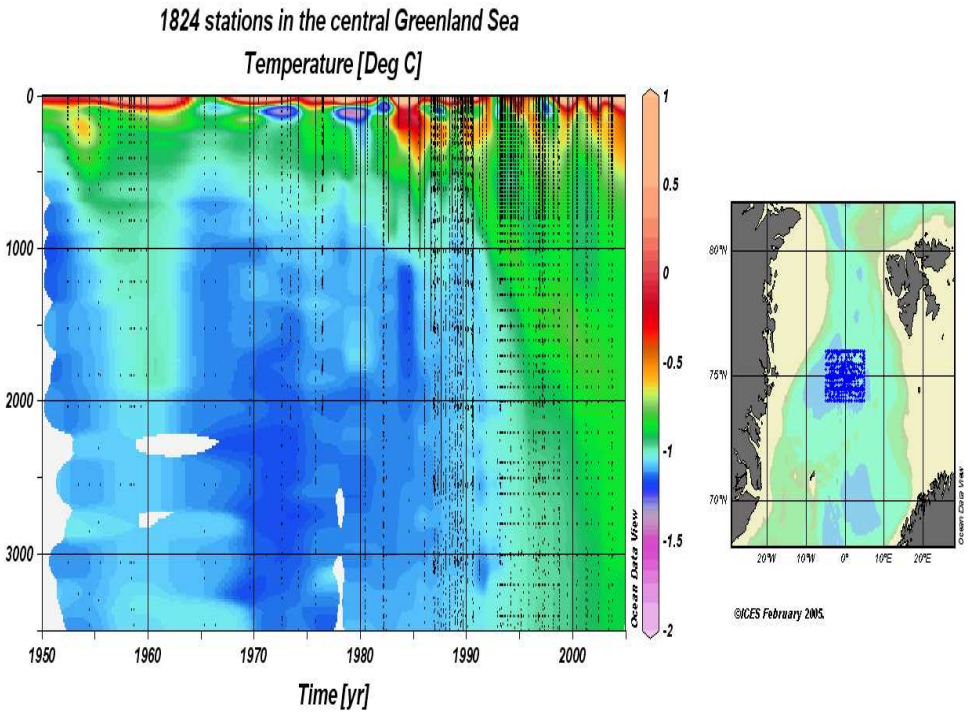

Figure 2.2: Contour plot of temperature over time for CTD casts in the centre of the Greenland Sea gyre showing the gradual warming of the bottom layers, indicating a reduction in the convective processes responsible for the production of GSDW and the maintenance of the strong stratification traditionally observed. Reproduced from ICES (2008).

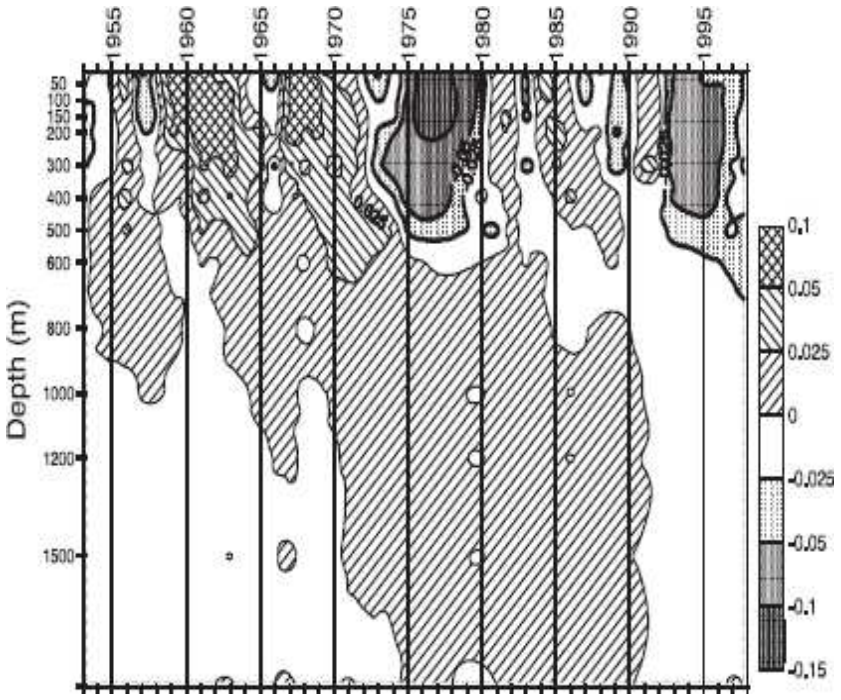

Figure 2.3: Contour plot of salinity anomaly over time observed by Ocean Weather Ship Mike in the Greenland Sea averaged from January - May during the latter half of the 20th century (Alekseev et al., 2001).

2.3.2 Bathymetry

Bathymetry can influence OODC in a number of ways. Ridges and seamounts can cause doming of the isopycnals locally. Ridges also act to isolate regions of water, allowing the stratification to remain undisturbed by lateral processes for long periods of time, and atmospheric-ocean interaction to take precedence.

The Greenland Sea is situated within a large basin separated from the Norwegian Sea by the Mohns and Knipovich Ridges, and from the Icelandic Sea by the Jan Mayen Fracture Zone. These ridges restrict the exchange of deep water between the seas. The Greenland Sea basin reaches depths of more than 3000m (GEBCO, 2003). Surface waters flow northwards through the Fram Strait into the Arctic Ocean with a flow rate of around $1Sv$, the remainder of Atlantic Water recirculating southwards. GSDW flows into the North Atlantic through three open boundaries to the south: Denmark Strait, Iceland-Faeroe Ridge and the Faeroe Bank Channel.

The Denmark Strait reaches a depth of up to 650m and a width of 290km. The overflow rate of GSDW from the Greenland Sea into the North Atlantic through the Denmark Strait is persistent and steady, typically $1.6 - 3.0Sv$, and has a density of $\sigma_t > 27.8$ ($1027.8kgm^{-3}$) (Wilkinson, 2005). The overflow water reaches great depths ($4000m$ at 26°N) in the North Atlantic (Mann, 1969). It is the coldest and densest of source waters for NADW. The Polar, Atlantic and Arctic water masses are all found in varying proportions in this narrow strait.

The Iceland-Faeroe Ridge is the widest (400km) and shallowest (480m) of all the channels. Outflow of waters with density greater than $1027.8kgm^{-3}$ is estimated between 0.5 and 1Sv (Dickson and Brown, 1994) but is notably weak and sporadic (Swift, 1991).

Situated in the Faeroe-Shetland Channel is the Faeroe Bank Channel, approximately 25km wide and a maximum depth of 850m, the primary exit point for Upper Norwegian Deep Water (UNDW) (Hopkins, 1991). This UNDW (more saline and warmer than Denmark Strait overflow water) is estimated to flow at 1.4-1.9Sv.

Fram Strait is the only deep boundary connecting the Greenland Sea and the Arctic Ocean, reaching up to 2600m (Wilkinson, 2005). Approximately $2Sv$ of Polar Water flows into the Greenland Sea through Fram Strait, bring-

ing with it a supply of Arctic Ocean ice (Hopkins, 1991).

2.3.3 Meteorology

OODC ultimately occurs once the preconditioned water column is forced by some external atmospheric force, such as the passage of a strong storm, inducing cooling and turbulence in the surface layer.

The meteorology of the Greenland Sea region is characterised in winter by the presence of a steep pressure gradient between the Icelandic low and the Greenland high, and the advent of polar night (24 hour darkness extends down from the pole to 66 degrees North in winter). There are a large number of atmospheric cyclones passing across the region, typically 7-10 per month in winter (Condron et al., 2006). This also results in strong, cold northerly winds over the Greenland Sea. The combination of high wind speeds and the air-sea temperature contrast cause large fluxes of sensible and latent heat into the atmosphere, necessary for the process of OODC to occur (Mertens, 2000). In winter, the air temperature is typically $-14°C$, and typical heat losses of $230 - 1000 Wm^{-2}$ occur, coinciding with the passage of cyclones. Mean wind speeds are typically $\sim 10 ms^{-1}$, but can be as high as $30 ms^{-1}$ during extreme events (Condron et al., 2006). The Greenland Sea is covered by ice in winter (November-January), as discussed subsequently in Section 2.3.4. In summer, the Greenland high pressure extends across the region causing predominantly stable, overcast conditions. Some typical values for meteorological parameters are given in Table 2.1.

Table 2.1: Typical Winter Meteorological Conditions and Fluxes in the Greenland Sea. Reproduced from Marshall and Schott (1999)

Parameter	Value
Air Temperature (dry), $°C$	-14
Air Temperature (wet), $°C$	-13
Wind Speed u_{10}, ms^{-1}	13
Net Heat Flux, Wm^{-2}	-530
Total Buoyancy Flux, $10^{-8} m^2 s^{-3}$	5

Renfrew and Moore (1999); Pickart et al. (2003); Bacon et al. (2003); Moore and Renfrew (2005) have produced evidence that deep convection can be initiated by meteorological phenomena such as the Greenland Sea tip jet,

barrier winds and katabatic winds in the Irminger Sea. These phenomena cause accelerated heat and momentum fluxes (upwards of $800 W m^{-2}$). However, few similar climatological studies of the GIN Seas region exist, due to a lack of reliable data, despite Greenland (and its topography) playing a major role in North Atlantic climate.

Variability in the intensity of deep convection in both the Greenland and Labrador Seas is linked to the North Atlantic Oscillation (NAO) (Dickson et al., 1996). In general, convective activity in the Greenland Sea is suppressed during a positive phase of the NAO, and the Labrador Sea becomes the location of strong OODC. However, this connection failed to be validated by the research of Mertens (2000), who compared total wintertime surface buoyancy loss calculated from NCEP/NCAR (National Centers for Environmental Prediction/National Center for Atmospheric Research) reanalysis data to the NAO index for 1959-1999 and showed a weak connection for the Labrador Sea that was not evident in the data for the Greenland Sea. It has been suggested that this see-saw effect is the result of freshwater balances (Oka et al. (2006)), but research into this area is ongoing.

Direct measurements of meteorological parameters (particularly air-sea fluxes) are not routinely available for the region (Mertens, 2000). As a result, climate reanalysis data from global data sets such as NCEP become important.

2.3.4 Sea Ice

Convection does not occur when the Greenland Sea region is covered by ice (Marshall and Schott, 1999), but it is expected that in the Greenland Sea the action of ice formation contributes to the preconditioning of the water column, brine rejection causing an increase in density and a deepening of the surface mixed layer throughout the winter months. Marshall and Schott (1999) suggest that the haline forcing contributes almost one quarter of the total buoyancy flux.

Figures 2.4 and 2.5 show concentrations of sea-ice in the Greenland Sea from satellite altimetry for the years 1997 and 2007. The decline in the extent of winter sea-ice and the formation of the Odden in the decade 1997 - 2007 is clearly evident. The reduction in the extent and concentration of sea ice may have implications for OODC.

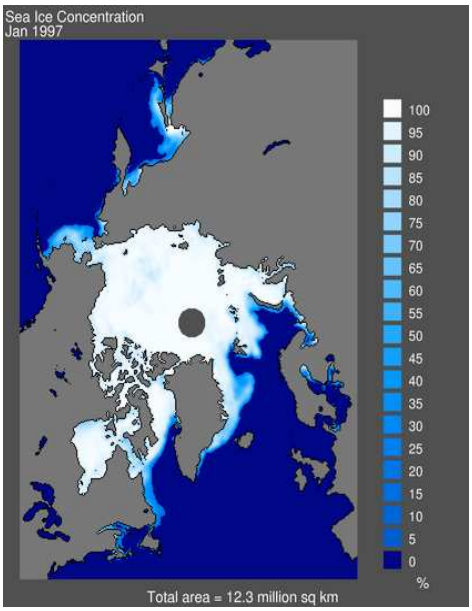

(a) January 1997

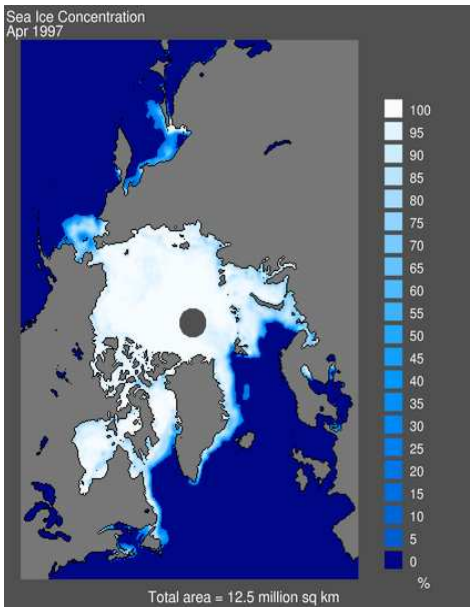

(b) April 1997

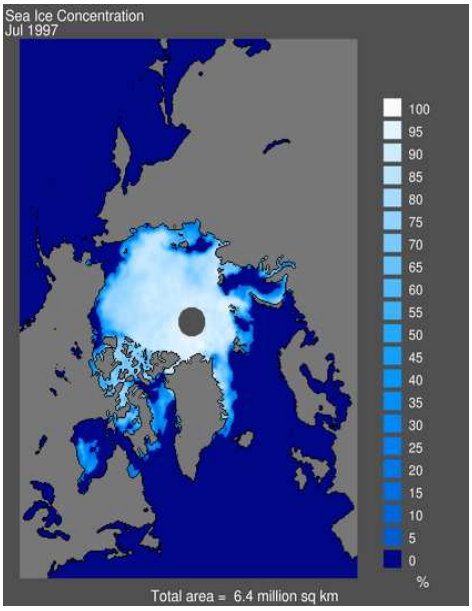

(c) July 1997

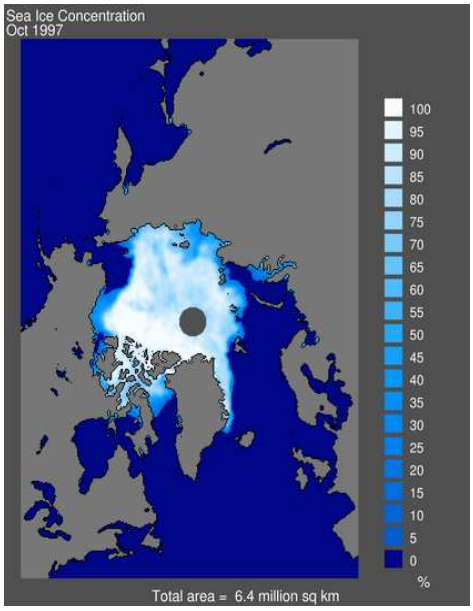

(d) October 1997

Figure 2.4: Northern Hemisphere sea ice concentration in 1997 from paths of satellite altimetry. The Is Odden is clearly visible in January, and sea ice is present in the Greenland Sea throughout the year with concentrations greater than 50 % . Reproduced from NSIDC (2008).

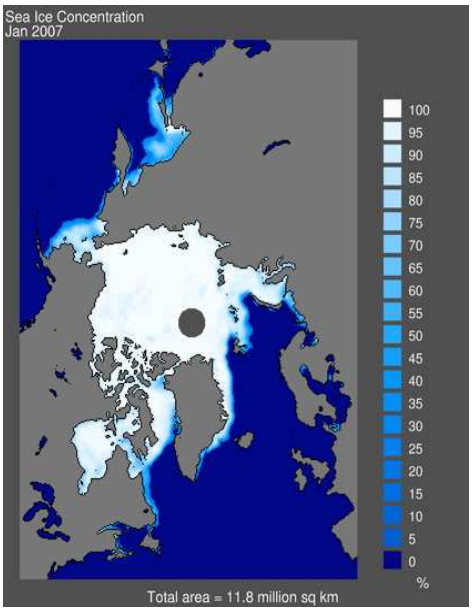

(a) January 2007

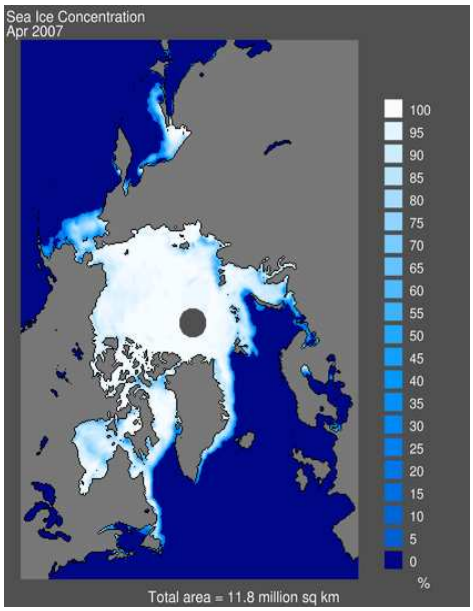

(b) April 2007

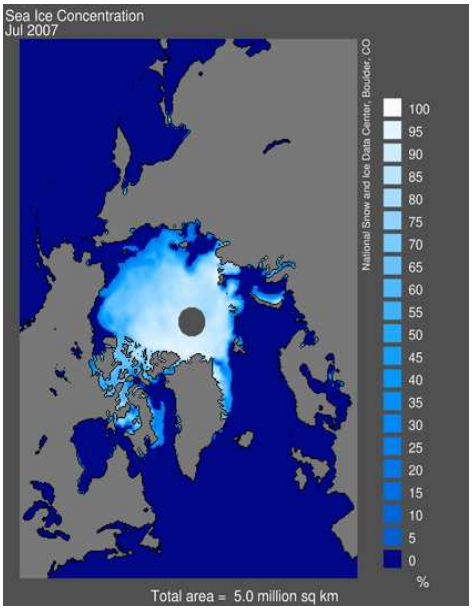

(c) July 2007

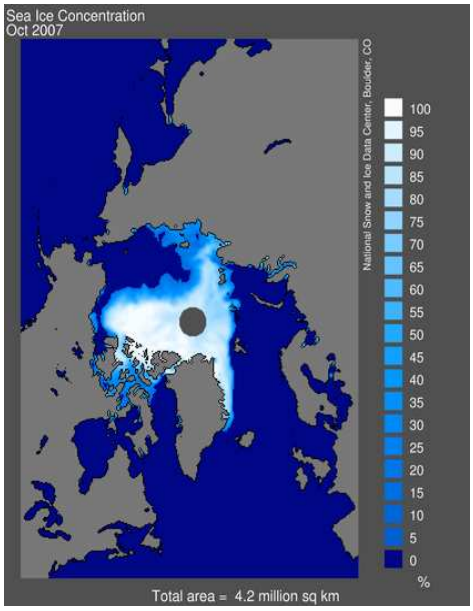

(d) October 2007

Figure 2.5: Northern Hemisphere sea ice concentration in 2007 from paths of satellite altimetry. The Is Odden is no longer visible in January, and there is a marked reduction in sea ice concentration and extent in summer less than 25 % . Reproduced from NSIDC (2008).

In early winter, ice begins to spread eastward across the Greenland Sea (Marshall and Schott, 1999). It is composed of locally produced pancake and frazil ice (Wadhams and Wilkinson, 1999) and remains in the pancake stage due to storm activity. Sea ice has a typical salinity of approximately 5 PSU compared with approximately 35 PSU for seawater. This discrepancy results from brine rejection from the ice and increases the density of the surface layer, which in turn causes a deepening of the mixed layer, reaching roughly 150m by mid-January. By late January the ice forms a wedge (called 'Odden ice' or 'Is Odden') extending northeastward. The extent of the traditional Odden ice is seen in the schematic map of the Greenland Sea, Figure 2.1. The Odden encloses an ice-free bay (The 'Nord Bukta') to its North as a result of ice export by strong Northerly winds. The mixed layer in the ice-free bay deepens to 300-400m in February, induced by strong winds. In March, preconditioning by ice is at such an advanced stage that deep convection may occur within the ice free bay, initiated by strong winds and a heat loss maximum.

Large amounts of ice also flow into the Greenland Sea from the Arctic Ocean every year (Wilkinson, 2005). Ice within the East Greenland Current is exposed to the turbulent nature of the ocean e.g. wind and waves, and rarely takes on the form of a solid sheet. Wilkinson (2005) identifies six distinct types or regions of ice found in the Greenland Sea:

1. Multi year ice: Originates in the Arctic Ocean and has spent more than one year circulating there before entering the Greenland Sea. Generally thick and deformed (ridges, hummocks, melt ponds).

2. First year ice: Forms between the multi year floes (in the leads) over winter in the Arctic Ocean and the East Greenland Current. Generally smooth in appearance. First year ice that survives the summer melt becomes multi year ice.

3. Fast ice: Found near the coast of Greenland and is stationary during winter but melts or breaks away during summer.

4. Icebergs: Originate from glaciers i.e. they are of non-maritime origin and observed in the East Greenland Current, generally calved from the Greenland ice cap.

5. Marginal ice zone: The eastward extent of the ice within the East Greenland Current, where wave and wind action cause the ice to break-up, leaving a mix of floes and brash. New ice (frazil, pancake) is also found within this zone. Strong winds blow the ice away from the main pack.

6. Odden ice: The only area in which new sea ice forms away from the east Greenland continental shelf, consisting of pancake and frazil.

Wilkinson (2005) makes a comparison of sea ice concentration from satellite mounted passive microwave data with ECMWF meteorological fields. The Odden has not been observed in recent years. At the same time OODC has not penetrated below intermediate depths. It is currently unclear what relationship, if any, exists between these two events.

2.4 Ocean modelling using finite elements

Numerical models of ocean circulation range in complexity from simplified models in which attempts are made to advance understanding of, for example, non linear terms, bottom topography, surface conditions (ice, meteorology), to realistic global ocean circulation models, often coupled to ice and atmosphere models (Griffies, 2004; Pond and Pickard, 1983).

Analytical models of ocean circulation (e.g. Ekman (1905); Sverdrup (1947); Stommel (1948); Munk (1950)) were superseded by the first numerical models of the ocean circulation (e.g. Bryan and Cox (1967); Bryan (1969)). Fix (1975) demonstrated the use of finite elements and unstructured meshes for ocean modelling, and Dumas et al. (1982) favoured their use; however, the use of finite difference methods of numerical discretisation in ocean modelling has dominated since the early work of Bryan and Cox. Similarly, the use of structured fixed meshes and z-coordinates because of numerical simplicity has also dominated ocean modelling. Griffies et al. (2000b) gives a review of co-ordinate choices, and Griffies (2004) and Pond and Pickard (1983) give accounts of the finite difference method. Until now, the use of finite elements has predominantly been within barotropic depth independent applications in coastal and tidal modelling (Lynch and Gray, 1979; Provost and Vincent, 1986; Lynch and Werner, 1991; Lynch et al., 1996).

There are a number of well documented drawbacks to the finite difference method (see Hanert (2004)). These are, firstly; the staircase representation of coastlines causing spurious forms of stress on the boundary current, and secondly; the expense of high resolution fixed meshes means important processes such as meso-scale eddies, western boundary currents and equatorial dynamics must be parameterised in global scale ocean circulation models.

The desirability of an unstructured adaptive mesh has led to renewed interest in the area of finite elements. Finite elements have a number of advantages over traditional finite difference methods, including conservation of energy for all methods of solving differential equations, natural treatment of boundary conditions, flexibility of triangulation, provision of finer resolution in regions of specific interest, and unstructured grids. Griffies et al. (2000a) highlighted two problems with unstructured grids, firstly, difficulty in representing geostrophic balance and secondly, unphysical wave scattering arising from changing grid spacing (see also Danilov et al. (2004)).

Pain et al. (2005) discuss the current status of finite element unstructured mesh modelling and review the development of a number of methods that address the issues of discretisation and advection, stability and representation of geostrophic balance. Ford et al. (2004a) present the formulation of a three-dimensional finite element model for oceanic simulations, and identify the methods used to overcome the traditional difficulties associated with finite element based ocean models.

Chapter 3

Methodology

3.1 Model formulation

3.1.1 Introduction

ICOM is a three-dimensional non-hydrostatic ocean model that utilizes finite element discretisations on structured or unstructured meshes. This section discusses the formulation of the model, and how it will be implemented for the purpose of investigating open ocean deep convection.

3.1.2 Equations of motion

The Boussinesq approximation to the 3D Navier Stokes equations states that density differences are sufficiently small to be neglected, except in buoyancy terms (terms multiplied by g, the acceleration due to gravity). The use of the non-hydrostatic variation of the equations enables us to investigate OODC without the need for parameterisation. The three-dimensional non-hydrostatic Boussinesq equations (Equations 3.1 - 3.3, presented in their un-discretised form) are discretised within a domain of three-dimensional Euclidean space.

$$\rho_0(\frac{\partial \mathbf{u}}{\partial t} + (\mathbf{u}.\nabla)\mathbf{u} + 2\mathbf{\Omega} \times \mathbf{u}) = -\nabla p - \rho g \mathbf{k} + \nabla.\bar{\bar{\tau}} + \mathbf{F} \tag{3.1}$$

$$\rho_0 \nabla . \mathbf{u} = 0 \tag{3.2}$$

$$\frac{\partial T}{\partial t} + \nabla . (\mathbf{u} T) = \nabla . (\kappa \nabla T) \tag{3.3}$$

Here, $\mathbf{u}$ represents the 3D velocity, p is the perturbation pressure, ρ_0 is the reference density, T is the temperature (or some tracer), $\mathbf{\Omega}$ is the rotation vector and F contains the source terms. The stress tensor $\bar{\bar{\tau}}$ represents the viscous terms (related to the deformation rate tensor using a simple model of sub-grid scale turbulence, see (Ford et al., 2004a) for more details), and κ is the diffusivity tensor.

The linear equation of state (Equation 3.4) is employed:

$$\rho = -\alpha(T - T_0) + \beta(S - S_0) \tag{3.4}$$

where ρ is the perturbation density $\frac{\rho - \rho_0}{\rho_0}$, α is the thermal expansion coefficient, β is the haline contraction coefficient, T_0 is the reference temperature, S is the perturbation salinity and S_0 is the reference salinity.

3.1.3 Boundary conditions

The model is formulated with a number of options for boundary conditions. These include Von Neumann (specifies the values of the normal derivative the solution is to take on the boundary e.g. heating or cooling), Dirichlet (specifies the values a solution takes on the boundary of the domain e.g. zero for velocity) and Robin or mixed boundaries (information is known about the values of a function and the values of its derivative on the boundary). In the following sections the velocity and temperature boundary conditions employed in ICOM are described.

Velocity boundary conditions

On the side walls (North, South, East and West), a no-slip Dirichlet boundary condition is applied as follows:

$$u = v = w = 0 \tag{3.5}$$

On the top and bottom, no normal flow plus free tangential stress (i.e. no force applied by the boundary to the fluid within the domain) is applied:

$$\mathbf{u}.\mathbf{n} = \mathbf{0} \tag{3.6}$$

$$\bar{\bar{\tau}}.\mathbf{n} = \mathbf{0} \tag{3.7}$$

where $\mathbf{n}$ is the normal to that boundary.

Temperature boundary conditions

At the surface, the temperature boundary condition is a combined Dirichlet and Neumann condition specifying the initial surface temperature and a surface temperature flux, and applied across a specified area at the surface nodes. For example, in the initial simplified experiments on 10km square boxes, a temperature flux of $-2.5 * 10^{-4} K m s^{-1}$ was applied to a disk of radius r, centred on the origin (co-ordinates x, y), corresponding to a heat flux of $\sim -1000 W m^{-2}$. Outside of the disk, the boundary condition is Dirichlet and the temperature flux is zero.

At the bottom, the temperature boundary condition is also zero i.e. there is no heat flux and $(\partial T/\partial z) = 0$.

3.1.4 Wind stress

Wind stress can be applied via a user given data file, or from realistic data obtained from climatologies such as ECMWF, and is effectively an alternative surface boundary condition to that given in Equation 3.7. Values of wind speed (u_w, v_w) (usually taken as the air speed at 10m) are interpolated onto the current locations of the mesh nodes at the sea surface. The stress (τ_x, τ_y) at the sea surface is then included as a surface integral of the quantities:

$$\tau_x = C_D \rho_a (u_w - u)(\sqrt{((u_w - u)^2 + (v_w - v)^2)}) \tag{3.8}$$

$$\tau_y = C_D \rho_a (v_w - v)(\sqrt{((u_w - u)^2 + (v_w - v)^2)}) \tag{3.9}$$

where u, v are the water velocity at the sea surface, C_D is a drag coefficient, and ρ_a is the density of air. When $u_w = uandv_w = v$, the wind stress will fall to zero.

The application of a simple wind stress, for example, in the shape of a sinusoidal wave, allows the surface of the domain to be effectively pushed or pulled in a given direction. This in turn has a feedback on the entire domain, forcing the circulation and creating a gyre.

3.1.5 Formulation of the ice field

The freezing point of seawater $T_f = -1.8°C$. For $T > T_f$ no ice is present and $\delta = 0$, where δ is the thickness of ice. Thus, boundary conditions for temperature (T) and salinity (S) are:

$$\kappa_T \frac{\partial T}{\partial z}(z = 0) = \frac{Q}{\rho_0 c_p} \tag{3.10}$$

$$\kappa_S \frac{\partial S}{\partial Z}(z = 0) = 0 \tag{3.11}$$

where κ_T, κ_S are thermal and saline diffusivities respectively, and Q is the surface heat flux, ρ_0 is density of water and c_p is the specific heat capacity of water.

If $T(z = 0) = T_f$, ice forms and $\delta = \epsilon$, where ϵ is $O(10^-5)$. For $T <= -1.8°C$, ice is present and $\delta > 0$:

$$\frac{\partial \delta}{\partial t} = \frac{1}{\rho_i L}[-Q - \rho_0 c_p K(T - T_f)] \tag{3.12}$$

where, ρ_i is density of ice, L is latent heat of ice and $d\delta/dt$ is the change in thickness of ice.

Boundary conditions for the surface when ice is present become:

$$\kappa_T \frac{\partial T}{\partial z} = -K(T - T_f) \tag{3.13}$$

$$\kappa_S \frac{\partial S}{\partial z} = \sigma \frac{\partial \delta}{\partial t} \tag{3.14}$$

where K is the turbulent exchange coefficient and $\sigma = S_s - S_i$, the difference

in salinity between seawater and ice. When the ice melts, $\delta = 0$, and the original boundary conditions are reinstated.

3.1.6 Relaxation of boundary conditions

One possible technique for simulating a gyre within the domain is to use sponge regions with a relaxation in temperature at the boundaries on the sidewalls to initiate a thermal gradient and drive flow. This is achieved using a combination of source and absorption terms. Source terms are already included in Equation 3.1 (**F**). The absorption terms take the form of a relaxation $-\lambda T$ on the right hand side of the field equations, acting to dissipate energy. The parameter λ has the dimensions $1/time$ and may be used to control the time over which the relaxation occurs $O(days)$.

By using such a relaxation in the temperature field, the flow of warm water into the domain via the South-East corner and cold water into the North-West corner (as seen in the Greenland Sea) can be replicated in the model domain.

3.1.7 Momentum and advection

The model (ICOM) contains a number of options for employing varying momentum and advection schemes. With the convective problem in mind, the momentum scheme employed for the treatment of the transport terms in the momentum equations throughout the duration of this investigation is for no balancing diffusion. This essentially means that no implicit numerical viscosity or diffusivity is added to the system; that is, it is a second order centred scheme in space. The advection scheme for the treatment of transport terms in temperature-like fields is the Crank-Nicolson method in time, and the standard Galerkin approach in space (these are again second order centred in time and space). For further details on the underlying numerical methods within ICOM, the reader is referred to Ford et al. (2004a) and Pain et al. (2005).

3.1.8 Numerical techniques

It is considered not necessary here to discuss the basis of the finite element method as it is not fundamental to the understanding and investigation of the convective problem. The reader is referred to Peiro and Sherwin (2005) for a concise description of numerical methods for partial differential equations, including finite difference, finite element and finite volume methods.

3.2 Experimental design

This investigation is intended to work towards the production of a simplified Greenland Sea basin in which a sensitivity study of model convection may be conducted. Initially a simplified, small scale box model will be employed to determine the model's ability to capture convection. The impact of numerical diffusivity and viscosity within the finite element model will be determined as a contribution to ongoing model validation, reflecting the developmental nature of ICOM. Similarly, the employment of adaptive mesh techniques and any advantages and disadvantages in their application to the convective problem will be determined in a quantitative manner through the use of various comparative model runs. This will enable informed decisions to be made concerning the ability of the adaptive mesh to capture convection and identify any drawbacks. Further investigations into the differences in observed model convection due to the choice of convective forcing will also be considered. Lastly, a study of ICOM's ability to model convection in an ever more realistic model domain will consider the impact of stratification similar to that which prevails in the Greenland Sea. The results gained from such a study will hopefully enable further work in future using gradually more complicated domains including the introduction of bathymetry, wind stress, thermal gradients and ice which have unfortunately been beyond the scope of this thesis.

Table 3.1 shows the parameters and their values which remain constant throughout the experiments analysed and discussed in Chapter's 5 and 6. The majority of experiments undertaken implement large viscosities and diffusivities in order to maintain numerical stability at the resolution used. Such viscosities and diffusivities are not reflective of the real environment however and this must be considered within any conclusions drawn in relation to

OODC in the Greenland Sea.

Table 3.1: Summary of parameters to remain constant/default values.

Parameter	Value	Units
Heat flux (surface)	-1000	Wm^{-2}
Viscosity x	5.0	m^2s^{-1}
Viscosity y	5.0	m^2s^{-1}
Viscosity z	0.2	m^2s^{-1}
Diffusivity x	5.0	m^2s^{-1}
Diffusivity y	5.0	m^2s^{-1}
Diffusivity z	0.2	m^2s^{-1}
Thermal expansion coefficient α	$2.5 * 10^{-4}$	K^{-1}
Coriolis parameter	$1.4 * 10^{-4}$	s^{-1}
Initial domain temperature	0.0	$^{\circ}C$
Domain size (x,y,z)	10 x 10 x 3.6	km
Timestep	300	s
Total run time	72	hours
Mesh adapt time	3599.9	s

The sequence of work commenced with a study into the presence of numerical diffusivity within ocean models. This was followed by a series of convective experiments comparing model convection on fixed and adaptive meshes. The use of adaptive meshes in investigating penetrative convection was finally considered.

3.2.1 Investigating numerical diffusivity

Because the use of an adaptive, unstructured mesh in the investigation of OODC is novel, it is useful to obtain some idea of the effective numerical diffusion within ICOM, in comparison with extant models. For this purpose, a simple 2D domain was used to replicate the linear instability as posed (and solved) by Chandrasekhar (1961). The methodology, results and discussion of this investigation comprise Chapter 4.

3.2.2 Modelling convection - small scale tests

In order to gain a useful insight into OODC using ICOM, it is important to ascertain the advantages and disadvantages of the use of an adaptive, unstructured mesh, and develop a model setup that enables the structure

and evolution of OODC to be studied in a quantitative way. To this end, a series of initial experiments are conducted using a small scale domain ($10km$ x $10km$). Quantitative comparisons of the impact on OODC of fixed and adaptive meshes, uniform and disk shaped cooling, and continuous and finite cooling periods are made. The results and discussion of the investigations are presented in Chapter 5.

Each model configuration was run for a period of 72 hours, and the development of convection monitored using the methods described in Section 3.3. In total, seven model configurations were designed. The details of each model run are given in Table's 3.2 - 3.8.

Table 3.2: Summary of model inputs and setup - continuous uniform cooling on a fixed, structured mesh.

Parameter	Value
Chapter and section reference	(5.2 1), (5.3 3), (5.4 2)
Cooling area	Uniform across the whole domain
Cooling duration	Continuous for 72 hours
Mesh option	Fixed
Mesh resolution (points) (x,y,z)	$50 * 50 * 24$
Mesh resolution (distance)(x,y,z) (km)	$0.2 * 0.2 * 0.15$

Table 3.3: Summary of model inputs and setup - continuous uniform cooling on an adaptive, unstructured mesh.

Parameter	Value
Chapter and section reference	(5.2 2)
Cooling area	Uniform across the whole domain
Cooling duration	Continuous for 72 hours
Mesh option	Adaptive
Initial mesh resolution (points) (x,y,z)	$30 * 30 * 10$
Mesh resolution (distance)(x,y,z) (km)	$0.33 * 0.33 * 0.36$
Maximum element size (x,y,z) (km)	$5.0, 5.0, 1.0$
Minimum element size (x,y,z) (km)	$0.2, 0.2, 0.1$

Table 3.4: Summary of model inputs and setup - finite uniform cooling on a fixed, structured mesh.

Parameter	Value
Chapter and section reference	(5.2 3), (5.3 4), (5.4 4)
Cooling area	Uniform across the whole domain
Cooling duration	Finite for 24 hours
Mesh option	Fixed
Mesh resolution (points) (x,y,z)	$50 * 50 * 24$
Mesh resolution (distance)(x,y,z) (km)	$0.2 * 0.2 * 0.15$

Table 3.5: Summary of model inputs and setup - finite uniform cooling on an adaptive, unstructured mesh.

Parameter	Value
Chapter and section reference	(5.2 4)
Cooling area	Uniform across the whole domain
Cooling duration	Finite for 24 hours
Mesh option	Adaptive
Initial mesh resolution (points) (x,y,z)	$30 * 30 * 10$
Mesh resolution (distance)(x,y,z) (km)	$0.33 * 0.33 * 0.36$
Maximum element size (x,y,z) (km)	$5.0, 5.0, 1.0$
Minimum element size (x,y,z) (km)	$0.2, 0.2, 0.1$

Table 3.6: Summary of model inputs and setup - continuous disk cooling on a fixed, structured mesh.

Parameter	Value
Chapter and section reference	(5.2 5), (5.3 1), (5.4 1)
Cooling area	Disk of radius $3km$
Cooling duration	Continuous for 72 hours
Mesh option	Fixed
Mesh resolution (points) (x,y,z)	$50 * 50 * 24$
Mesh resolution (distance)(x,y,z) (km)	$0.2 * 0.2 * 0.15$

Table 3.7: Summary of model inputs and setup - continuous disk cooling on an adaptive, unstructured mesh.

Parameter	Value
Chapter and section reference	(5.2 6)
Cooling area	Disk of radius $3km$
Cooling duration	Continuous for 72 hours
Mesh option	Adaptive
Initial mesh resolution (points) (x,y,z)	$30 * 30 * 10$
Mesh resolution (distance)(x,y,z) (km)	$0.33 * 0.33 * 0.36$
Maximum element size (x,y,z) (km)	$5.0, 5.0, 1.0$
Minimum element size (x,y,z) (km)	$0.2, 0.2, 0.1$

Table 3.8: Summary of model inputs and setup - finite disk cooling on a fixed, structured mesh.

Parameter	Value
Chapter and section reference	(5.3 2), (5.4 3)
Cooling area	Disk of radius $3km$
Cooling duration	Finite for 24 hours
Mesh option	Fixed
Mesh resolution (points) (x,y,z)	$50 * 50 * 24$
Mesh resolution (distance)(x,y,z) (km)	$0.2 * 0.2 * 0.15$

3.2.3 Penetrative convection into a stratified domain

In an extension to the simplified experiments outlined in Section 3.2.2, the impact of the inclusion of a background stratification on model convection was designed. The details of this model run are presented in Table 3.9, and the results of the investigation comprise Chapter 6. The inclusion of stratification represents an initial step towards the gradual complication of the model domain and the use of a more realistic domain within which to study convective behaviour. The introduction of stratification presents an opportunity to ascertain whether ICOM is capable of resolving interesting convective behaviour such as penetrative convection (whereby convective plumes 'dip' into denser layers of stratification), as opposed to the 'pure' convective problem into an unstratified domain as experimented with initially.

Table 3.9: Summary of model inputs and setup - continuous uniform cooling on an adaptive, unstructured mesh with stratification.

Parameter	Value
Chapter and section reference	6.2
Cooling area	Uniform across the whole domain
Cooling duration	Continuous for 168 hours
Mesh option	Adaptive
Initial mesh resolution (points) (x,y,z)	$30 * 30 * 10$
Mesh resolution (distance)(x,y,z) (km)	$0.33 * 0.33 * 0.36$
Maximum element size (x,y,z) (km)	$5.0, 5.0, 1.0$
Minimum element size (x,y,z) (km)	$0.2, 0.2, 0.1$
Diffusivity z $m^2 s^{-1}$	0.01
Thermal expansion coefficient α K^{-1}	$5.0 * 10^{-5}$
Run duration	168 hours

The background stratification was set as follows:

$$T = T_0 + T_1(z - z_0) + T_2 tanh((z - z_0)/\lambda) \tag{3.15}$$

where $z_0 = 2000m$, $T_1 = 1 * 10^{-5\circ}C$, $\lambda = 100m$ and $T_2 = 5.0 * 10^{-2\circ}C$. This produces a stratification comprised of 2 layers, a weakly stratified layer down to approximately 2000m, and a bottom layer of strongly stratified fluid. The strong cooling of the upper layer allows the assessment of the scale and penetrative power of convective plumes into the stratified domain.

3.3 Diagnostics

To quantify the variations in model convection between comparative runs, times series of mean temperature at depths within the model domain and depth profiles of mean temperature at discrete time intervals are used. From these, the onset and nature of convection can be estimated. The strength and depth of convection is identified from depth profiles of mean horizontal velocity and mean vertical velocity. Skewness of the vertical velocity is used to determine associated upwelling and downwelling. Cross-sections of the temperature field through the centre of the domain along the line x=5km (i.e. north-south) every 24 hours enable visualisation of the convective process and identification of the theoretical stages of convection. Contour plots of vertical velocity with overlaid directional velocity vectors at varying depths within the domain enable visualisation of the dynamical nature of the convective process.

The scaling ideas presented in Chapter 2 Sections 2.2.2 and 2.2.2 present an opportunity to make a comparison of the model simulations with expectations from theory. Consequently, the ratio of observed model vertical velocity to w_{norot} and w_{rot} are compared, in order to quantify the agreement of model observations with theoretical scaling predictions, and identify the regime in which the observed model convection falls.

Chapter 4

Quantifying numerical diffusivity within ocean models using linear instability theory

4.1 Introduction

Because numerical fluid models depend on a discretisation of a continuous problem, issues of accuracy and stability feature heavily in comparisons between models. In the case of oceanographic models, observations suggest that effective ('eddy') diffusivities, either lateral or isopycnal, are small. Extant model schemes, however, not only require explicit diffusivities and viscosities large enough to give numerical stability, but also imply intrinsic numerically-induced mixing of order $u\Delta$, where u and Δ are a typical velocity and nodal separation. For a coarse resolution climate model, $u = 0.02ms^{-1}$, $\Delta = 100km$, the numerical mixing is of order $2 \times 10^3 m^2 s^{-1}$, which is typically the order of magnitude of the applied explicit mixing. Numerical models are thus rather more diffusive and viscous than modellers would wish.

Measuring the effective mixing present in a model is not easy, since oceanographers lack good test cases against which to run (Paluskiewicz and Romea, 1997). Here a useful test case is presented which enables the fairly accurate diagnosis of the product of the total (explicit plus implicit) diffusiv-

ity and viscosity in non-hydrostatic ocean models. This unfortunately limits the applicability of the test, as most ocean models are hydrostatic. However, the test is applied to two models: the MITGCM, and the Imperial College Ocean Model (ICOM) (in fixed, structured and adaptive, unstructured grid modes). The MITGCM is a fixed, hexahedral finite volume ocean model with a non-hydrostatic capability, enabling a direct comparison with ICOM in fixed, hexahedral mode. The difference in the underlying mathematical basis of the two models is likely to result in some differences in the presence of numerical viscosity and diffusivity. The finite element basis of ICOM allows higher-order conservation than finite volume methods, and as such, it may be reasonably expected that ICOM will show reduced numerical diffusion in comparison with MITGCM in this mode. However, the assessment of numerical diffusion within MITGCM will provide a benchmark value for comparison with other modes within ICOM, including the adaptive tetrahedral mode.

4.2 Background

As the use of an adaptive, unstructured mesh model is novel in investigating Greenland Sea open ocean deep convection, it is of interest to assess the accuracy of the ICOM model, and the amount of numerical diffusion present. Parallel plate convection, whose linear stability was solved by Chandrasekhar (1961), provides a simple test problem for this purpose. An infinitely wide pair of horizontally oriented parallel plates are separated by a depth h, and between them is a fluid with viscosity μ and diffusivity κ. The fluid is at rest, in which a uniform unstable temperature gradient is maintained by heating from below, giving a bottom-to-top temperature difference of ΔT. The top and bottom temperatures are held fixed (at 0, ΔT without loss of generality). As a result of thermal expansion, the fluid at the bottom will be lighter than the fluid at the top, thus the arrangement is potentially unstable. There is therefore a tendency for the fluid to redistribute itself. Such redistribution, however, is inhibited by the fluid's own viscosity. Thus the unstable temperature gradient maintained must exceed some value before instability can set in. What decides the stability, or otherwise, of a layer of fluid heated from below is the numerical value of the non-dimensional

Rayleigh number, R defined as:

$$R = \frac{g\alpha\Delta T}{\kappa\nu}d^3 \tag{4.1}$$

where g is acceleration due to gravity, d is the depth of the layer, ΔT is the temperature difference between the plates, α, κ and ν are the coefficients of thermal expansion, thermal diffusivity and kinematic viscosity respectively. Instability must set in when R exceeds a critical value R_c (with a corresponding critical temperature gradient).

For an idealised problem with a set of physical parameters with known properties, a solution for R_c can be calculated. Chandrasekhar (1961) calculated R_c for 3 combinations of top and bottom boundary conditions, summarised in Table 4.1. MITGCM and ICOM were configured to simulate as closely as possible the same problem as posed by Chandrasekhar (1961). The fluid is contained between the planes $z = 0$ and $z = 1$. The surfaces are maintained at constant temperatures, and the normal velocity vanishes. The boundary conditions for vertical velocity (w) and the perturbation in temperature from the background state ($\hat{\theta}$) are as follows:

$$\hat{\theta} = 0 \text{ and } w = 0, \text{ and } \frac{d^2\hat{\theta}}{dz^2} = \frac{d^2w}{dz^2} = 0 \text{ at } z = 0, 1 \tag{4.2}$$

Table 4.1: R_c for varying boundary conditions. Reproduced from Chandrasekhar (1961).

Boundary conditions (top and bottom)	R_c
Both free	657.511
Both rigid	1707.762
One rigid and one free	1100.65

By initialising the problem in a numerical scheme with infinitesimal random fluctuations in the temperature field, it is simple to monitor the kinetic energy of the system. If numerically stable, the kinetic energy will fluctuate and decay; if unstable, it will grow, and during the time in which the perturbations remain sufficiently small the growth rate so estimated will asymptote to what, in a continuous problem, would be the predicted growth rate for the specified Rayleigh number. Long numerical runs are not required, as all that

is necessary is to locate the numerical critical Rayleigh number R_n, which will be larger than R_c. This implies that the effective numerical values of viscosity and diffusivity (ν_n, κ_n) have a product given by:

$$E = \frac{\nu_n \kappa_n}{\kappa \nu} = \frac{R_n}{R_c} > 1 \tag{4.3}$$

The amount by which this ratio exceeds unity is thus a measure of the effective mixing induced by the tracer advection scheme acting on the temperature field.

It is hard to tell which of κ and ν is of most importance for the stability criteria. For small perturbations, the momentum equations do not contain advection, so the ratio is biased towards dependency on κ rather than ν, but to an unspecified degree. However, if we assume that the order of implicit (numerical) numerical mixing induced by κ is the same as for ν, the individual weights may be estimated as follows:

$$\nu\kappa = (\nu_0 + \nu_n)(\kappa_0 + \kappa_n) \tag{4.4}$$

where ν_0 and κ_0 are the explicit (defined) values of viscosity and diffusivity respectively.

For $\nu_n, \kappa_n \sim u\Delta x << \nu_0, \kappa_0$:

$$\nu\kappa \sim \nu_0\kappa_0 + \nu_0(Au.\Delta x) + \kappa_0(Bu.\Delta x) \tag{4.5}$$

where A and B are the respective weights for implicit viscosity and diffusivity respectively.

Initially, the MITgcm and ICOM were run for varying Rayleigh numbers by setting the temperatures at the top and bottom boundaries. The horizontal boundaries had the condition rigid and Dirichlet. The domain within the ICOM model was a thin rectangle of 20m length, 0.01m width and 1m depth, with 400 points in the horizontal x-direction, 1 point in the y-direction (i.e. an idealised 2D domain - ocean models are almost always configured in 3D), and 50 points in the vertical. The timestep was 0.25s. MITgcm was run at a lower resolution (200 points in x, 2 points in y, and 40 points in z) but smaller time step, in order to preserve numerical stability (see Table 4.2). Although the configurations are not strictly the same, Killworth (Personal Communication) has shown that once a certain critical vertical resolution is

Table 4.2: ICOM and MITgcm configurations for the investigation of numerical diffusivity.

Parameter	ICOM	MITgcm
Viscosity, ν (ms^{-2})	0.01	0.01
Diffusivity, κ (ms^{-2})	0.01	0.01
ΔT (s)	0.25	0.01
Model Run Time (s)	500.0	500.0
Δx (m)	0.05	0.1
Δy (m)	0.01	0.1
Δz (m)	0.02	0.025

exceeded, the ability to resolve the critical Rayleigh number does not improve, and both runs are above this resolution (see Appendix A for the work by Killworth on the impact of varying vertical resolution within a finite difference discretisation of the solution found by Chandrasekhar (1961)). The initial model setup included a ratio of vertical to horizontal diffusivity equal to 1. This ratio impacts the numbers expected from theory (Killworth has also shown this, and the work is included in Appendix B). In particular, for this case, the expected critical Rayleigh number for two free boundaries is 657.511 as in the theory, however, for varying ratio of vertical and horizontal diffusivity, the critical Rayleigh number will also vary.

ICOM was run for $R = 100, 200, 300, 400, 500, 600, 700, 800, 900$ and 1000 on three mesh configurations - fixed structured hexahedral, fixed structured tetrahedral and adaptive unstructured tetrahedral. Examples of the mesh configurations can be seen in Figure 4.1. MITgcm was run for $R = 600-1000$, on a structured grid similar to that shown in Figure 4.1(a).

By extracting the kinetic energies over time for each model run, the growth rate, σ, of any instability can be calculated from Equation 4.6 by plotting a graph of $\log \sqrt{KE}$ against time and fitting a regression analysis to the part of the graph exhibiting linear growth.

$$KE = e^{2\sigma t} \tag{4.6}$$

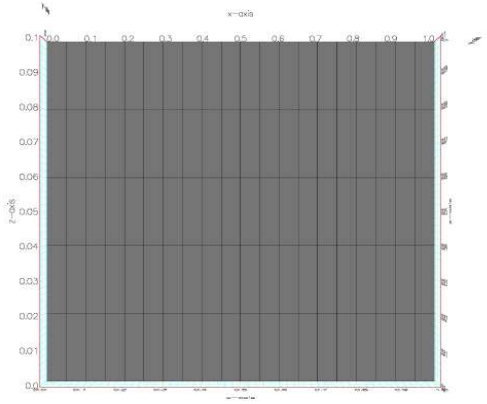

(a) Fixed hexahedral ICOM mesh

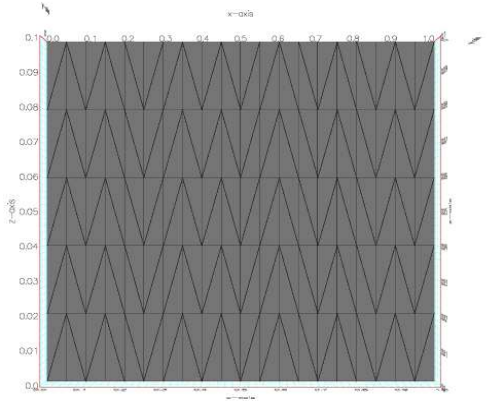

(b) Fixed tetrahedral ICOM mesh

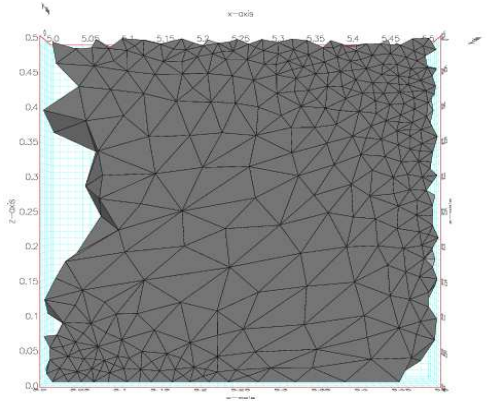

(c) Adaptive tetrahedral ICOM mesh

Figure 4.1: Examples of each of the mesh options available within ICOM.

4.3 Quantifying numerical diffusivity

4.3.1 Calculating the numerical diffusivity within ICOM using a fixed hexahedral mesh

Figures 4.2, 4.3, 4.4, 4.5 and 4.6 show the square root of kinetic energy plotted on a logarithmic scale for the ICOM fixed hexahedral mesh model runs $R = 100$ to $R = 1000$. The graph implies that for a temperature gradient between the top and bottom boundaries corresponding to Rayleigh numbers of 100 - 600, no instability is amplified. Thus, the critical Rayleigh number for this configuration must be greater than 600.

For the model run $R = 700$, a rise in the kinetic energy contained in the system over time in comparison with the lower Rayleigh number runs was detected. It can be seen that significant periods of linear growth are observed in runs corresponding to Rayleigh numbers greater than 700. The gradient of the line during these periods corresponds to the growth rate of the instability, and is calculated across all Rayleigh numbers. These growth rates are then plotted against Rayleigh number, and the Rayleigh number at the intersection of the line of best fit with $\sigma = 0$ is used to infer the model critical Rayleigh number (R_n) (Figure 4.7). Figure 4.6 shows that for the $R = 1000$ run the period of linear growth is finite, and from this it can be inferred that the timescale of linear growth decreases as the Rayleigh number increases.

For the ICOM fixed hexahedral mesh, a model critical Rayleigh number R_n of approximately 699 was found using linear interpolation.

A clear signature of the growth of the instability can be seen in the temperature field (Figure 4.8). The initial gradient varies from 0°C at the top boundary to approximately 50°C at the bottom boundary in the $R = 1000$ run, and visibly perturbs at 300s (Figure 4.8(d)) developing a characteristic cell-like structure by 500s (Figure 4.8(f)). This pattern also manifests itself in the vertical velocity field (Figure 4.9), where the instability of the arrangement is evident initially as weak cells. These cells become gradually stronger and more defined with time. It may be noted that some cells exhibit higher vertical velocities than others, thought to result from the random perturbation applied to the initial state. The maximum absolute vertical velocity observed is approximately $0.03ms^{-1}$.

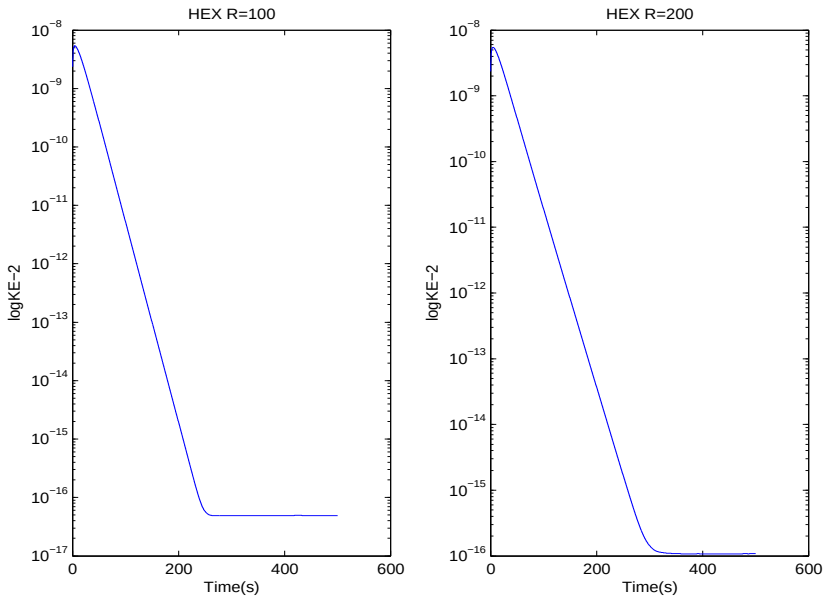

Figure 4.2: Plot of $\log \sqrt{KE}$ against time for ICOM fixed hexahedral runs $R = 100$ and $R = 200$ showing a decrease in the kinetic energy of the system over time, implying a negative growth rate.

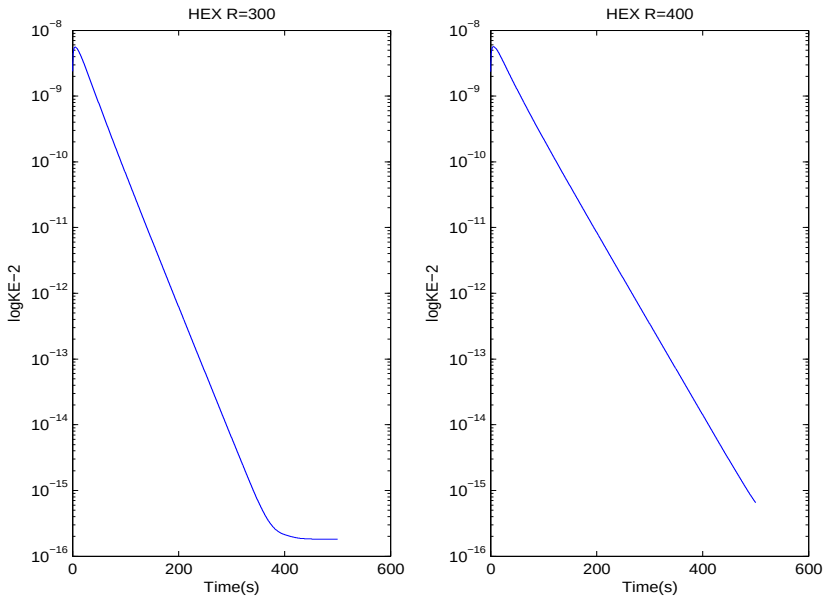

Figure 4.3: Plot of $\log \sqrt{KE}$ against time for ICOM fixed hexahedral runs $R = 300$ and $R = 400$ showing a decrease in the kinetic energy of the system over time, implying a negative growth rate.

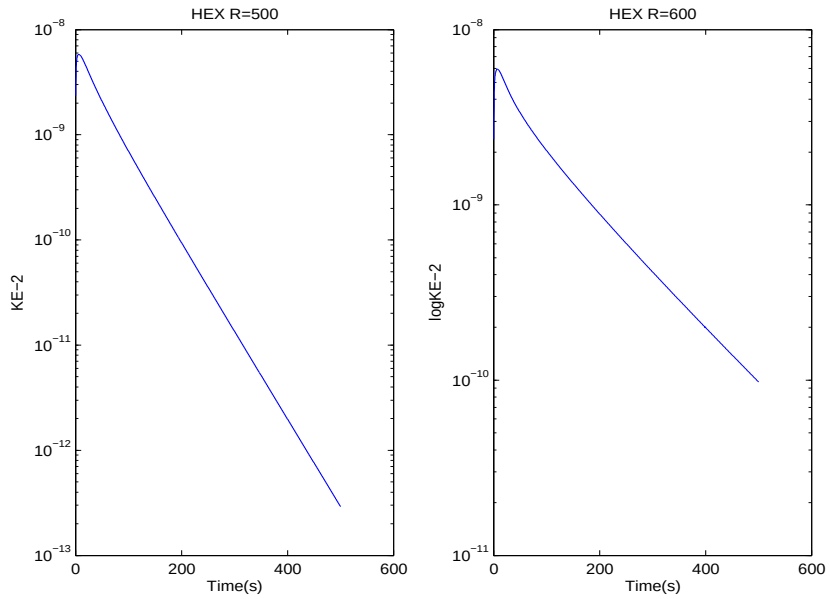

Figure 4.4: Plot of $\log \sqrt{KE}$ against time for ICOM fixed hexahedral runs $R = 500$ and $R = 600$, showing a decrease in the kinetic energy of the system over time, implying a negative growth rate.

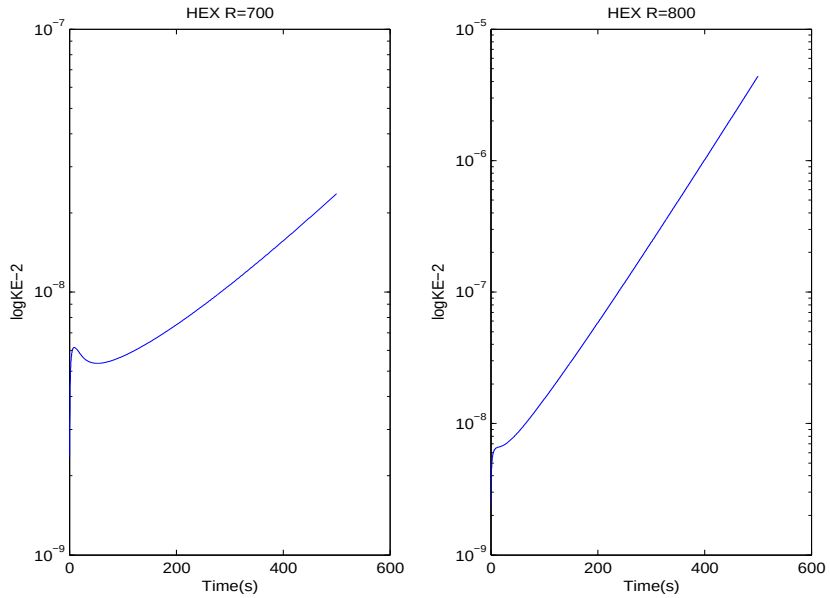

Figure 4.5: Plot of $log\sqrt{KE}$ against time for ICOM fixed hexahedral runs $R = 700$ - 800, showing an increase in the kinetic energy of the system, implying a positive growth rate. The onset of increasing kinetic energy in the $R = 700$ run suggests the numerical critical Rayleigh number R_n for the fixed hexahedral ICOM configuration lies somewhere between $R = 600$ and $R = 700$.

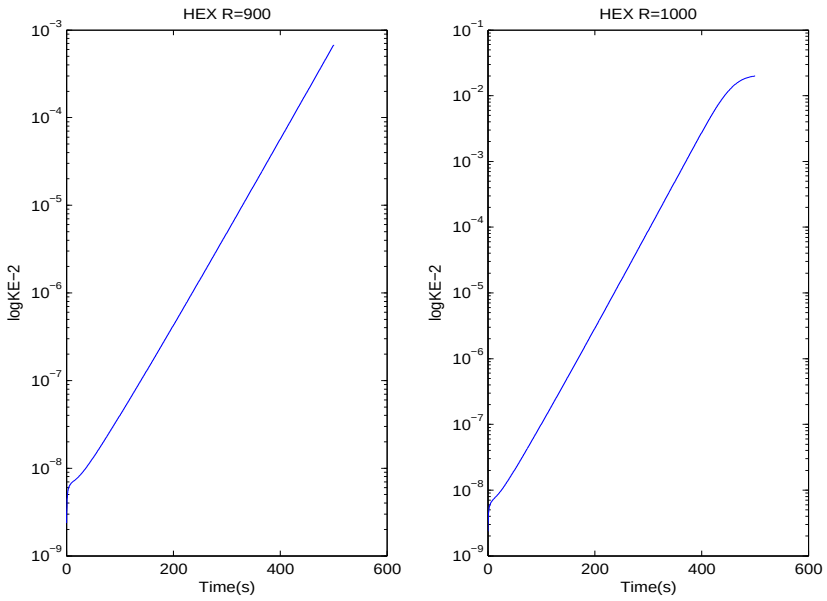

Figure 4.6: Plot of $\log \sqrt{KE}$ against time for ICOM fixed hexahedral runs $R = 900$ and $R = 1000$, showing continued increases in the amount of kinetic energy in the system over time, suggesting an increasing growth rate with increasing Rayleigh number.

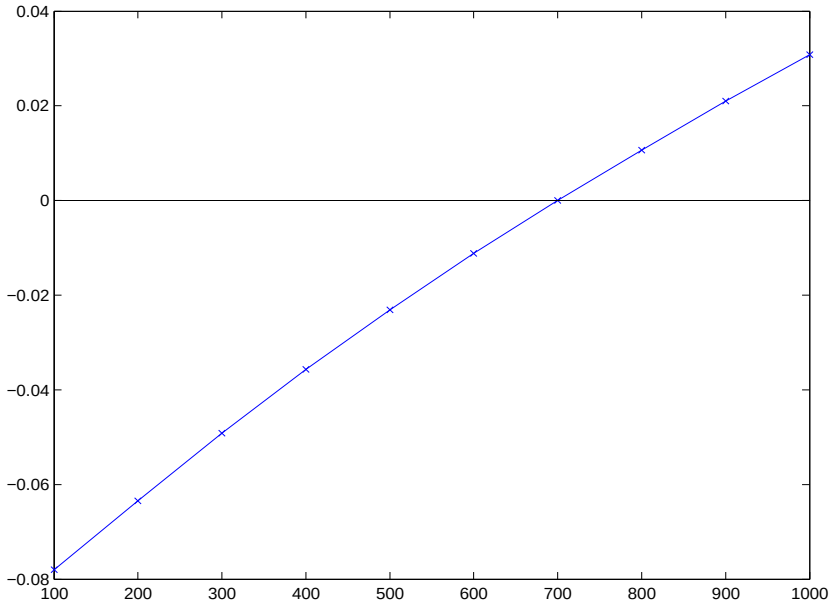

Figure 4.7: Plot of σ against Rayleigh number for each ICOM fixed hexahedral run $R = 100$ - 1000, showing an increase in growth rate with increasing Rayleigh number. The point at which $\sigma = 0$ indicates the critical Rayleigh number for the fixed hexahedral model configuration in ICOM, and is in this case approximately 700.

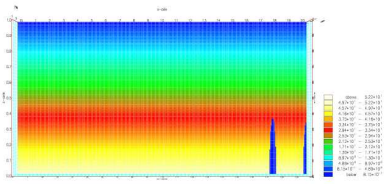

(a) t=0s

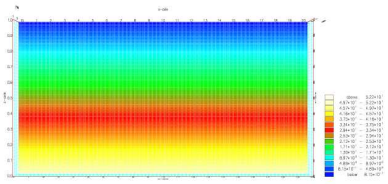

(b) t=100s

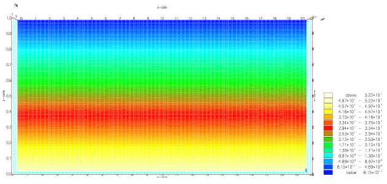

(c) t=200s

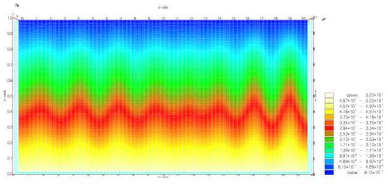

(d) t=300s

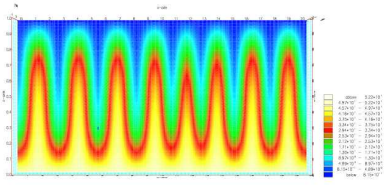

(e) t=400s

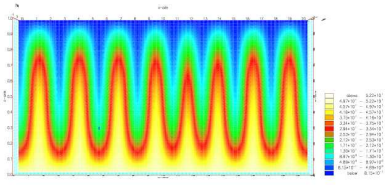

(f) t=500s

Figure 4.8: Evolution of the temperature field over time for the fixed hexahedral ICOM R=1000 runs, showing the initial stratification at time zero, through to the onset of instability evident at 300s and the fully perturbed state at 500s.

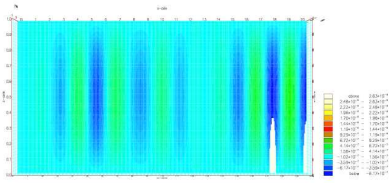

(a) t=0s

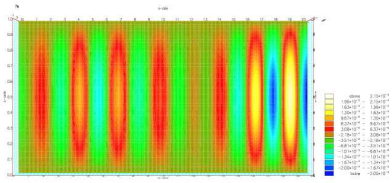

(b) t=100s

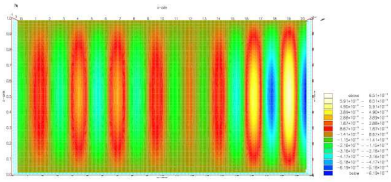

(c) t=200s

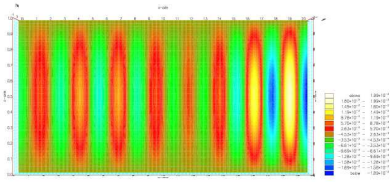

(d) t=300s

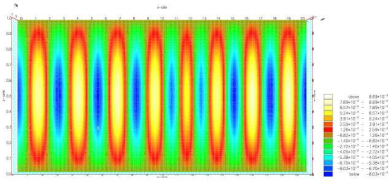

(e) t=400s

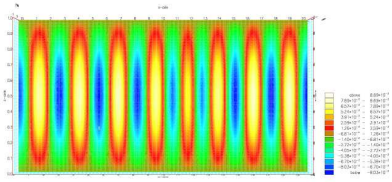

(f) t=500s

Figure 4.9: Evolution of the vertical velocity field over time for the fixed hexahedral ICOM R=1000 runs, showing the presence of weak cells at time zero (implying instability is present) and the development of well defined symmetrical cells as the instability grows over time.

4.3.2 Calculating the numerical diffusivity within ICOM using a fixed tetrahedral mesh

Figures 4.10, 4.11, 4.12, 4.13 and 4.14 show the square root of kinetic energy plotted on a logarithmic scale for the ICOM fixed tetrahedral mesh model runs for $R = 100$ to $R = 1000$. For a temperature gradient between the top and bottom boundaries corresponding to Rayleigh numbers of 100 - 700 no instability is amplified. This suggests that the critical Rayleigh number for this configuration must be greater than 700. For the model run $R = 800$, a rise in the kinetic energy contained in the system over time in comparison with the lower Rayleigh number runs was observed. Significant periods of linear growth are observed in runs corresponding to Rayleigh numbers greater than 800. The gradient of the line, corresponding to the growth rate of the instability, was calculated for all Rayleigh numbers. These growth rates were then plotted against Rayleigh number, and the Rayleigh number at the intersection of the line of best fit with $\sigma = 0$ used to infer the model critical Rayleigh number (R_n) (Figure 4.15).

For the ICOM fixed tetrahedral mesh, a model critical Rayleigh number R_n of 706 was found. This suggests that the fixed tetrahedral mesh configuration produces a slightly higher amount of numerical diffusivity in comparison with the fixed hexahedral configuration.

The higher numerical diffusivity observed in the fixed tetrahedral run is due to the complexity of the mathematics underlying the formulation of the tetrahedral mesh in comparison with the hexahedral mesh, making the hexahedral mesh more accurate for the same mesh resolution (this is a developmental issue - ICOM does not presently have the ability to adapt hexahedral meshes, which is why tetrahedral meshes are employed at the small cost of accuracy demonstrated in this series of experiments).

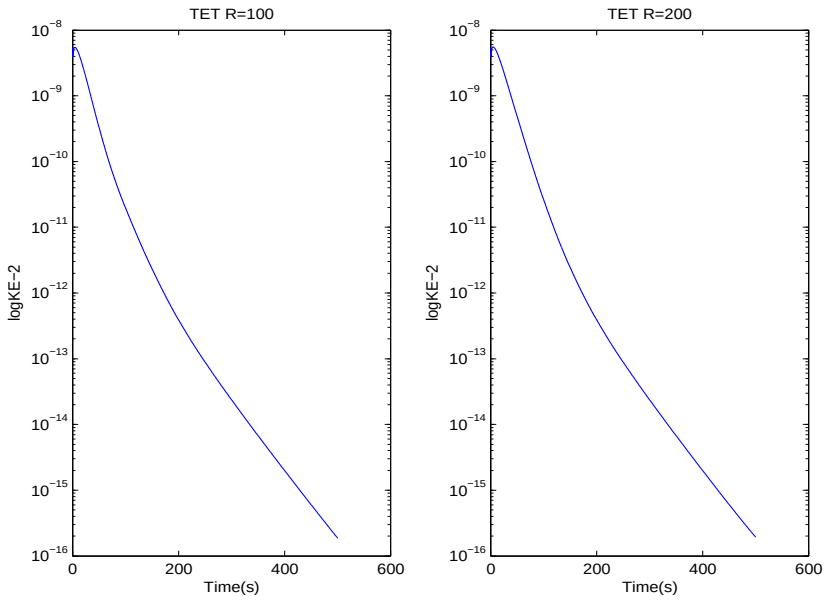

Figure 4.10: Plot of $\log \sqrt{KE}$ against time for ICOM fixed tetrahedral runs $R = 100$ and $R = 200$ showing a decrease in the kinetic energy of the system over time, implying a negative growth rate.

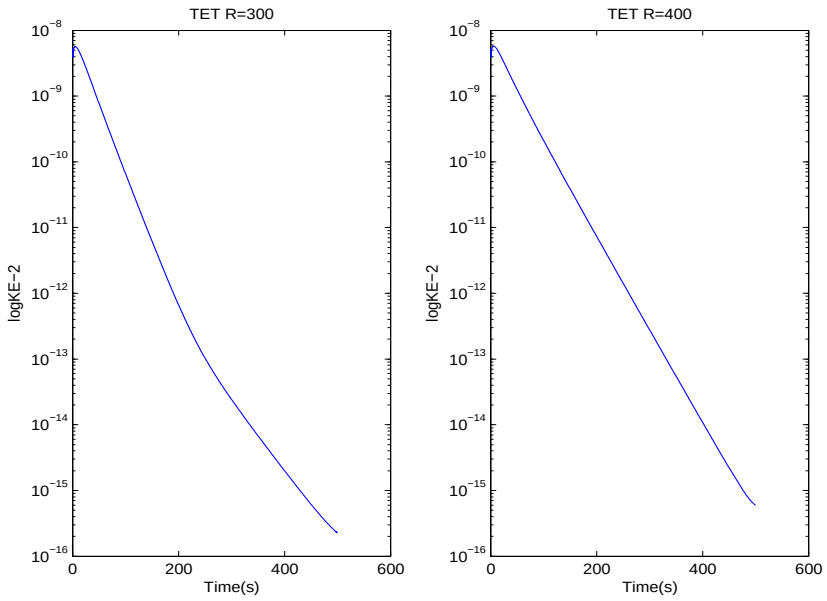

Figure 4.11: Plot of $\log \sqrt{KE}$ against time for ICOM fixed tetrahedral runs $R = 300$ and $R = 400$ showing a decrease in the kinetic energy of the system over time, implying a negative growth rate.

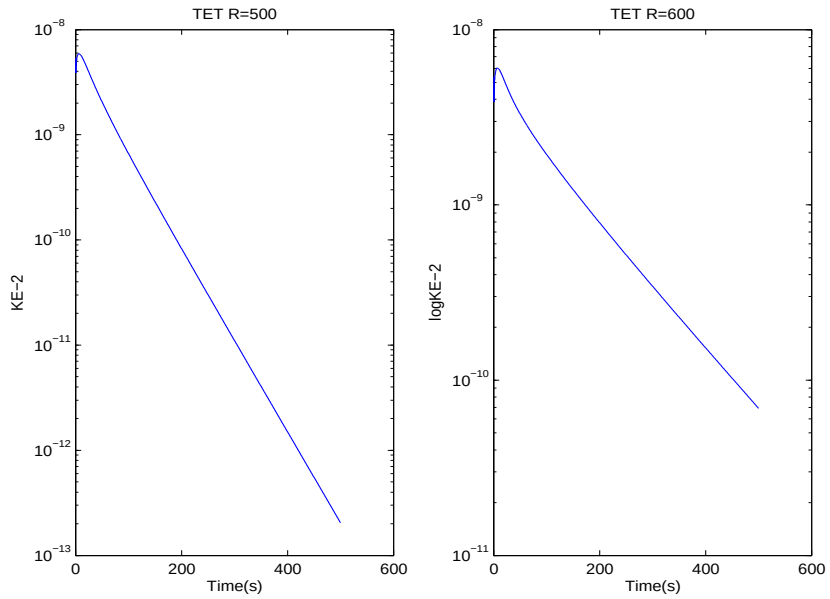

Figure 4.12: Plot of $\log \sqrt{KE}$ against time for ICOM fixed tetrahedral runs $R = 500$ and $R = 600$, showing a decrease in the kinetic energy of the system over time, implying a negative growth rate.

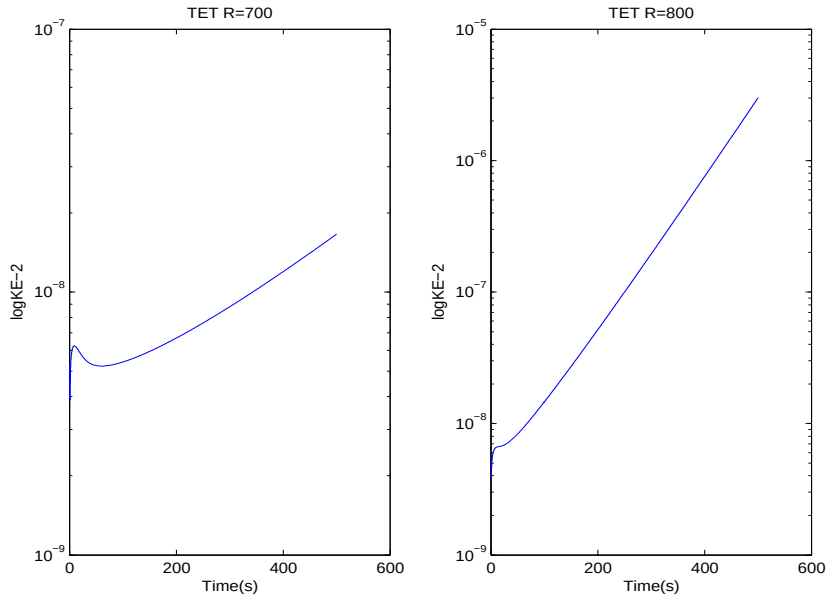

Figure 4.13: Plot of $\log \sqrt{KE}$ against time for ICOM fixed tetrahedral runs $R = 700$ and $R = 800$, showing an increase in the kinetic energy of the system, implying a positive growth rate. The onset of increasing kinetic energy in the $R = 800$ run suggests the numerical critical Rayleigh number R_n for the fixed tetrahedral ICOM configuration lies somewhere between $R = 700$ and $R = 800$.

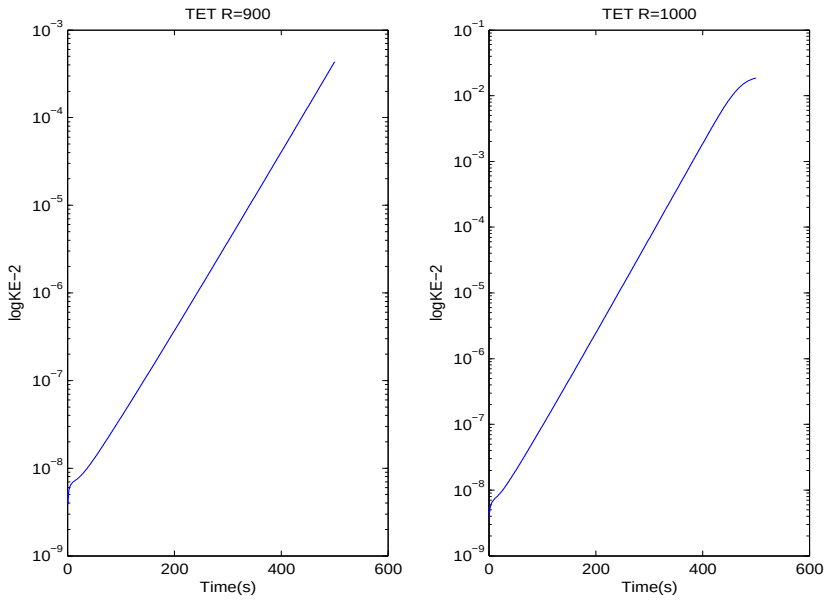

Figure 4.14: Plot of $\log \sqrt{KE}$ against time for ICOM fixed tetrahedral runs $R = 900$ and $R = 1000$, showing continued increases in the amount of kinetic energy in the system over time, suggesting an increasing growth rate with increasing Rayleigh number.

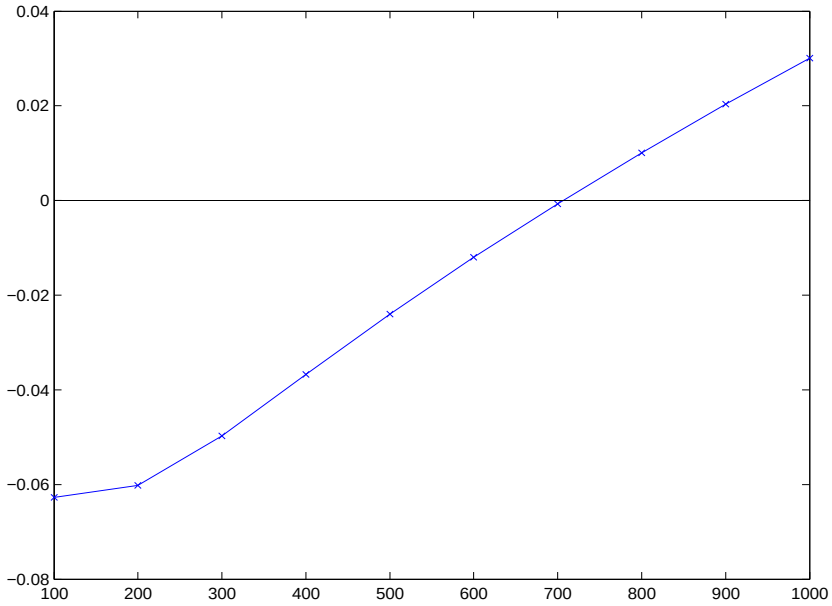

Figure 4.15: Plot of σ against Rayleigh number for each ICOM fixed tetrahedral run $R = 100$ - 1000, showing an increase in growth rate with increasing Rayleigh number. The point at which $\sigma = 0$ indicates the critical Rayleigh number for the fixed tetrahedral model configuration in ICOM, and is in this case approximately 706.

4.3.3 Calculating the numerical diffusivity within ICOM using an adaptive tetrahedral mesh

Figures 4.16, 4.17, 4.18, 4.19 and 4.20 show the square root of kinetic energy plotted on a logarithmic scale for the ICOM adaptive tetrahedral mesh model runs $R = 100$ to $R = 1000$. The trend in kinetic energy is obvious despite the presence of spikes, resulting from an issue with continuity when interpolating between adapted meshes (a model development issue). The order of magnitude associated with these spikes is so small that for runs where instability occurs, kinetic energy is so large these spikes become insignificant. No instability is amplified for a temperature gradient between the top and bottom boundaries corresponding to Rayleigh numbers of 100 - 700. Thus, the critical Rayleigh number for this configuration must be greater than 700. For the model run $R = 800$, a rise in the system kinetic energy over time was observed (in comparison with the lower Rayleigh number runs). Significant periods of linear growth are observed in runs corresponding to Rayleigh numbers greater than 800. The gradient of the line during these periods (corresponding to the growth rate of the instability) is calculated across all Rayleigh numbers. These growth rates are plotted against Rayleigh number, and the Rayleigh number at the intersection of the line of best fit with $\sigma = 0$ used to identify the model critical Rayleigh number (R_n) (Figure 4.21).

For the ICOM adaptive tetrahedral mesh, a R_n of 712 was found. This suggests that the adaptive tetrahedral mesh configuration produces a higher amount of numerical diffusivity in comparison with both the fixed tetrahedral configuration and the fixed hexahedral configuration.

The higher numerical diffusivity observed in the adaptive tetrahedral runs results not only from the discretisation (the mathematical detail underlying the mesh formulation), but also the interpolation resulting from the adaptive modification of the mesh (the method by which new mesh nodes are situated within the model domain, depending on the gradients of velocity between present nodes). However, the benefits of an adaptive mesh (allowing higher resolution of small scale processes in large scale domains, for example) can far outweigh the added numerical diffusivity, which is of the same order experienced when moving from hexahedral to tetrahedral elements.

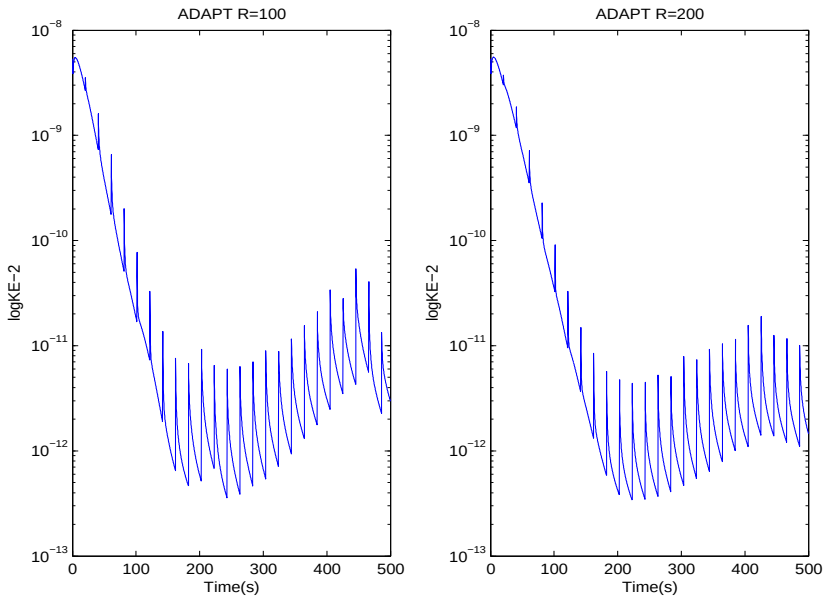

Figure 4.16: Plot of $\log \sqrt{KE}$ against time for ICOM adaptive tetrahedral runs $R = 100$ and $R = 200$ showing a decrease in the kinetic energy of the system over time, implying a negative growth rate.

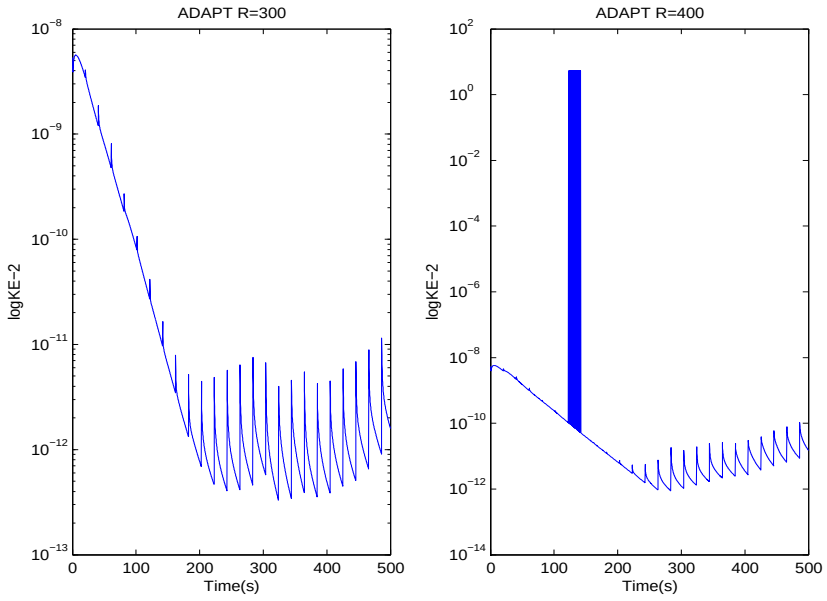

Figure 4.17: Plot of $\log \sqrt{KE}$ against time for ICOM adaptive tetrahedral runs $R = 300$ and $R = 400$ showing a decrease in the kinetic energy of the system over time, implying a negative growth rate. The large column observed in the $R = 400$ run may be the result of some numerical instability, but this is un-confirmed.

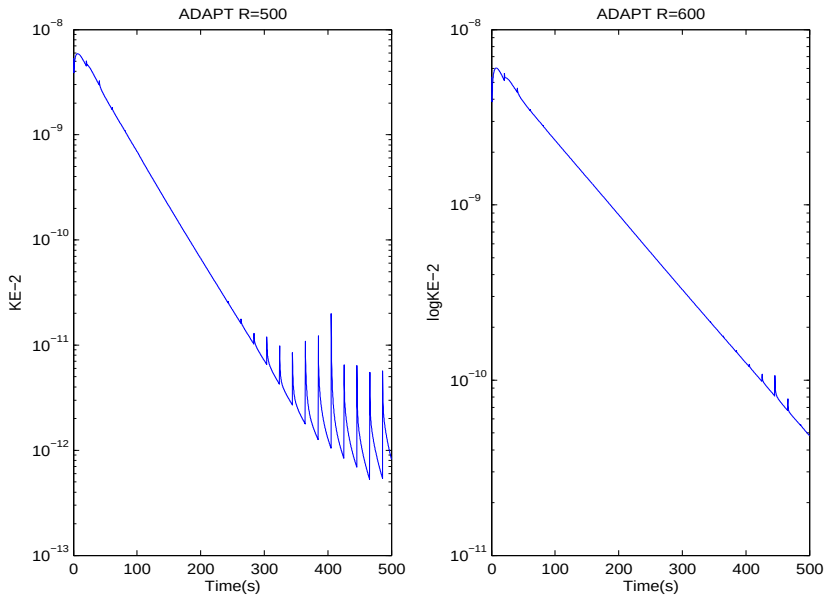

Figure 4.18: Plot of $\log \sqrt{KE}$ against time for ICOM adaptive tetrahedral runs $R = 500$ and $R = 600$, showing a decrease in the kinetic energy of the system over time, implying a negative growth rate.

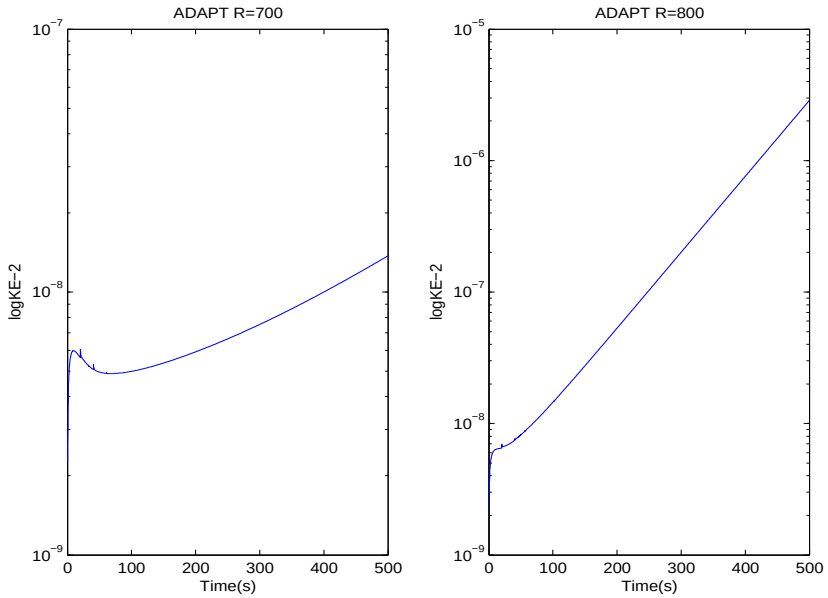

Figure 4.19: Plot of $\log \sqrt{KE}$ against time for ICOM adaptive tetrahedral runs $R = 700$ and $R = 800$, showing an increase in the kinetic energy of the system, implying a positive growth rate. The onset of increasing kinetic energy in the $R = 800$ run suggests the numerical critical Rayleigh number R_n for the adaptive tetrahedral ICOM configuration lies somewhere between $R = 700$ and $R = 800$.

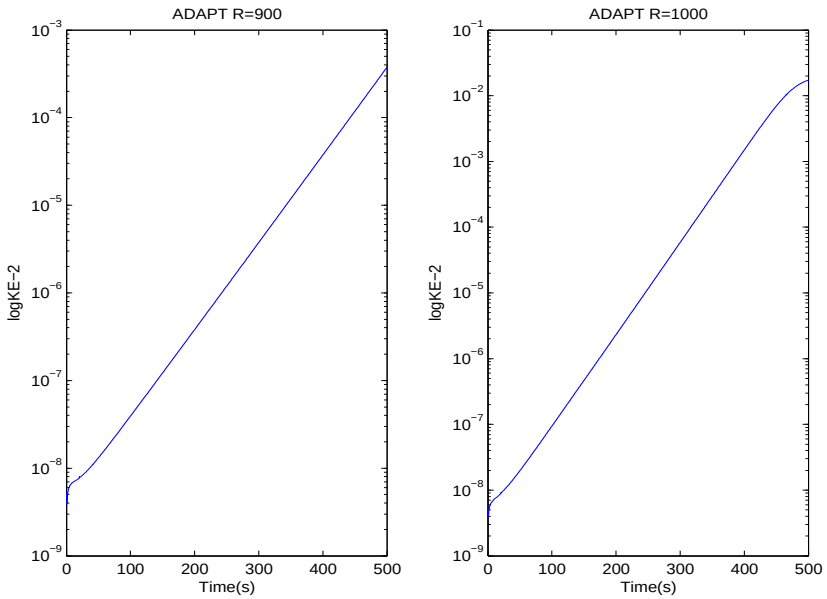

Figure 4.20: Plot of $\log \sqrt{KE}$ against time for ICOM adaptive tetrahedral runs $R = 900$ and $R = 1000$, showing continued increases in the amount of kinetic energy in the system over time, suggesting an increasing growth rate with increasing Rayleigh number.

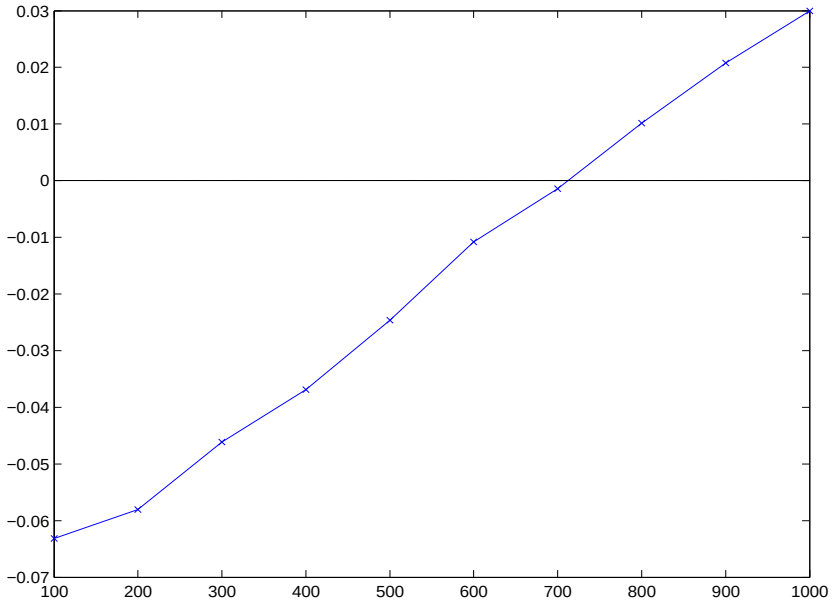

Figure 4.21: Plot of σ against Rayleigh number for each ICOM adaptive tetrahedral run $R = 100$ - 1000, showing an increase in growth rate with increasing Rayleigh number. The point at which $\sigma = 0$ indicates the critical Rayleigh number for the adaptive tetrahedral model configuration in ICOM, and is in this case approximately 712.

4.3.4 Calculating the numerical diffusivity within MITgcm using a fixed hexahedral mesh

Figures 4.22, 4.23 and 4.24 show the square root of kinetic energy plotted on a logarithmic scale for MITgcm (fixed hexahedral mesh) model runs $R = 600$ to $R = 1000$. For a temperature gradient between the top and bottom boundaries corresponding to Rayleigh numbers of up to 700 no instability is amplified. The critical Rayleigh number for this configuration must therefore be greater than 700. For the model run $R = 800$, a rise in the kinetic energy contained in the system over time in comparison with the lower Rayleigh number runs is evident. Significant periods of linear growth are observed for runs with Rayleigh number 800 and above. The gradient of the line during these periods corresponds to the growth rate of the instability, and is calculated across all Rayleigh numbers. These growth rates are subsequently plotted against Rayleigh number, and the Rayleigh number at the intersection of the line of best fit with $\sigma = 0$ is used to infer the model critical Rayleigh number (R_n) (Figure 4.25).

For the MITgcm fixed hexahedral mesh, a R_n of 710 was found. This falls between the R_n predicted for the ICOM fixed and adaptive tetrahedral configurations.

The higher numerical diffusivity observed in the MITgcm runs in comparison with the fixed hexahedral ICOM runs is likely to result from the underlying mathematical techniques, however, the difference is only 1.5% and, as such, tracing the additional numerical diffusivity is difficult. The amount of numerical diffusivity present in MITgcm falls within the range of numerical diffusivity in ICOM, and it can be concluded that the representation of the physics in this problem is as good as that in MITgcm, a leading non-hydrostatic structured mesh model.

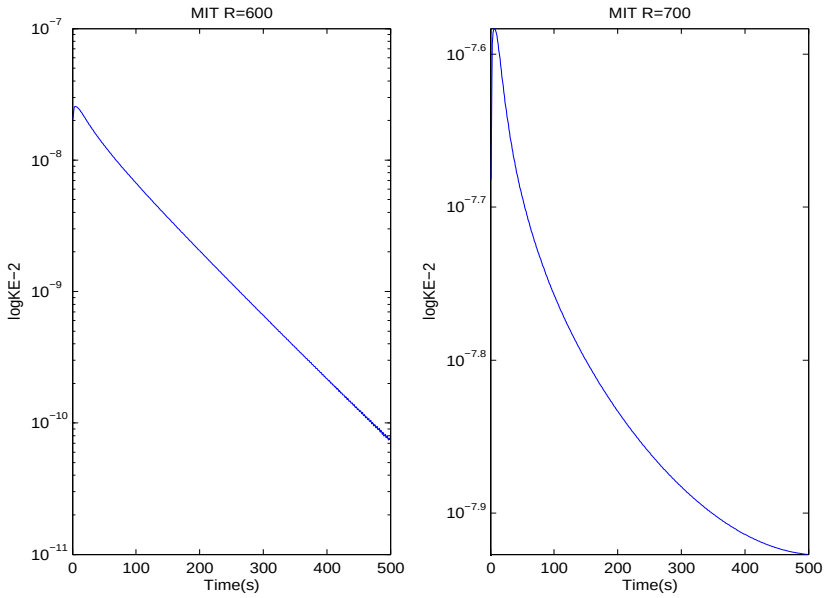

Figure 4.22: Plot of $\log \sqrt{KE}$ against time for MITgcm runs $R = 600$ and $R = 700$ showing a decrease in the kinetic energy of the system over time, implying a negative growth rate.

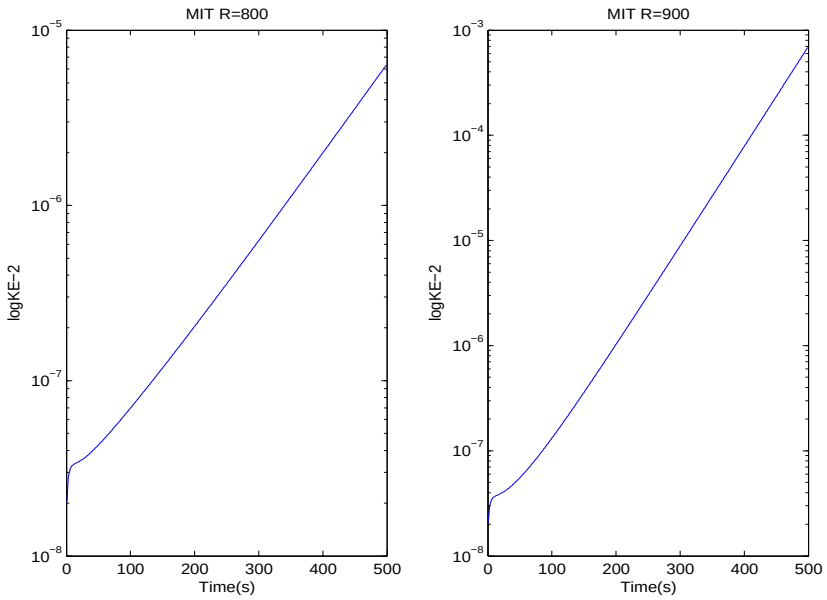

Figure 4.23: Plot of $\log \sqrt{KE}$ against time for MITgcm runs $R = 800$ and 900, showing an increase in the kinetic energy of the system, implying a positive growth rate. The onset of increasing kinetic energy in the $R = 800$ run suggests the numerical critical Rayleigh number R_n for the MITgcm configuration lies somewhere between $R = 700$ and $R = 800$.

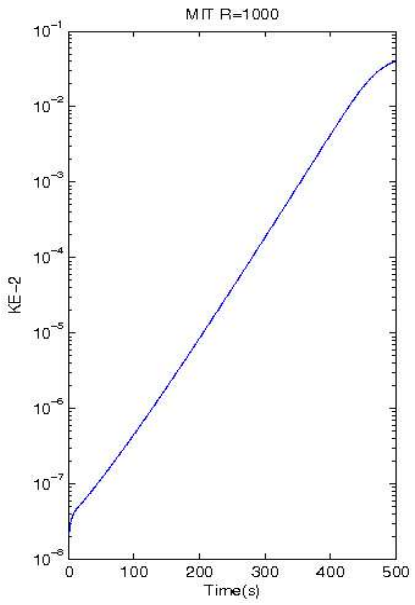

Figure 4.24: Plot of $\log\sqrt{KE}$ against time for MITgcm run $R = 1000$, showing a continued increase in the amount of kinetic energy in the system over time, suggesting an increasing growth rate with increasing Rayleigh number.

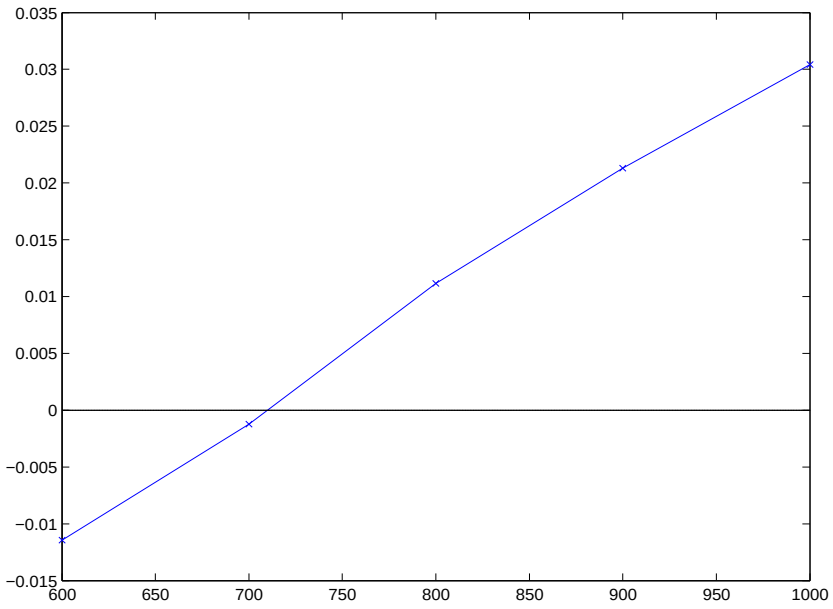

Figure 4.25: Plot of σ against Rayleigh number for each ICOM adaptive tetrahedral run $R = 100$ - 1000, showing an increase in growth rate with increasing Rayleigh number. The point at which $\sigma = 0$ indicates the critical Rayleigh number for the fixed hexahedral model configuration in MITGCM, and is in this case approximately 712.

4.4 Comparison of ICOM and MITgcm results with the iterative analytical solution

Chandrasekhar (1961) calculated the solution for the dimensionless theoretical linear instability problem for the boundary conditions stated in 4.2 as follows:

$$(D^2 - a^2)(D^2 - a^2 - \sigma)W = (\frac{g\alpha}{\kappa}d^2)a^2\Theta \tag{4.7}$$

$$(D^2 - a^2 - Pr\sigma)\Theta = -(\frac{\beta}{\kappa}d^2)W, \tag{4.8}$$

where D is the differential operator d/dz, Pr is the Prandtl number ($= \mu/\kappa$), a is the wavenumber and σ is the growth rate. As the transition between stability and instability is via some stationary state, the theoretical critical Rayleigh number R_c must coincide with $\sigma = 0$. In order to determine the ability of ICOM and MITgcm to replicate the theoretical problem, the system of ordinary differential equations (ODE's) 4.7 and 4.8 with the boundary conditions (4.2) were transformed into matrix form using a finite difference scheme. The matrix was then discretised over 40 levels to give an eigenproblem where eigenvalues are growth rates (σ) and eigenvectors are composed of the $\hat{\theta}$ and w at the grid points, which were solved using the Fortran NAG Library (F02 - Eigenvalues and Eigenvectors). The Fortran program designed for this can be seen in Appendix C. The vertical profile of $\hat{\theta}$, the perturbation in temperature from the background temperature gradient, and w, the vertical velocity, were extracted from the ICOM fixed hexahedral, fixed tetrahedral and adaptive tetrahedral runs for $R = 1000$ and similarly the fixed hexahedral MITgcm for $R = 1000$. These profiles were obtained by taking a vertical profile of the required field from the centre of the model domains at the end of the modelling period ($t = 500s$). The eigenvectors were scaled in order to compare with the numerical model results as follows:

$$\hat{\theta}_{model} = c\Delta T\hat{\theta}_{theory} \tag{4.9}$$

$$w_{model} = cw_{scale}w_{theory}, \tag{4.10}$$

where c is some constant (chosen so that ΔT_{max} for the eigenvector matches ΔT_{max} for the modelled values), and $w_{scale} = \frac{g\alpha\beta d^3}{\mu}$. As a result, the graphical comparison of the vertical velocity eigenvectors provides greater insight into the inconsistencies between the modelled and analytical results.

Figures 4.26, 4.27, 4.28, 4.29, 4.30, 4.31, 4.32 and 4.33 show the vertical velocity and temperature perturbation profiles for each model configuration and the corresponding re-scaled w and $\hat{\theta}$ eigenvectors.

The limitations of this method arise from the selection of the same point within the domain for the vertical profile of $\hat{\theta}$ and w. Because of the slight variation in the position of the convective cells across the different mesh options, the mid-point of the domain may fall in a positive or negative cell. However, the symmetrical nature of parallel plate convection produces cells of equal but opposite strengths. As a result, some plots appear inverted, as with Figure 4.33, but this may be discounted. Secondly, a number of the following plots show variation between the theoretical eigenvalues and the model results in terms of fit. This is the result of choosing the same time in each run to make the vertical profile ($500s$). Because this time is at the later end of the linear instability regime some non-linear instability is exhibited (particularly evident in the near surface in Figures 4.27, 4.29 and 4.33). Taking this into account, it is a reasonable statement to say that all model and mesh configurations produce a good approximation of the theoretical problem. However, the vertical velocities observed in the fixed mesh ICOM and MITgcm runs consistently underestimate the vertical velocities (Figures 4.26, 4.28 and 4.32) in comparison with the analytical solution. Only the adaptive ICOM run attains a similar value for the vertical velocity eigenvector.

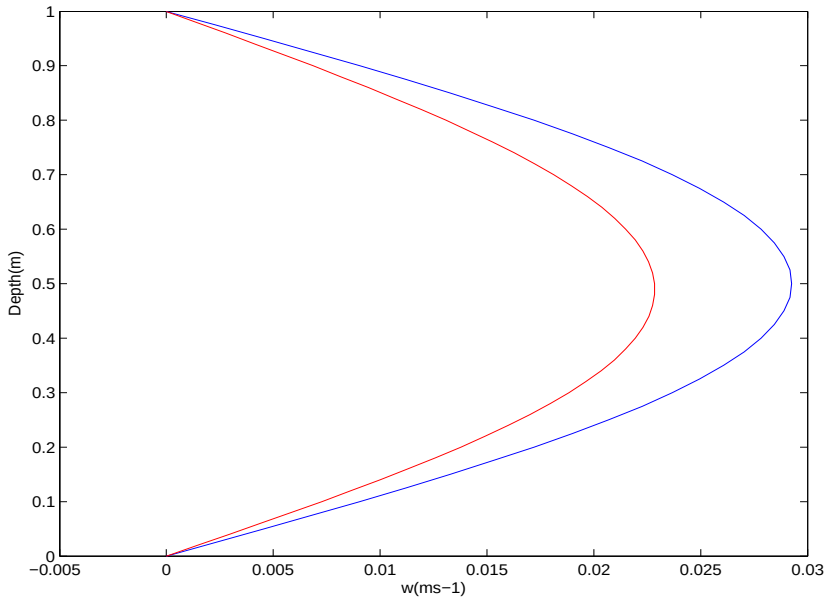

Figure 4.26: Plot of vertical velocity w against depth for fixed hexahedral ICOM run (red) and the analytical eigenvector (blue) for $R = 1000$.

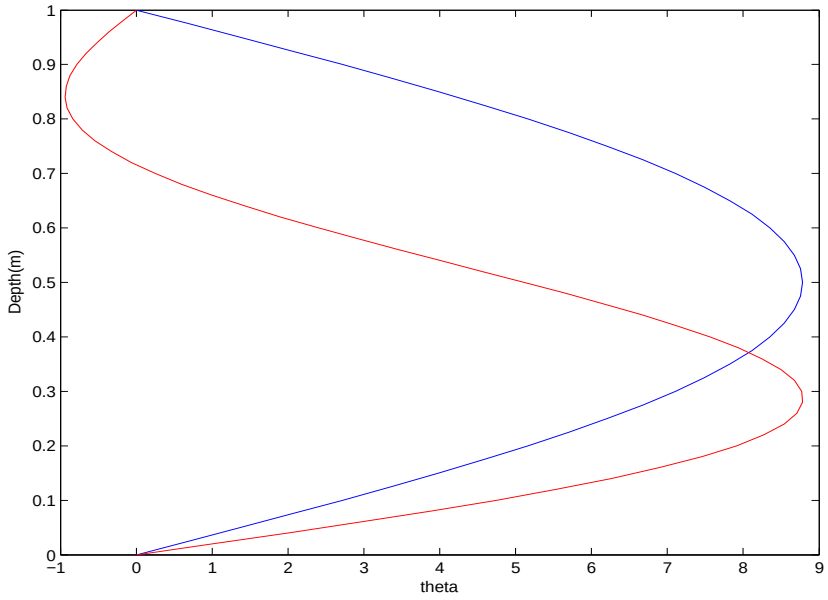

Figure 4.27: Plot of temperature perturbation from the background temperature gradient $\hat{\theta}$ against depth for fixed hexahedral ICOM run (red) and the analytical eigenvector (blue) for $R = 1000$.

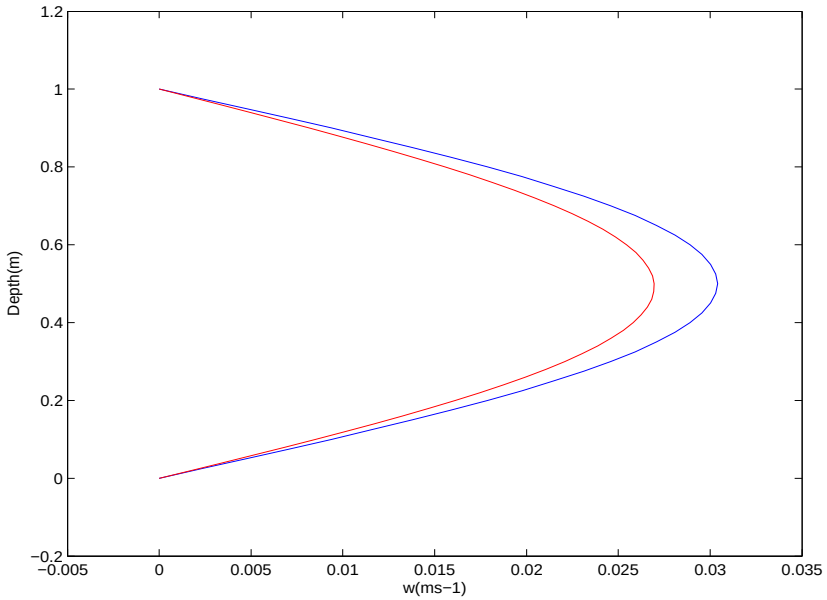

Figure 4.28: Plot of vertical velocity w against depth for fixed tetrahedral ICOM run (red) and the analytical eigenvector (blue) for $R = 1000$.

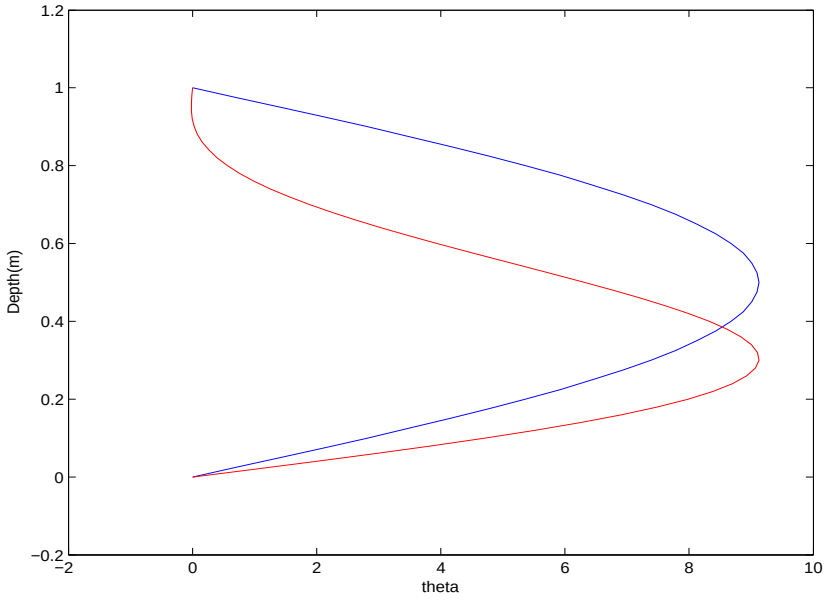

Figure 4.29: Plot of temperature perturbation from the background temperature gradient $\hat{\theta}$ against depth for fixed tetrahedral ICOM run (red) and the analytical eigenvector (blue) for $R = 1000$.

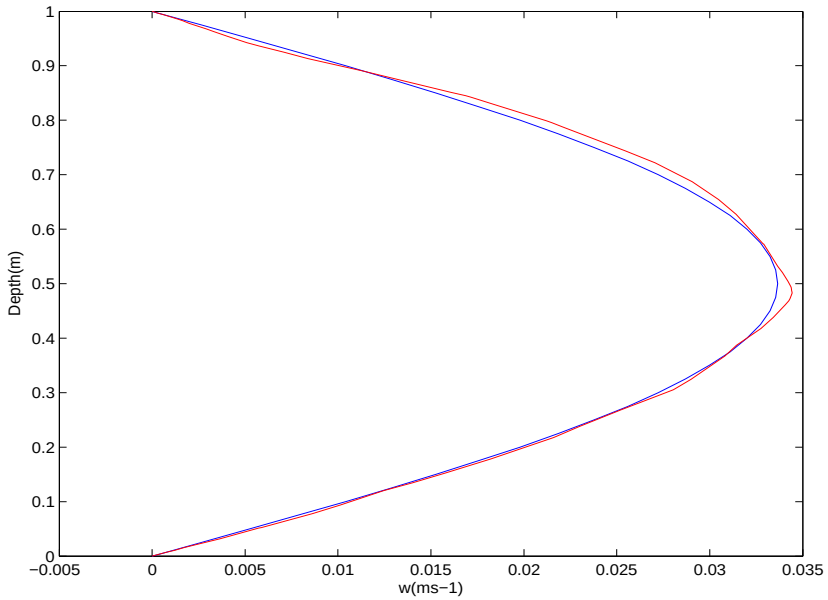

Figure 4.30: Plot of vertical velocity w against depth for adaptive tetrahedral ICOM run (red) and the analytical eigenvector (blue) for $R = 1000$.

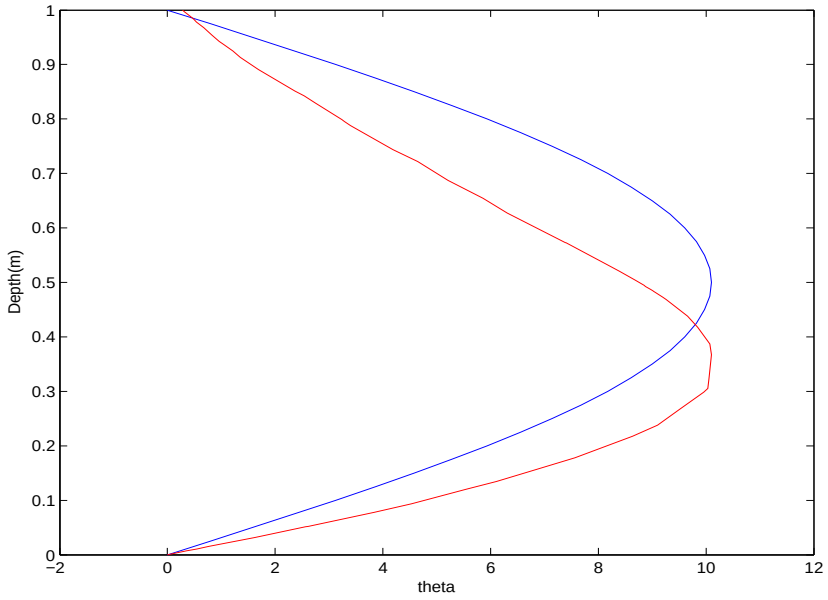

Figure 4.31: Plot of temperature perturbation from the background temperature gradient $\hat{\theta}$ against depth for adaptive tetrahedral ICOM run (red) and the analytical eigenvector (blue) for $R = 1000$.

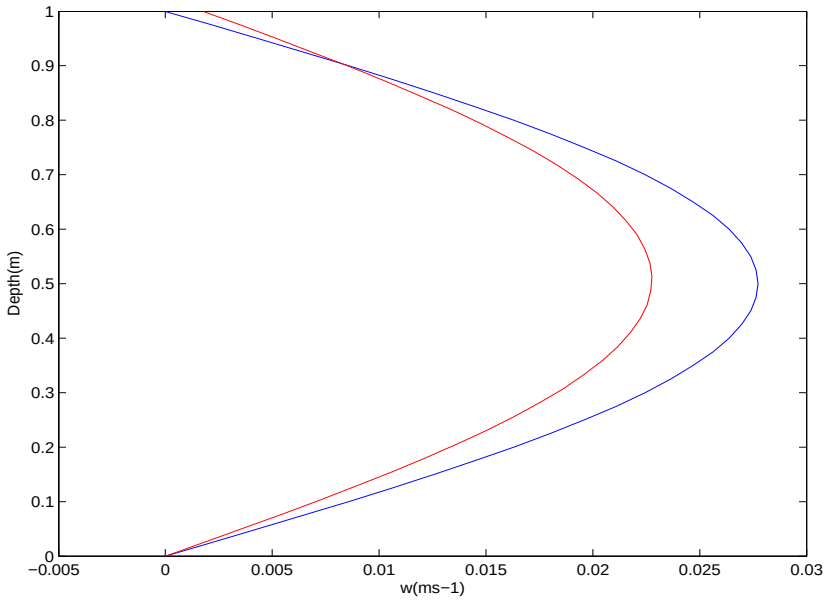

Figure 4.32: Plot of vertical velocity w against depth for the MITgcm run (red) and the analytical eigenvector (blue) for $R = 1000$.

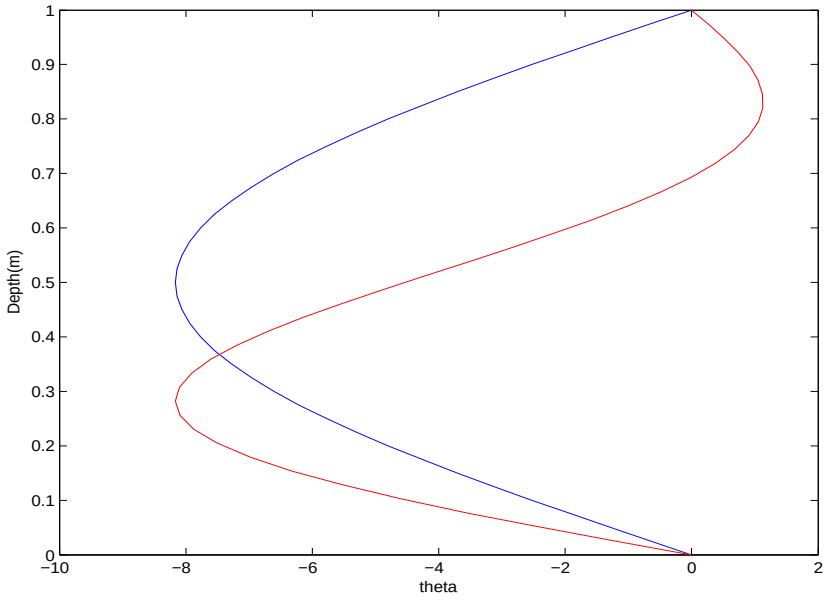

Figure 4.33: Plot of temperature perturbation from the background temperature gradient $\hat{\theta}$ against depth for the MITgcm run (red) and the analytical eigenvector (blue) for $R = 1000$.

4.5 Summary and Conclusions

In order to assess the additional numerical diffusivity present within ICOM, a series of tests replicating linear instability theory for various temperature gradients were performed. A comparison of hexahedral, tetrahedral and adaptive meshes was made within ICOM, and ICOM was further compared with a leading GCM (MITgcm) using a similar configuration. By extracting the growth rates of the instabilities observed within the model runs, the numerical critical Rayleigh number (R_n) was identified for each configuration. Table 4.3 presents a summary of R_n and ratio of effective mixing (E). The ratio is a measure of the effective mixing induced by the tracer advection scheme acting on the temperature field and identifies that numerical mixing is present if $E > 1$. All model configurations contained some added viscosity/diffusion as a result of their numerical formulation. The highest effective mixing ratio occurred in the adaptive ICOM configuration, and the lowest in the fixed hexahedral ICOM configuration. The MITgcm showed an effective mixing ratio comparative with the adaptive ICOM configuration. The additional numerical diffusivity present within all models varied between approximately 6.5% and 8.3% in comparison with theory. Overall, the ICOM fixed hexahedral mesh was associated with the lowest amounts of implicit diffusivity. The ICOM adaptive tetrahedral mesh configuration exhibited the largest implicit diffusivity. However, the adaptive mesh compared well with the MITgcm fixed mesh.

As predicted, MITgcm displayed a higher numerical diffusivity in comparison with the fixed hexahedral ICOM run. This is likely to result from the difference in the underlying numerical formulation between the models, and indicates that the use of finite elements may improve model accuracy, particularly in ocean modelling.

The growth rates associated with each model run are contained in Table 4.4, shown to 4 decimal places. The values of the growth rates highlight the similarities (and differences) between the model runs at each Rayleigh number. For $R = 700$, only the ICOM fixed tetrahedral configuration shows positive growth, again showing a lower implicit diffusivity. At this Rayleigh number, the MITgcm shows better correlation with the adaptive ICOM configuration, again demonstrating that for a fixed hexahedral mesh model it contains comparatively large implicit diffusivities.

Table 4.3: Summary of results: Effective numerical diffusivity associated with each model configuration. Theoretical value 657.511 (for comparison

Model Configuration	Numerical (model) critical Rayleigh number R_n	Effective mixing ratio E (Eq. 4.5)
ICOM fixed hexahedral	699.982	1.065
ICOM fixed tetrahedral	706.361	1.074
ICOM adaptive tetrahedral	712.251	1.083
MITgcm	710.071	1.08

It may therefore be concluded that, although somewhat more numerically diffusive, the adaptive mesh configuration makes a good approximation of the theoretical solution (supported by the comparison of the analytical and model eigenvectors). The adaptive mesh best represents the amplitude of vertical velocity. Furthermore, the advantages of the adaptive mesh in its ability to vary resolution between areas of interest within the domain acts to offset the disadvantage of a small amount of additional diffusion. This additional amount of diffusion is comparative to that observed in the MITgcm and, as such, the amount of implicit diffusion within adaptive ICOM configuration may be termed acceptable.

The use of the linear instability problem has proved to be a useful case against which to test numerical models in an attempt to diagnose implicit diffusivity and viscosity. This presents an opportunity for such investigations to become commonplace in the testing and validation of new numerical models. A further opportunity lies with the possibility of extending this research to identify the individual contributions of implicit diffusivity and viscosity.

Table 4.4: Summary of results: Growth rates $\sigma(kgm^2s^{-3})$ associated with each model configuration and Rayleigh number

Rayleigh Number	ICOM Hexahedral	ICOM Tetrahedral	ICOM Adaptive	MITGCM
100	-0.0780	-0.0627	-0.0632	
200	-0.0634	-0.0602	-0.0581	
300	-0.0492	-0.0498	-0.0461	
400	-0.0357	-0.0367	-0.0369	
500	-0.0231	-0.0240	-0.0246	
600	-0.0112	-0.0120	-0.0108	-0.0114
700	0.0000	-0.0007	-0.0014	-0.0012
800	0.0107	0.0100	0.0102	0.0112
900	0.0210	0.0203	0.0208	0.0213
1000	0.0308	0.0301	0.0300	0.0304

Chapter 5

Modelling convection - small scale experiments

5.1 Introduction

A series of small scale experiments are initially conducted as part of an investigation into Greenland Sea open ocean deep convection (OODC) using the Imperial College Ocean Model (ICOM). These study the nature of model convection under varying model configurations and methods of inducing model convection.

In Chapter 4, the variations in model results were discussed with reference to numerical diffusion induced by the choice of model mesh. Here, a comparison of convective strength is made between fixed and adaptive mesh options, using disk shaped cooling and uniform cooling to induce convection, and the impact of finite and continuous application of cooling. There has been some discussion within the literature over the method of inducing convection within numerical models (e.g. Straneo and Kawase (1999); Visbeck et al. (1996)), the following results should contribute to the debate. The timescale of application of cooling and its impact on convection is also investigated - in reality, periods of intense cooling induced by the passage of atmospheric depressions last approximately 24 hours. However, in order to understand the nature of model convection (and hence, by implication, the nature of Greenland Sea convection), the application of continuous cooling

provides useful insights.

A simple 10km by 10km box of 3600m depth is considered. Each model configuration is run for a period of 72 hours. Convection is forced by applying a cooling rate of $-2.5 * 10^{-4} K m s^{-1}$ to the surface of the domain in either a disk of radius 3km centred on the mid-point of the domain, or uniformly across the whole domain. The Coriolis parameter is set to $1.4 * 10^{-4} s^{-1}$, a realistic value for the high latitudes of the Greenland Sea. The thermal expansion coefficient (α) is set to $2.5 * 10^{-4\circ} K^{-1}$, a value that is somewhat higher than that observed in the Greenland Sea, and hence may exaggerate vertical movement in comparison to that of reality. The full suite of inputs and parameters can be see in Chapter 3.

The scale of the cooling disk in comparison to the scale of the domain gives rise to the potential for edge effects to impact the convection observed in the model. Numerical models can never truly replicate reality, in part because of their use of equations that are at best an approximation of the real physical system, and partly because the scale of the domain must always be finite. Theoretical investigations, such as linear instability presented in Chapter 4, are horizontally infinite, and therefore do not suffer edge effects. The potential for edge effects must therefore be taken into account in this study. Often, in order to reduce the impact on the physical process being studied using numerical models, the domain size is increased so that the process of interest happens away from the boundaries. This, however, incurs a computational cost. In this way, numerical modelling becomes a balance between cost and accuracy.

For convection into an unstratified domain, the eddy turnover timescale is given by $t_{scale} = h/w_{scale}$, where h is the depth of the domain and w_{scale} is given by Equation 2.10 in Chapter 2 Section 2.2.2. The eddy turnover time is the time it takes for a water parcel to move from the surface to the bottom of the domain.

For $h = 3600m$, $w_{scale} = 0.13 m s^{-1}$ and $t = 2.8 * 10^4 s$, or approximately 8 hours. The parameter that determines whether rotation is important is the natural Rossby number, R_0*, the ratio of the rotational timescale to the eddy turnover timescale. If $R_0* >> 1$, the eddy turnover timescale is much shorter than the rotational timescale and convection is non-rotating. For $R_0* << 1$, convection is rotating, and convection falls under the rotating scaling regime (Section 2.2.2).

Here, the convective Rossby number, $R_{0c}* \equiv 1/ft_{scale} \sim 0.25$, and the natural Rossby number $R_0* \sim R_{0c}^{3/2} = 0.125$. This is characteristic of the ocean at high latitudes where heat fluxes of $1000Wm^{-2}$ and mixed layer depths of up to $300m$ are observed. It is therefore important that the rotational scaling ideas presented in Equations 2.13, 2.14 and 2.15 are taken into account in the current study, and we may expect to observe vertical velocities $w_{rot} \sim \sqrt{B_0/f} \sim 0.07ms^{-1}$, where $B_0 = \alpha gF$, and horizontal plumes scales of $l_{rot} \sim \sqrt{B_0 f} \sim 0.5km$.

Mironov et al. (2000) performed an investigation into the impact of rotation on oceanic convection using large eddy simulation (LES) methods. Their paper provides a useful reference for comparison of the present study. In particular, their model run R2 has an associated natural Rossby number of ~ 0.2 which may be compared directly with our runs where a similar value of R_0* is obtained.

In the final stages of the convective process, the convected water breaks up into eddies that may be advected horizontally away from the convection site. The scale of these eddies is set by the Rossby radius of deformation (L_R). For an unstratified model domain, however, a prediction of L_R cannot be obtained (as N, the buoyancy frequency, is imaginary for unstable stratification's, and zero for no stratification). In reality, L_R ranges from 5-10km in the Greenland Sea. The scale of eddies produced in the model may therefore be compared to this value in order to estimate the models ability to capture the convective process in its entirety.

5.2 Investigating the effects of fixed and adaptive meshes on model convection

Because of the novel use of adaptive, unstructured mesh modelling techniques, it is of interest to make a full comparison of the convective problem on both fixed and adaptive meshes in order to identify differences between model convection induced in either configuration. To achieve this, six model configurations were investigated:

1. Continuous uniform cooling on a fixed, structured mesh
2. Continuous uniform cooling on an adaptive, unstructured mesh
3. Finite uniform cooling on a fixed, structured mesh
4. Finite uniform cooling on an adaptive, unstructured mesh
5. Continuous disk cooling on a fixed, structured mesh
6. Continuous disk cooling on an adaptive, unstructured mesh

The results of 1 and 2, 3 and 4, and 5 and 6 are directly compared using the approaches outlined above. The results of these comparisons follow below.

5.2.1 Comparison of continuous uniform cooling forced convection on fixed and adaptive meshes

Figure 5.1 shows the development of the temperature field using a cross section through the centre of the domain at 1 hour, 24 hours, 48 hours and 72 hours for the uniform continuous cooling fixed mesh run. The stages of the convective process discussed in Chapter 2 are evident.

At 1 hour, cooling at the surface is visible. At 24 hours, a number of convective plumes can be seen extending from the surface towards the floor of the domain, reaching depths of approximately 3.2km. At 48 hours, the plumes have reached the bottom of the domain and vertical mixing is evident throughout the entire domain. By 72 hours, the entire domain is well-mixed,

allowing further identifiable plumes of convection to occur. Spreading cannot be distinguished as the convection is across the whole model domain.

Of particular note, the fixed mesh exhibits some unphysical behaviour in the top layers - numerical noise due to insufficient grid resolution. Some cold water spreads along the lines of vertical resolution at each time. This is a major drawback to the use of fixed meshes, but does not have a large inhibiting effect on convection.

The arrangement of the fixed mesh is shown in Figure 5.2. The same resolution is applied in all fixed mesh runs discussed in this Chapter.

Figure 5.3 shows the development of the temperature field using a cross section through the centre of the domain at 1 hour, 24 hours, 48 hours and 72 hours for the continuous uniform cooling adaptive mesh run. The corresponding mesh at each time is shown in Figure 5.4 so that the nature of adaptivity can be visualised. The stages of the convective process are also clearly identifiable. At 1 hour, cooling at the surface is visible and the mesh resolution is concentrated in this region. Away from the surface, the mesh coarsely resolves the domain and large element sizes up to 1.5km in length are observed.

At 24 hours, a convective plume is observed descending from the surface to the domain floor, and spreading horizontally along the bottom. There is evidence of a previous convective plume to the south of the domain (in these plots, y unconventionally increases southwards), where an area of stratified fluid is observed below 1800m. The mesh has placed high resolution across the majority of the domain, indicating high velocities are present everywhere.

At 48 hours, the domain shows two identifiable layers of fluid. Further plumes can be seen descending from the surface, penetrating to about 2400m.

By 72 hours, the erosion of the initially (relatively) warm water is complete, and convection continues to cool the domain extensively. Note that the unphysical behaviour observed on the fixed mesh is not present in the adaptive mesh run.

Figure 5.5 shows the mean temperature at three depths within the domain. The onset of convection occurs earlier in the adaptive run than in the fixed run at 400m, as observed in the disk cooling runs (Section 5.2.3). However, both runs cool to the same temperature in the initial cooling event ($-1.2 * 10^{-3\circ}C$). The adaptive run shows the onset of cooling is consistently earlier at all three depths. The adaptive run also shows a cooler final tem-

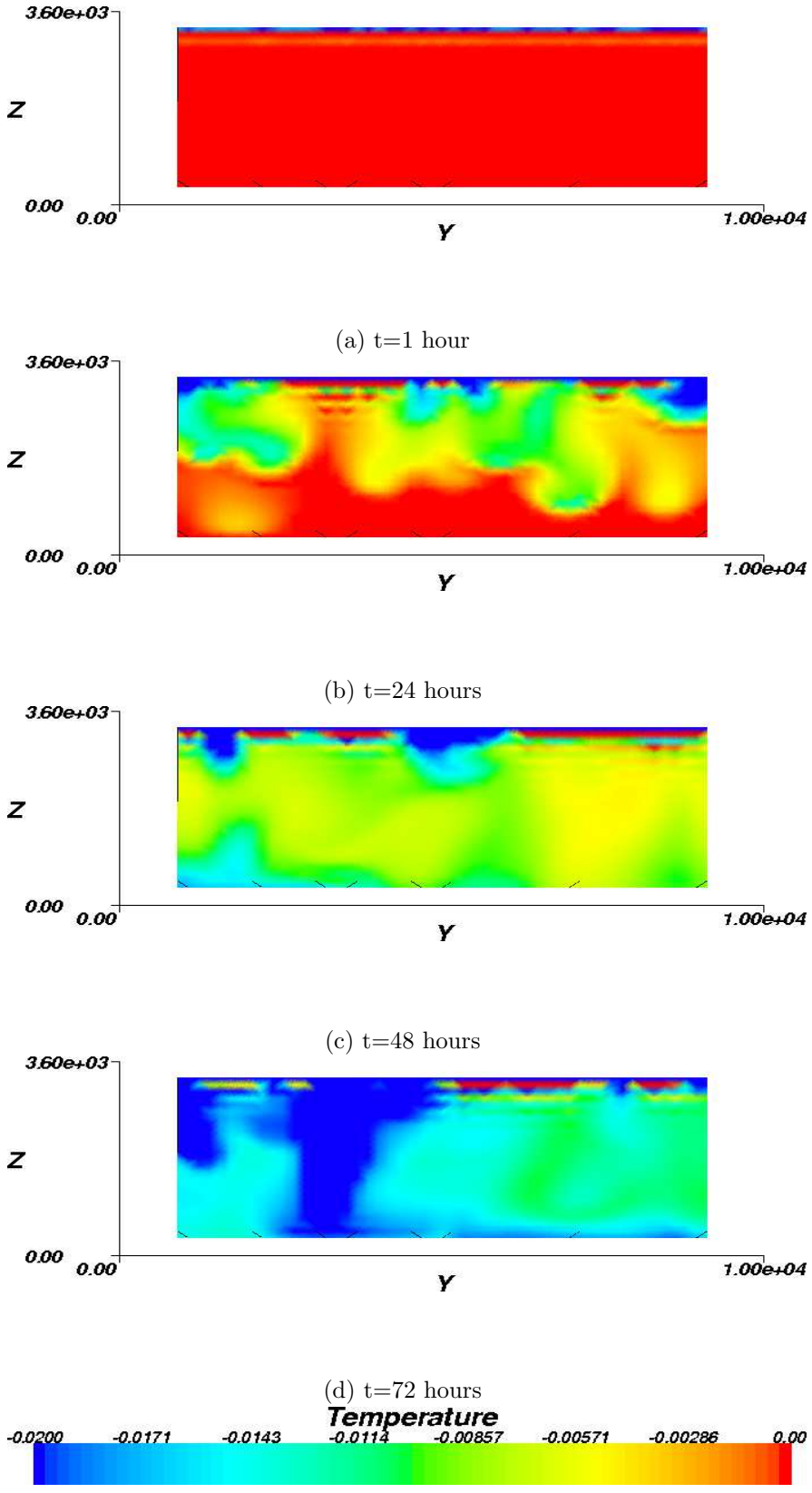

Figure 5.1: Cross-section through the centre of the domain of temperature for the continuous uniform cooling fixed mesh run.

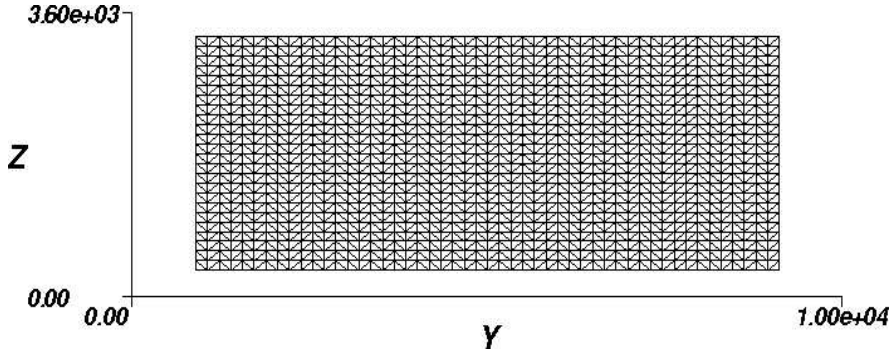

Figure 5.2: Example of the mesh used throughout the fixed mesh runs for comparison to the adaptive mesh.

perature than the fixed mesh configuration at all depths.

Figure 5.6 shows the variation in the profile of horizontally averaged temperature at 12, 24, 36, 48, 60 and 72 hours for the fixed (a) and adaptive (b) mesh uniform cooling runs. For the fixed run, convection is signified by the evident cooling of the water column between 24 and 36 hours, however, it has not completely penetrated the full depth of the water column. Convection is active throughout the remaining time period, showing a continuous cooling of the temperature profile and producing a well mixed water column. Similar trends are observed in the adaptive run, however, cooling is slightly larger throughout the water column, producing a profile at 72 hours that is approximately $0.01°C$ cooler than the fixed mesh profile at this time.

The structure of the velocity field is captured by Figures 5.7 and 5.8, where vertical velocity is plotted as shaded contours and vectors of horizontal velocity are overlaid. The fixed mesh uniform continuous cooling run exhibits little horizontal flow and no vertical flow after 1 hour (Figure 5.7 (a)). At 24 hours, individual plumes can be identified by strong negative vertical velocities. Horizontal flow occurs into the downwelling plumes, away from the regions of upwelling indicated by positive vertical velocity. These areas of upwelling surround the plumes. At 48 hours, the plumes begin to merge, and the strength of downwelling increases in some regions. By 72 hours, significant deformation of the merged plumes is visible - the result of the rotational influence.

The adaptive mesh uniform continuous cooling run in comparison shows significantly more defined plumes, and strong horizontal flow vectors in the regions of upwelling at 24 hours (Figure 5.8 (b)). A 48 hours, the plumes merge, but at 72 hours re-definition occurs indicating the onset of a second

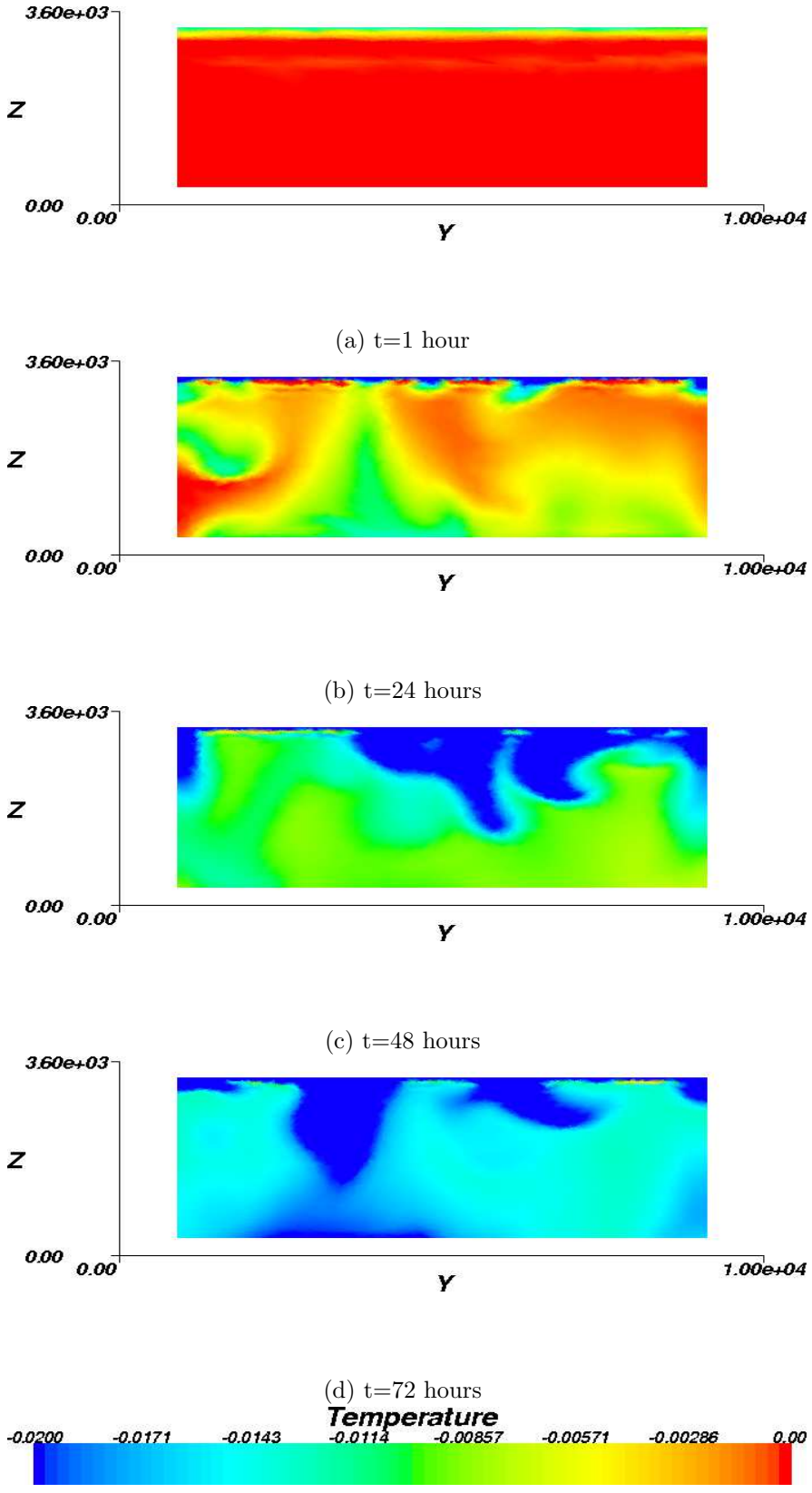

Figure 5.3: Cross-section through the centre of the domain of temperature for the continuous uniform cooling adaptive mesh run.

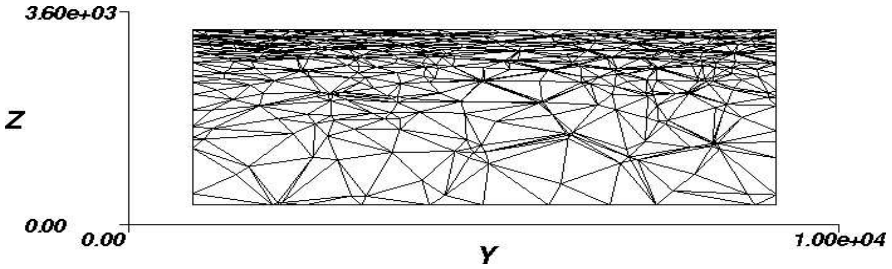

(a) t=1 hour

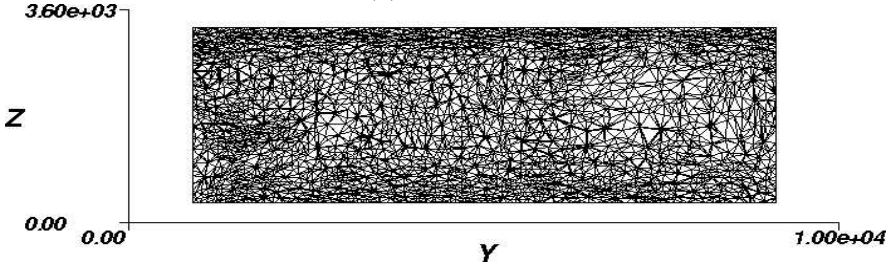

(b) t=24 hours

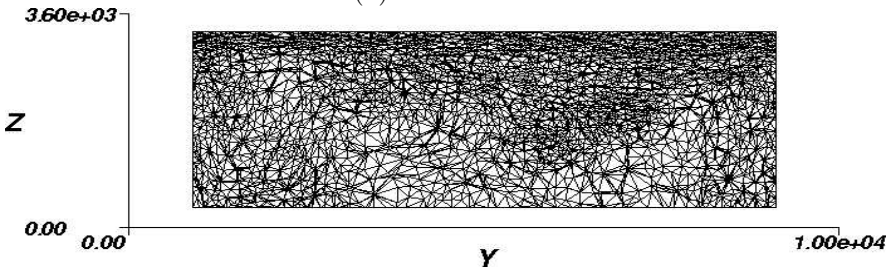

(c) t=48 hours

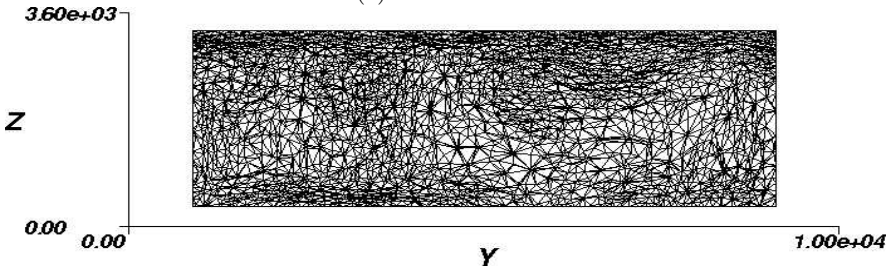

(d) t=72 hours

Figure 5.4: Corresponding mesh distribution for the continuous uniform cooling adaptive mesh run.

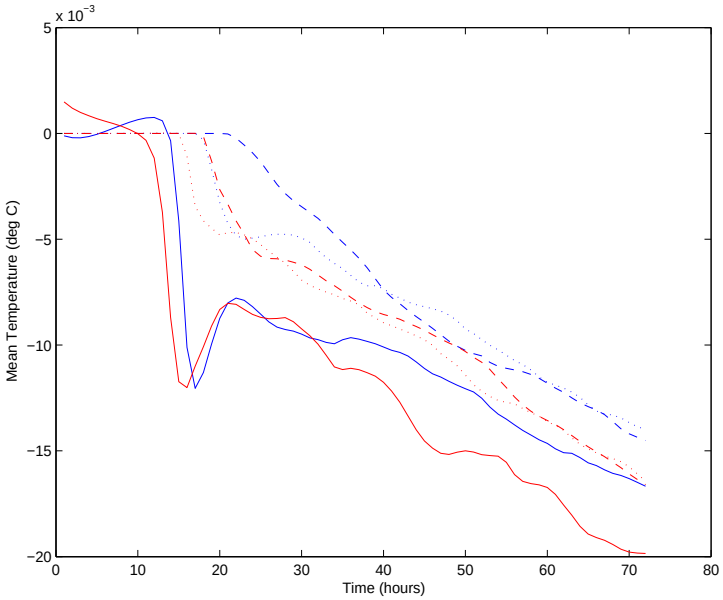

Figure 5.5: Variation in (a) mean temperature at 400m (solid line), 1800m (dotted line) and 3200m (dashed line) for the adaptive (red) and fixed (blue) uniform cooling runs.

wave of convection.

Figure 5.9 shows the variation in horizontally averaged velocity with depth at a number of times throughout the run for the fixed (a) and adaptive (b) uniform cooling runs. Although similar, it is evident that the adaptive run exhibits higher velocities overall, and velocities are distinctly higher at 24 hours compared with the fixed run. Figure 5.10 shows vertical profiles of horizontally averaged vertical velocity at various times throughout the fixed (a) and adaptive (b) runs. For both configurations, peaks in vertical velocity occur at 24 hours, at a depth of 1600m in the fixed run, and 1700m in the adaptive run. The velocities are slightly higher for the adaptive mesh ($4.0 * 10^{-3} ms^{-1}$ compared with $3.8 * 10^{-3} ms{-}1$). In contrast to Figure 5.10, the skewness of the vertical velocity - a measure of the dominance of downwelling (Figure 5.11), indicates that downwelling is slightly stronger in the fixed mesh run. Skewness is also observed to be lower at the surface for the adaptive run indicating that the fixed run does not resolve the associated scales of convection in the region of the surface.

To assess the extent of agreement of observed model vertical velocities with those predicted by the scaling ideas presented in Chapter 2, the horizontally averaged vertical velocity profile at 24 hours was scaled against

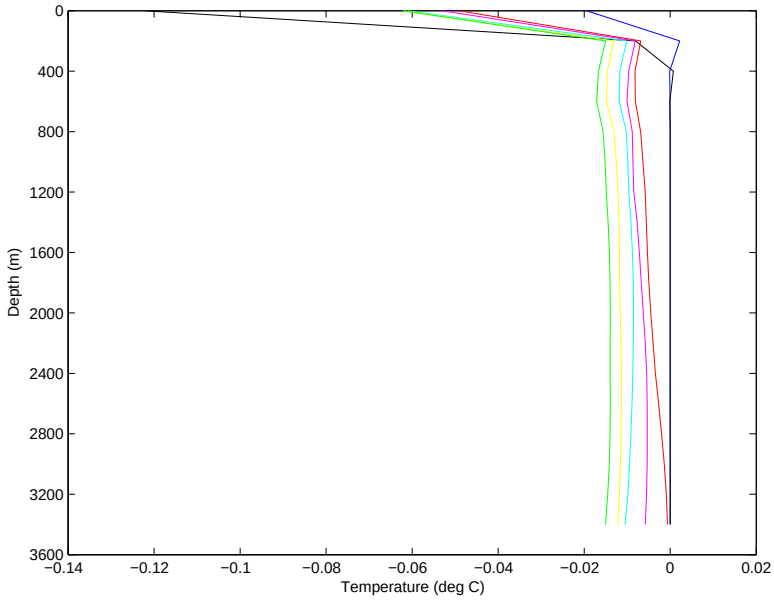

(a)

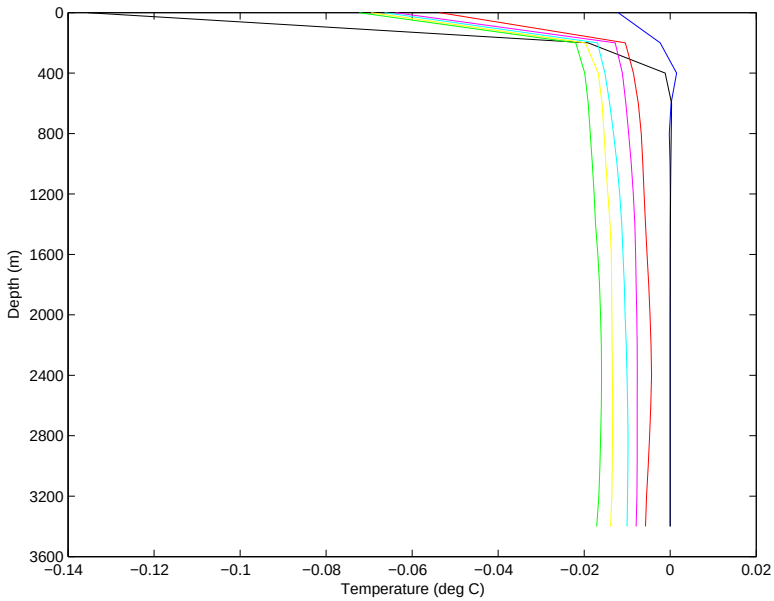

(b)

Figure 5.6: Comparison of the fixed (a) and adaptive (b) continuous uniform cooling runs using variation in horizontally averaged temperature profiles with depth at times 12 hours (blue), 24 hours (black), 36 hours (red), 48 hours (magenta), 60 hours (cyan) and 72 hours (green).

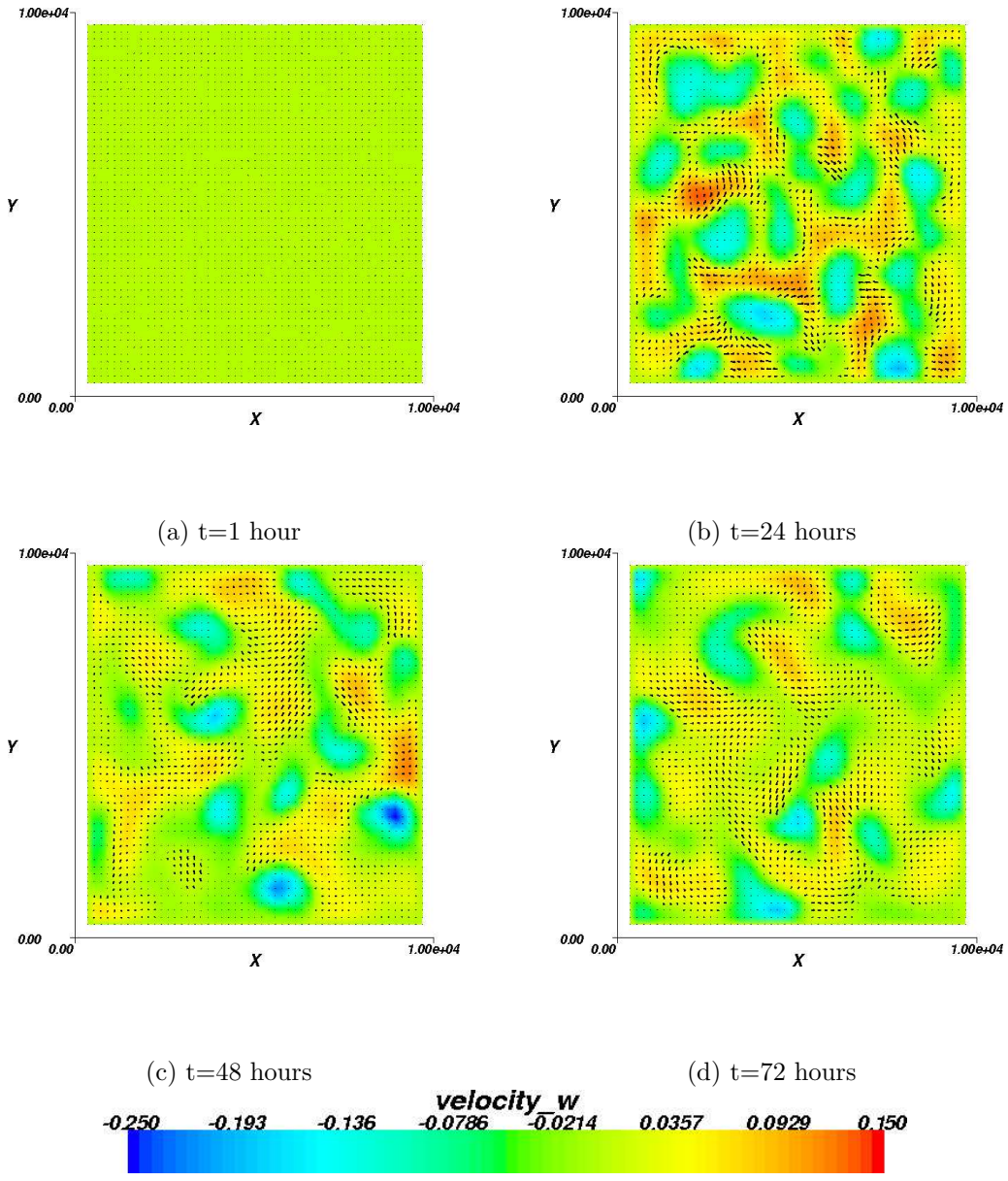

(a) t=1 hour

(b) t=24 hours

(c) t=48 hours

(d) t=72 hours

Figure 5.7: Vertical section of the domain showing the direction of the horizontal velocity vectors and contours of vertical velocity at 1800m for the continuous uniform cooling fixed mesh run.

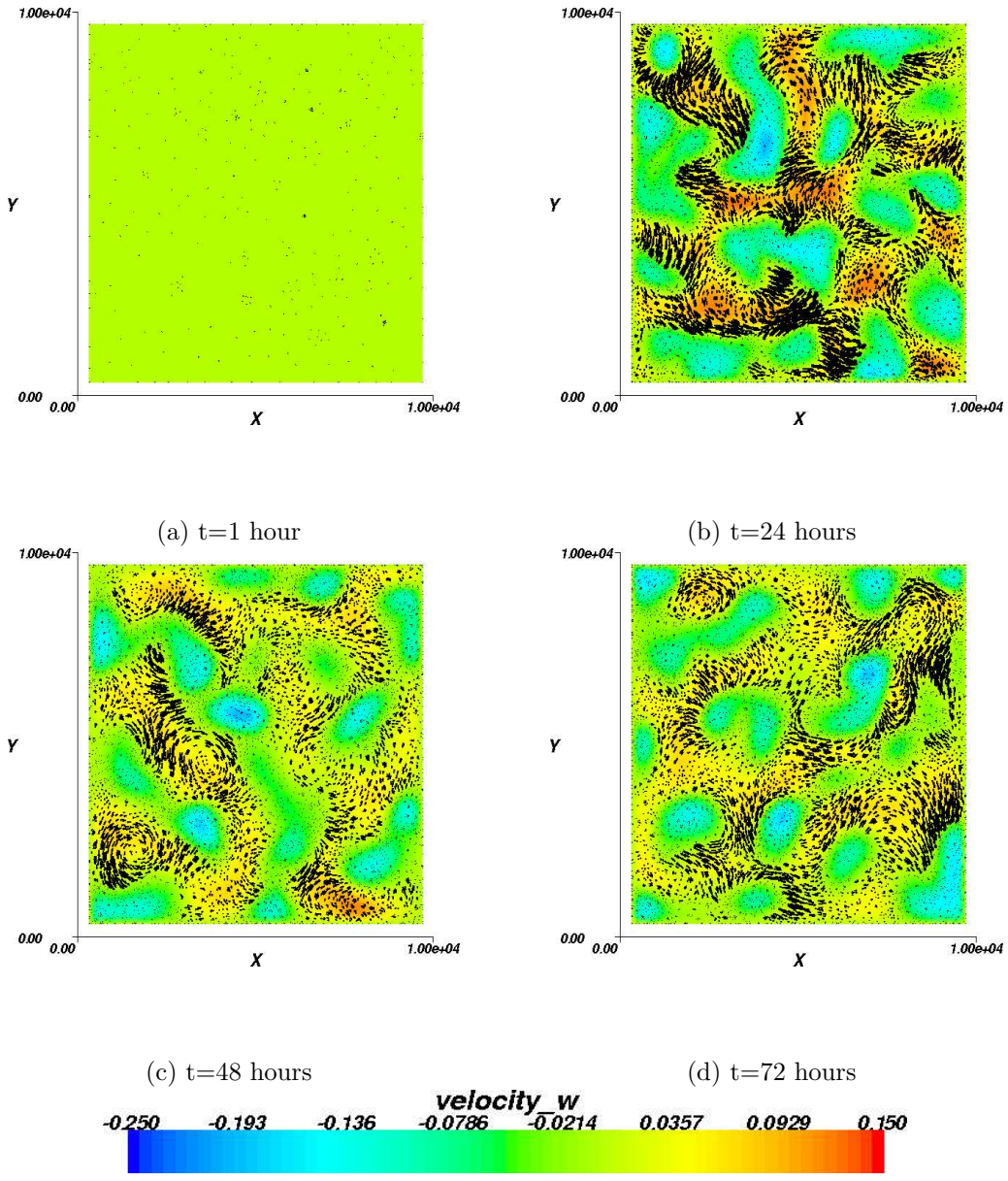

(a) t=1 hour

(b) t=24 hours

(c) t=48 hours

(d) t=72 hours

Figure 5.8: Vertical section of the domain showing the direction of the horizontal velocity vectors and contours of vertical velocity at 1800m for the continuous uniform cooling adaptive mesh run.

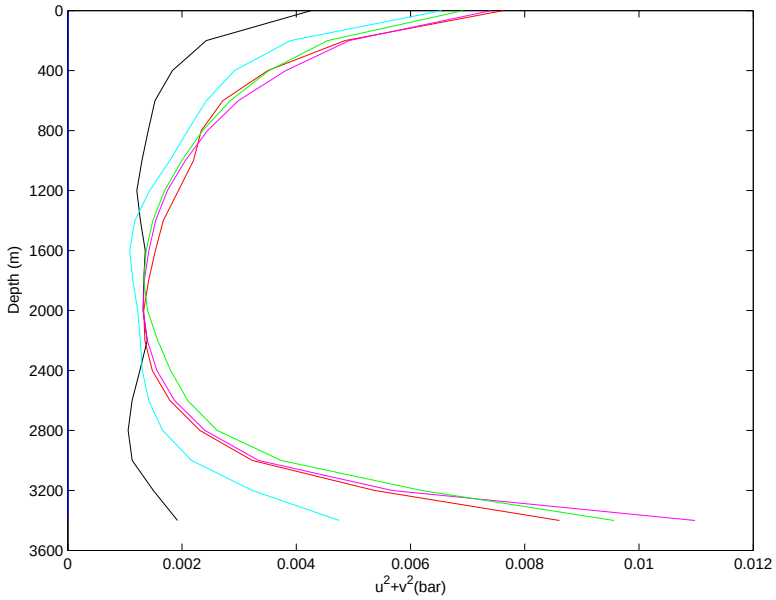

(a)

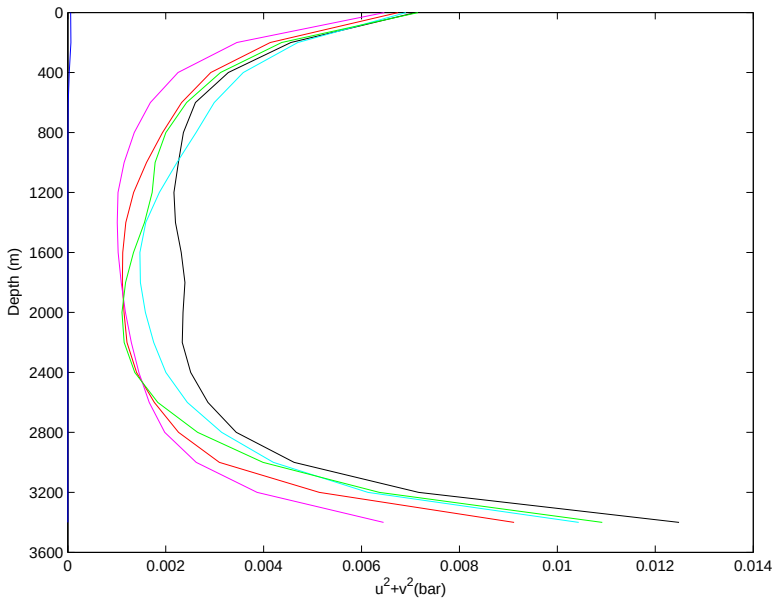

(b)

Figure 5.9: Comparison of the fixed (a) and adaptive (b) continuous uniform cooling runs using variation in horizontally averaged velocity profiles with depth at times 12 hours (blue), 24 hours (black), 36 hours (red), 48 hours (magenta), 60 hours (cyan) and 72 hours (green).

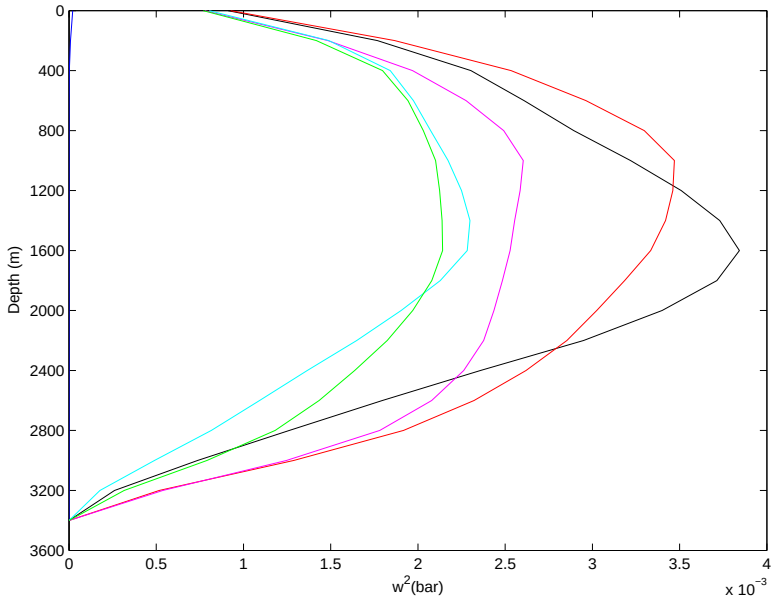

(a)

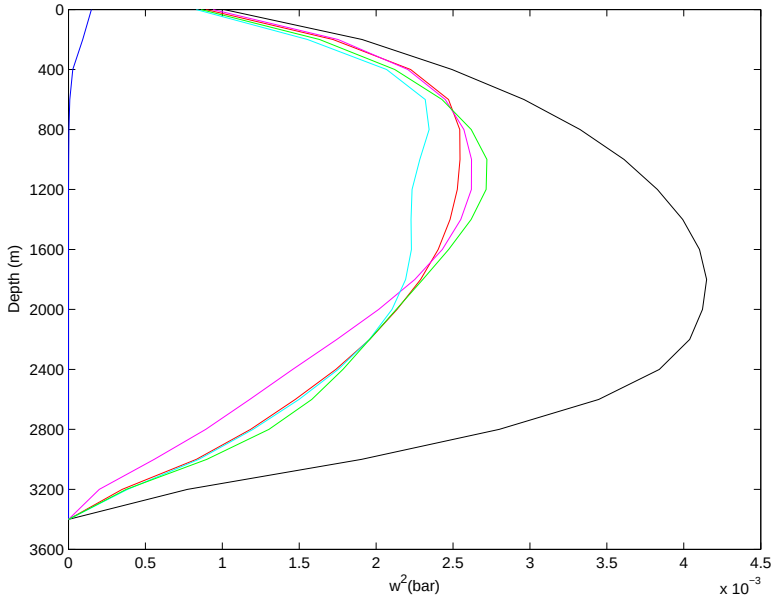

(b)

Figure 5.10: Comparison of the fixed (a) and adaptive (b) continuous uniform cooling runs using variation in horizontally averaged vertical velocity profiles with depth at times 12 hours (blue), 24 hours (black), 36 hours (red), 48 hours (magenta), 60 hours (cyan) and 72 hours (green).

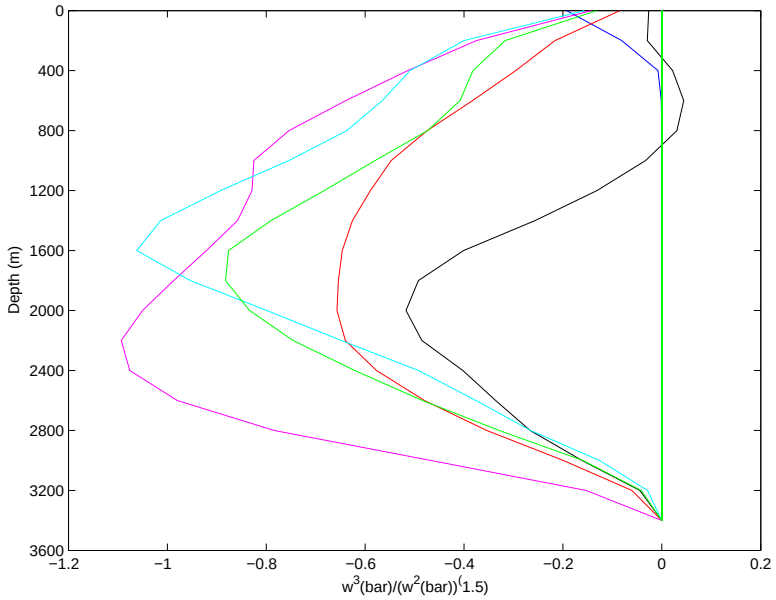

(a)

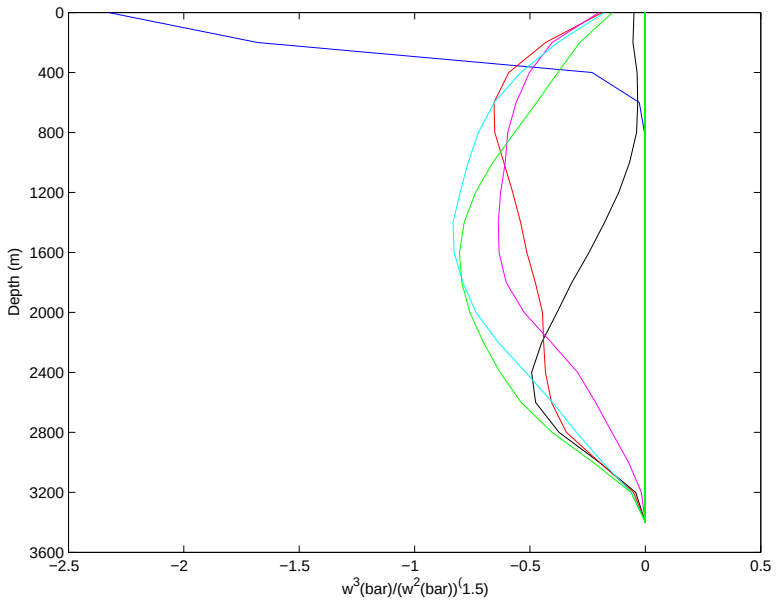

(b)

Figure 5.11: Comparison of the fixed (a) and adaptive (b) continuous uniform cooling runs using variation in skewness of vertical velocity profiles with depth at times 12 hours (blue), 24 hours (black), 36 hours (red), 48 hours (magenta), 60 hours (cyan) and 72 hours (green).

the predicted theoretical non-rotational ($w_{norot} \sim 0.13ms^{-1}$) and rotational ($w_{rot} \sim 0.07ms^{-1}$) vertical velocity scale (Figure 5.12), from Section 5.1. Unity represents full agreement with the theoretical prediction, and it is seen that the observed model vertical velocities scale strongly with the rotational regime on both the fixed and adaptive meshes. This is in agreement with the values obtained by Mironov et al. (2000), and it is concluded that vertical velocity is strongly inhibited by rotation.

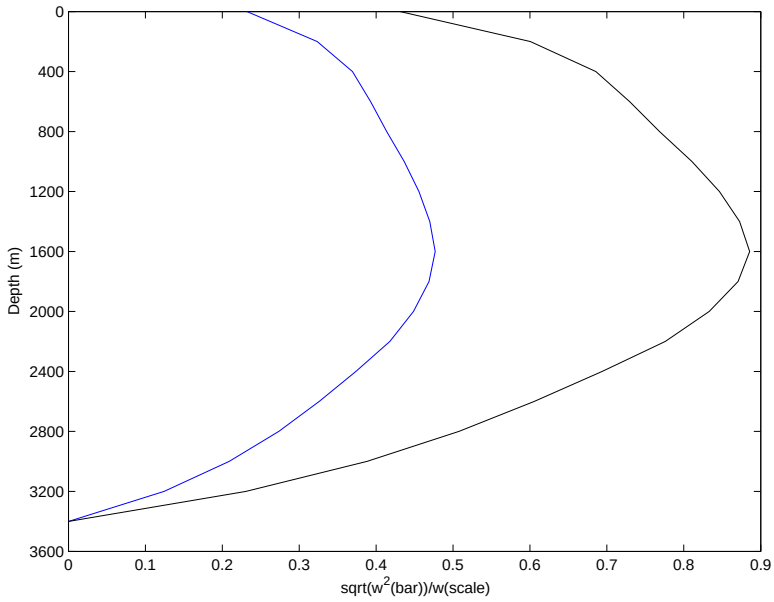

(a)

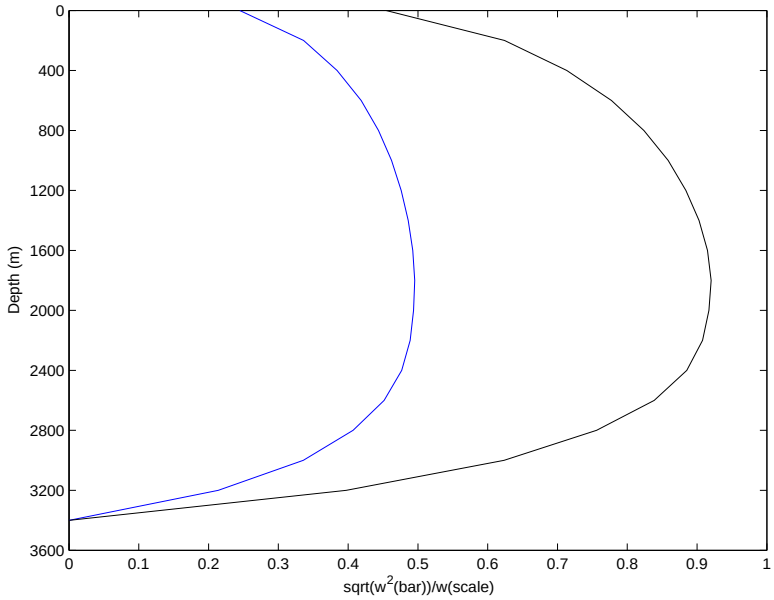

(b)

Figure 5.12: Comparison of the fixed (a) and adaptive (b) continuous uniform cooling runs using variation in horizontally averaged vertical velocity profiles with depth scaled against non-rotational (blue) and rotational (black) scaling predictions at 24 hours.

5.2.2 Comparison of finite uniform cooling forced convection on fixed and adaptive meshes

The variation in model convection resulting from the choice of fixed or adaptive mesh was further investigated by comparing model convection initiated by finite duration uniform cooling. Two model runs are considered: uniform cooling applied for a period of 24 hours on a fixed mesh and on an adaptive mesh. One important observation resulting from these runs is that the model captures all features of the convective process described by theory, including the final stage of re-stratification.

Figure 5.13 shows the development of the temperature field using a cross section through the centre of the domain at 1 hour, 24 hours, 48 hours and 72 hours for the continuous uniform cooling fixed mesh run. The stages of the convective process identified in the previous section are also evident here.

At 1 hour, cooling in the surface layer is visible. At 24 hours, a number of convective plumes can be seen extending from the surface towards the floor of the domain, reaching depths of approximately 3.2km. These plumes are not as individually defined as those observed in the disk cooled fixed mesh run, occurring predominantly in two distinct patches. It may also be noted that the field at 24 hours is identical to that observed in the uniform continuous cooling run (Figure 5.1) as would be expected. Similarly, the unphysical behaviour noted in Section 5.2.1 is again observed.

At 48 hours, the plumes have reached the bottom of the domain and two chimney-like structures can be distinguished within the domain. These two chimneys spread along the floor of the domain and begin to merge. By 72 hours, the chimneys have merged and convection is no longer active because of the absence of the cooling forcing, and sinking and re-stratification is evident. The presence of a colder denser bottom water mass within the domain is notable.

Figure 5.14 shows the development of the temperature field using a cross section through the centre of the domain at 1 hour, 24 hours, 48 hours and 72 hours for the continuous uniform cooling adaptive mesh run. The corresponding mesh structure is shown in Figure 5.15, revealing the intricacies of adaptivity as it acts to resolve the convective process. The stages of the convective process are again clearly identifiable. At 1 hour, cooling in the surface layer is visible. A concentration of resolution is observed in the region of the

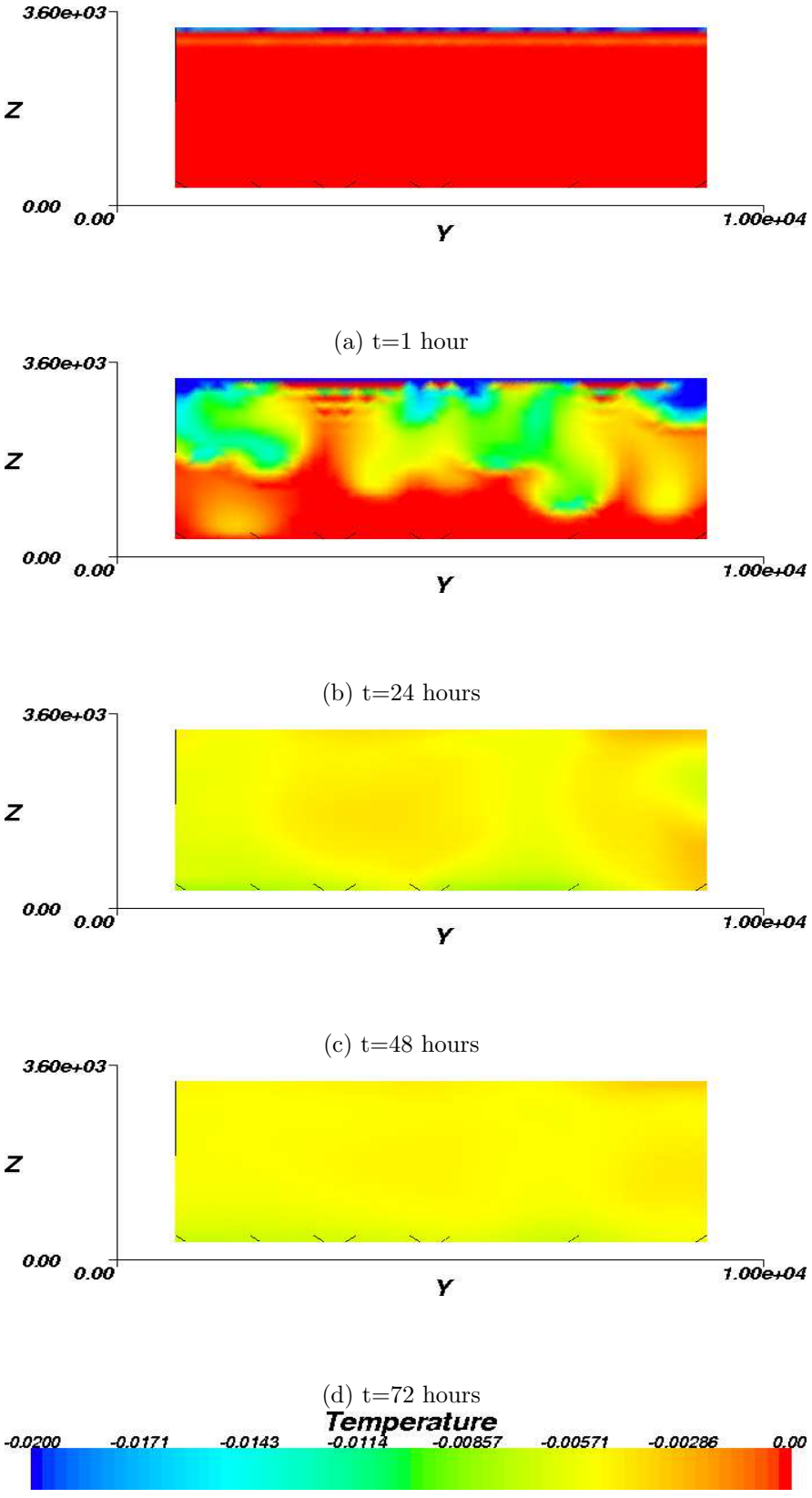

Figure 5.13: Cross-section through the centre of the domain of temperature for the 24 hour uniform cooling fixed mesh run.

cooling (that is, at the surface). Away from the surface, the mesh coarsely resolves the domain and element sizes up to 5km in length are evident.

At 24 hours, convective plumes can be seen extending approximately 1.8km from the surface towards the floor of the domain. These plumes are not completely independent of one another, but appear to be interconnected in a horizontal plane, not unlike a layer of water with a uniform temperature - or a mixed layer. The mesh acts to highly resolve the region containing the plumes, placing larger elements away from the region of convective activity (Figure 5.15).

At 48 hours, the plumes have reached the bottom of the domain. Sinking and spreading of the convected water has occurred, leaving in its place a domain of stratified water.

By 72 hours, re-stratification dominates, and the bottom water mass is notably cooler in comparison with the water mass observed on the fixed mesh. The mesh adapts to this more stable state by placing larger elements throughout the domain.

Figure 5.16 shows the horizontally averaged temperature for three depths throughout the duration of the fixed (blue) and adaptive (red) uniform finite duration cooling runs. From this plot, it may be inferred than the onset of convection generally occurs earlier in the fixed run than in the adaptive run (in contrast with Sections 5.2.3 and 5.2.1). However, at 400m, the adaptive run exhibits a more marked decrease in temperature during the cooling period. The final temperature at 1800m and 3200m is significantly lower in the adaptive run. At 400m, the final temperature is the same as for the fixed run. The final temperature for the fixed mesh is similar at all depths. The variation in final temperatures for the adaptive run indicates the presence of a stably stratified fluid throughout the water column, whereas the fixed run exhibits a well mixed vertical profile.

The character of convection in the two configurations is further exemplified by Figure 5.17, which shows the profile of temperature throughout the water column at various times. Here, it can be seen that in the fixed run, convection has almost penetrated throughout the water column to the floor by 36 hours. In comparison, convection has penetrated to approximately 1800m in the adaptive run by this time. However, the presence of a well mixed water column at subsequent times in the fixed run indicates that it does not fully capture the restratification stage of the convective process. In

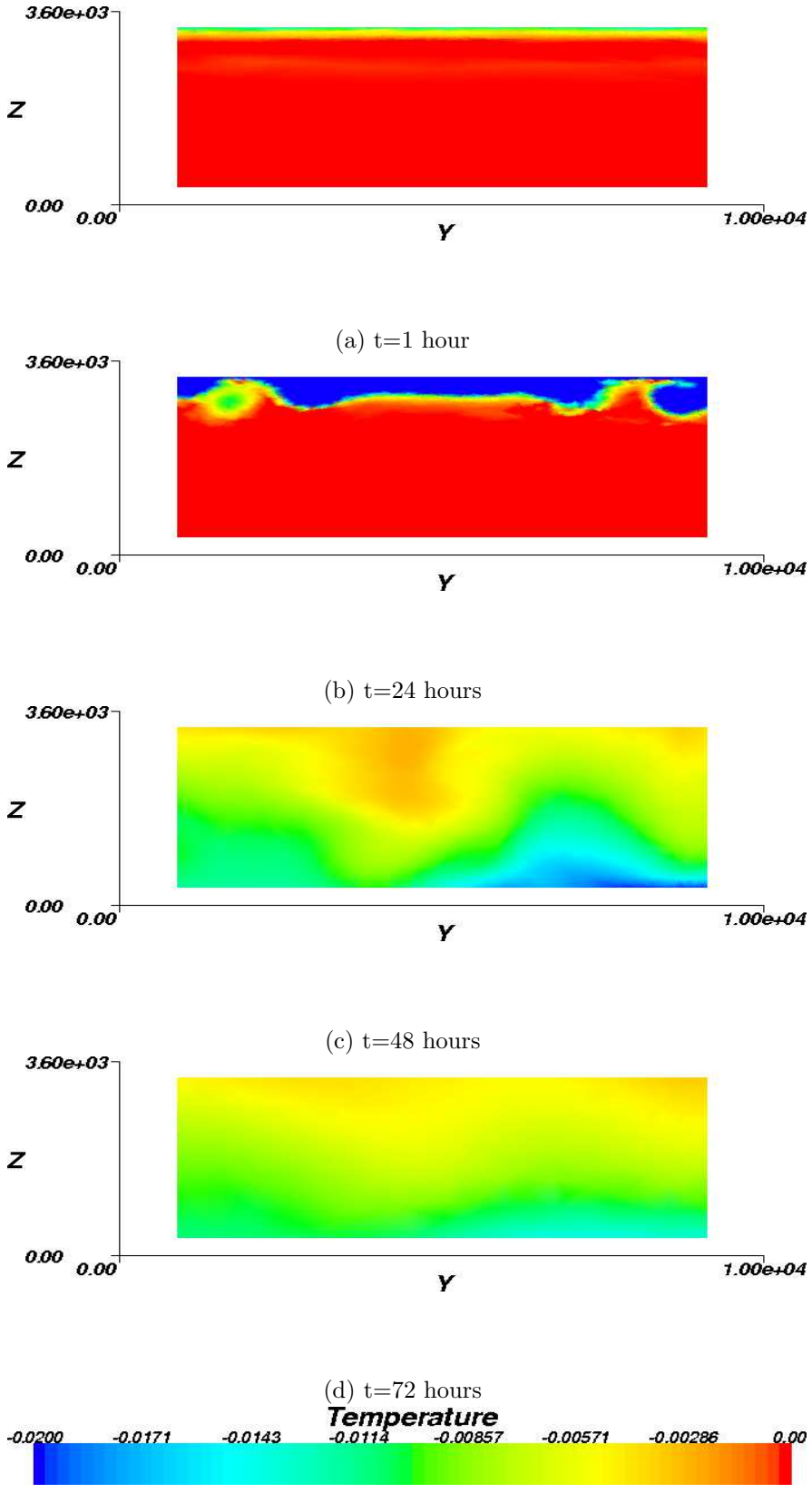

Figure 5.14: Cross-section through the centre of the temperature domain for the 24 hour uniform cooling adaptive mesh run, showing the variation of the mesh.

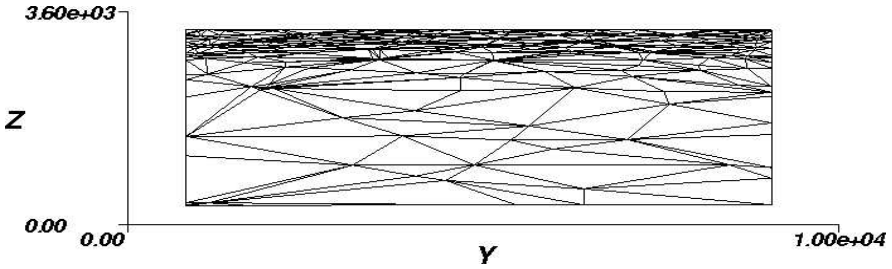

(a) t=1 hour

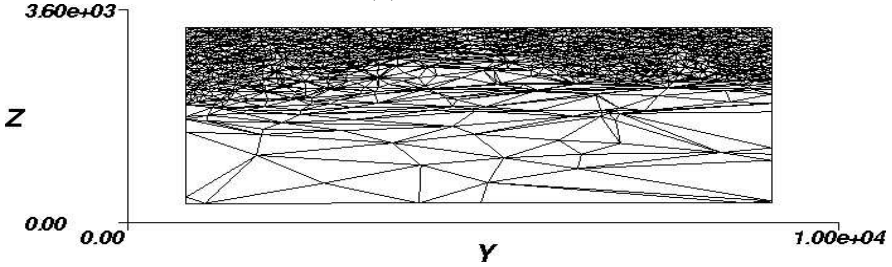

(b) t=24 hours

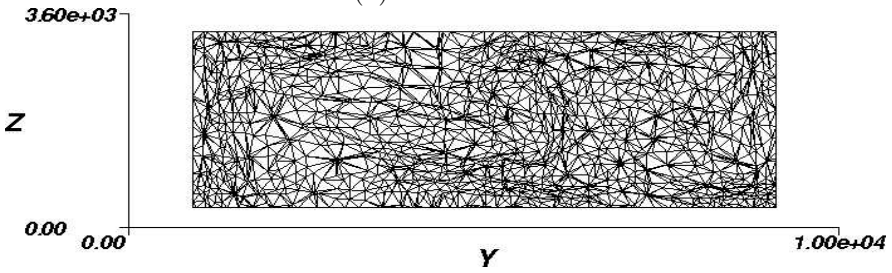

(c) t=48 hours

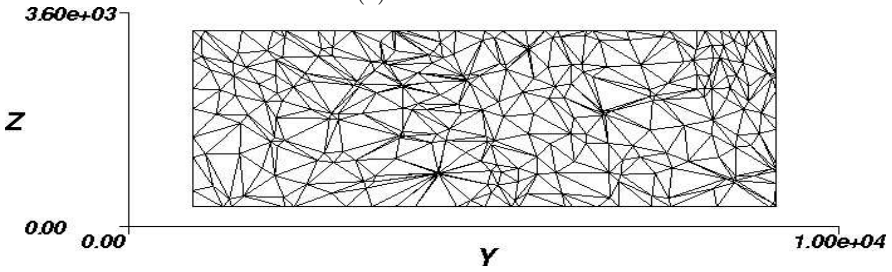

(d) t=72 hours

Figure 5.15: Corresponding mesh for the adaptive uniform finite duration cooling run.

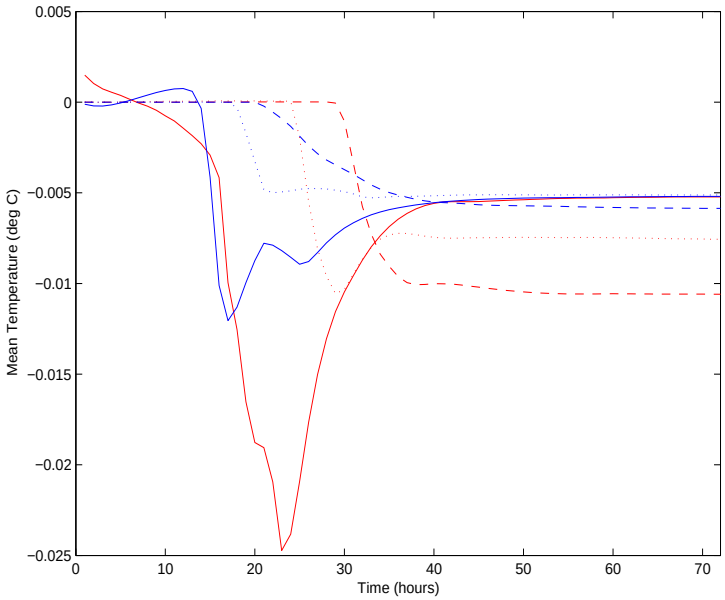

Figure 5.16: Variation in mean temperature at 400m (solid line), 1800m (dotted line) and 3200m (dashed line) for the adaptive (red) and the fixed (blue) uniform finite duration cooling runs.

contrast, the adaptive run exhibits a stably stratified profile (warmer at the surface, cooler at depth) at subsequent times.

The structure of the velocity field in the fixed finite uniform cooling at 24 hours exhibits well defined plumes and corresponding regions of upwelling (Figure 5.18 (b)). By 48 hours, the definition and strength of these plumes has become significantly weaker as a result of the absence of the surface cooling forcing. At 72 hours, a patch of cyclonic circulation depicting a relic of the convective regime is evident. This horizontal flow occurs as convected water redistributes.

The adaptive mesh finite duration uniform cooling run demonstrates significant differences (Figure 5.19). Pluming is not well defined at 24 hours, indicating the convective layer has not penetrated to 1800m. At 48 hours, evidence that convection has occurred can be identified from the increased horizontal flow, and undefined regions of low vertical velocities. The final time shows a region of strong horizontal flow that does not coincide with the patch of flow observed in the fixed configuration.

Figures 5.20, 5.21 and 5.22 show the variation in horizontally averaged velocity, horizontally averaged vertical velocity, and skewness respectively for the fixed (a) and adaptive (b) uniform finite duration cooling runs. The

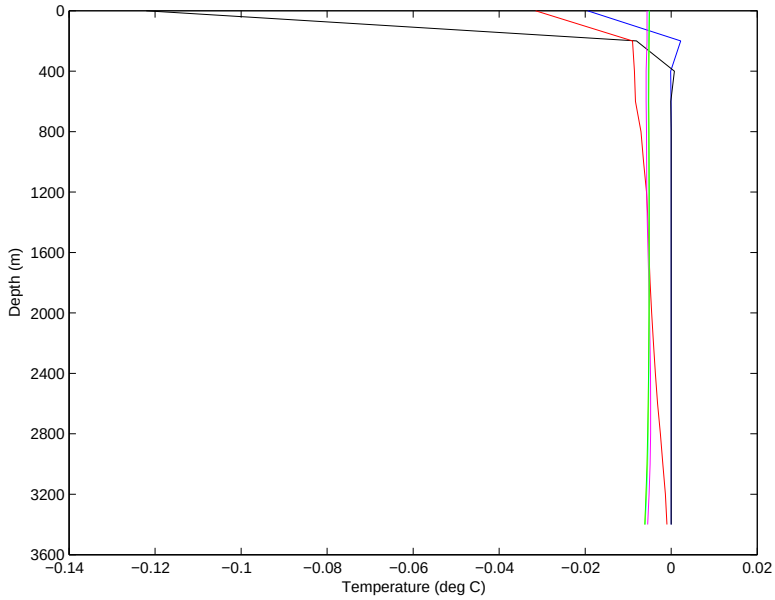

(a)

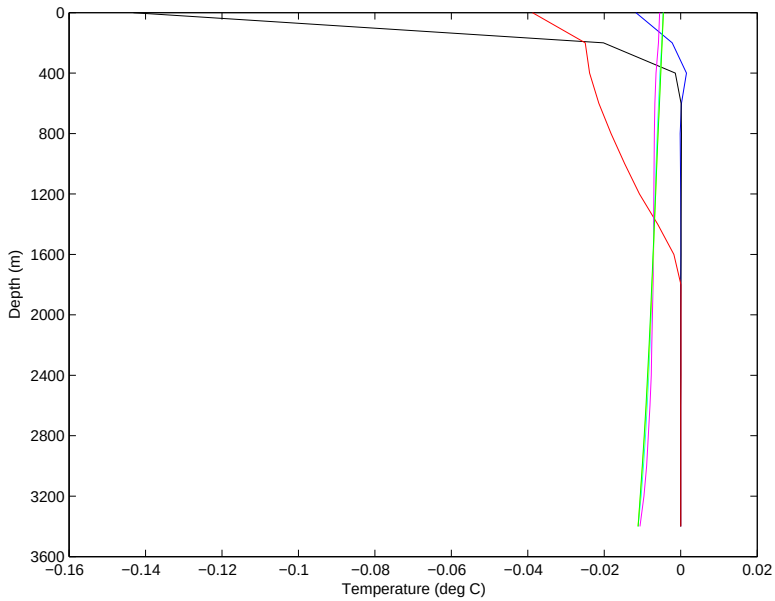

(b)

Figure 5.17: Comparison of the fixed (a) and adaptive (b) uniform finite cooling runs using variation in horizontally averaged temperature profiles with depth at times 12 hours (blue), 24 hours (black), 36 hours (red), 48 hours (magenta), 60 hours (cyan) and 72 hours (green).

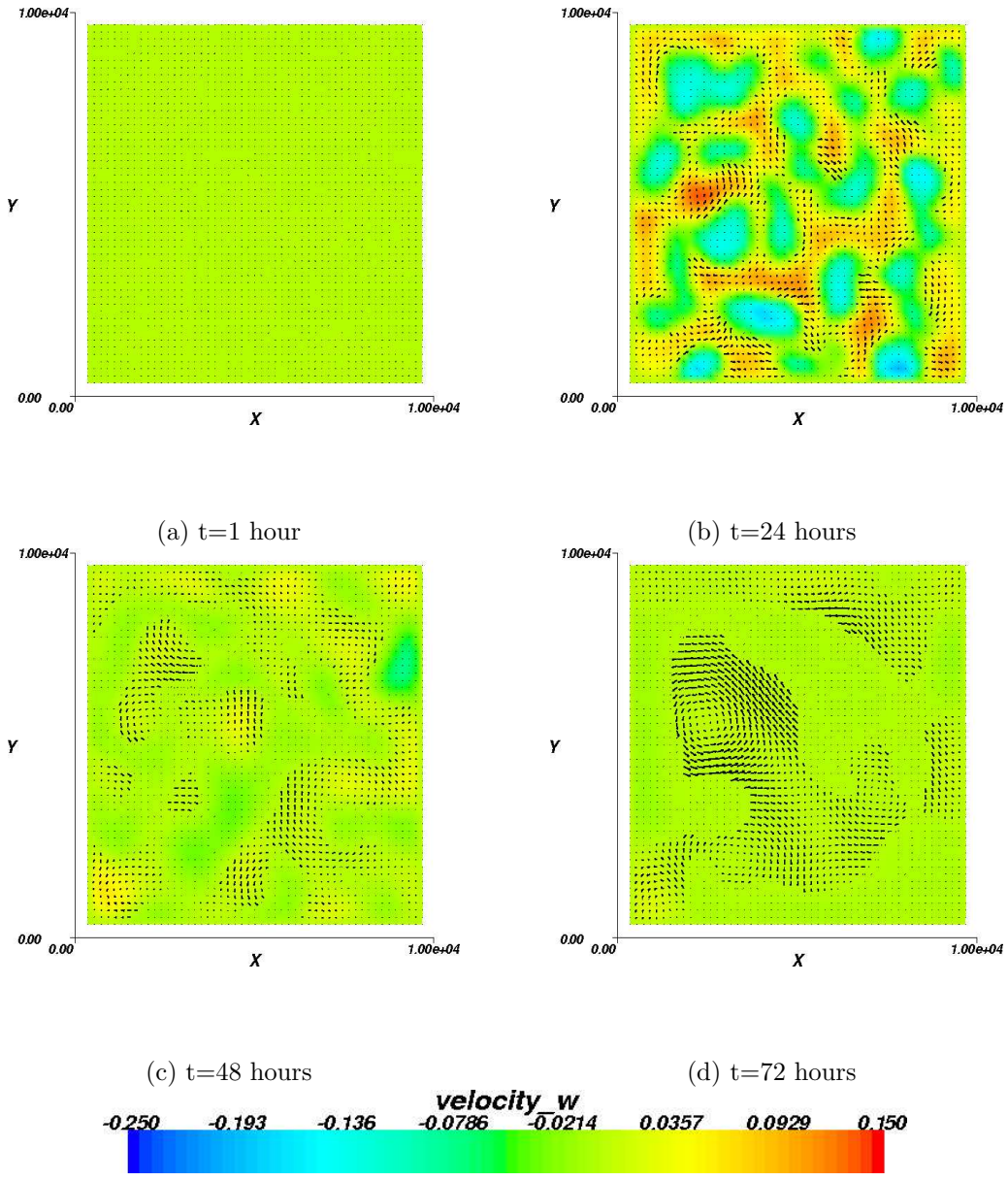

(a) t=1 hour

(b) t=24 hours

(c) t=48 hours

(d) t=72 hours

Figure 5.18: Vertical section of the domain showing the direction of the velocity vectors and contours of vertical velocity at 1800m for the finite duration uniform cooling fixed mesh run.

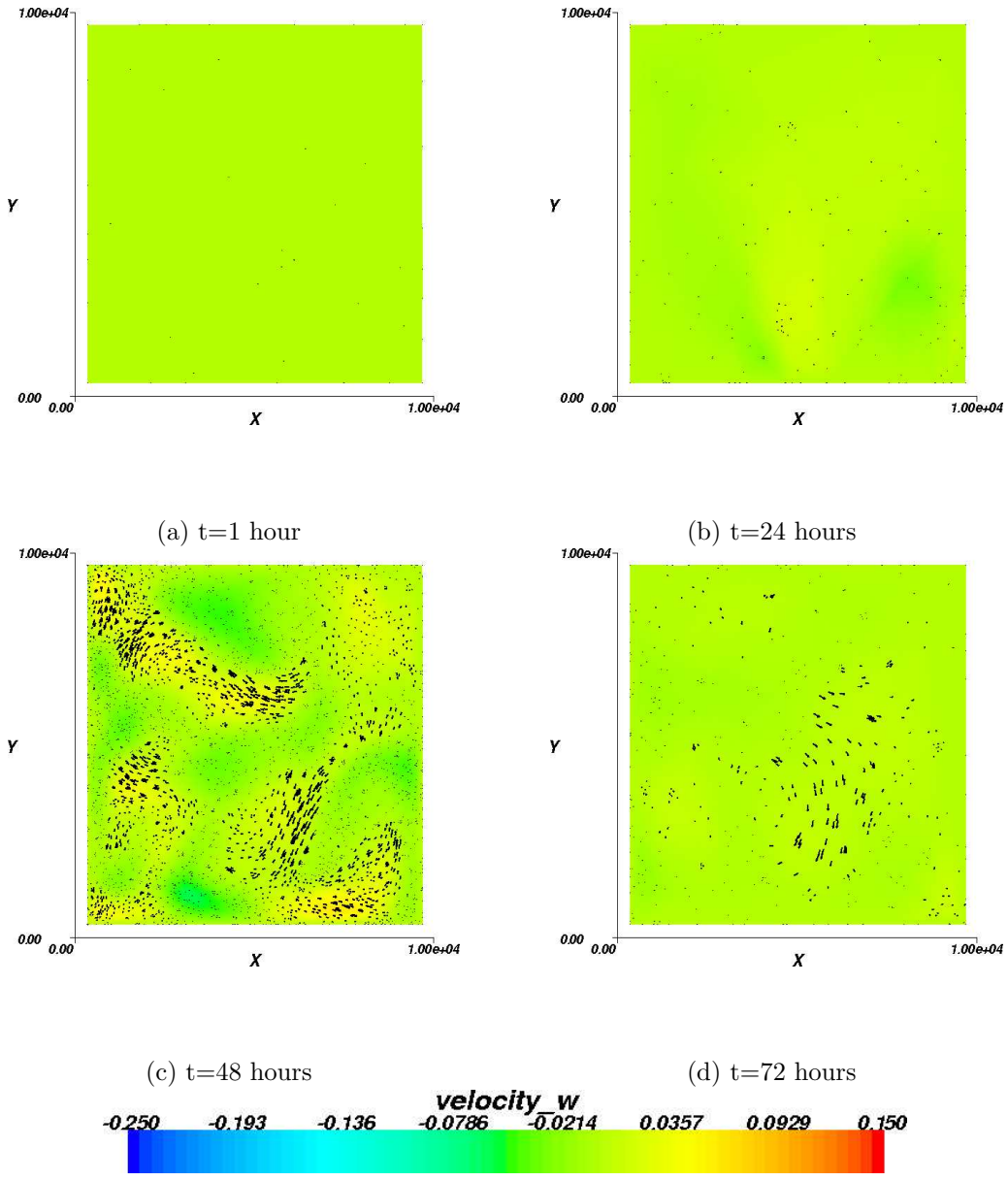

(a) t=1 hour

(b) t=24 hours

(c) t=48 hours

(d) t=72 hours

Figure 5.19: Vertical section of the domain showing the direction of the velocity vectors and contours of vertical velocity at 1800m for the finite duration uniform cooling adaptive mesh run.

adaptive mesh run shows markedly higher horizontal velocities at 36 hours compared with the fixed mesh run. However, velocities at subsequent times are higher for the fixed mesh. The fixed mesh exhibits a peak in vertical velocity at depth 1600m at 24 hours. A similar peak in magnitude occurs at this time in the adaptive run, but at a depth of just 400m. The adaptive run demonstrates a higher maximum in vertical velocity than the fixed mesh run, occurring at 36 hours and 2200m. Vertical movement in the adaptive run is restricted at later times because of the formation of a stable stratification. The skewness indicates that violent downwelling occurs earlier in the adaptive mesh run, but also shows an associated period of upwelling. Both runs produce comparable maximums in skewness.

The horizontally averaged vertical velocity profile at 24 hours was scaled against the predicted theoretical non-rotational (w_{norot}) and rotational (w_{rot}) vertical velocity. These results are presented in Figure 5.23.

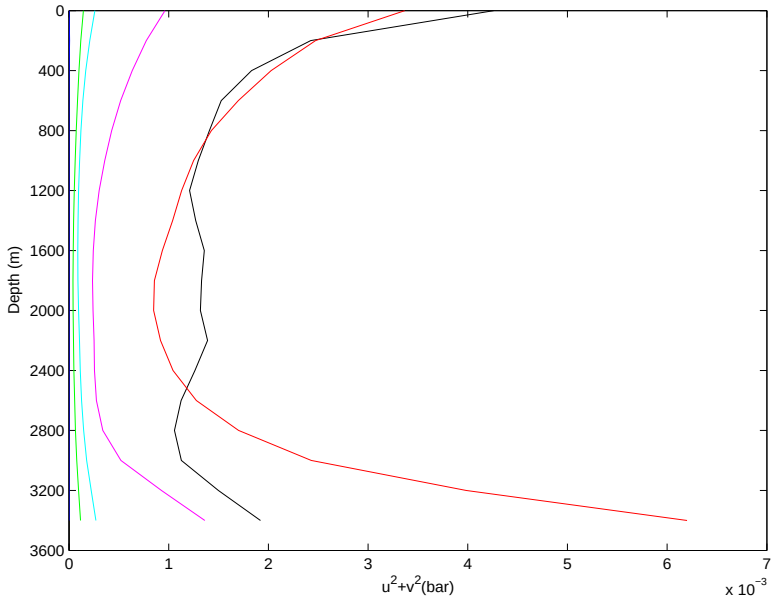

(a)

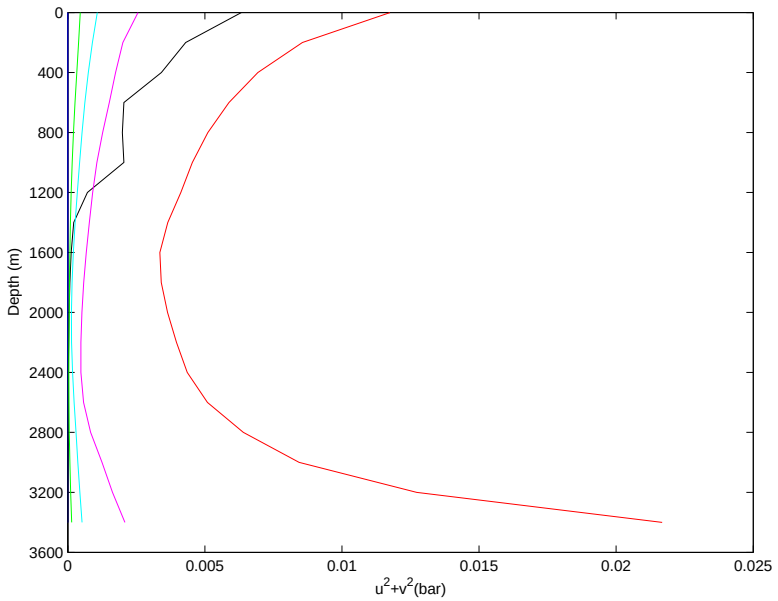

(b)

Figure 5.20: Comparison of the fixed (a) and adaptive (b) uniform finite cooling runs using variation in horizontally averaged velocity profiles with depth at times 12 hours (blue), 24 hours (black), 36 hours (red), 48 hours (magenta), 60 hours (cyan) and 72 hours (green).

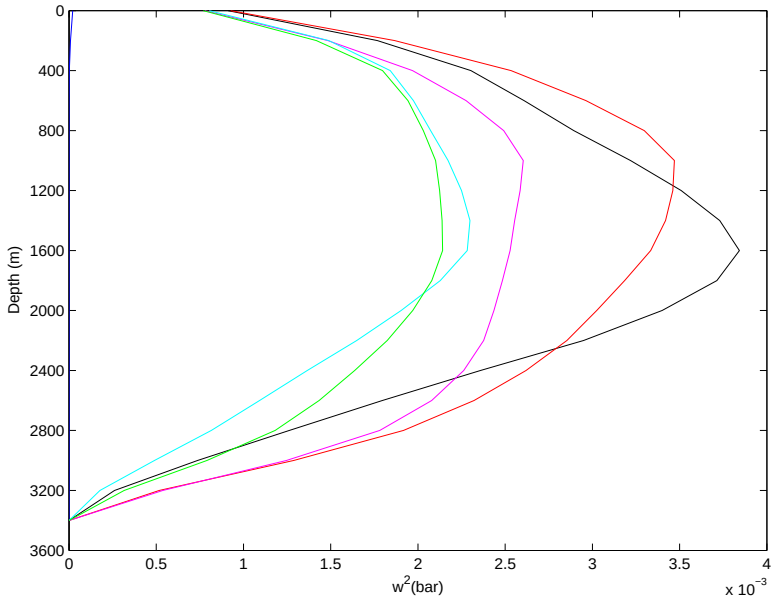

(a)

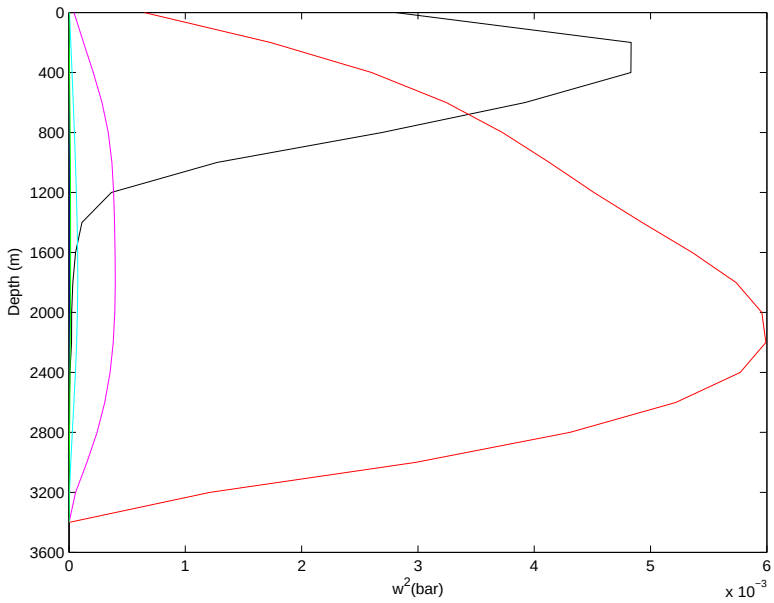

(b)

Figure 5.21: Comparison of the fixed (a) and adaptive (b) uniform finite cooling runs using variation in horizontally averaged vertical velocity profiles with depth at times 12 hours (blue), 24 hours (black), 36 hours (red), 48 hours (magenta), 60 hours (cyan) and 72 hours (green).

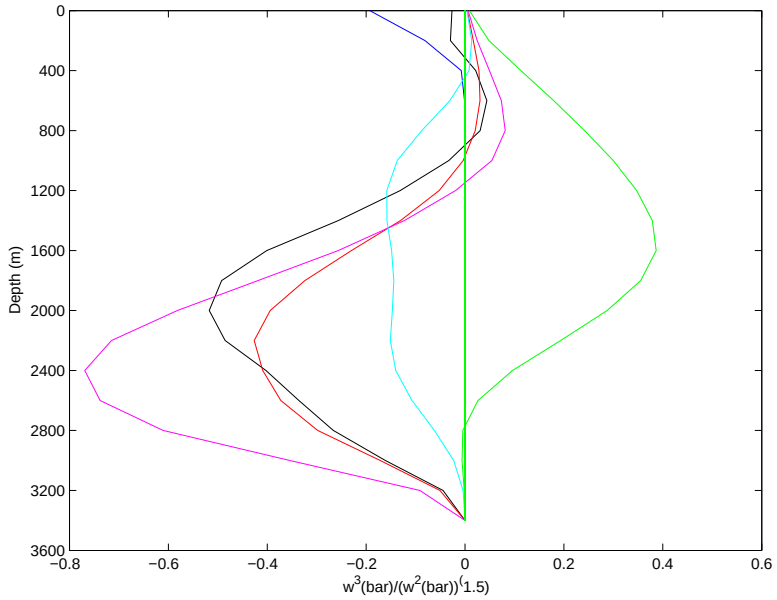

(a)

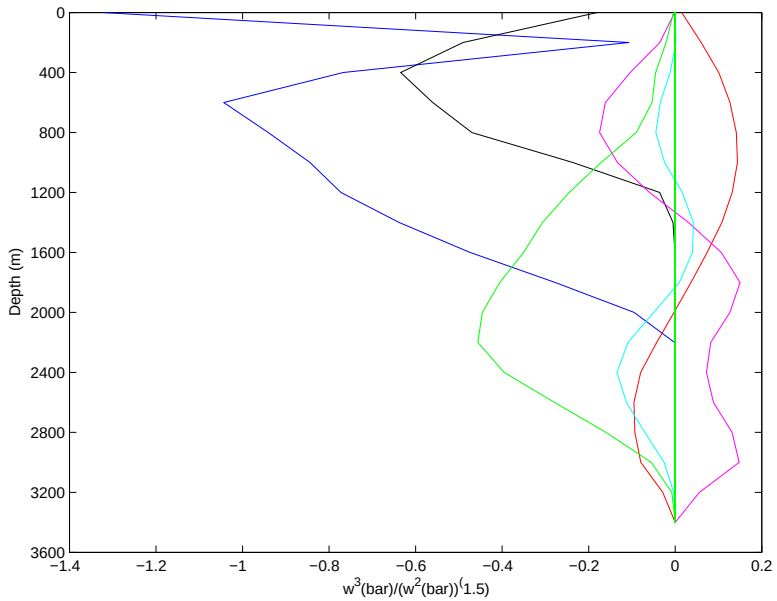

(b)

Figure 5.22: Comparison of the fixed (a) and adaptive (b) uniform finite cooling runs using variation in skewness of vertical velocity profiles with depth at times 12 hours (blue), 24 hours (black), 36 hours (red), 48 hours (magenta), 60 hours (cyan) and 72 hours (green).

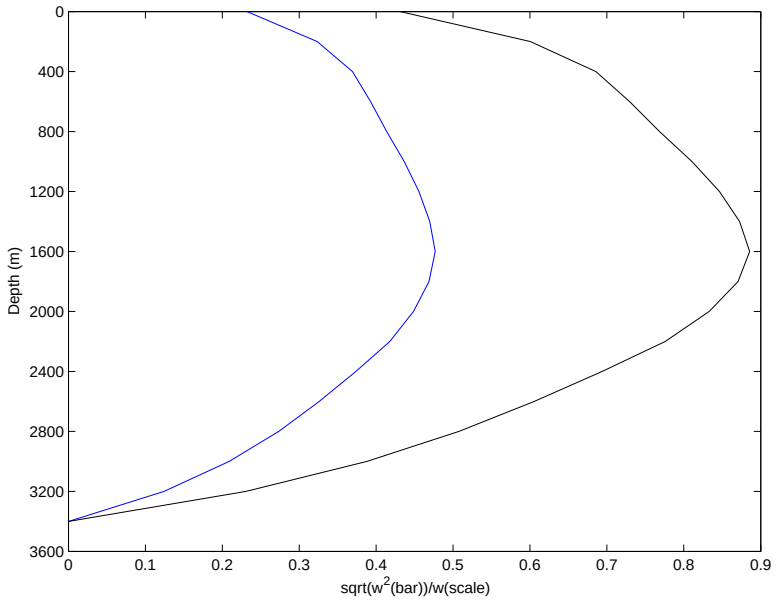

(a)

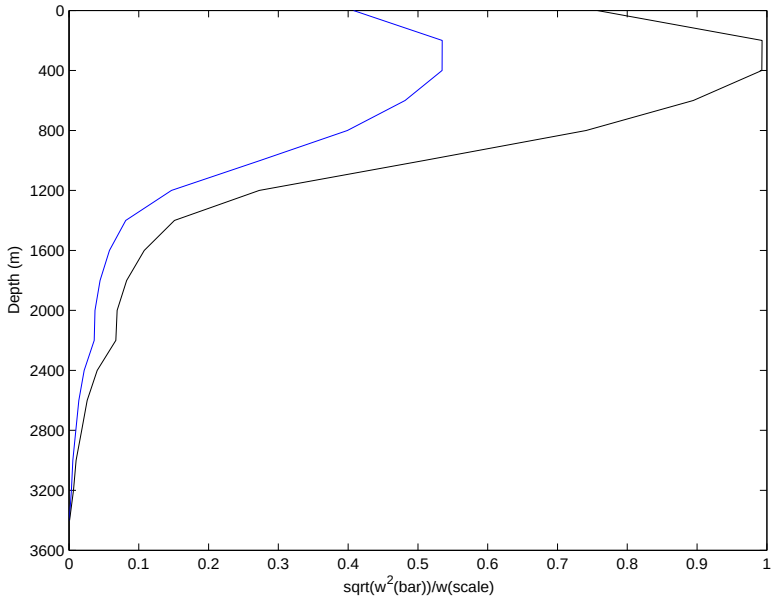

(b)

Figure 5.23: Comparison of the fixed (a) and adaptive (b) uniform finite cooling runs using variation in horizontally averaged vertical velocity profiles with depth scaled against non-rotational (blue) and rotational (black) scaling predictions at 24 hours.

5.2.3 Comparison of continuous disk cooling forced convection on fixed and adaptive meshes

Figure 5.24 shows the development of the temperature field using a cross section through the centre of the domain at 1 hour, 24 hours, 48 hours and 72 hours for the continuous disk cooling fixed mesh run. The stages of the convective process discussed in Chapter 2 Section 2.2.2 can be clearly identified. At 1 hour, cooling in the surface disk is visible. At 24 hours, three convective plumes can be seen extending from the surface towards the floor of the domain, each approximately 1 - 1.5km in width. At 48 hours, the plumes have reached the bottom of the domain and a chimney-like structure is evident. By 72 hours, the chimney is well established, but some spreading is obvious along the floor of the domain. The chimney takes on the scale of the initial cooling disk - extending approximately 6km in diameter.

Figure 5.25 shows the development of the temperature field at 1 hour, 24 hours, 48 hours and 72 hours for the continuous disk cooling adaptive mesh run. The mesh is shown in Figure 5.26. At 1 hour, cooling in the surface disk is visible. A concentration of resolution is observed in the region of the cooling disk. Away from the disk, the mesh coarsely resolves the domain and element sizes up to 5km in length are evident.

At 24 hours, three convective plumes can be seen extending approximately 2.5km from the surface towards the floor of the domain, each approximately 1 - 1.5km in width. The mesh acts to highly resolve the region containing the plumes, placing larger elements away from the region of convective activity.

At 48 hours, the plumes have reached the bottom of the domain and a chimney-like structure is evident, the high resolution mesh extends throughout the entire domain. Spreading at the bottom of the chimney occurs, particularly on the south side of the domain (right hand side). At the surface, a small region of cold water can be identified to the right hand side of the cooling disk, possibly an eddy spawned from the distortion of the rim current around the disk, related to the impact of rotation and the onset of baroclinic instability.

By 72 hours, the chimney is well established, becoming more defined than at previous times, but the chimney is not as extensive as at previous times. Further pluming, reaching the bottom of the domain as it is no longer impeded by the presence of an opposing water mass, is evident. The chimney

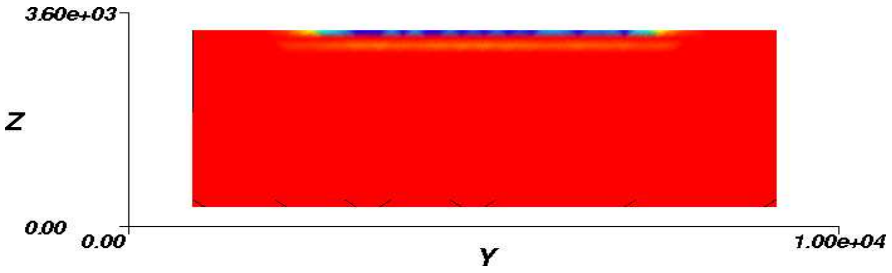

(a) t=1 hour

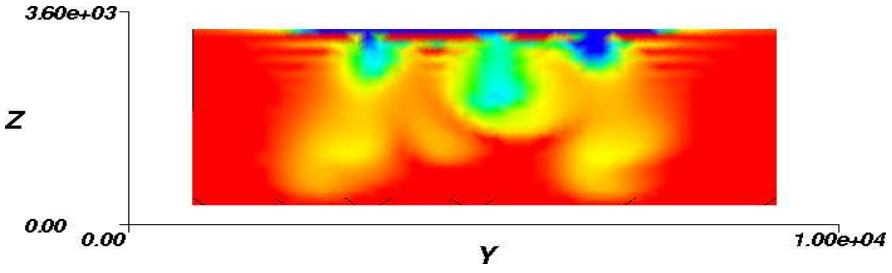

(b) t=24 hours

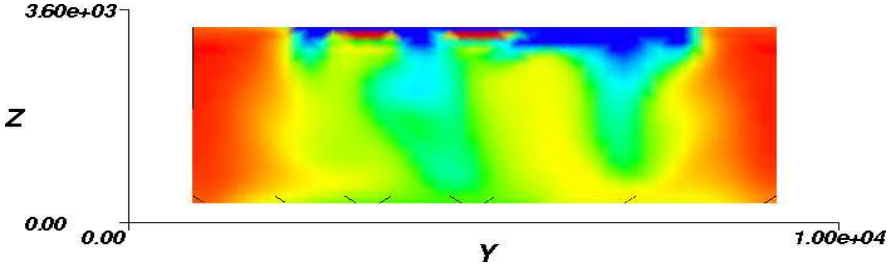

(c) t=48 hours

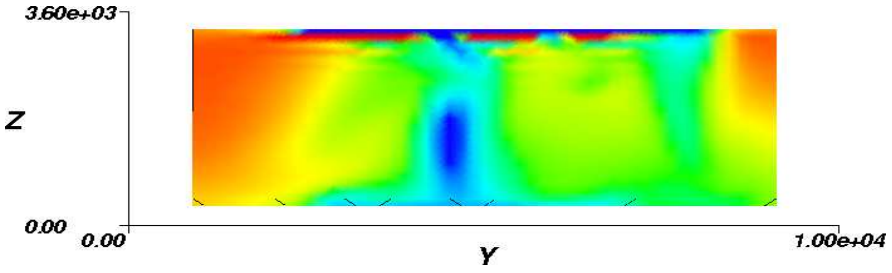

(d) t=72 hours

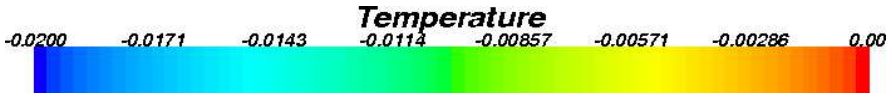

Figure 5.24: Cross-section through the centre of the domain of temperature for the continuous disk cooling fixed mesh run.

takes on the scale of the initial cooling disk (as observed on the fixed mesh) - extending approximately 6km in diameter. The pocket of cold dense water to the south of the cooling disk has increased in depth.

Figure 5.27 shows the mean temperature for 3 depths (400m, 1800m and 3200m) evolving over time. The adaptive cooling disk run is shown in red, and the fixed disk cooling run in blue. At 400m, it can be seen that the cooling in the adaptive run onsets slightly earlier. The initial convective cooling event is stronger, cooling to $-5.2 * 10^{-3\circ}C$ in $\sim$ 2 hours, compared with $-3.0 * 10^{-3\circ}C$ for the fixed mesh. However, at 1800m and 3600m the onset of cooling occurs earlier in the fixed mesh run, although the amount of cooling is larger for the adaptive mesh. At 400m and 1800m, the adaptive run exhibits the lowest final temperature. At 3200m, both runs exhibit similar final temperatures.

Figure 5.28 shows the variation in vertical average temperature profile at 12, 24, 36, 48, 60 and 72 hours. For the fixed mesh run at 12 hours the thermocline (the region near the surface that demonstrates a sharp gradient in temperature with depth) reaches 200m, below which the water column remains at a constant initial temperature. The thermocline extends to 800m at 24 hours. At 36 hours, the water column below the thermocline has cooled by approximately $-1.0 * 10^{-3\circ}C$, and continues to show cooling throughout a well mixed water column over the remaining times, exhibiting a final temperature of roughly $-5.0 * 10^{-3\circ}C$. A notable feature is the formation of a density gradient below 2800m, perhaps indicating the formation of a new water mass and restratification.

The thermocline formed in the adaptive run extends to 400m at 12 hours, and 800m at 24 hours. At 36 hours, the water column below the thermocline has cooled by $3.0 * 10^{-3}$ to a depth of 1900m. The water column is well mixed at subsequent times and cools to $-6.0 * 10^{-3\circ}C$ at 72 hours, but remains slightly unstable above 1800m.

Figure 5.29 depicts the flow field associated with the disk shaped cooling. At 24 hours, the signature of the surface disk cooling at 1800m is evident - a ring of upwelling indicates the edge of the convective chimney, within which a concentric ring of downwelling is contained. An inner region contains two well defined plumes, and two clear regions of upwelling. Horizontal flow coincides with the regions of upwelling. At 48 hours, this structured flow field exhibits deformation as the convective chimney comes under rotational

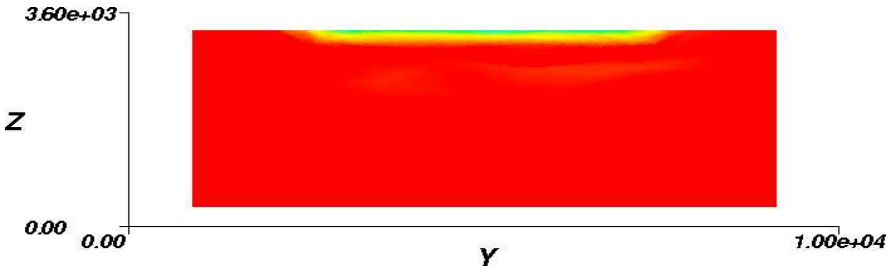

(a) t=1 hour

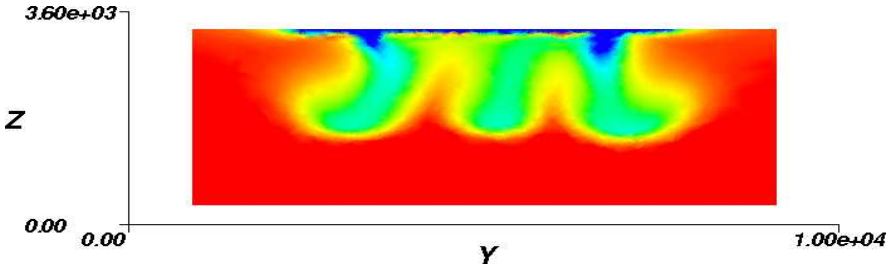

(b) t=24 hours

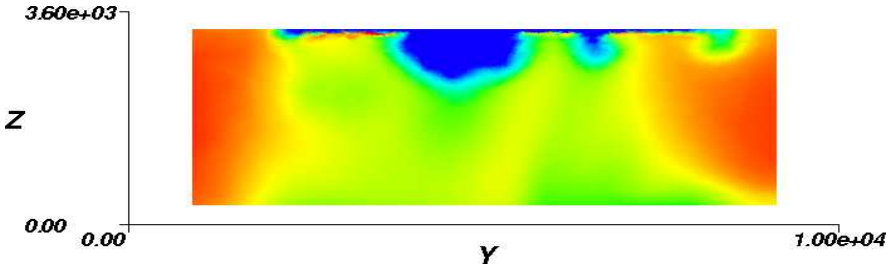

(c) t=48 hours

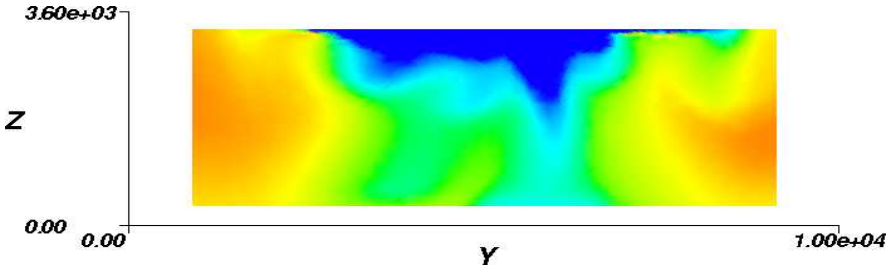

(d) t=72 hours

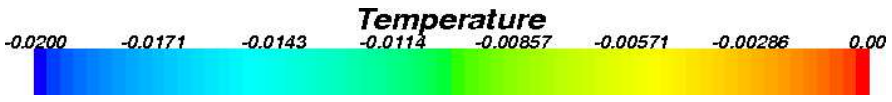

Figure 5.25: Cross-section through the centre of the domain of temperature for the continuous disk cooling adaptive mesh run.

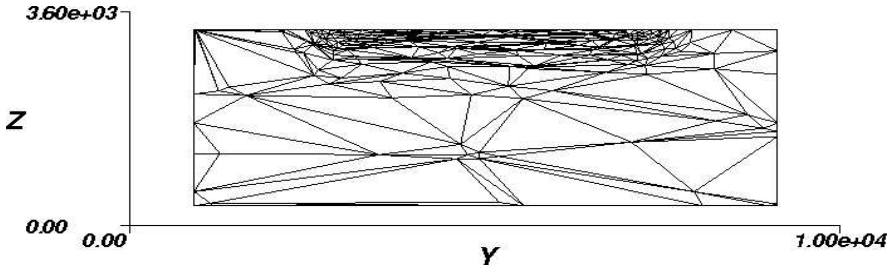

(a) t=1 hour

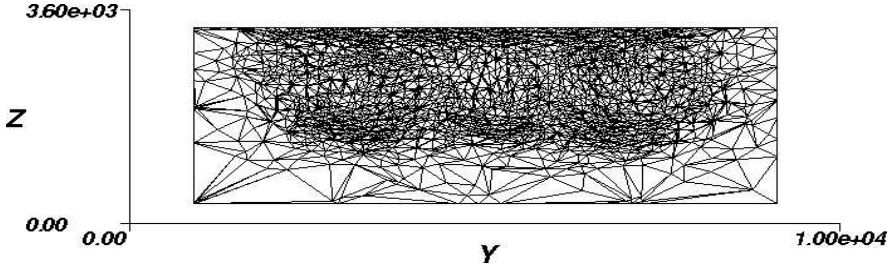

(b) t=24 hours

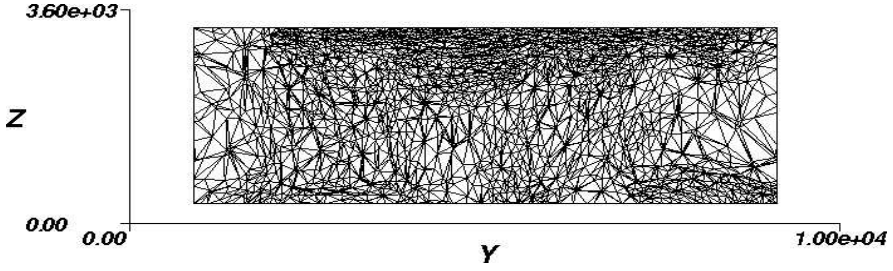

(c) t=48 hours

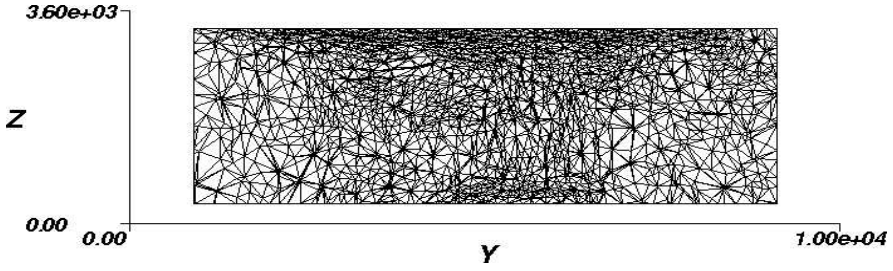

(d) t=72 hours

Figure 5.26: Corresponding mesh distribution for the continuous disk cooling adaptive mesh run.

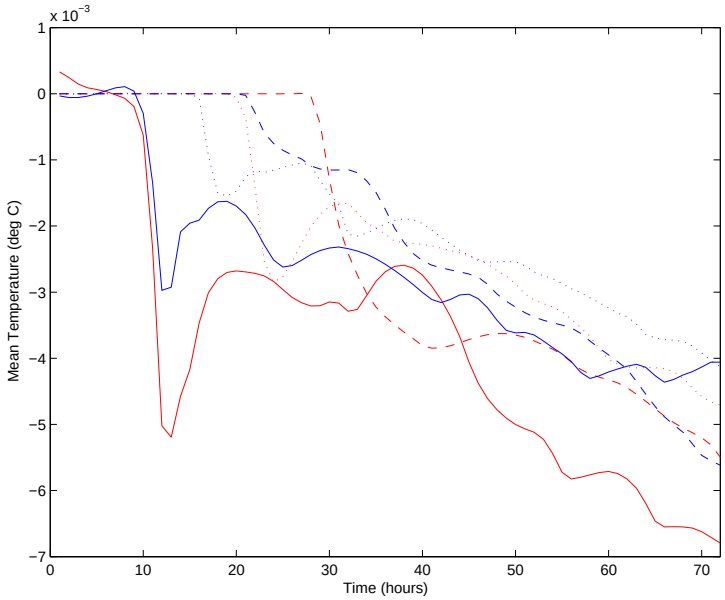

Figure 5.27: Variation in mean temperature at 400m (solid line), 1800m (dotted line) and 3200m (dashed line) for the adaptive (red) and fixed (blue) cooling runs.

control. By 72 hours, the previous chimney structure is no longer evident as eddies are transported by the horizontal baroclinic flow around the whole domain.

The convective signature demonstrated in Figure 5.30 (b) illustrates the flow field associated with the adaptive disk cooling run. The field structure allows 4 concentric rings of flow to be identified. At the outer rim, a ring of upwelling coincides with a cyclonic horizontal velocity. The second ring indicates a region of convective downwelling on the rim of the convective chimney. Within this a smaller ring of upwelling occurs, and within this a small region of downwelling occurs. By 48 and 72 hours, the cooling disk edge becomes distorted as the convective chimney is impacted by rotation.

The disk cooling problem allows the std of the formation of eddies associated with the break-up of the convective chimney. The images presented in Figures 5.29 and 5.30 show defined eddies forming at 48 and 72 hours. In the fixed mesh case, individual eddies have a scale of approximately $2-3km$. The adaptive mesh, however, produces larger eddies approximately $3-5km$ in length. The adaptive mesh eddies scale better with the expected values of the Rossby deformation radius (L_R) from reality ($5-10km$).

Figure 5.31 (a) shows the horizontally averaged velocity for the fixed disk

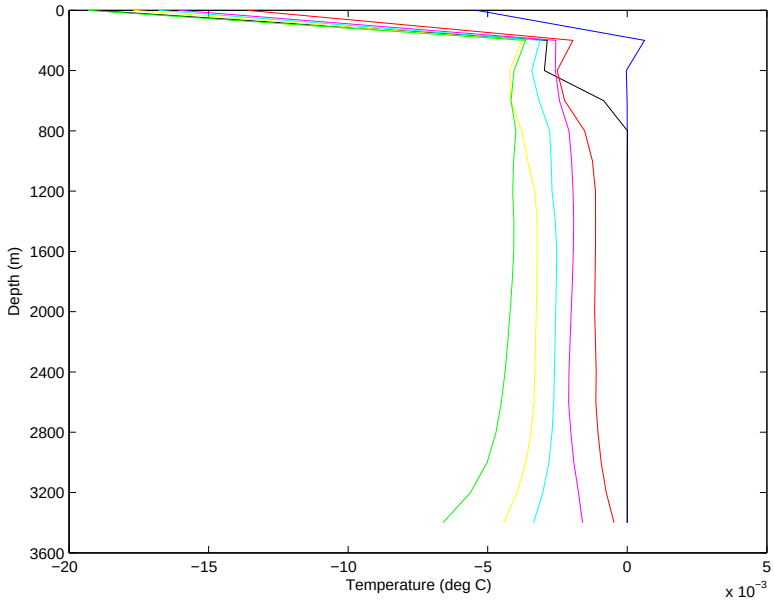

(a)

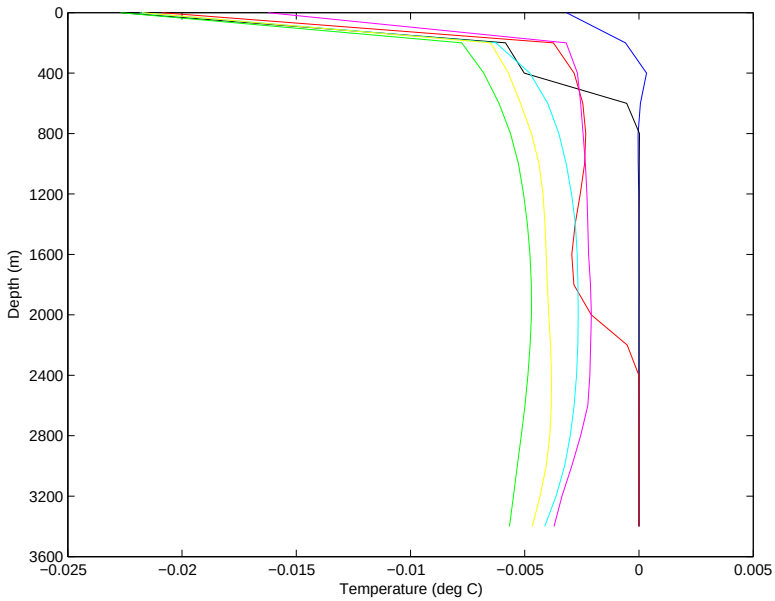

(b)

Figure 5.28: Comparison of the fixed (a) and adaptive (b) continuous disk cooling runs using variation in horizontally averaged temperature profiles with depth at times 12 hours (blue), 24 hours (black), 36 hours (red), 48 hours (magenta), 60 hours (cyan) and 72 hours (green).

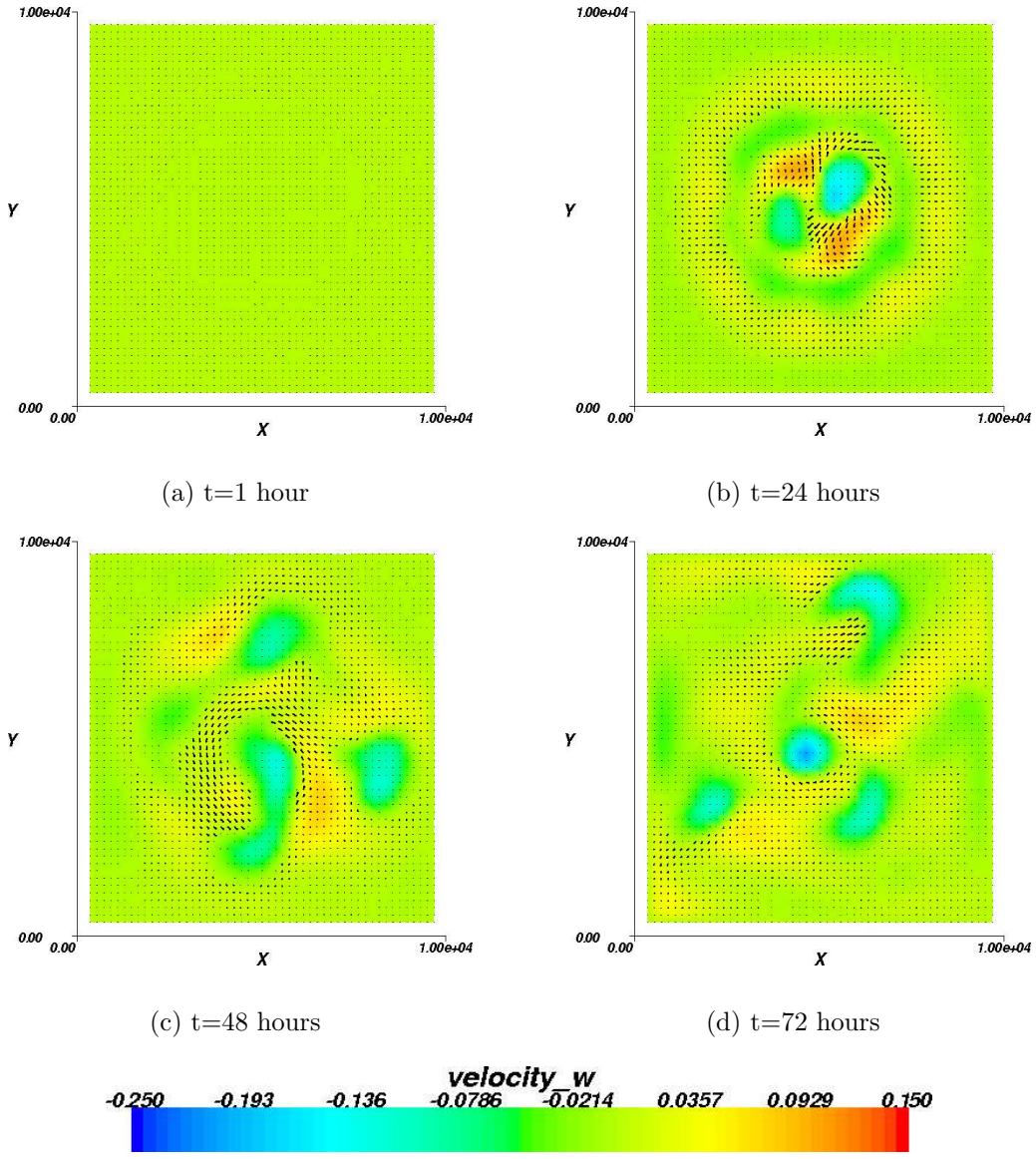

(a) t=1 hour

(b) t=24 hours

(c) t=48 hours

(d) t=72 hours

Figure 5.29: Vertical section of the domain showing the direction of the horizontal velocity vectors and contours of vertical velocity at 1800m for the continuous disk cooling fixed mesh run.

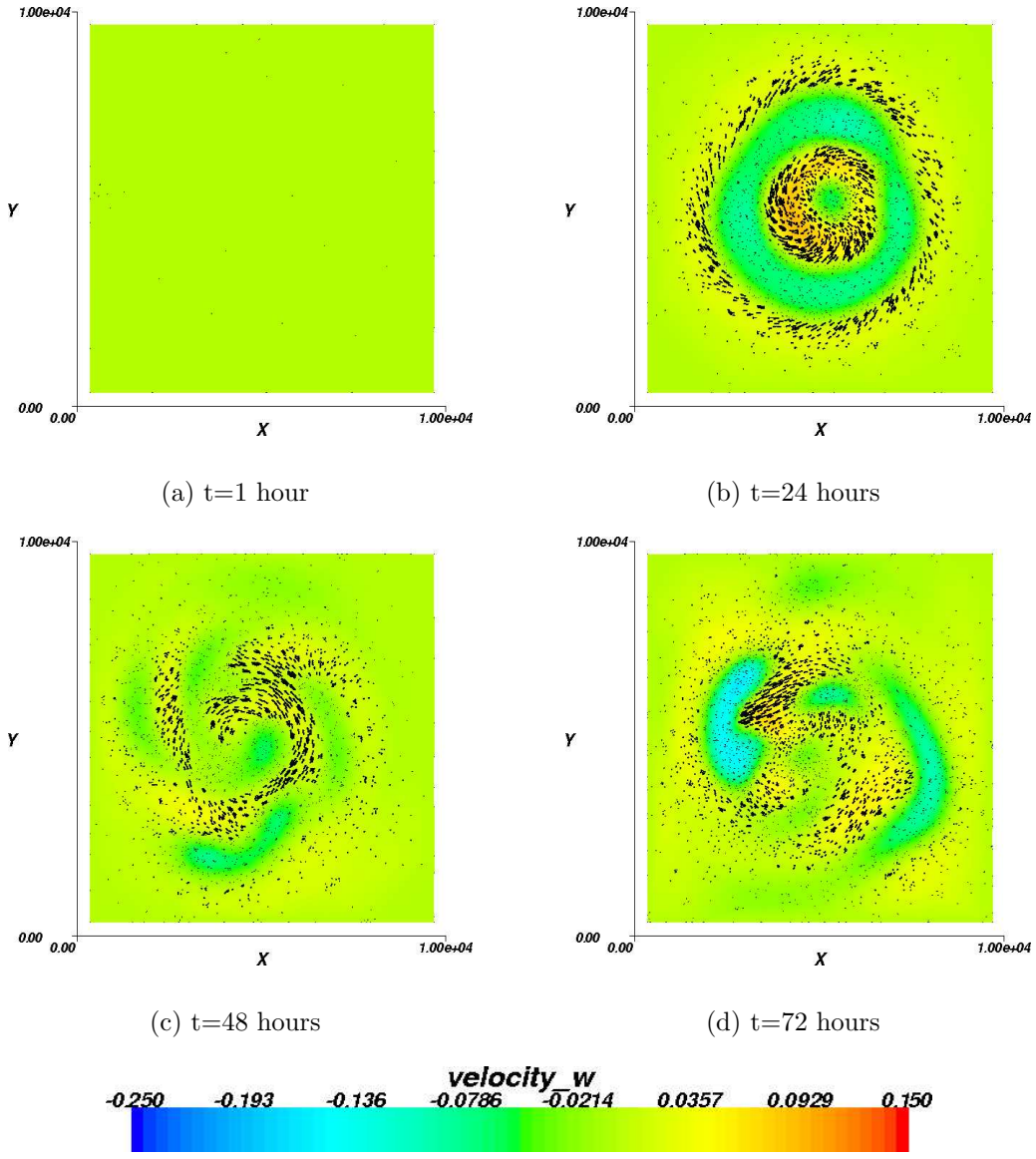

(a) t=1 hour

(b) t=24 hours

(c) t=48 hours

(d) t=72 hours

Figure 5.30: Vertical section of the domain showing the direction of the horizontal velocity vectors and contours of vertical velocity at 1800m for the continuous disk cooling adaptive mesh run.

cooling run. At 12 hours, the speed is zero. By 24 hours, the speed at the surface and bottom has increased, and lowest horizontal velocities occur at intermediate depths. The highest velocity occurs at the lowest depth at 72 hours ($\sim 0.01 ms^{-1}$). Figure 5.31 (b) shows the horizontally averaged velocity for the adaptive run. At 24 hours the velocity increases at the surface but decreases to zero with depth. The highest velocities occur at the surface at 72 hours and at the bottom at 36 hours. At 48 and 60 hours the bottom velocities are lower than observed in the fixed mesh run. The adaptive mesh exhibits the highest bottom velocities ($0.013 ms^{-1}$), and the fixed mesh the highest surface velocities ($0.007 ms^{-1}$).

Figure 5.32 shows the horizontally averaged vertical velocities for the fixed (a) and adaptive (b) cooling disk runs. This is a good indication of the depth of penetration of convection over time. The fixed mesh exhibits a peak in vertical velocity at 2000m after 36 hours. The adaptive mesh run exhibits two phases of convection, with a peak in vertical velocity at 1600m after 24 hours, and a second peak at 72 hours. Both configurations demonstrate similar maximum vertical velocities (about $1.3 * 10^{-3} m^2 s^{-2}$).

Figure 5.33 shows skewness of the vertical velocity. Figure 5.33 (a) shows that, for the fixed mesh cooling disk run, downwelling is stronger at all times except at 24 hours, when upwelling dominates above 1200m. For the adaptive mesh run (Figure 5.33 (b)), downwelling dominates at all times, with the strongest downwelling occurring at 1800m after 72 hours.

Figure 5.34 presents the horizontally averaged vertical velocity profile at 24 hours scaled against the predicted theoretical non-rotational (w_{norot}) and rotational (w_{rot}) vertical velocity. As observed in previous runs, both configurations scale more with the rotational scale, and the adaptive configuration scales most strongly with the predicted W_rot.

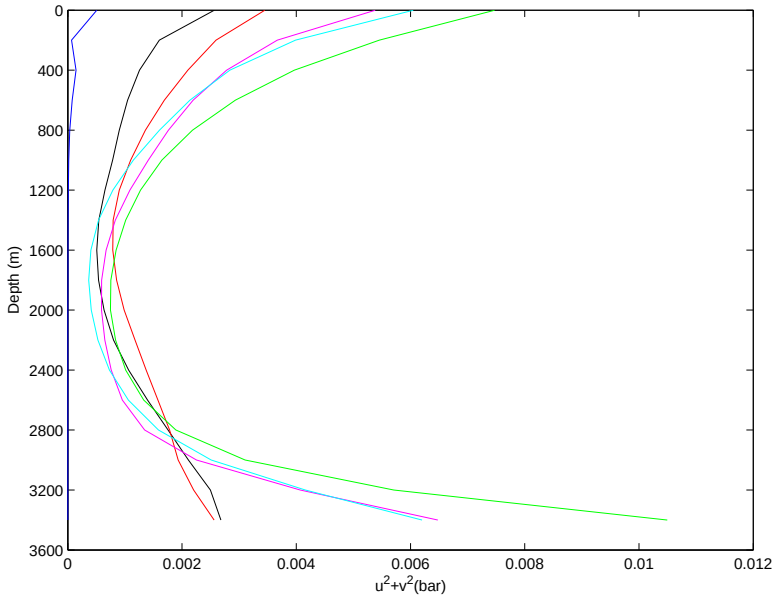

(a)

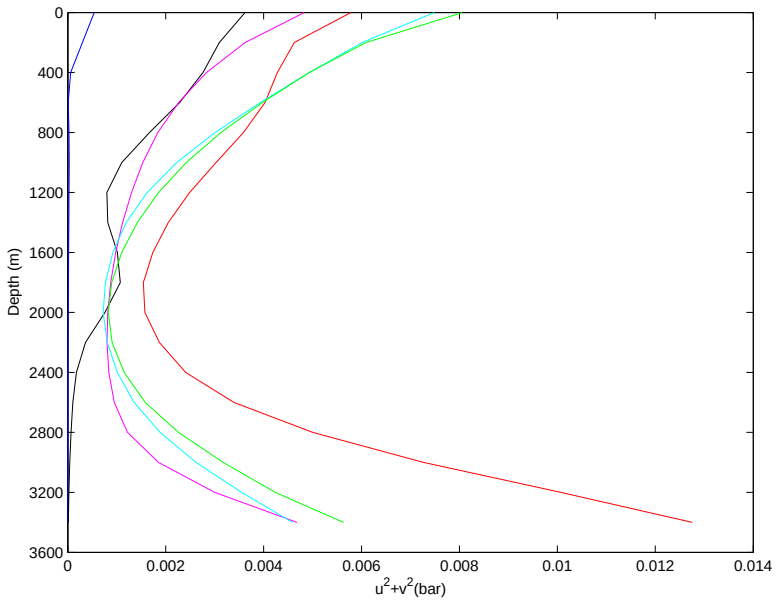

(b)

Figure 5.31: Comparison of the fixed (a) and adaptive (b) continuous disk cooling runs using variation in horizontally averaged velocity profiles with depth at times 12 hours (blue), 24 hours (black), 36 hours (red), 48 hours (magenta), 60 hours (cyan) and 72 hours (green).

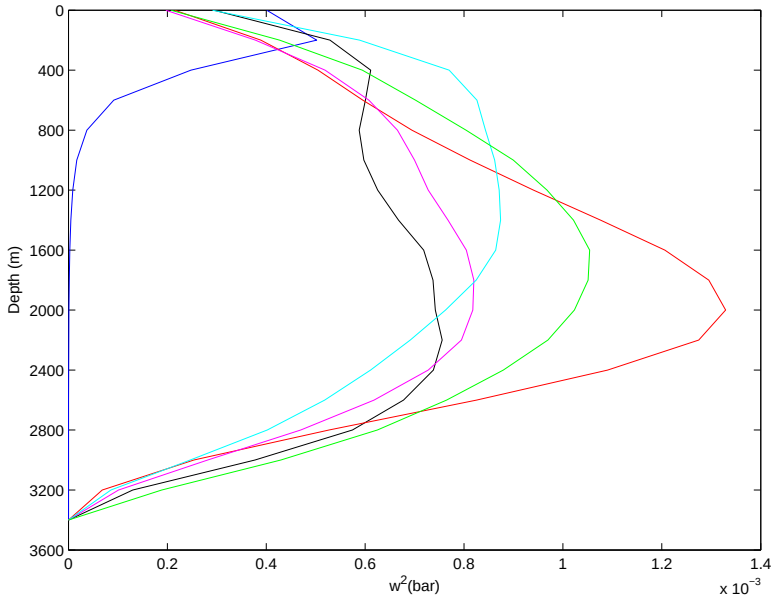

(a)

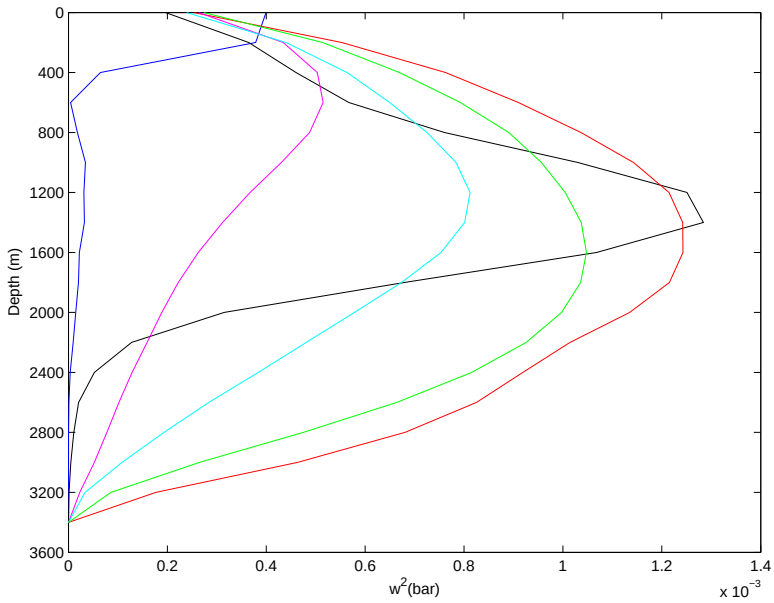

(b)

Figure 5.32: Comparison of the fixed (a) and adaptive (b) continuous disk cooling runs using variation in horizontally averaged vertical velocity profiles with depth at times 12 hours (blue), 24 hours (black), 36 hours (red), 48 hours (magenta), 60 hours (cyan) and 72 hours (green).

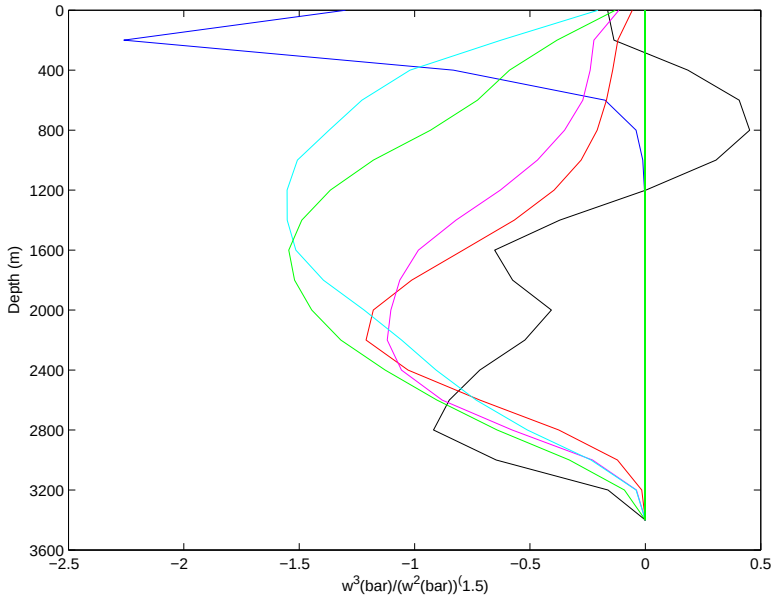

(a)

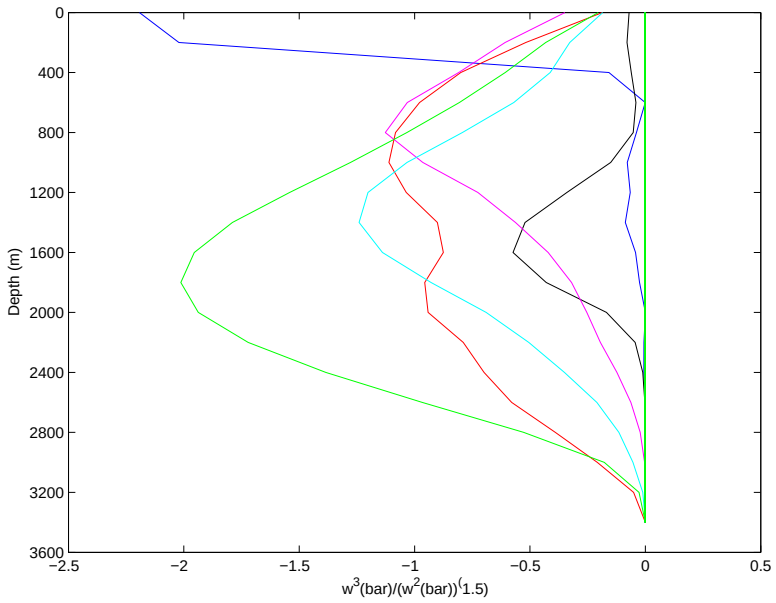

(b)

Figure 5.33: Comparison of the fixed (a) and adaptive (b) continuous disk cooling runs using variation in skewness of vertical velocity profiles with depth at times 12 hours (blue), 24 hours (black), 36 hours (red), 48 hours (magenta), 60 hours (cyan) and 72 hours (green).

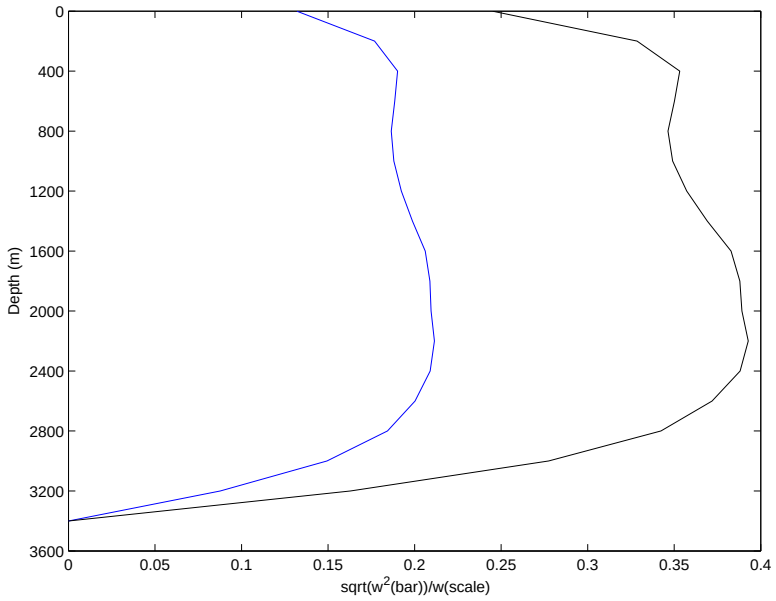

(a)

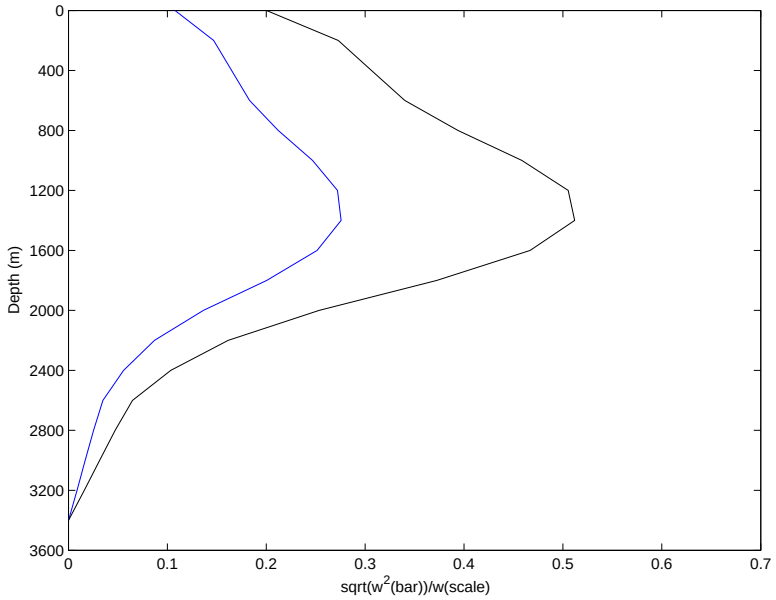

(b)

Figure 5.34: Comparison of the fixed (a) and adaptive (b) continuous disk cooling runs using variation in horizontally averaged vertical velocity profiles with depth scaled against non-rotational (blue) and rotational (black) scaling predictions at 24 hours.

5.3 Investigating the effects of finite and continuous cooling on model convection

In nature, convective events are induced and driven by surface forces, usually in the form of strong winds associated with atmospheric cyclones. Extreme cooling events tend to be finite in nature, and have the same timescales as the length of time for the storm to pass. However, for the purposes of numerical modelling, cooling is often applied continuously, enabling more detailed investigation of the processes present. It is suspected that a compromise must be achieved, and here a number of investigations are presented in order to deduce the advantages and disadvantages of either approach. Four model configurations were investigated:

1. Continuous disk cooling on a fixed, structured mesh
2. Finite disk cooling on a fixed, structured mesh
3. Continuous uniform cooling on a fixed, structured mesh
4. Finite uniform cooling on a fixed, structured mesh

The results of 1 and 2, and 3 and 4 were directly compared using the approach outlined above. The results of this comparison follow below.

5.3.1 Comparison of finite and continuous disk cooling on a fixed mesh

Figure 5.24 shows the development of the temperature field using a cross section through the centre of the domain at 1 hour, 24 hours, 48 hours and 72 hours for the continuous disk cooling fixed mesh run and is described in Section 5.2.3. Figure 5.35 shows the development of the temperature field at the corresponding times for the 24 hour disk cooling fixed mesh run. The signature of convection in the temperature field is comparable between both runs up until 24 hours. Subsequently, convective pluming shuts off due to the absence of cooling to drive it in the finite cooling run. A chimney of well mixed cold water manifests itself by 48 hours, and is still obvious at 72

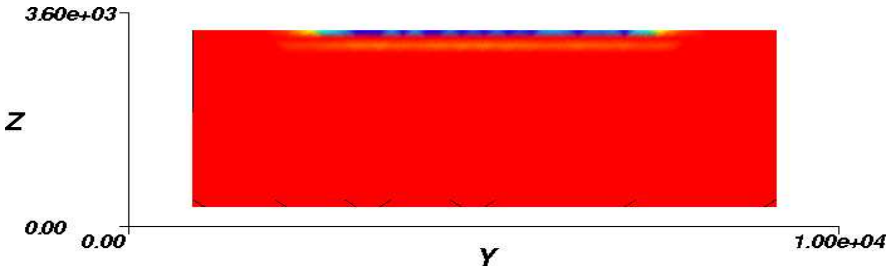

(a) t=1 hour

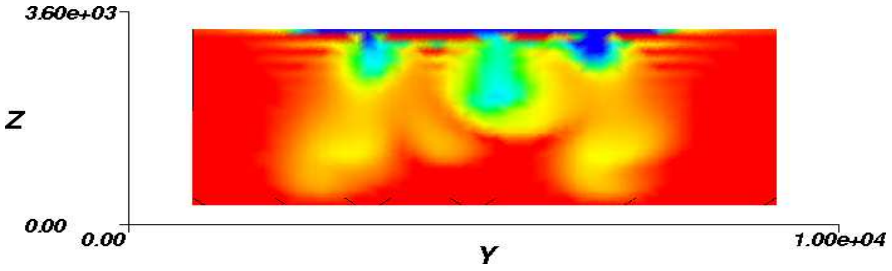

(b) t=24 hours

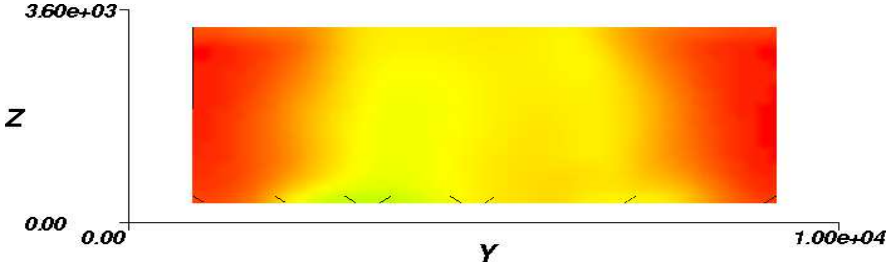

(c) t=48 hours

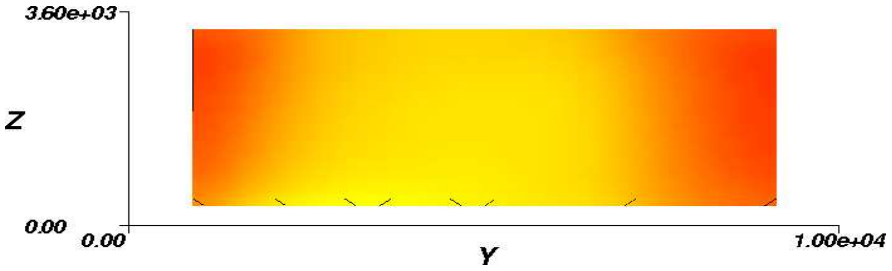

(d) t=72 hours

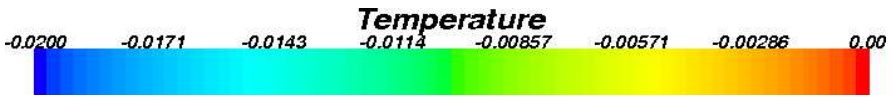

Figure 5.35: Cross-section through the centre of the domain of temperature for the 24 hour disk cooling fixed mesh run.

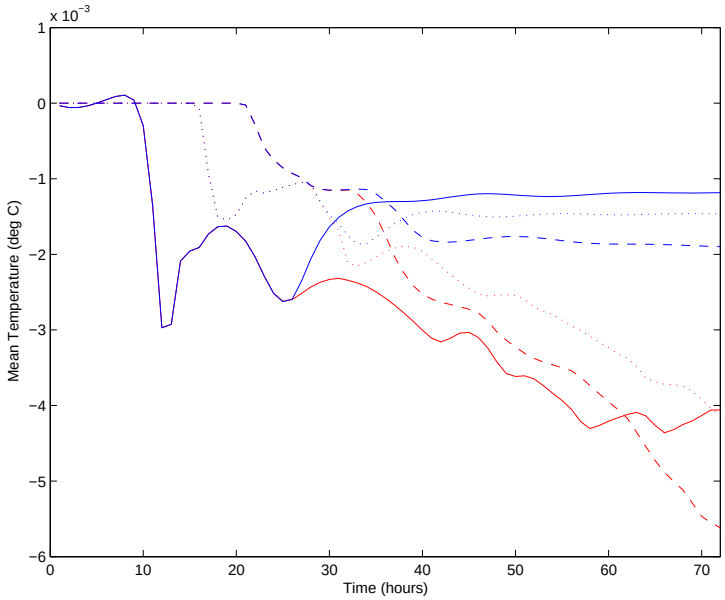

Figure 5.36: Variation in mean temperature at 400m (solid line), 1800m (dotted line) and 3200m (dashed line) for the continuous (red) and 24 hour (blue) disk cooling runs.

hours. In comparison, the run forced by continuous cooling shows distinct convective plumes persisting throughout the remainder of the run.

Figure 5.36 shows the horizontally averaged temperature at three depths within the domain with time. As may be expected, the temperature signature for both the finite and the continuous runs at a depth of 400m follows the same path of variation up until approximately 24 hours. After this, the continuous cooling run exhibits just that, continuous cooling. The temperature of the finite cooling run however increases slightly and then remains almost constant in accordance with the presence of the well mixed chimney of water observed in Figure 5.35. At 1800m, the temperature of the two runs coincides up until 30 hours, showing a delay in cooling indicating that it takes the convective layer approximately 6 hours to penetrate to this depth. The time lag between cooling at the surface and cooling of the bottom layer (3200m) is roughly 10 hours. The 24 hour cooling run results in a roughly linear stratified state at 72 hours. The continuous cooling run shows a temperature at 3200m that is about $1.5 * 10^{-3\circ}C$ cooler than the surface and mid-depths at the final time.

Figure 5.37 shows the profile of horizontally averaged temperature throughout the domain at various times throughout the fixed disk shaped finite du-

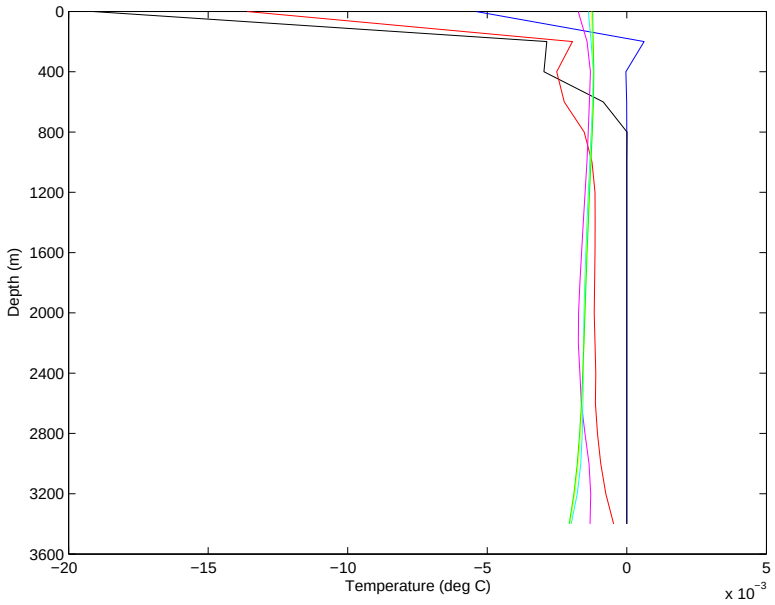

Figure 5.37: Variation in horizontally averaged temperature profiles with depth at times 12 hours (blue), 24 hours (black), 36 hours (red), 48 hours (magenta), 60 hours (cyan) and 72 hours (green) for the fixed disk finite cooling run.

ration cooling run. The convective layer has extended to 800m by 24 hours. At 36 hours the convective layer has extended to the floor of the domain and the water column has cooled by approximately $1.0 * 10^{-3\circ}C$. This is comparable with the cooling observed in the fixed continuous duration disk cooling run (Figure 5.6 (a)), however, at subsequent times, further cooling is not observed. The finite duration cooling disk run results in a well mixed temperature profile with a temperature of roughly $-2.0 * 10^{-3\circ}C$, in comparison with the final temperature observed in the continuous duration run $(-6.0 * 10^{-3\circ}C)$.

The flow field at 1800m is depicted by Figure 5.38. The ring like structure at 24 hours correlates with that of the previous disk cooled runs. At 48 and 72 hours the flow field becomes significantly weaker in the absence of cooling, in contrast with Figure 5.29.

Plots of horizontally averaged velocity, vertical velocity and skewness are presented in Figures 5.39, 5.40 and 5.41 for the fixed mesh finite duration disk cooling run. Velocities are highest at 24 hours, coinciding with the end of the cooling period, and weaken throughout the remaining duration. Vertical velocity indicates that at 24 hours convection is active down to a depth of

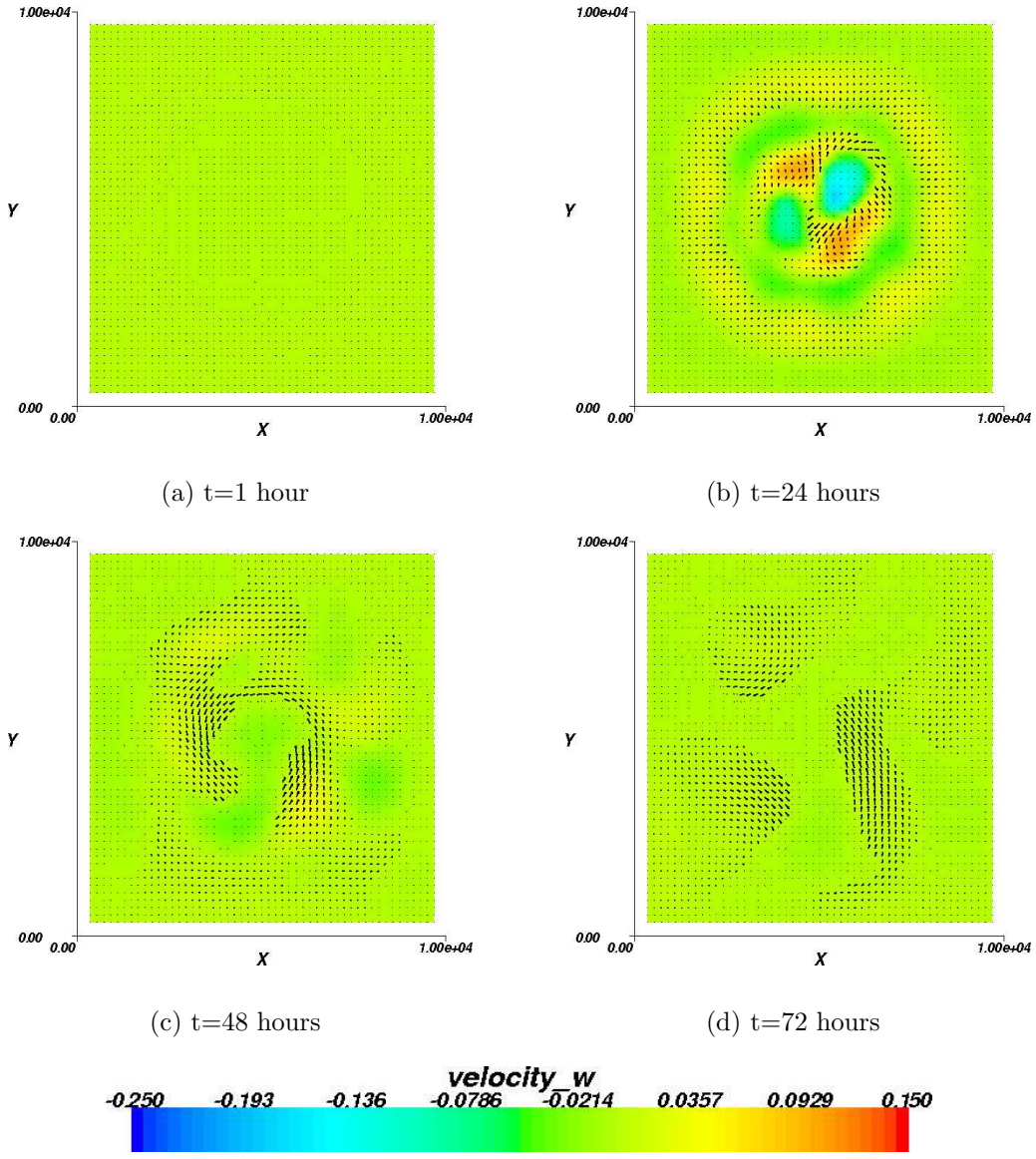

(a) t=1 hour

(b) t=24 hours

(c) t=48 hours

(d) t=72 hours

Figure 5.38: Vertical section of the domain showing the direction of the horizontal velocity vectors and contours of vertical velocity at 1800m for the finite duration disk cooling fixed mesh run.

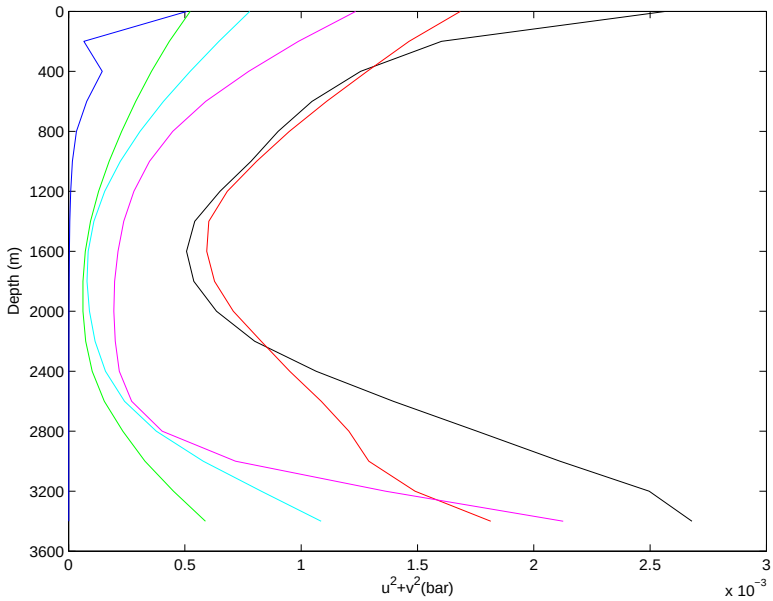

Figure 5.39: Variation in horizontally averaged velocity profiles with depth at times 12 hours (blue), 24 hours (black), 36 hours (red), 48 hours (magenta), 60 hours (cyan) and 72 hours (green) for the fixed disk finite cooling run.

2200m, peaking at $7.5 * 10^{-4} m^2 s^{-2}$. Contrast this with Figures 5.31 and 5.32 (a), and it can be seen that the absence of forcing effectively ends convective pluming. It should also be noted that for the continuous duration run, the bottom velocities are strongest, and vertical velocity peaks at a later time (72 hours) and a depth of 2000m with a magnitude approximately double that observed in the finite duration run. Skewness is very similar in the two runs, indicating downwelling is dominant.

Figure 5.42 shows a comparison of observed model vertical velocities with those predicted by the scaling theory discussed in Chapter 2.

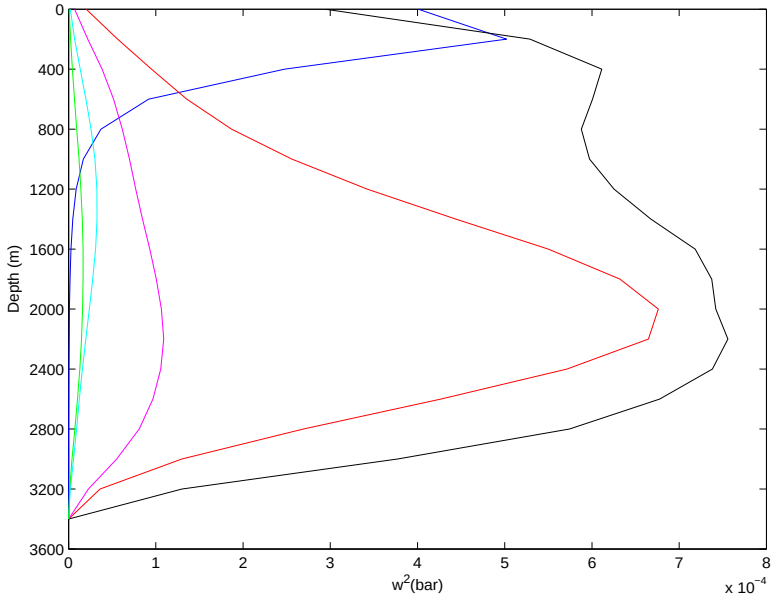

Figure 5.40: Variation in horizontally averaged vertical velocity profiles with depth at times 12 hours (blue), 24 hours (black), 36 hours (red), 48 hours (magenta), 60 hours (cyan) and 72 hours (green) for the fixed disk finite cooling run.

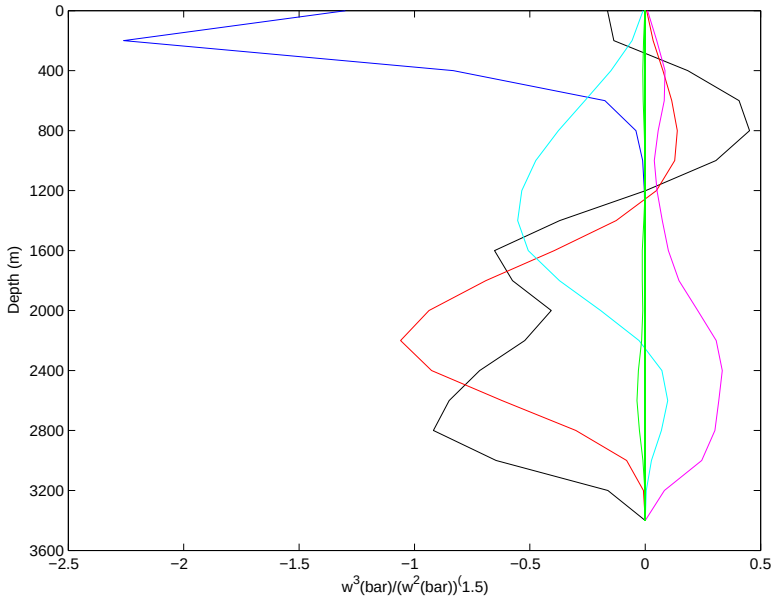

Figure 5.41: Variation in skewness of vertical velocity profiles with depth at times 12 hours (blue), 24 hours (black), 36 hours (red), 48 hours (magenta), 60 hours (cyan) and 72 hours (green) for the fixed disk finite cooling run.

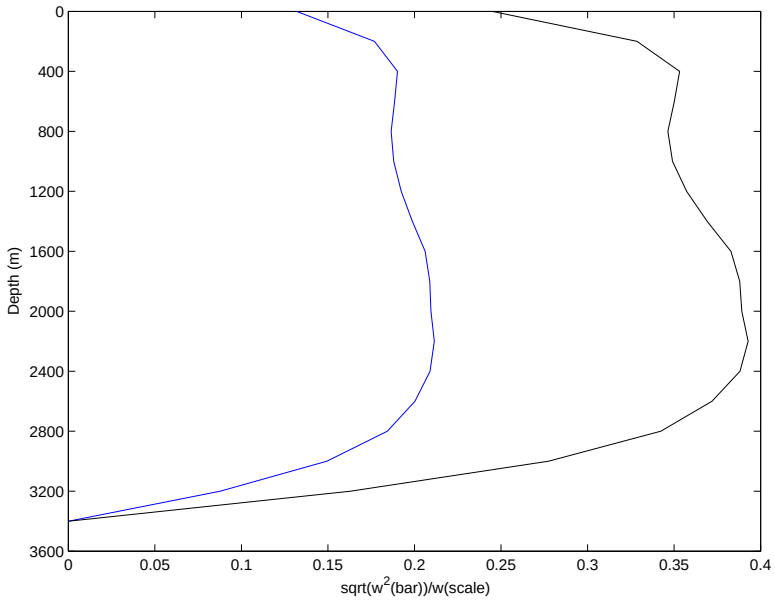

Figure 5.42: Comparison of the fixed disk finite cooling run against theoretical scaling predictions using variation in horizontally averaged vertical velocity profiles with depth scaled against non-rotational (blue) and rotational (black) scaling predictions at 24 hours.

5.3.2 Comparison of finite and continuous uniform cooling on a fixed mesh

The development of the temperature field for the finite and continuous uniform cooling runs is shown in Figures 5.13 and 5.1 and described in Sections 5.2.2 and 5.2.1 respectively. When comparing the two figures one main distinction is evident, that is, the presence of the final sinking, spreading and restratification stages of convection in the finite cooling run. In comparison, the run forced by continuous cooling shows distinct convective plumes persisting throughout the remainder of the run.

Figure 5.43 shows the variation in mean temperature at three depths as it evolves over time. As observed in the disk cooling runs, the temperature signature for both the finite and the continuous uniform cooling runs follows the same path of variation up until 20 hours at a depth of 400m. After this, the continuous cooling run exhibits falling temperature for the remainder of the duration. At 1800m, there is a delay in the onset of cooling by 5 hours. The temperature at this depth remains the same until 30 hours, after which point the finite cooling run remains at approximately the same temperature.

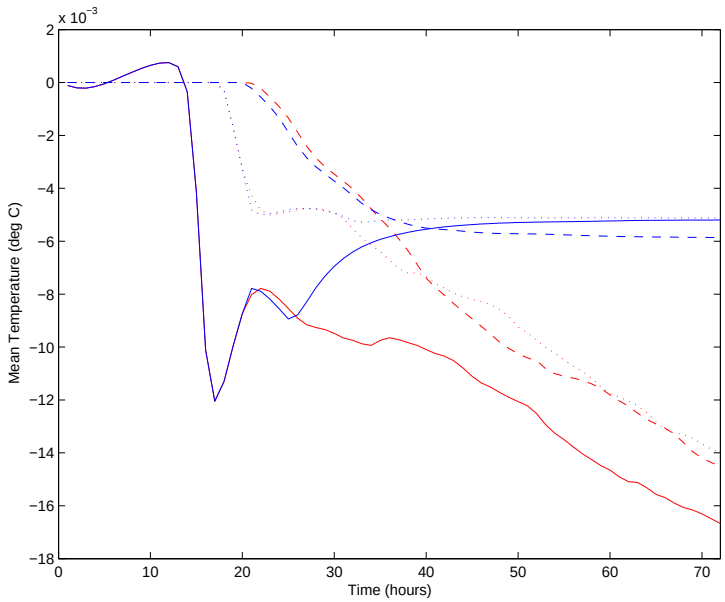

Figure 5.43: Variation in mean temperature at 400m (solid line), 1800m (dotted line) and 3200m (dashed line) for the continuous (red) and 24 hour (blue) uniform cooling runs.

The temperature at 3200m begins to fall after 20 hours, indicating the convective layer has penetrated to this depth. The split occurs at about 32 hours, after which the finite cooling run does not show further cooling. All depths exhibit a similar final temperature at 72 hours. In comparison, the 400m depth exhibits a final temperature approximately $2.0 * 10^{-3\circ}C$ cooler than the deeper layers.

Figures 5.17 and 5.6 in Sections 5.2.2 and 5.2.1 demonstrate the differences observed in the vertical profile of mean temperature at various times throughout the duration of the runs. The most obvious difference is that the continuous cooling run exhibits a lower temperature at 72 hours. The convection itself is similar in character, penetrating through the depth of the domain leaving a well mixed column of water in its wake.

Continuous uniform cooling results in a well-distributed plume field that is reinforced by the ongoing surface cooling (Figure 5.7). In comparison, the finite cooling run demonstrates a reduction in overall flow once the surface forcing ends (Figure 5.18).

Higher velocities are observed in the continuous cooling run (Figure 5.9 (a)). Horizontal velocity peaks after 24 hours and then falls away in the finite cooling run (Figure 5.20 (a)). A similar pattern is observed in vertical

velocity, however, maximum vertical velocities are observed at 36 hours in the finite duration run. Skewness indicates the dominance of downwelling in the both configurations.

5.4 Investigating the effect of disk shaped and uniform cooling on model convection

Realistically, the scale of convective chimneys is largely determined by the area over which large heat fluxes occur. This area is governed by a combination of preconditioning processes, including ice coverage, isopycnal doming and strong winds. In order to capture this highly localised chimney formation in a simplified ocean model (as demonstrated here) that does not have the option (or the necessary resources) for applying such complex preconditioning methods, the modeller is forced to approximate the combined effect of such preconditioning by applying direct cooling over a finite area, such as a disk. This is, unfortunately, quite unrealistic and results in strong density gradients around the edge of the disk that are not observed in nature (Straneo and Kawase, 1999; Visbeck et al., 1996). A second option to the modeller is to apply surface forcing uniformally across the entire domain. This, again, is not completely representative of the combined preconditioning observed in nature, but allows investigation of the convective process in absence of the strong density gradients at the edge of the disk. Although neither option offers perfection, they are nonetheless useful in investigating convection using a numerical model. A short investigation was conducted in which the two methods of inducing convection were compared against one another using the following four model configurations:

1. Continuous disk cooling on a fixed, structured mesh
2. Continuous uniform cooling on a fixed, structured mesh
3. Finite disk cooling on a fixed, structured mesh
4. Finite uniform cooling on a fixed, structured mesh

The results of 1 and 2, and 3 and 4 were directly compared using the approach outlined above. The results of this comparison follow below.

5.4.1 Comparison of disk shaped and uniform continuous cooling on a fixed mesh

The development of the temperature field for the disk shaped and uniform continuous cooling runs is shown in Figures 5.24 and 5.1 and described in Sections 5.2.3 and 5.2.1 respectively. When comparing the two figures one main distinction is evident, that is, the horizontal extent of convective pluming. As would be expected, pluming in the disk forced run is constrained to the scale of the applied disk. Similarly, the development of the convective chimney takes on the scale of the convective disk. In contrast, pluming in the uniformally forced run is across the full horizontal scale of the domain, along with chimney formation, although towards the end of the run, some preferential pluming is observed to the south (left) of the domain centre.

Figure 5.44 shows the mean temperature at three depths as it evolves with time. The temperature variation for both the disk and uniform cooling forced runs follows a visibly similar trend. However, the disk cooling run exhibits higher temperatures, a result of the cooling being constrained to the region of the disk. Cooling is indicated sooner in the disk cooling run, but the associated cooling at this depth in the uniform cooling run is a magnitude of 6 higher. The temperature at 1800m shows a similar trend, cooling in the disk run onsetting earlier, but a higher magnitude of cooling associated with the uniform run.

Similar trends in horizontal velocity are observed (Figures 5.9 (a) and 5.31 (a)), however, at mid-depths the velocity is suppressed in the disk forced run. Vertical velocities are almost a factor of 3 higher in the uniform cooling run (Figures 5.10 (a) and 5.32 (a)). Skewness again illustrates the dominance of downwelling, although at 24 hours there is comparable upwelling in the disk forced run above 1200m (Figures 5.11 (a) and 5.33 (a)).

By comparing Figure 5.29 and Figure 5.7 the restriction on the distribution of convective pluming caused by the disk cooling is evident. A significant difference is also demonstrated by the concentric nature of the convective bands within the chimney. In comparison with the localised, distributed pluming forced by uniform cooling, the disk forced run has a flow structure that is unlikely to be observed in nature.

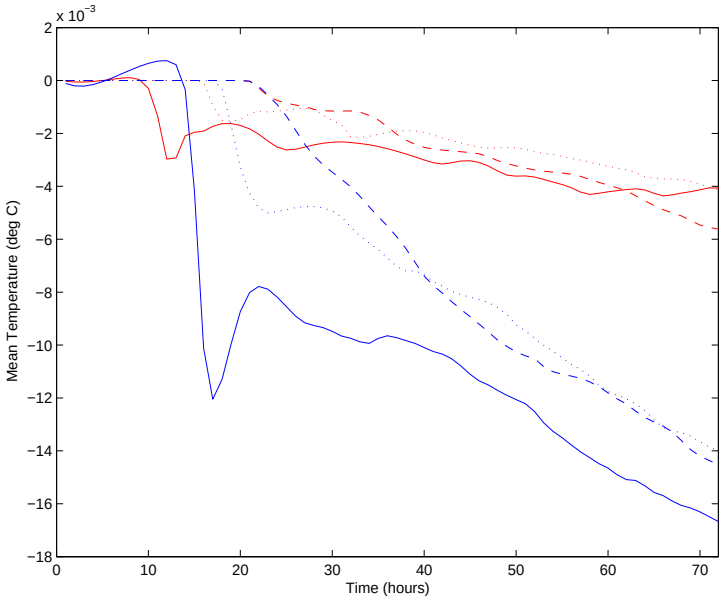

Figure 5.44: Comparison of mean temperature at 400m (solid line), 1800m (dotted line) and 3200m (dashed line) for the fixed mesh disk (red) and uniform (blue) continuous cooling runs.

5.4.2 Comparison of disk shaped and uniform finite cooling on a fixed mesh

The development of the temperature field for the disk shaped and uniform finite cooling runs is shown in Figures 5.35 and 5.13 and described in Sections 5.2.3and 5.2.2 respectively. When comparing the two figures two main distinctions are evident. Firstly the horizontal extent of convective pluming. As previously discussed, pluming in the disk forced run is constrained to the scale of the applied disk, and in the uniformally forced run is across the full horizontal scale of the domain, along with chimney formation. Secondly, the uniform run is somewhat more distinctly stratified in the final stages of the run, as the disk cooling run has more surrounding ambient fluid to mix with horizontally.

Figure 5.45 shows the mean temperature at three depths within the domain over time. The temperature variation for both the disk and uniform cooling forced runs follows a visibly similar trend. However, the uniform cooling run exhibits the lowest temperature at 18 hours ($-12.0 * 10^{-3\circ}C$), resulting from the smaller overall cooling due to the horizontal restraint on cooling in the disk forced run. The final temperature observed in the uniform

cooling run is approximately $4.0 * 10^{-3\circ}C$ lower than the disk cooling run.

The flow field associated with the two runs is evident in Figures 5.38 and 5.18. The disk run produces a short-lived chimney with a structure and extent determined by the scale of the disk shaped forcing. The well distributed pluming initiated by the uniform forcing is also short lived, but the magnitudes of upwelling and downwelling are visibly higher.

Figures 5.20 (a) and 5.39 show horizontally averaged velocity with depth and time. The highest velocities in the uniform cooling run are observed at 24 and 36 hours, reducing to almost zero at subsequent times. A similar distribution of velocity is observed in the disk cooled run, although the magnitude of the velocities are somewhat smaller in comparison.

Variation in vertical velocity is shown in Figures 5.21 and 5.40. The uniform cooling run experiences maximum velocities at 36 hours, in comparison with the maximum velocities at 24 hours in the disk run. The development of the vertical velocity profiles in the uniform run show a peak mid-depths whereas in the disk cooled run the high vertical velocities are not confined to the middle of the domain. A similar profile, however, emerges at 36 hours.

Skewness identifies predominant downwelling in both configurations, although both runs show a tendency towards upwelling at later times (Figures 5.22 and 5.41).

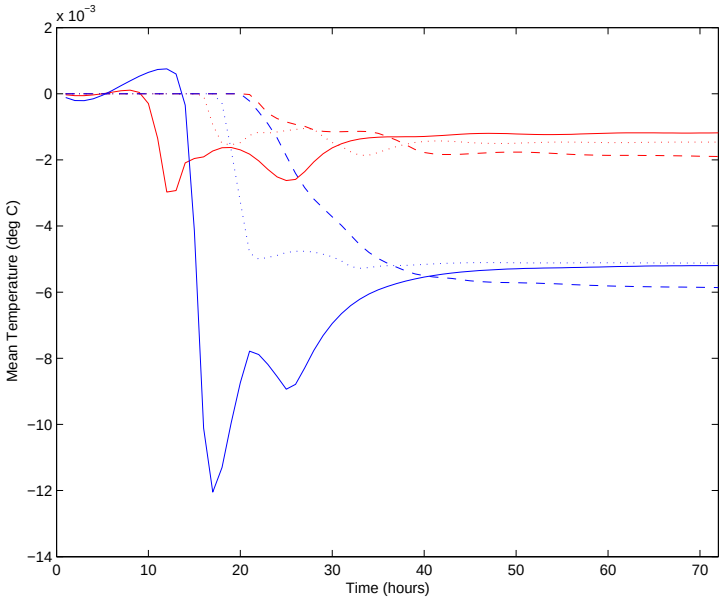

Figure 5.45: Comparison of (a) mean temperature at 400m (solid line), 1800m (dotted line) and 3200m (dashed line) for the fixed mesh disk (red) and uniform (blue) 24 hour cooling runs.

5.5 Summary and Conclusions

The experiments detailed in this Chapter in determining the nature of model convection are by no means exhaustive, but are intended to provide the reader with an understanding of the models capability (including restrictions) in capturing the convective process in a physical sense.

Section 5.2 details a series of experiments conducted in order to identify any prevailing differences between model convection in fixed and adaptive mesh configurations. Firstly, convection forced by the application of a continuous heat flux applied uniformally across the surface of the domain was examined. Both the fixed and adaptive configuration demonstrated an ability to capture the stages of the convective process. In particular, the pluming, development of the convective mixed layer and some restratification is evident. The pattern of convective pluming observed is well distributed across the domain in both cases. However, visualisation of the temperature and velocity fields indicate that model convection is better defined in the adaptive configuration. Vertical velocities are also observed to be slightly higher, and the onset of convection was found to occur earlier in the adaptive case. This may indicate that convection is inhibited by the fixed mesh, even at high resolution.

Secondly, convection forced by finite duration cooling applied uniformally across the domain for 24 hours enabled observation of the sinking and re-stratification stages of the convective process more precisely. The adaptive run exhibits a more defined stratification at the end of the model period. Similarly, it also exhibits the lowest average temperatures and the highest vertical velocities. However, the onset of convection in the adaptive run lags behind that of the fixed mesh run.

Lastly, a comparison of continuous duration cooling applied within a disk of radius 3km was made for the fixed and adaptive cases. The disk cooling problem is commonly used in convective studies, and the disk acts to restrict the spatial distribution of convection producing a localised chimney of mixed water within the centre of the domain. It is debatable whether such a restriction is realistic, as cooling in nature occurs over large areas and convection itself is usually initiated by a combination of other factors, such a strong wind and wave preconditioning action. However, for the purposes of this study, the examination of the convective chimney is still useful. Both configurations exhibit the expected spatial restriction and chimney formation. Of particular note, however, is the variation in the velocity field. The dynamical structure of convection is significantly different to the uniformally distributed case, with the formation of concentric rings of upwelling and downwelling within the chimney. Furthermore, the definition of these rings is greatly increased by the use of the adaptive mesh. Convection is also observed to be stronger and occur earlier in the adaptive configuration, but the temperature signature of convection is observed later at depth. The adaptive mesh captures the progress of convection in more detail than the fixed mesh as a result of its use of resolution in the regions of most activity. The break-up of the convective chimney towards the end of the model runs allowed the scale of the eddies formed to be compared with the Rossby deformation radius expected from reality (L_R=5-10km for the Greenland Sea). In this too, the adaptive configuration performed best, producing eddies of approximately 4-5km.

Although observations of convection between the two model configurations sometimes appear to be contradictory, the comparison of observed convective scales with theoretical scaling laws indicates that the adaptive mesh is significantly better at modelling convection in all cases. In all cases the adaptive configuration scaled more strongly with the predicted theoretical scales. Unsurprisingly, the three convective forcing scenarios all demonstrate

behaviour more akin to the rotational regime as predicted at the beginning of this Chapter. The suitability of the adaptive mesh for the investigation of the convective problem is demonstrable.

Two further comparisons of model convection were made using the fixed mesh configuration. The variation in the duration of applied cooling resulted in weaker convective events and the formation of a well stratified fluid in the finite duration scenarios. The horizontal scale of the convective forcing produced large contrasts in velocity fields and spatial distribution of convective pluming. From this, we conclude that a combination of uniform cooling of finite duration may produce the most realistic results when studying the convective problem.

5.5.1 Computational cost of adaptivity

An assessment of the cost on resources of adaptivity was attempted by monitoring the number of nodes within the model configurations over time. The fixed mesh configurations contained $\sim$ 60000 nodes, whereas the adaptive runs had the possibility to run with up to $\sim$ 90000 nodes. It should be noted that this method is extremely crude, for example it does not take into account the presence of other model runs and processes occurring on the same computer processor. For comparison, the approximate CPU time required for each model run was also noted. From Figure 5.46 and Table 5.1, it can be deduced that adaptivity is relatively cost effective in comparison with the fixed mesh ICOM runs, in terms of both number of nodes over time and total CPU time required. The adaptive mesh does not take advantage of the high number of nodes available to it.

Table 5.1: CPU time (approximate Hours) for the model runs

Run Description	Fixed	Adaptive
Disk continuous	66.5	7.5
Uniform Continuous	79.0	42.5
Uniform finite	66.0	23.5
Disk finite	95.5	X

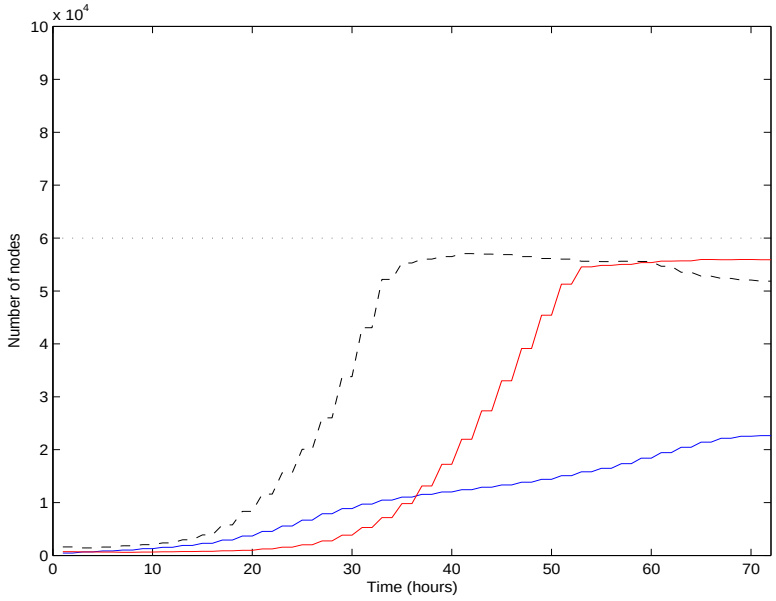

Figure 5.46: Number of nodes for the adaptive continuous disk cooling run (red), the adaptive uniform continuous cooling run (black) and the adaptive uniform finite cooling run (blue). The dotted line represents the constant number of nodes within the fixed mesh runs.

Chapter 6

Modelling convection - the impact of stratification

6.1 Introduction

In the previous Chapter, the suitability of ICOM and adaptivity for the modelling of convection was demonstrated. Here, the impact of the introduction of stratification to the small scale domain on observed model convection is investigated.

In nature, strong stratification acts to impede convection. It is for this reason that the doming of the isopycnals caused by cyclonic circulation within the basin gyre is a preconditioning requirement for convection. Convective plumes are observed to descend to the layer at which the water they contain is neutrally buoyant relative to the surrounding water. At this point, horizontal spreading and mixing becomes important. However, in some instances, the momentum of the descending plume may be strong enough that the plume punches down into layers of stratification that are relatively more dense. This is termed penetrative convection. The plume, surrounded by the denser layer becomes positively buoyant. As a result, entrainment of fluid from below and a reverse buoyancy flux occurs. This reverse flux leads to a sharpening of the pycnocline (strong salinity gradient) and a faster rate of deepening of the convective layer (Marshall and Schott, 1999).

Penetrative convection is characterised by steps in the temperature and

salinity profiles. Such steps are often observed in the Mediterranean Sea. However, such steps are not observed during convective events in the Greenland Sea, suggesting that in this region, convection is non-penetrative (Marshall and Schott, 1999).

Rotation has the opposite effect - significantly reducing entrainment at the base of the convective layer and simultaneously reducing the reverse buoyancy flux. Paluskiewicz et al. (1994) observed that for non-thermobaric cases (i.e. thermally forced scenarios), convective plumes are non-penetrative in investigations using LES methods, and the deepening of the convective layer is restricted.

6.2 Investigating the impact of stratification and identifying penetrative convection

Penetrative convection may be an important feature of the convective process, acting to enhance the production of deep water. In general, common parameterisations of convection within GCMs are unable to simulate penetrative convection, thus omitting a significant part of the process enhancing deep water formation. However, the strong rotational effects at the high latitudes of the Greenland Sea may mean penetrative convection does not play a significant role in this region.

In order to investigate the significance and possible occurrence of penetrative convection in the Greenland Sea, convection into a stratified domain was modelled using ICOM's adaptive mesh. This omits any restriction imposed by the use of the fixed grid, and may lead to observations of penetrative convection on timescales less than $1/f$. Similarly, it is also of interest to observe the behaviour of adaptivity when stratification and cooling are combined within one domain.

A background temperature stratification similar to that observed in the Greenland Sea was applied to the domain. This consisted of a strongly stratified but relatively warmer layer down to approximately 1800m. Below this, the bottom 1800m was initialised with a weaker, but relatively cold, stratification. The background stratification in the domain was set as follows:

$$T = T_0 + T_1 * (z - z_0) * T_2 * tanh((z - z_0)/\lambda) \tag{6.1}$$

where $T_0 = 0.0°C$, $z_0 = 2000m$, $T_1 = 1.0 * 10^{-5} Km^{-1}$, $\lambda = 100m$, $T_2 = 5.0 * 10^{-4\circ} K$.

Figure 6.1 shows the initial stratification within the domain. Uniform, continuous duration cooling at a rate of $-2.5 * 10^{-4} Kms^{-1}$ was applied across the surface of the domain. This cooling is expected to initiate convective pluming that punches through the surface stratification into the weaker stratified layer below. The model was run for a total period of 7 days.

The vertical temperature structure of the domain was observed as a north-south cross section every 24 hours throughout the model run. Similarly, contour plots of vertical velocity at three depths overlaid by directional horizontal velocity vectors are used to identify the velocity structure of convection. Profiles of average temperature, average horizontal and vertical velocity and skewness are also represented. Penetrative convection is diagnosed by warming and downwards heat flux at the base of the convective layer.

Assuming convection is non-penetrative (at least for timescales $< 1/f$), the depth D of the convective layer should satisfy:

$$D \sim \sqrt{\frac{2\Delta F}{dT/dz}} \tag{6.2}$$

where $\Delta F = -2.5 * 10^{-4} Kms^{-1} * 8.64 * 10^4 s = 21.6Km$, $dT/dz \sim 1.0 * 10^{-5} Km^{-1}$ in the top layer (Marshall and Schott, 1999). Therefore, the depth of the convective layer after one day is expected to be $\sim 2100m$. Pluming below this level may therefore be termed penetrative.

For a thermal expansion coefficient $\alpha = 0.5 * 10^{-5} K^{-1}$, w_{scale} (or w_{norot}) from Equation 2.10 in Chapter 2 is $\sim 5.7 * 10^{-2} ms^{-1}$. This gives a timescale for convective overturning $\sim 7.5 hours$, greater than the rotational timescale ($1/f \sim 7200s \sim 2hours$). Convective plumes must therefore be affected by the Earth's rotation, and penetrative convection may be restricted as a result. The convective Rossby number, R_{0c}, is calculated as ~ 0.265, and the natural Rossby number (R_0*)is effectively ~ 0.14.

The initial stratification of the domain allows us to estimate a value for

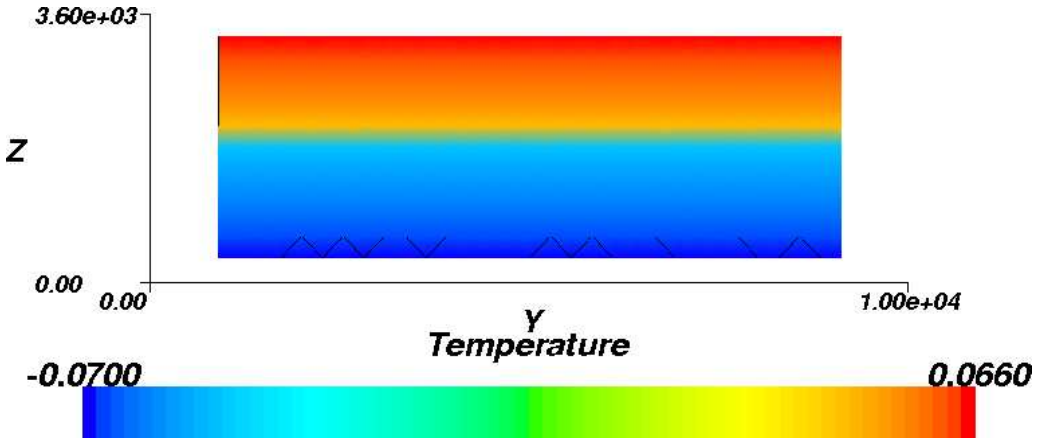

Figure 6.1: Cross section of temperature within the domain at time zero.

the model Rossby deformation radius (L_R). In this case:

$$L_R = \frac{NH}{f} = \frac{\sqrt{g.\alpha.\frac{dT}{dz}}.H}{f} \sim 1km \tag{6.3}$$

In reality, L_R in the Greenland Sea is approximately 5-10km. Comparison of the scale of model eddies with these values for L_R will be indicative of the models ability in replicating the dynamics of convection at each stage.

Figures 6.2 and 6.3 show the evolution of the temperature field over time. The initial two layer stratification is obvious after 2 hours. The mesh places high resolution in the upper 200m, enabling the capture of small scale convective eddies. At 24 hours, cooling across the surface of the domain is obvious, and individual convective plumes can be distinguished. At 48 and 72 hours, cooling of the convective layer is evident, and the sharp stratification at the boundary of the two layers is perturbed as it begins to be eroded. Over the following times, the convective layer deepens, eroding the layer of stronger stratification below.

In comparison with Figure 5.3 (Chapter 5) for the uniform continuous cooling problem into an unstratified domain, it can be seen that convective pluming is restricted to the upper layer of the stratification, and the convective mixed layer is easily differentiable from the strongly stratified, colder bottom layer.

Figures 6.4 and 6.5 show the development of the mesh resolution in response to convection. Initially, the mesh acts to resolve the stratification but over time the resolution is observed to deepen in accordance with the

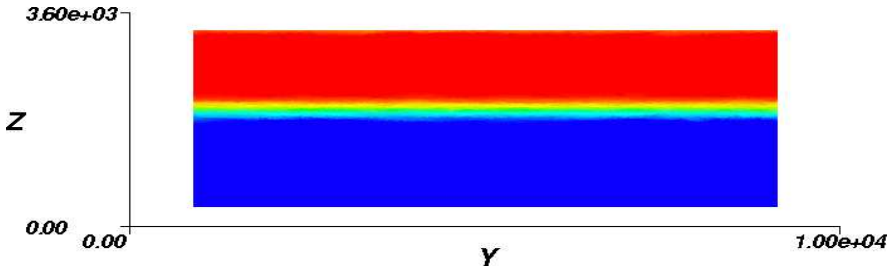

(a) t=2 hours

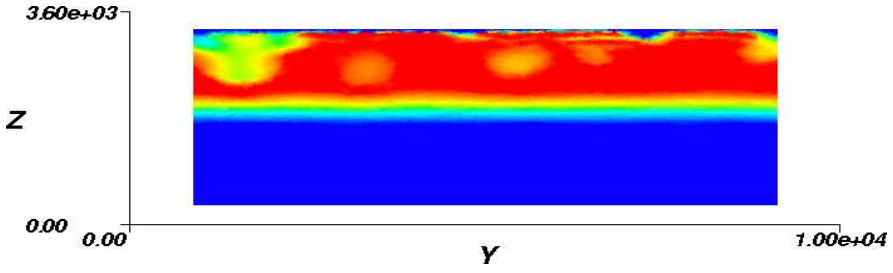

(b) t=24 hours

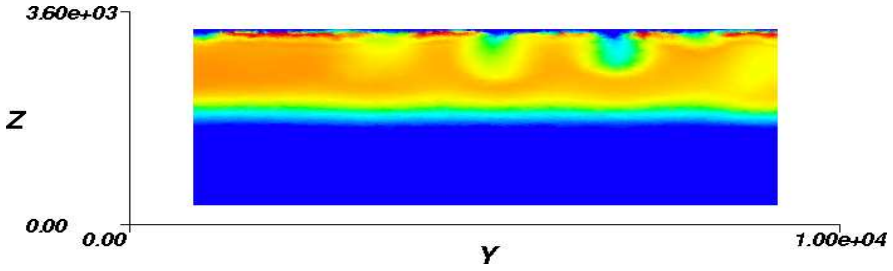

(c) t=48 hours

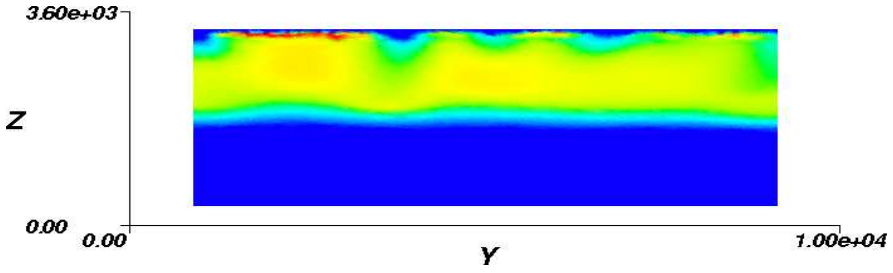

(d) t=72 hours

Figure 6.2: Cross-section through the centre of the domain of temperature for the stratified uniform cooling adaptive mesh run for times 2 - 72 hours.

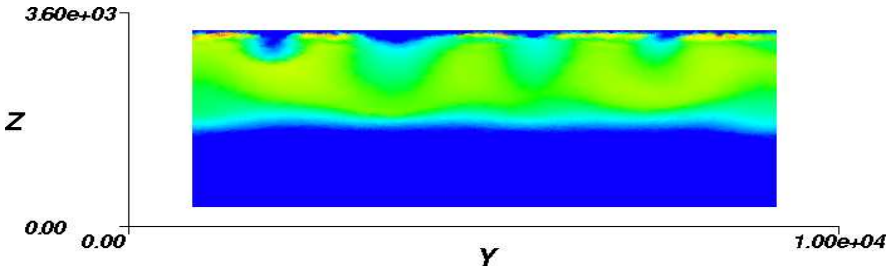

(a) t=96 hours

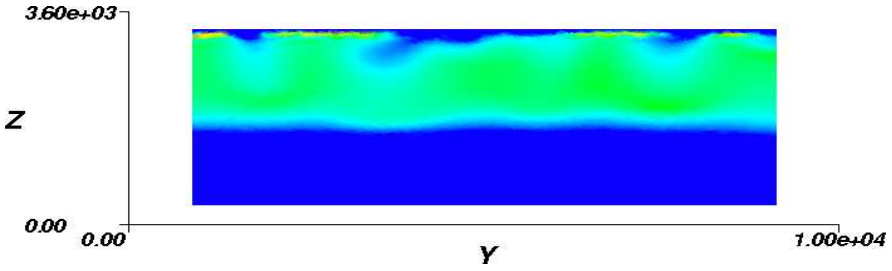

(b) t=120 hours

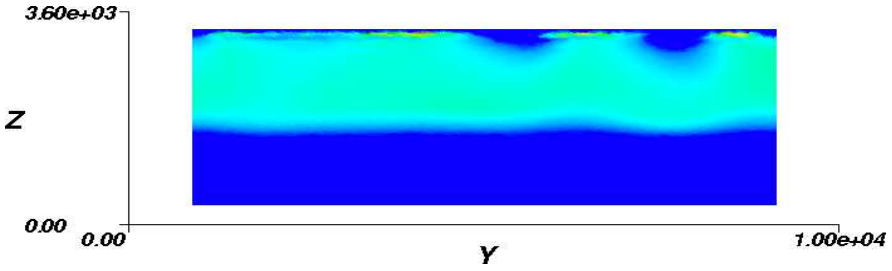

(c) t=144 hours

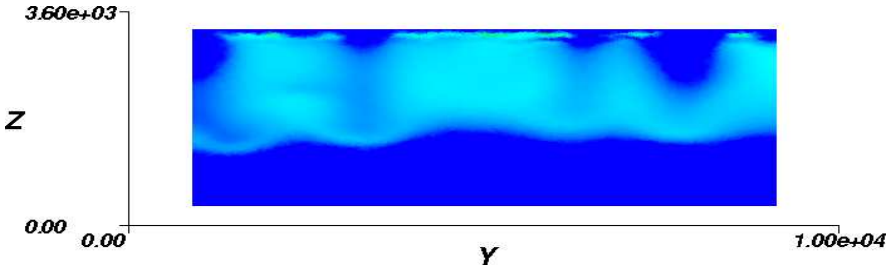

(d) t=168 hours

Figure 6.3: Cross-section through the centre of the domain of temperature for the stratified uniform cooling adaptive mesh run for times 96 -168 hours.

deepening of the convective layer.

The variation of temperature at selected levels throughout the domain is presented in Figure 6.6. The surface layers at 100m and 400m are observed to cool continuously over time. However, at 1000m, the temperature is observed to warm over time. At 1800m, 2600m and 3200m the temperature remains constant throughout the duration of the model run, indicating convection does not penetrate to these depths. This is in contrast with Figure 5.5 in Chapter 5 (for the non-stratified domain), where cooling is experienced at all depths. In the stratified run, cooling is restricted to the upper levels.

The profile of temperature with depth every 24 hours provides further insight into the development of convection within the domain (Figure 6.7). Convection acts to iron out the initial stratification, cooling the top layer towards the temperature of the bottom. The temperature at approximately 1800m warms gradually over time, and this warming extends to 2500m by 168 hours. At this point (168 hours), convective behaviour becomes qualitatively different, as it is no longer opposed by the presence of a strongly stratified fluid. It is likely that the warming below the upper stratified fluid is a consequence of vertical diffusion rather than convection, backed up by the absence of strong vertical velocities in Figure 6.15. The vertical diffusion was set to $0.01ms^{-1}$. Mironov et al. (2000) also noted particularly large vertical diffusion's at the base of the convective layer.

The temperature profiles show similar cooling in the surface layer to those observed in the non-stratified case (Chapter 5 Figure 5.6), although the range in temperatures are larger in the stratified case because of a higher initial temperature in the surface layer. Cooling is restricted to the convective surface layer.

Figures 6.8 and 6.9 demonstrate the structure of the velocity field at 400m every 24 hours throughout the duration of the model run. Convective plumes, identified by strong negative region of vertical velocity, occur consistently from 24 hours onwards. These plumes merge and distort into one another. Similar patterns of velocity where observed previously in the unstratified case (Chapter 5, Figure 5.8), although occur here only in the upper layer.

At 1000m, the convective plumes are more individually defined, and the layer is dominated by upwelling (Figures 6.10 and 6.11).

At 1800m (Figures 6.12 and 6.13), which is within the boundary layer between the two stratification's, weaker plumes are identified, offset by up-

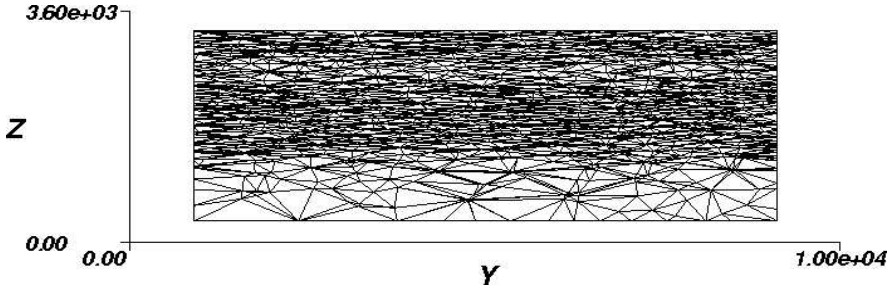

(a) t=2 hours

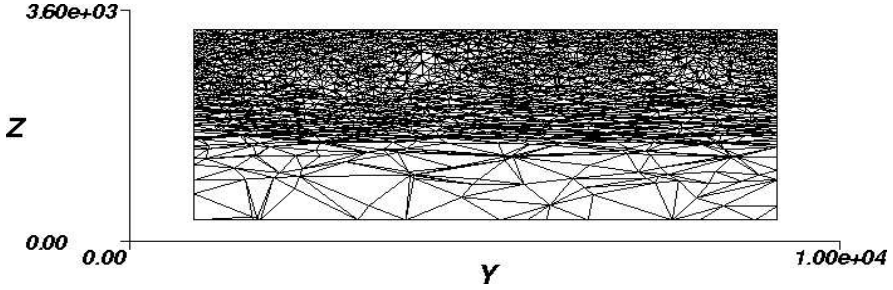

(b) t=24 hours

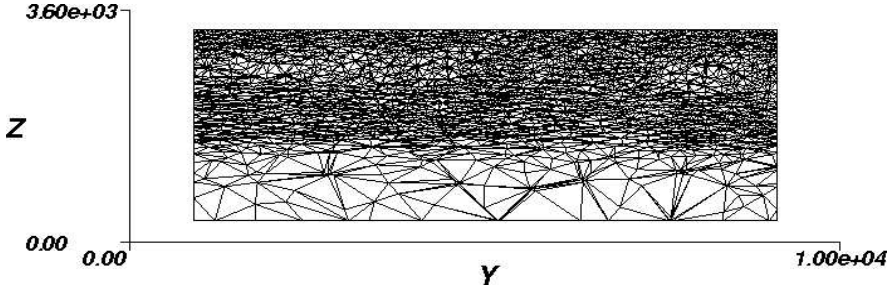

(c) t=48 hours

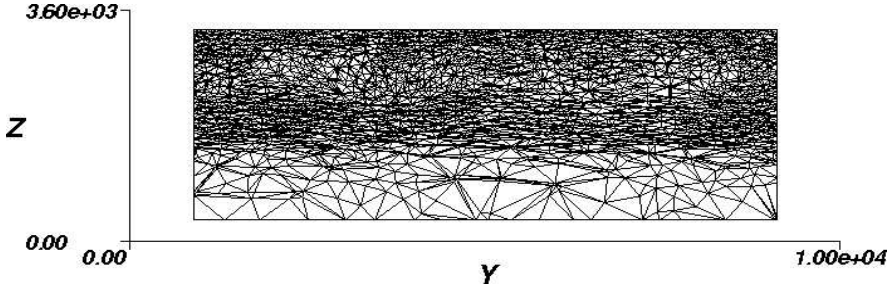

(d) t=72 hours

Figure 6.4: Corresponding mesh variation throughout the stratification experiment for times 2 - 72 hours.

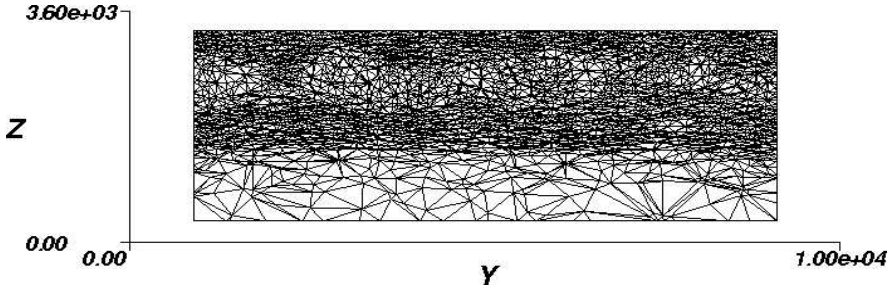

(a) t=96 hours

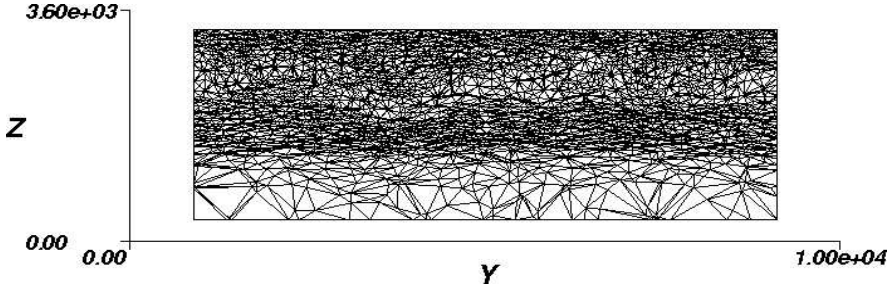

(b) t=120 hours

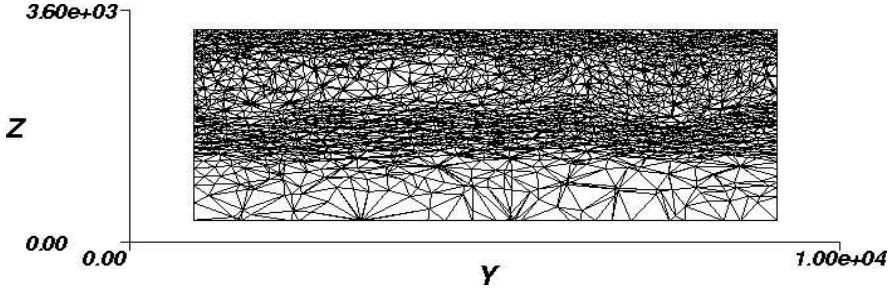

(c) t=144 hours

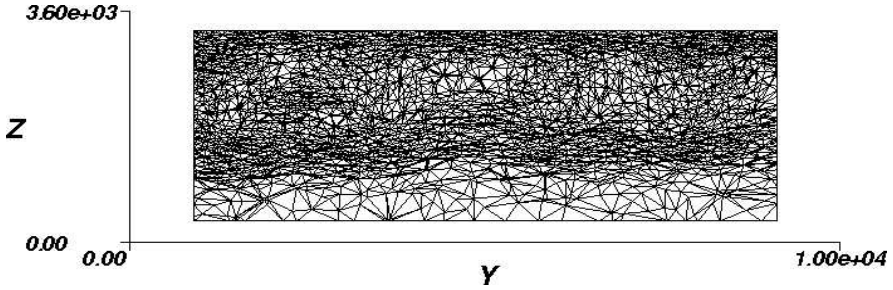

(d) t=168 hours

Figure 6.5: Corresponding mesh variation throughout the stratification experiment for time 96 - 168 hours.

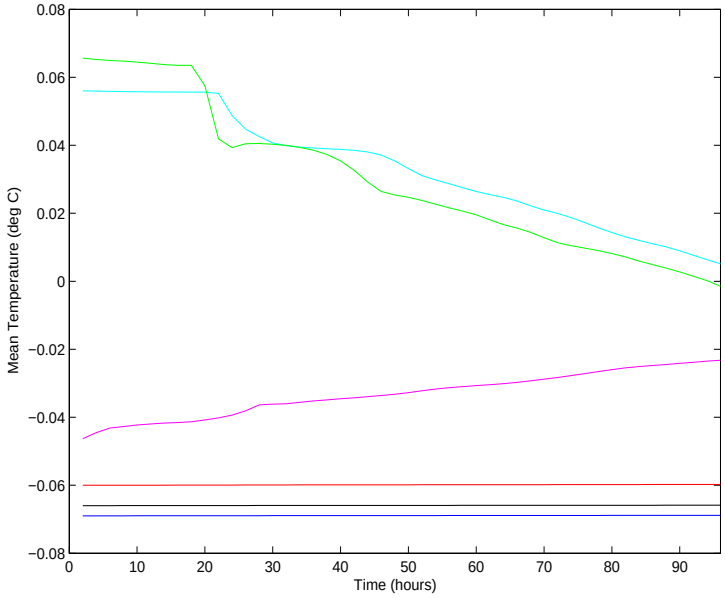

Figure 6.6: Variation in mean temperature at 100m (green), 400m (cyan), 1000m (magenta), 1800m (red), 2600m (black) and 3200m (blue) for the stratified uniform cooling run.

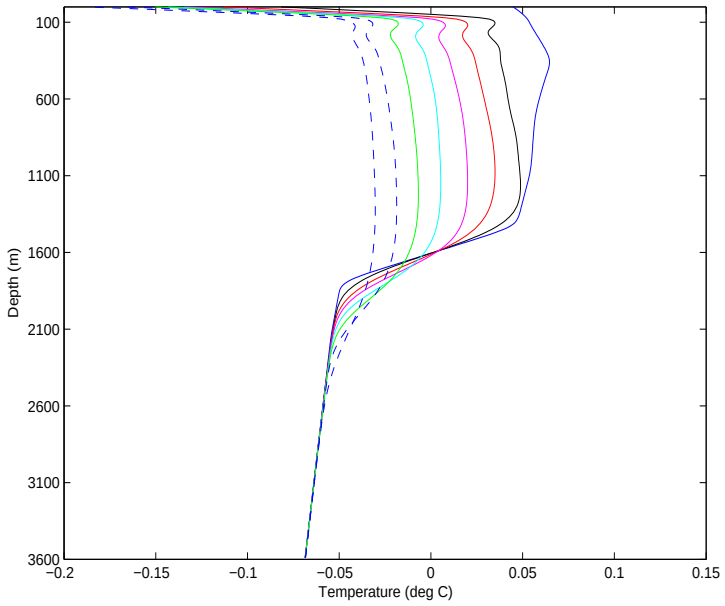

Figure 6.7: Variation in horizontally averaged temperature profiles with depth at times 2 hours (blue), 24 hours (black), 48 hours (red), 72 hours (magenta), 96 hours (cyan), 120 hours (green), 144 hours (blue dashed) and 168 hours (black dashed) for the stratified cooling run.

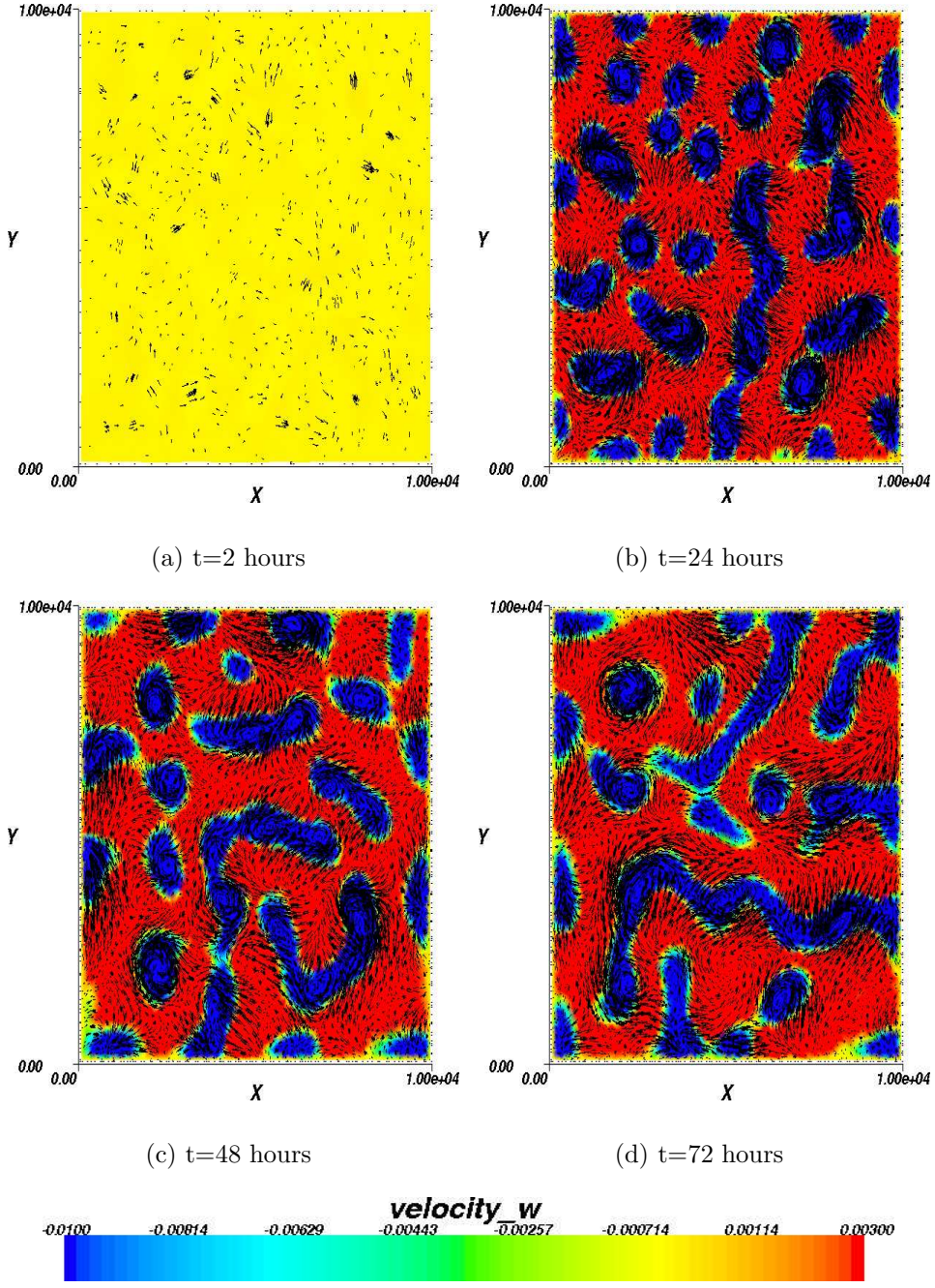

(a) t=2 hours

(b) t=24 hours

(c) t=48 hours

(d) t=72 hours

Figure 6.8: Contours of vertical velocity overlaid by horizontal velocity vectors at a depth of 400m for the stratified run, for 2 - 72 hours.

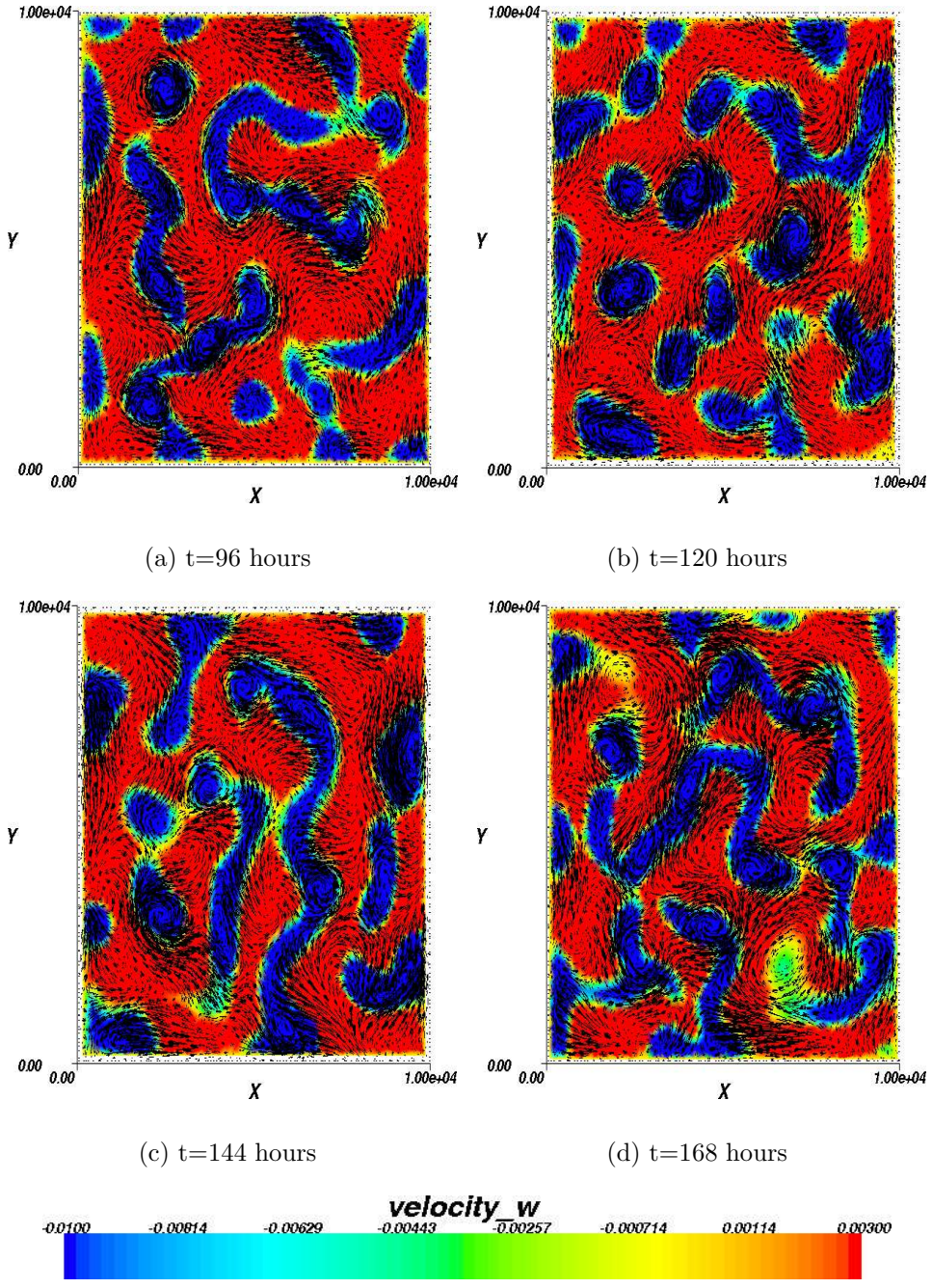

(a) t=96 hours

(b) t=120 hours

(c) t=144 hours

(d) t=168 hours

Figure 6.9: Contours of vertical velocity overlaid by horizontal velocity vectors at a depth of 400m for the stratified run, for 96 - 168 hours.

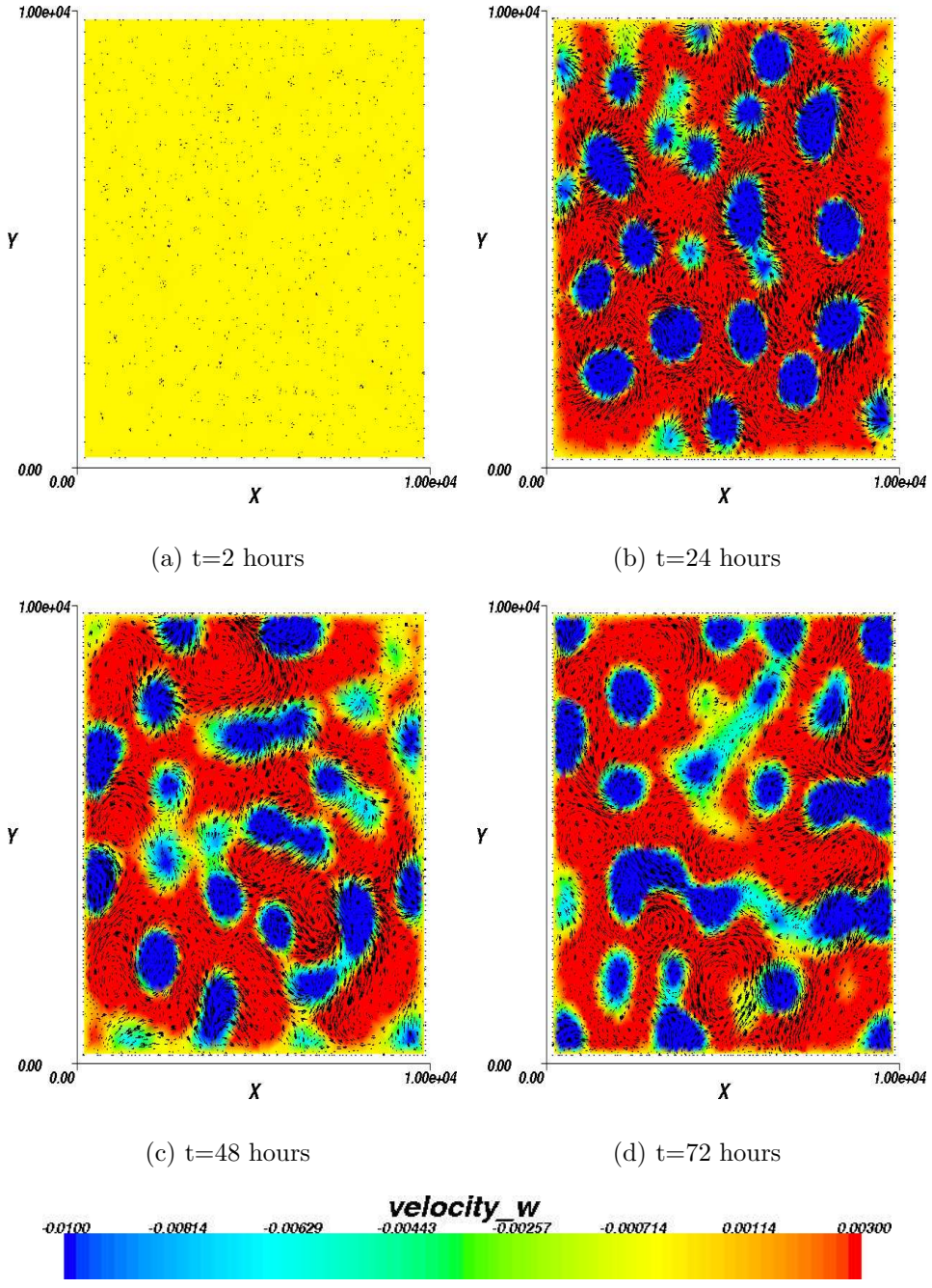

(a) t=2 hours

(b) t=24 hours

(c) t=48 hours

(d) t=72 hours

Figure 6.10: Contours of vertical velocity overlaid by horizontal velocity vectors at a depth of 1000m for the stratified run, for 2 -72 hours.

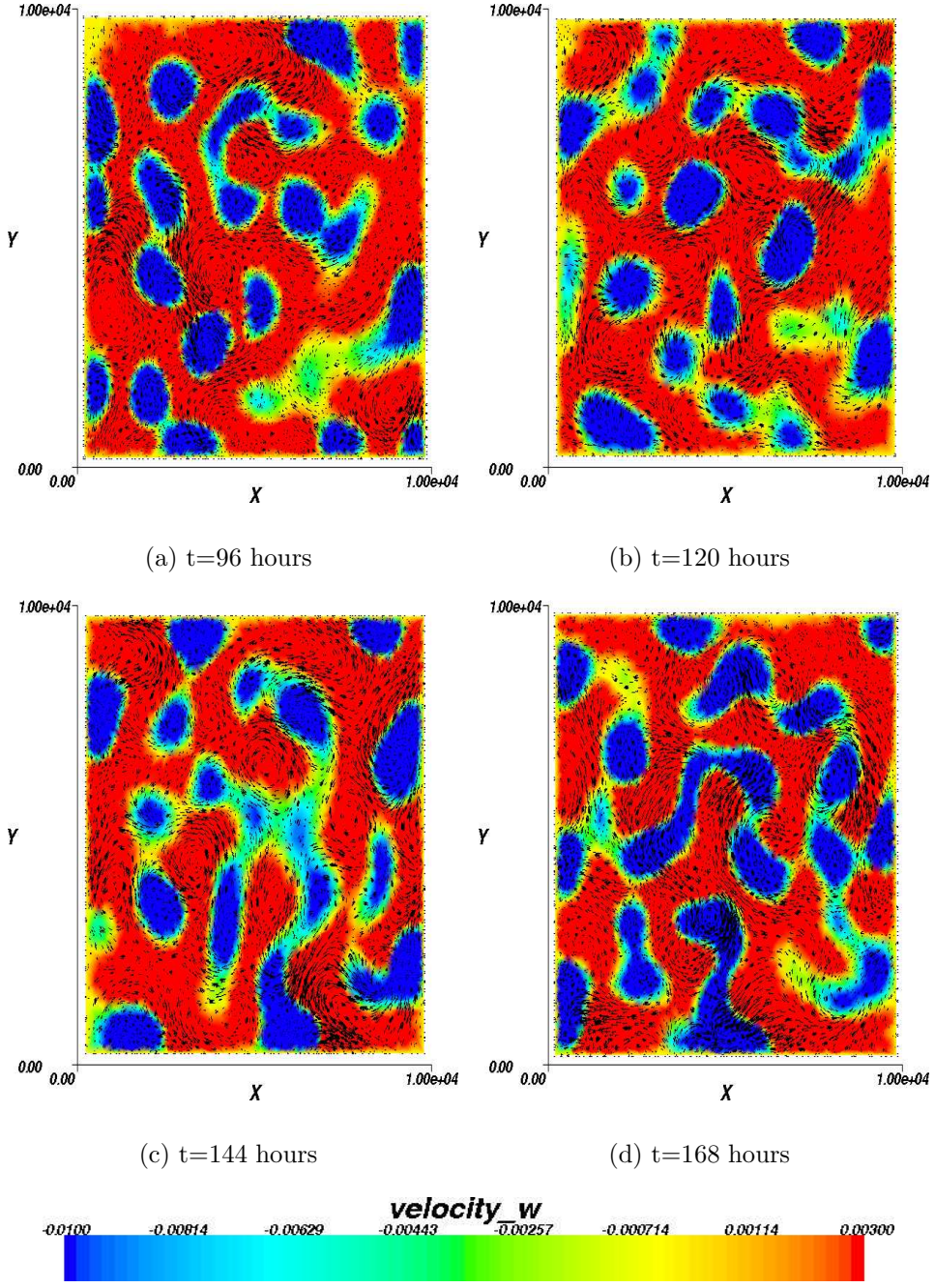

(a) t=96 hours

(b) t=120 hours

(c) t=144 hours

(d) t=168 hours

Figure 6.11: Contours of vertical velocity overlaid by horizontal velocity vectors at a depth of 1000m for the stratified run, for 96 - 168 hours.

welling from the layer below. These plumes occur much more sporadically, and have a more random spatial distribution than those observed in the upper layers. The presence of some plumes at this level infer penetrative convection is present.

Figures 6.8 - 6.13 all display similar scales for individual eddies formed in the latter stages of the model run. These eddies have an approximate scale of 1-2km, showing good agreement with the predicted model L_R, and of the same magnitude as the L_R expected from reality.

Figure 6.14 demonstrates the development of the horizontal velocity field with depth and time. Strong velocities are, in general, confined to the upper layer. However, velocity is observed to increase at lower depth over time, as the convective layer deepens. In comparison with the unstratified run in Chapter 5 (Figure 5.9 (b)), velocity is mainly constrained to the upper layer.

A similar pattern is observed in the vertical velocity field (Figure 6.15). Again, this contrasts with the unstratified case (Chapter 5 Figure 5.10 (b)), where the highest vertical velocities are observed in the middle of the domain. In the stratified case, the highest venial velocities occur in the middle of the upper layer.

Figure 6.16 shows that downwelling is predominant in the upper layer, but upwelling occurs at 48 hours in the top 400m of the domain. Downwelling is also predominant in the non-stratified case (Chapter 5 Figure 5.11 (b)), but occurs throughout the whole depth of the domain.

Profiles of temperature flux at 24 hour intervals throughout the stratified run are presented in Figure 6.17. The strongest temperature fluxes are observed in the surface layer (as a result of the cooling applied across the domain), and buoyant water parcels ascend towards the surface, creating a sink of gravitational potential energy (GPE). At 24 hours, a large negative temperature flux is observed at a depth of approximately 1500m (around the base of the convective layer), indicative of penetrative convection at the base of the convective layer. Here, $w'b'$ is negative and buoyant water parcels are descending, creating GPE.

The instantaneous production of turbulent kinetic energy (TKE) was calculated from the integral of temperature flux with depth at 24 hours intervals. The amount of TKE (expressed as percentage of total potential energy within the system) required to drive penetrative convection is shown in Table 6.1. The lowest instantaneous value (1.00%) occurs at 24 hours and implies

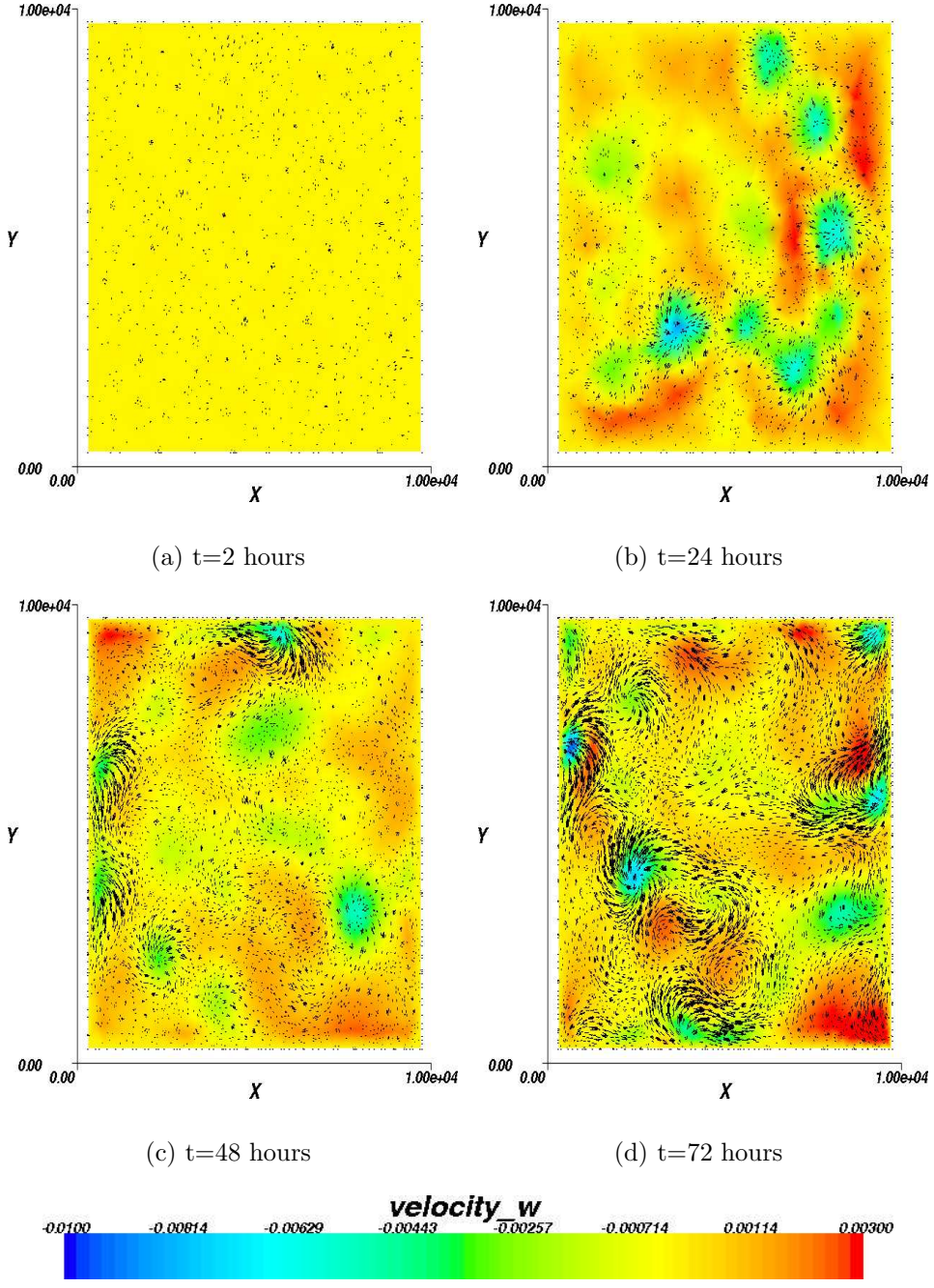

(a) t=2 hours

(b) t=24 hours

(c) t=48 hours

(d) t=72 hours

Figure 6.12: Contours of vertical velocity overlaid by horizontal velocity vectors at a depth of 1800m for the stratified run, for 2 - 72 hours.

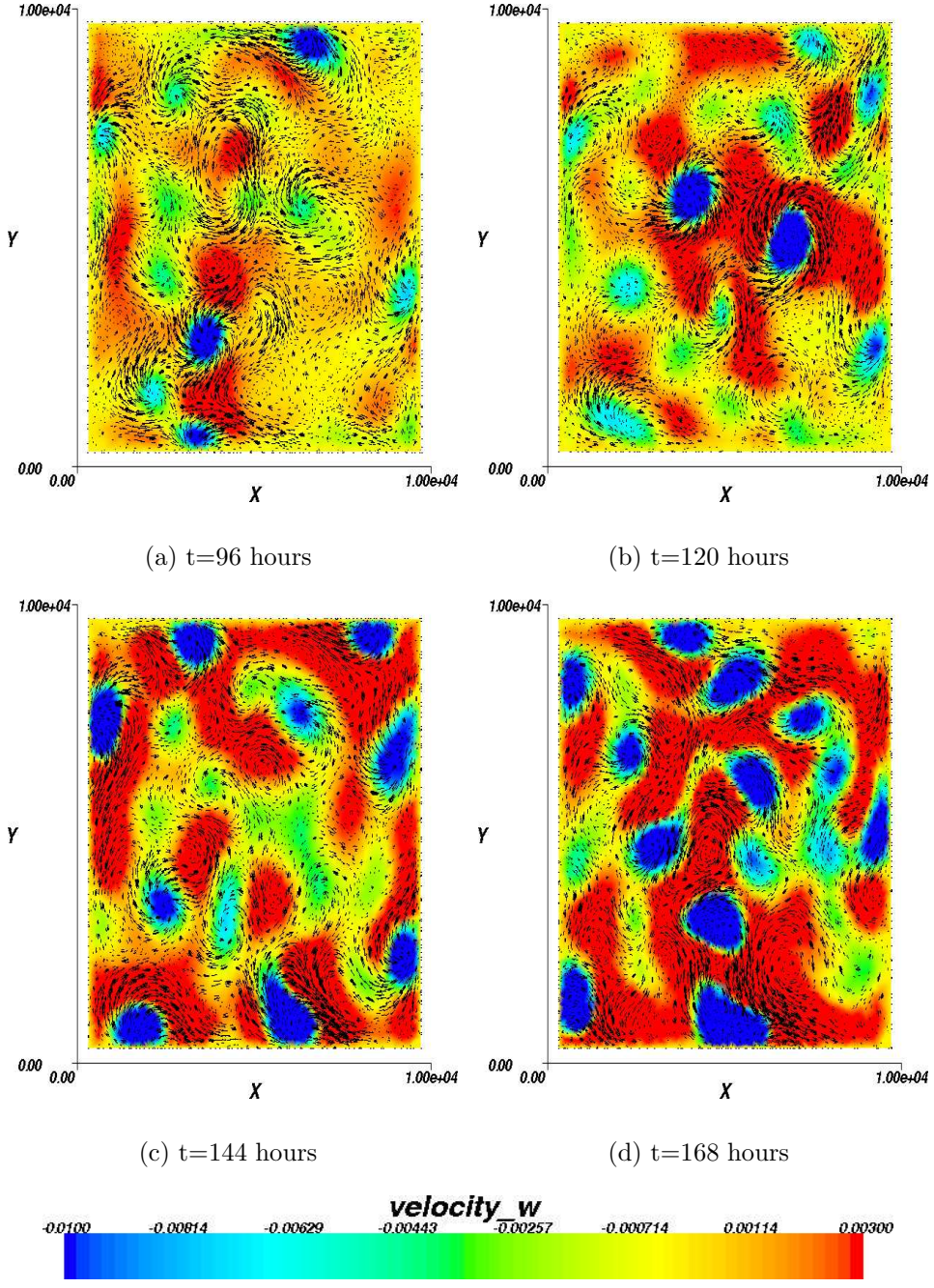

(a) t=96 hours

(b) t=120 hours

(c) t=144 hours

(d) t=168 hours

Figure 6.13: Contours of vertical velocity overlaid by horizontal velocity vectors at a depth of 1800m for the stratified run, for 96 - 168 hours.

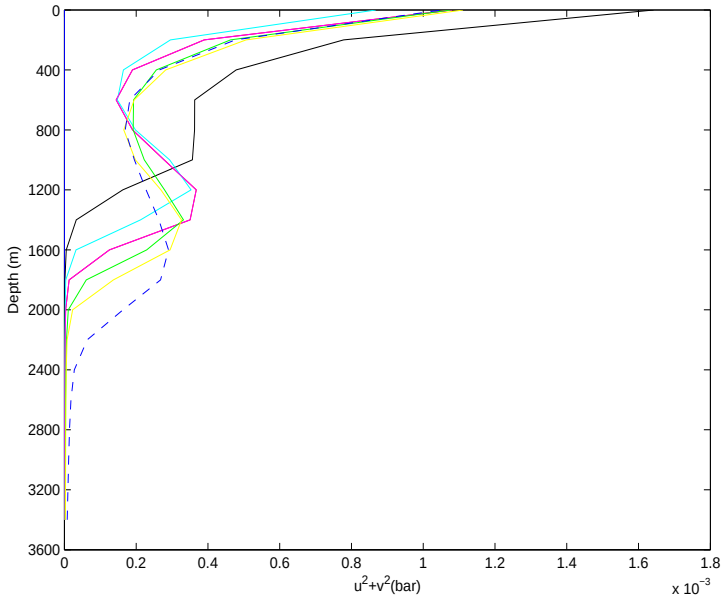

Figure 6.14: Variation in horizontally averaged velocity profiles with depth at times 2 hours (blue), 24 hours (black), 48 hours (red), 72 hours (cyan), 96 hours (magenta), 120 hours (green), 144 hours (yellow) and 168 hours (dashed blue) for the stratified uniform cooling run.

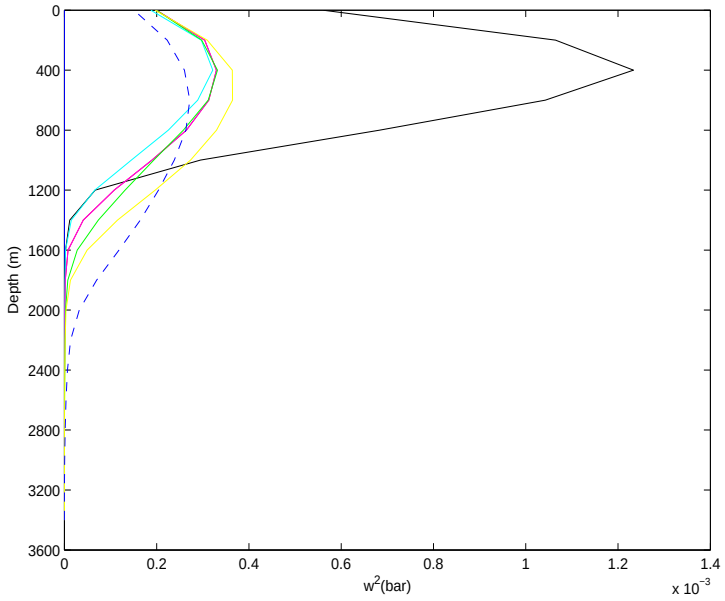

Figure 6.15: Variation in horizontally averaged vertical velocity profiles with depth at times 2 hours (blue), 24 hours (black), 48 hours (red), 72 hours (cyan), 96 hours (magenta), 120 hours (green), 144 hours (yellow) and 168 hours (dashed blue) for the stratified uniform cooling run.

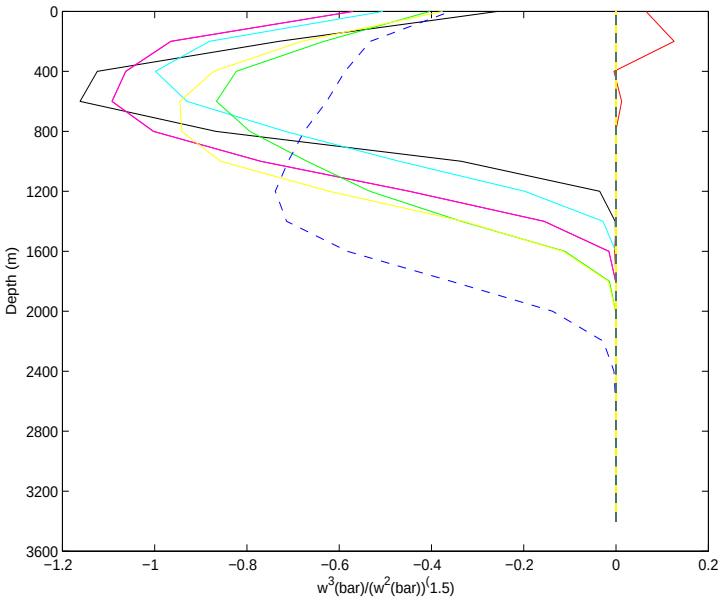

Figure 6.16: Variation in skewness of vertical velocity profiles with depth at times 2 hours (blue), 24 hours (black), 48 hours (red), 72 hours (cyan), 96 hours (magenta), 120 hours (green), 144 hours (yellow) and 168 hours (dashed blue) for the stratified uniform cooling run.

a peak in GPE, in agreement with the creation of the sinking of buoyant parcels associated with penetrative convection.

Beyond 24 hours a smaller negative temperature flux persists as the base of the convective layer erodes down into the bottom layer. Penetrative convection becomes harder to diagnose as the top layer cools to a temperature closer to that of the bottom layer.

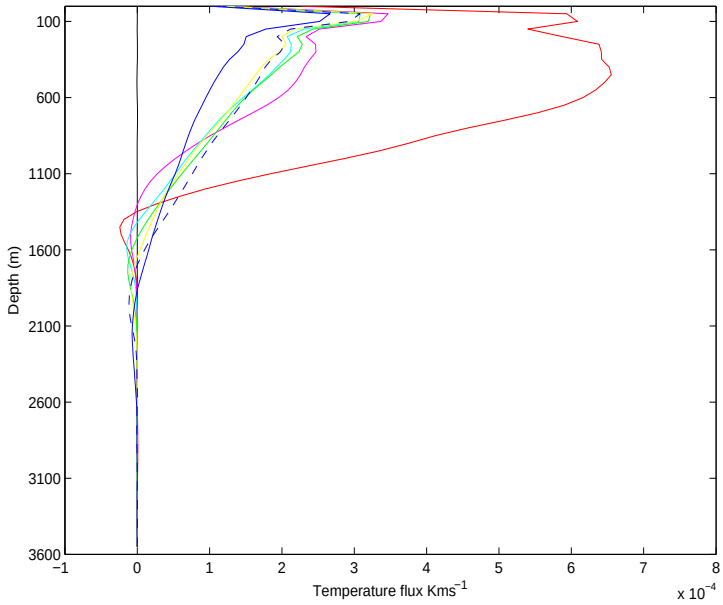

Figure 6.17: Temperature flux profiles with depth at times 2 hours (black), 24 hours (rd), 48 hours (cyan), 72 hours (magenta), 96 hours (green), 120 hours (yellow), 144 hours (dashed blue) and 168 hours (blue) for the stratified uniform cooling run.

Table 6.1: Turbulent kinetic energy (TKE) used to drive penetrative convection expressed as a percentage of total available potential energy

Time (hours)	TKE (%)
24	1.00
48	1.54
72	2.27
96	2.25
120	1.58
144	2.21
168	2.45

6.3 Summary and Conclusions

The introduction of stratification represents the first step towards the development of a more realistic domain within which to to experiment and investigate OODC within the Greenland Sea. The small scale domain used within Chapter 5 was complicated by the presence of a two layer stratification, not unlike the stratification traditionally observed in the Greenland Sea. Uniform cooling was applied across the surface of the domain, and the development of a convective layer was observed within the initial upper layer of the stratification. Over time, this convective layer gradually eroded the 2 layer stratification, and beyond 6 days, convection became qualitatively different, resembling the convection observed in previous experiments into an unstratified fluid.

Penetrative convection was observed within the model run, identified at 24 hours by the negative temperature flux in Figure 6.17 and by the diminished turbulent kinetic energy within the system at that instance (Table 6.1). Beyond this, warming at the base of the convective layer through elevated diffusion was observed. This is in agreement with observations by Mironov et al. (2000). The adaptive configurations ability to capture penetrative convection, at the predicted scales for vertical velocity and L_R, stand it in good stead to become a useful tool in future investigations.

Chapter 7

Summary, Conclusions and Discussion

7.1 Conclusions and Discussion

The work presented within this thesis is intended to contribute to the aims of the RAPID Climate Change Programme. As such, a number of investigations have been performed using the Imperial College Ocean Model (ICOM) to increase understanding of open ocean deep convection (OODC) and its contribution to large-scale ocean circulation, with particular reference to the Greenland Sea. A primary focus of the project has been validation of ICOM and research into ICOM's ability to model OODC as a result of its developmental nature.

The context for this project has been outlined in Chapter 1. In a warming climate, the impact on the thermohaline circulation (THC) of a reduction in OODC, as has been observed in the Greenland Sea, is of particular significance for North West Europe, which benefits from the heat transported northwards in the Atlantic Ocean. Understanding of OODC and its contribution to the THC is, however, impeded by the difficulty of obtaining direct observations and because of the requirement for parameterisation of the process in large-scale climate models. The development of finite-element based adaptive, unstructured mesh models therefore presents us with an opportunity to study OODC without the need to highly resolve entire domains.

The present state of knowledge concerning OODC is presented in Chapter 2. OODC is known to occur in only a few remote regions around the world, and is notably sporadic both spatially and temporally. Observational data on OODC is, therefore, limited. Theoretically, OODC is known to require a number of features, such as cyclonic circulation and preconditioning, and to occur in stages. These stages include the formation of individual plumes, the development of a well-mixed 'chimney', chimney break-up and restratification. This theoretical process is corroborated by laboratory and numerical experiments. Theory also predicts that the convective process is associated with a number of scales constrained by timescale, depth and rotation. In general, convection in the Greenland Sea falls into the rotational scaling regime due to the large Coriolis force at high latitude and the depth of the region, which is so deep that the timescale of convective overturning is large.

The Greenland Sea is known to be an important region for the formation of North Atlantic Deep Water (NADW). NADW forms the lower arm of the Meridional Overturning Circulation (MOC) observed in the North Atlantic. The Greenland Sea is a prime convective site, being a region of complex hydrography, strong meteorological variation, ice formation and due to its isolation by bathymetry. However, in recent years, deep convection has not been observed in the region. Concurrently, the reduction in ice coverage in the Greenland Sea has been notable. The brine rejection associated with ice formation is thought to play a major role in the preconditioning stage of deep convection at this particular site, and OODC in the Greenland Sea has been known historically to be haline forced.

The use of ICOM in the investigation of OODC is novel. Chapter 3 outlines the formulation of the model, including the development of additional forcing fields such as wind and ice that play a key role in the convective process. ICOM is a three-dimensional non-hydrostatic ocean model based on finite element discretisation of the Boussinesq approximation of the Navier Stokes equations of motion on unstructured meshes. It is currently formulated with a linear equation of state.

Because of the developmental nature of ICOM, and the novel use of ICOM in the convective investigation, model validation is an important consideration. For these reasons, a preliminary study of model accuracy was conducted using the classical fluid dynamics problem of parallel plate convection and linear instability, based on the work of Chandrasekhar (1961). This classical

problem, for which Chandrasekhar (1961) obtained an analytical solution, allows us to make a quantitative assessment of numerical diffusivity within an ocean model. The amount of numerical diffusivity is an important consideration for model accuracy, and it is felt that no sufficient test for diagnosis of numerical diffusion currently exists for ocean models. The development of such a test is therefore a primary achievement of this thesis. However, such a test is constrained to application only in non-hydrostatic ocean models, of which few exist. Using a model configuration that resembles as closely as possible the problem defined by Chandrasekhar (1961), the model critical Rayleigh number (a non-dimensional measure for the prediction of the onset of instability) was obtained for ICOM in fixed hexahedral, fixed tetrahedral, and adaptive tetrahedral modes. A similar test was conducted using the leading non-hydrostatic ocean model, MITgcm, for comparison. It was found that ICOM compared well with the amount of numerical diffusivity present in MITgcm, but that the adaptive tetrahedral configuration had the most numerical diffusion of all the configurations. However, in comparison to the analytical solution of the theory, the adaptive ICOM configuration showed the best agreement. The MITgcm performed poorly in comparison to the fixed hexahedral ICOM configuration, exhibiting a much higher implicit diffusivity. The full investigation, including the theoretical background and analysis of results, comprises Chapter 4 of this thesis.

Further validation of ICOM for use in the investigation of OODC was conducted using comparisons of convection on fixed and adaptive mesh configurations within a small domain. The results of this study comprise the majority of Chapter 5. Uniform cooling across the surface of the domain for both continuous and finite duration, along with cooling within a disk shaped region at the centre of the domain for continuous duration, was considered. Using observations of the evolution of the temperature field, the theoretical stages of convection were diagnosed. Studies of the variation of temperature within the domain with depth and time were used to infer the depth of convection, and analysis of the associated variations in the velocity fields were used to infer the strength of convection. In general, the adaptive configuration produced the best representation of OODC. This was confirmed by comparison of model convection with the scales predicted by the theoretical scaling regimes. As expected, model convection was constrained by the effect of the Earth's rotation, scaling better with the vertical velocities predicted

by this scaling regime. The scale of horizontal eddies occurring during the break-up of the convective chimney formed in the disk cooled runs was compare with realistic values of the Rossby deformation radius, and indicated that the adaptive configuration was best at simulating such eddies.

The variation of convection induced by finite and continuous duration cooling was also examined. The continuous cooling scenario, in both uniform and disk application, showed convective pluming to occur in waves, and result in the formation of a well mixed layer of convectively cooled fluid throughout the depth of the domain. In contrast, finite cooling periods resulted in the formation of a stable stratification. In nature, cooling events are episodic. The results of this short study are perhaps indicative that the timescale of cooling may dictate the final stages of the convective process. For example, in short-lived convective events, vertical transport of the cooled water is most important, but in longer term convective events, the baroclinic breakup and horizontal transport of the convected water by eddies becomes important. In relation to the Greenland Sea, the formation of deep water may rely wholly on one or other of these processes. It is perhaps significant that presently in the Greenland Sea, convection is only observed to mid-depths, indicating an absence of strong surface forcing or the necessary preconditioning processes to initiate the violent mixing stage. It may be that resultant convected water is exported away from the Greenland Sea basin by horizontal transport after long periods of cooling.

From a modelling perspective, the use of the disk forced case (which has been widely used in numerical studies of OODC) is compared to the uniform case because of issues regarding its realism. Indeed, the use of a cooling disk results in a severe restriction on the horizontal extent of convective pluming. Furthermore, the cooling disk exhibits large constraints in the velocity fields, forming concentric rings of upwelling and downwelling that may be compared to doughnut shaped plumes. In contrast, the uniform cooling configuration produces well distributed individual convective plumes throughout the domain. Similar studies using disk shaped forcing, such as Jones and Marshall (1993), have not presented plots of vertical velocity structure, so it is difficult to ascertain whether the concentric rings are a factor of the forcing shape - grid resolution relationship, or the result of the internal mechanisms of ICOM itself.

Other outcomes of note resulting from the work conducted in Chapter

5 include the conclusion that the use of the adaptive mesh was less computationally expensive than the fixed mesh, and also that the adaptive grid was exempt from the numerical noise observed near the surface on the fixed mesh.

Diagnosing the sensitivity of convection to theoretical influencing factors such as stratification, wind, ice and bathymetry was outlined as a primary objective in this thesis. To this end, an investigation into the impact of stratification on the convective process was conducted. A background stratification similar to that observed in the Greenland Sea was set within a small scale domain, to which a continuous uniform cooling at the surface was applied. The formation of a convective layer and its progress over time was examined. Of particular interest was identifying whether convective pluming was penetrative or non-penetrative. Convection in the Greenland Sea is hypothesised to be non-penetrative (in contrast with the Mediterranean Sea). In this study, convective pluming was observed to be penetrative in the early stages of the model run, identified using profiles of temperature flux and estimates of turbulent kinetic energy. It must be noted that for this case, convection was largely constrained to a convective layer above approximately 1800m (in comparison to the non-stratified case presented in Chapter 5), but accelerated diffusion was observed at the base of the convective layer after 24 hours in accordance with observations by Mironov et al. (2000). Because the adaptive mesh places fine resolution around the base of the convective layer (where eddies are small-scale), the model should be able to represent entrainment well. It is suggested that this study would be enhanced by the modelling of the non-rotating case for comparison.

Further studies into the sensitivity of convection to various preconditioning forces, including wind and ice, fell outside of the scope of this thesis due to the developmental nature of the model. However, the outcome of the investigation presented here indicates that ICOM is, indeed, a useful tool for studies of this kind and there are therefore a number of opportunities for further studies. The limitations of the present study are outlined in the next section (Section 7.2), and a discussion of suggestions for further work arising from the outcomes of this study is presented in Section 7.3.

7.2 Limitations of the study

The progress of this project and the success of the studies outlined in this thesis were largely hampered by developmental issues associated with ICOM. The use of a linear equation of state may have a large impact on the convective study because this effectively omits the thermobaric effect which is known to have a large impact on convection in the Greenland Sea. A further restriction resulted from the absence of a salinity field, meaning that the contribution of brine rejection to preconditioning was beyond our scope, hence, all studies presented here represent thermal convection. Because of the known importance of ice, the development of an ice field was initiated and to a limited extent successful, but the absence of salinity hindered this also.

As a result of these restrictions, and a change in focus of the work towards more validation based studies, a number of original objectives were not fully realised. These included progress towards the formulation of a more suitable convective parameterisation for use in General Circulation Models (GCMs), the development of both an idealised and realistic Greenland Sea, and a full suite sensitivity study combining stratification, bathymetry, ice and wind.

However, in work not presented as part of this thesis, some progress towards these initial aims was made. The application of wind to the small scale domain was attempted with some success, and the use of realistic GEBCO bathymetry was also experimented with. The use of sponge regions to drive a thermal gyre was also attempted with limited success.

A further restriction to the achievements of this thesis was caused by resource issues. ICOM was never successfully transported from Imperial College computing systems to computing systems hosted by the National Oceanography Centre. As a result, all of the work presented here was conducted remotely and on single processors, significantly reducing the size of the domains that could be used.

7.3 Future work

The investigations conducted as part of this thesis validated use of ICOM for the convective problem and demonstrated an example of convection in a stratified domain. As a result, a number of further investigations are now pos-

sible. These include a full suite of sensitivity studies focusing on convection in the Greenland Sea and the impact of varying stratification, bathymetry and wind. With some further development, the ability to model ice and its impact on convection may be realised. Furthermore, the gradual complication of the domain to include realistic bathymetry, winds from re-analysis data, ice and a gyre circulation is achievable. With increased computing resources, a move towards realistic, large scale domains is also possible.

The results of model runs presented in Chapter 5 demonstrated the suitability of the adaptive mesh capability within ICOM for study of the convective problem. It is felt that future models of the Greenland Sea should incorporate a compromise between uniform and disk shaped cooling (for example, areas of cooling where the edge of the 'disk' is a gradient in temperature). Cooling should be applied on finite timescales in order for such a model to capture the final stages of convection. The use of scaling ideas provide a technique with which to examine the accuracy of model convection in comparison with theoretical predictions.

The demonstration of the adaptive model's ability to resolve penetrative convection presents an opportunity for further study of the penetrative convection problem. Successive investigations should incorporate more complex stratification's and realistic parameters such as explicit viscosity and thermal expansion, specific to the Greenland Sea. Further studies should also consider other regions where penetrative convection is reported to occur on a regular basis (e.g. Mediterranean Sea).

Appendix A

Identifying the required resolution for investigating linear instability

Supplied courtesy of P. Killworth (personal communication).

The system of ordinary differential equations (ODE's) (Chapter 4 Eqs. 4.7 and 4.8) calculated by Chandrasekhar (1961) as the solution of the theoretical liner instability problem for the boundary conditions Eq. 4.2 were transformed into a matrix using a finite difference scheme. This matrix was discretised over 40 levels to produce an eigenproblem for the comparison of model and theoretical values of vertical velocity and temperature perturbation. The minimum number of levels required to obtain an accurate solution of R_c was determined as follows.

In the horizontal, the differential operator squared in Eqs. 4.7 and 4.8 becomes $2(cosa\Delta x - 1)/\Delta x^2$ which is simply $-\hat{a}^2$ for some $\hat{a}$. We now drop the hat. In the vertical, where the structure will be at the kth point:

$$sin(\pi k \Delta z) \tag{A.1}$$

The second derivative operator is, similarly:

$$-\frac{\partial^2}{\partial z^2} \rightarrow \phi \equiv 2(1 - cos(\pi \Delta z))/\Delta z^2 \tag{A.2}$$

Then the pair of equations require, for $\sigma = 0$, a simple replacement of π^2 by ϕ , which gives:

$$a^2 = \phi c \tag{A.3}$$

$$c = \frac{1}{4r}(\sqrt{1+8r} - 1) \tag{A.4}$$

$$R = \phi^2 \frac{(1+c)^2(1+rc)}{c} \tag{A.5}$$

For $r = 1$, $c = 1/2$, and we find the result seen in Figure A.1, so that as far as simple finite-differences are concerned, 10 or more points in the vertical ($\Delta z = 0.1$) should yield an accurate solution.

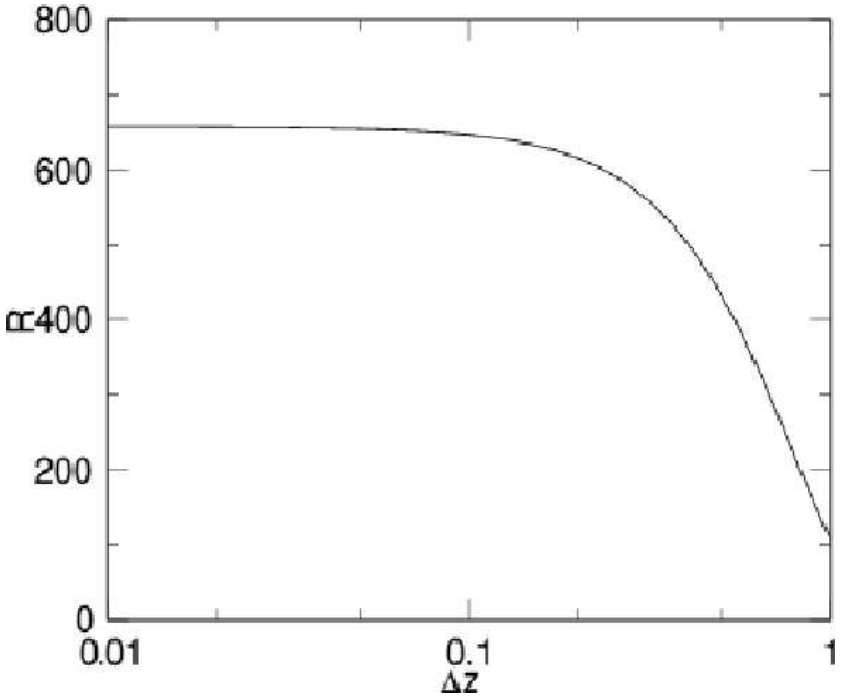

Figure A.1: Variation of Rayleigh number with vertical resolution for a finite difference discretisation of the solution calculated by Chandrasekhar (1961).

Appendix B

Impact of varying the ratio of vertical to horizontal explicit diffusivity

Supplied courtesy of P. Killworth (personal communication).

The ratio of explicit (specified) model horizontal (κ_H) and vertical (κ_V) diffusivity impacts the value of the critical Rayleigh number (R_c) expected from theory (Chapter4, Eq. 4.1), as follows.

When $\kappa_H \neq \kappa_V$, the two equations (4.7) and (4.8) become:

$$w'''' - 2a^2 w'' + a^4 w - a^2\theta = \sigma(w'' - a^2 w) \tag{B.1}$$

$$Rw + \theta'' - ra^2\theta = Pr\sigma\theta \tag{B.2}$$

where r is the ratio κ_H/κ_V and R is the Rayleigh number (based on κ_V), and Pr is the Prandtl number (again based onκ_V). We note that all the boundary conditions permit solutions in which w and θ are proportional to $sin\pi z$, so that the system becomes algebraic:

$$(\pi^2 + a^2)^2 w - a^2\theta = -\sigma(\pi^2 + a^2)w \tag{B.3}$$

$$Rw - (\pi^2 + ra^2)\theta = Pr\sigma\theta \tag{B.4}$$

If, further, we seek solutions which are just critical, we can put $\sigma = 0$. This gives a pair of equations:

$$(\pi^2 + a^2)^2 w - a^2\theta = 0 \tag{B.5}$$

$$Rw - (\pi^2 + ra^2)\theta = 0 \tag{B.6}$$

whose solution is (using the determinant):

$$(\pi^2 + a^2)^2(\pi^2 + ra^2) = Ra^2 \tag{B.7}$$

In addition, the gradients of the l.h.s. and r.h.s. must be identical for the lowest (kissing) solution, so differentiating w.r.t. a^2 gives:

$$2(\pi^2 + a^2)(\pi^2 + ra^2) + r(\pi^2 + a^2)^2 = R \tag{B.8}$$

Substituting this value of back into the previous equation yields:

$$\pi^4 = \pi^2 a^2 + 2ra^4 \tag{B.9}$$

whose solution becomes (resubstituting for R):

$$a^2 = \pi^2 c \tag{B.10}$$

$$c = \frac{1}{4r}(\sqrt{1 + 8r} - 1) \tag{B.11}$$

$$R = \pi^4 \frac{(1 + c)^2(1 + rc)}{c} \tag{B.12}$$

where for $r = 1$ (the 'correct' problem!) $c = 1/2$, $R = 27\pi^4/4 = 657.5$ as usual.

For varying ratios of κ_H/κ_V, the solution of R can be plotted, as seen in Figure B.1.

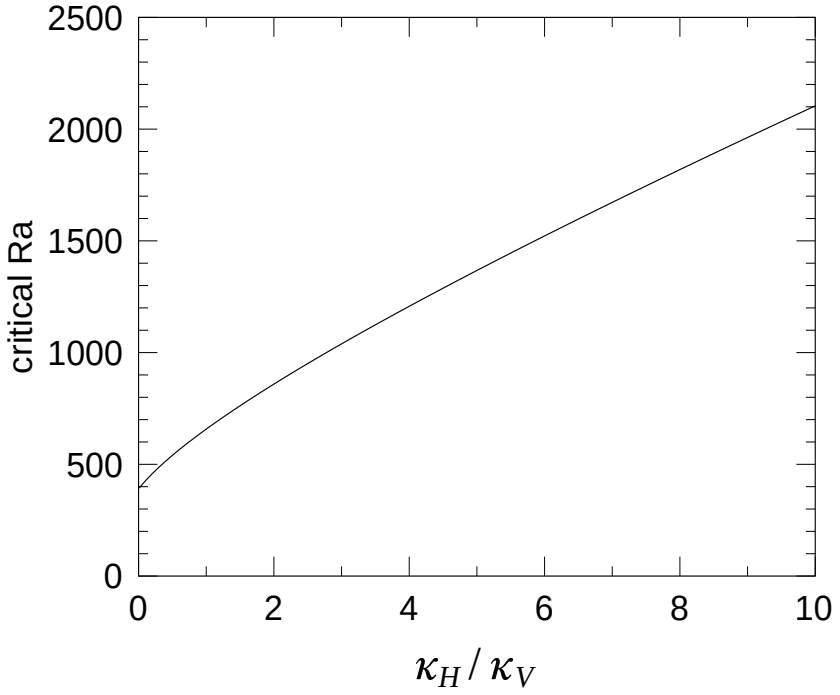

Figure B.1: Variation of Rayleigh number with ratio of horizontal to vertical diffusivity for a finite difference discretisation of the solution calculated by Chandrasekhar (1961).

Appendix C

Fortran code for calculating the eigenvectors of the linear instability problem

Supplied courtesy of P. Killworth (personal communication).

```
implicit double precision (a-h,o-z)
parameter (n=41,np1 = n + 1, nn=2*n,dz=1.d0/(n-1),dz1 = 1.d0/dz)
parameter (dz2 = dz1**2, dz4 = dz2**2)
dimension aa(nn,nn),bb(nn,nn),v(nn,nn),alfr(nn),alfi(nn),beta(nn)
integer iter(nn)
*
* W:i = 1 is z= 0;i = n is z = 1;
* Thetahat: i = n+1 is z = 0; i = nn is z = 1
* rigid lid thetahat = W = DW = 0 top and bottom
* vector arrangement is: 1 - n is W; n+1 to nn is thetahat
*
* set variables
```

```
*
*100   continue

      a = 2.d0
      pr = 1.d0
      r=1000.0
      a2 = a**2
      a4 = a**4
*
* insert values in matrices!
*
      do j=1,nn
      do i=1,nn
        aa(i,j) = 0.d0
        bb(i,j) = 0.d0
      enddo
      enddo
*
      aa(1,1) = 1.d0
      aa(n,n) = 1.d0
      aa(np1,np1) = 1.d0
      aa(nn,nn) = 1.d0
*
* that did W = thetahat = 0 top and bottom
*
* now do D2W = 0 top and bottom
*
      aa(2,1) = 2.d0
```

```
      aa(2,2) = -5.d0
      aa(2,3) = 4.d0
      aa(2,4) = -1.d0
      aa(n-1,n-3) = -1.d0
      aa(n-1,n-2) = 4.d0
      aa(n-1,n-1) = -5.d0
      aa(n-1,n) = 2.d0
*
* now do main rows
*
      do i=3,n-2
        ip = i+n
*
* the fourth order W equation
*
        aa(i,i-2) = dz4
        aa(i,i-1) = -4.d0*dz4 -2.d0*a2*dz2
        aa(i,i) = 6.d0*dz4 +4.d0*a2*dz2 + a4
        aa(i,i+1) = -4.d0*dz4 -2.d0*a2*dz2
        aa(i,i+2) = dz4
        aa(i,ip) = -a2
* that was the thetahat term
        bb(i,i-1) = dz2
        bb(i,i) = -2.d0*dz2 -a2
        bb(i,i+1) = dz2
      enddo
*
* now the second order thetahat equation
```

```
*
      do ip = np1+1,nn-1
        i = ip-n
        aa(ip,i) = r
* that was the W term
        aa(ip,ip-1) = dz2
        aa(ip,ip) = -2.d0*dz2 -a2
        aa(ip,ip+1) = dz2
        bb(ip,ip) = pr
      enddo
*      do i=1,nn
*        write(6,444)i,(aa(i,j),j=1,nn)
*444     format(i4,(/,1p,20d10.2))
*      enddo
*      do i=1,nn
*        write(6,444)i,(bb(i,j),j=1,nn)
*      enddo
* solve problem
      ifail = 0
      call f02bjf(nn,aa,nn,bb,nn,-1.d0,alfr,alfi,beta,.true.,v,nn,
     *            iter,ifail)
      eig = 0.d0
      do i=1,nn
        if (beta(i) .ne. 0.d0) then
          sigma = alfr(i)/beta(i)
          if (sigma .gt. 0.d0) then
            eig = sigma
            ii = i
```

```
            goto 600
          endif
        endif
      enddo
600   continue
      if (eig .eq. 0.d0) then
        print *,'no solutions with positive growth rate for a = ',a
       else
         write(6,401) eig,a
      endif
401   format('growth rate = ',1p,d12.3, 'for a = ',d12.3)
*
* print out eigenvector for W and thetahat
*
      print *,'eigenvector (W and thetahat)'
      do i=1,n
        write(6,400)(i-1)*dz, v(i,ii),v(i+n,ii)
400     format(f12.3,1p,2d12.3)
      enddo
*      enddo !ia
*      goto 100
      stop
      end
```

Bibliography

Alekseev, G., Johannessen, O., Korablev, A., Ivanov, V., Kovalevsky, D., 2001. Interannual variability in water masses in the Greenland Sea and adjacent areas. Polar Research 20, 201–208.

Backhaus, J., Kampf, J., 1999. Simulations of sub-mesoscale oceanic convection and ice-ocean interactions in the Greenland Sea. Deep-Sea Research II 46, 1427–1455.

Bacon, S., Gould, W., Jia, Y., 2003. Open-ocean convection in the Irminger Sea. Geophysical Research Letters 30, 1246.

Bakker, A., 2005. Large eddy simulation, the colourful fluid mixing gallery. http://www.bakker.org/cfm/webdoc16a.htm.

Barbosa, J. P., Metais, O., 2000. Large eddy simulations of deep ocean convection: analysis of the vorticity dynamics. Journal of Turbulence 1, 1–31.

Broecker, W. S., 1997. Thermohaline Circulation, the Achilles Heel of Our Climate System: Will Man-Made CO2 Upset the Current Balance? Science 278, 1582–1588.

Broecker, W. S., Sutherland, S., Peng, T., 1999. A possible 20th-century slowdown of Southern Ocean deep water formation. Science 286, 1132–1135.

Bryan, K., 1969. A numerical method for the study of the circulation of the world ocean. Journal of Computational Physics 4, 347–376.

Bryan, K., Cox, M., 1967. A numerical investigation of the oceanic general circulation. Tellus 19, 54–80.

Budeus, G., Schneider, W., Krause, G., 1998. Winter convective events and bottom water warming in the Greenland Sea. J. Geophys. Res. 103, 18,513–18,527.

Chandrasekhar, S., 1961. Hydrodynamic and Hydromagnetic Instability. Oxford Press.

Clarke, R., Gascard, J., 1983. The formation of Labrador Sea water. Part I: Large scale processes. J. Phys. Oceanogr. 26, 2196–2213.

Coates, M., Ivey, G., Taylor, J., 1995. Unsteady, turbulent convection into a rotating linearly stratified fluid: Modeling deep ocean convection. J. Phys. Oceanogr. 25, 3032–2050.

Condron, A., Bigg, G., Renfrew, I., 2006. Polar Mesoscale Cyclones in the Northeast Atlantic: Comparing Climatologies from ERA-40 and Satellite Imagery. Monthly Weather Review 134, 1518–1533.

Cox, M., 1984. A primitive equation, 3 dimensional model of the ocean. Tech. rep., GFDL Ocean Group Technical Report No.1, Geophysical Fluid Dynamics Laboratory, P.O.Box 308, Princeton, New Jersey, 08542.

Danilov, S., Kivman, G., Schroter, J., 2004. A finite-element ocean model: principles and evaluation. Ocean Modelling 6, 125–150.

Denbo, D., Skyllingstad, E., 1996. An ocean large-eddy simulation model with application to deep convection in the Greenland Sea. J. Geophys. Res. 101, 1095–1110.

Dickson, R., Brown, J., 1994. The production of North Atlantic Deep Water: sources, rates and pathways. J. Geophys. Res. 99, 12,319–12,341.

Dickson, R., Lazier, J. R. N., Meincke, J., Rhines, P., Swift, J., 1996. Long-term coordinated changes in the convective activity of the North Atlantic. Progress in Oceanography 38, 241–295.

Divine, D., Dick, C., 2006. Historical variability of sea ice edge position in the Nordic Seas. J. Geophys. Res. 111, C01001.

Dumas, E., Provost, C. L., Poncet, A., 1982. Vol. 5, 4th International Conference on Finite Element in Water resources. Springer-Verlag, Ch. Feasability of finite element methods for oceanic general circulation modelling, pp. 43–55.

Ekman, V., 1905. On the influence of the earth's rotation on ocean currents. Arkiv Matematik, Astronomi och Fysik 2, 1–53.

England, M., Rahmstorf, S., 1999. Sensitivity and ventilation rates and radio carbon uptake to subgrid-scale mixing in ocean models. J. Phys. Oceanogr. 29, 2802–2827.

Fix, G., 1975. Finite element models for ocean circulation problems. SIAM J. App. Math. 3, 371–387.

Ford, R., Pain, C., Piggott, M., Goddard, A., de Oliveira, C., 2004a. A non-hydrostatic finite element model for three-dimensional stratified oceanic flows. Part 1: Model formulation. Monthly Weather Review 132, 2816–2831.

Ford, R., Pain, C., Piggott, M., Goddard, A., de Oliveira, C., 2004b. A non-hydrostatic finite element model for three-dimensional stratified oceanic flows. Part 2: Model validation. Monthly Weather Review 132, 2832–2844.

Garwood, J., Isakari, S. M., Gallacher, P. C., 1994. The Polar Ocean and their role in shaping the Global Environment, Geophys. Monogr. Ser. Vol. 85. AGU, Washington D.C., Ch. Thermobaric Convection, pp. 199–209.

Gascard, J., Watson, A., Messias, M. R., Olsson, K., Johannessen, T., Simonsen, K., 2002. Long-lived vortices as a mode of deep ventilation in the Greenland Sea. Nature 416, 525–527.

GEBCO, 2003. Ioc, iho and bodc. centenary edition of the gebco digital atlas, published on cd-rom on behalf of the intergovernmental oceanographic commission and the international hydrographic organization as part of the general bathymetric chart of the oceans, british oceanographic data centre, liverpool, u.k.

Griffies, S., 2004. Fundamentals of Ocean Climate Models. Princeton University Press, Princeton and Oxford.

Griffies, S., Boening, C., Bryan, F., Chassignet, E., Gerdes, R., Hasumi, H., Hirst, A., Treguier, A., Webb, D., 2000a. Developments in ocean climate modelling. Ocean Modelling 2, 123–192.

Griffies, S., Pacanowski, R., Hallberg, R., 2000b. Spurious Diapycnal Mixing Associated with Advection in a z-Cordinate Ocean Model. Monthly Weather Review 128, 538–564.

GSP-Group, 1990. Greenland Sea project: A venture toward improved understanding of the oceans' role in climate. Eos. AGU 71, 750–755.

Hanert, E., 2004. Towards a finite element ocean circulation model. PhD thesis.

Hopkins, T., 1991. The GIN Sea - a synthesis of its physical oceanography and literature review 1972-1985. Earth Science Reviews 30, 175–318.

ICES, 2008. International Council for the Exploration of the Sea Oceanographic Database and Services. `http://www.ices.dk/ocean`.

IPCC, 2007. Climate Change 2007: the physical science basis. IPCC Fourth Assessment Report of the Intergovernmental Panel on Climate Change. `http://www.ipcc.ch`.

Jones, H., Marshall, J., 1993. Convection with rotation in a neutral ocean: A study of open ocean deep convection. J. Phys. Oceanogr. 23, 1009–1039.

Karstensen, J., Schlosser, P., Wallace, D., Bullister, J., Blindheim, J., 2005. Water mass transformation in the Greenland Sea during the 1990s. J. Geophys. Res. 110, C07022.

Killworth, P., 1976. The mixing and spreading phases of medoc, i. Progress in Oceanography 7, 59–90.

Killworth, P., 1983. Deep convection in the world ocean. Reviews of Geophysics 21, 1–26.

Killworth, P., 1989. Parameterization of small-scale processes. Hawaii Institute of Geophysics, Ch. On the parameterisation of deep convection in ocean models, pp. 59–74.

Klinger, B., Marshall, J., Send, U., 1996. Representation of convective plumes by vertical adjustment. J. Geophys. Res. 101, 18175–18182.

Kyoto, 1997. Kyoto Protocol.

LabSea-Group, 1998. The Labrador Sea Deep Convection Experiment. Bull. Am. Meteorol. Soc. 79, 2033–2058.

Lavender, K., Davis, R., Owens, W., 2002. Observations of open-ocean deep convection in the Labrador Sea from subsurface floats. J. Phys. Oceanogr. 32, 511–526.

Legg, S., 2004. A Simple Criterion to Determine the Transition from a Localized Convection to a Distributed Convection Regime. J. Phys. Oceanogr. 34, 2843–2846.

Lilley, J., Rhines, P., Visbeck, M., Davis, R., Lazier, J., Schott, F., Farmer, D., 1999. Observing deep convection in the Labrador Sea during winter 1994/1995. J. Phys. Oceanogr. 29, 2962–2970.

Lynch, D., Gray, W., 1979. A wave equation model for finite-element tidal computations. Computers and Fluids 7, 207–208.

Lynch, D., Ip, J., Naimie, C., Werner, F., 1996. Comprehensive coastal circulation model with application to the gulf of maine. Continental Shelf Research 16, 875–906.

Lynch, D., Werner, F., 1991. Tidal Hydrodynamics. John Wiley and Sons, New York, Ch. Three-dimensional velocities from a finite-element model of English Channel Southern Bight tides, pp. 183–200.

Malmberg, S., 1983. Hydrographic Investigations in the Iceland and Greenland Seas in late winter 1971 deep water project'. Jokull 33, 133–140.

Mann, C., 1969. Temperature and salinity characteristics of the Denmark Strait overflow. Deep-Sea Research 16, 125–137.

Marotzke, J., 1989. Oceanic circulation models: Combining data and dynamics, 501–511.

Marotzke, J., 1991. Influence of convective adjustment on the stability of the thermohaline circulation. J. Phys. Oceanogr. 21, 903–907.

Marshall, J., Schott, F., 1999. Open-ocean convection: Observations, theory, and models. Reviews of Geophysics 37, 1–64.

Maxworthy, T., Narimousa, S., 1994. Unsteady turbulent convection into a homogeneous, rotating fluid, with oceanographic applications. J. Phys. Oceanogr. 26, 2316–2343.

MEDOC-Group, 1969. Observations of formation of deep water in the Mediterranean Sea. Nature 27, 1037–1040.

Mertens, C., 2000. Open-Ocean Convection in the Labrador and Greenland Seas: Plume Scales and Interannual Variability. PhD thesis.

Mironov, D., Gryanik, V., Moeng, C., Olbers, D., Warncke, T., 2000. Vertical turbulence structure and second-moment budgets in convection with rotation: A large-eddy simulation study. Quart. J. Roy. Meteorol. Soc. 126, 477–515.

MIT, 2008. Massachusetts Insitute of Technology General Circulation Model. `http://mitgcm.org`.

Moore, G., Renfrew, I. A., 2005. Tip jets and barrier winds: A Quikscat climatology of high wind speed events around Greenland. Journal of Climate 18, 3713–3725.

Munk, W., 1950. On the wind-driven ocean circulation. J. Fluid Mechanics 7, 79–93.

Nobel, 2007. Nobel peace prize. `www.nobelprize.org`.

NOC, 2004. National oceanography centre, southampton - thermohaline circulation. `www.noc.soton.ac.uk`.

Noh, Y., Cheon, W. G., Raasch, S., 2003. The role of preconditioning in the evolution of open-ocean deep convection. J. Phys. Oceanogr. 33, 1145–1166.

Noh, Y., Jang, C., Kim, J., 1999. Large eddy simulation of open ocean deep convection with application to the deep water formation in the east sea (Japan Sea). Journal of Oceanography 55, 347–367.

NSIDC, 2008. National Snow and Ice Data Center. `http://nsidc.org`.

Oka, A., Hasumi, H., Okada, N., Sakamoto, T., Suzuki, T., 2006. Deep convection seesaw controlled by freshwater transport through the Denmark Strait. Ocean Modelling 15, 157–176.

Oscars, 2007. Academy awards. `http://www.oscars.org`.

Pain, C., Piggott, M., Goddard, A., Fang, F., Gorman, G., Marshall, D., Eaton, M., Power, P., de Oliveira, C., 2005. Three-dimensional unstructured mesh ocean modelling. Ocean Modelling 10, 5–33.

Paluskiewicz, T., Garwood, R., Denbo, D., 1994. Deep Convective Plumes in the Ocean. Oceanography 7, 37–44.

Paluskiewicz, T., Romea, R., 1997. A one-dimensional model for the parameterization of deep convection in the ocean. Dynamics of Atmosphere and Oceans 26, 95–130.

Peiro, J., Sherwin, S., 2005. Handbook of materials modelling. Springer, Berlin, Ch. Finite difference, finite element and finite volume methods for partial differential equations, pp. 1–30.

Pickart, R., Smethie, W., Lazier, J., Jones, E., Jenkins, W., 1996. Eddies of newly formed upper Labrador Sea water. J. Geophys. Res. 101, 20711–20726.

Pickart, R., Spall, M., Ribergaard, M., Moore, G. W. K., Milliff, R., 2003. Deep convection in the Irminger Sea forced by the Greenland tip jet. Nature 424, 152–156.

Pond, S., Pickard, G., 1983. Introductory Dynamical Oceanography. Pergamon Press.

Provost, C. L., Vincent, P., 1986. Extensive tests and precision for a finite element model of Ocean Tides. Journal of Computational Physics 65, 273–291.

Raasch, S., Etling, D., 1998. Modelling deep ocean convection: Large Eddy Simulation in comparison with laboratory experiments. J. Phys. Oceanogr. 28, 1786–1802.

Rahmstorf, S., 1993. A fast and complete convection scheme for ocean models. Ocean Modelling 101, 9–11.

Rapid, 2008. NERC Rapid Climate Change. www.noc.soton.ac.uk/rapid/rapid.php.

Rasmussen, E., Pietrzak, J., Brandt, R., 1999. A coupled ice-ocean model for the Greenland, Iceland and Norwegian Seas. Deep-Sea Research II 46, 1169–1198.

Renfrew, I., Moore, G., 1999. An extreme cold air outbreak over the Labrador Sea: roll vortices and air-sea interaction. Monthly Weather Review 127, 2379–2394.

Ronski, S., Budeus, G., 2005a. How to identify winter convection in the Greenland Sea from hydrographic summer data. J. Geophys. Res. 110, C11010.

Ronski, S., Budeus, G., 2005b. Time series of winter convection in the Greenland Sea. J. Geophys. Res. 110, C04015.

Rudels, B., Quadfasel, D., Friedrich, H., Houssais, M., 1989. Greenland Sea convection in the winter of 1987/1988. J. Geophys. Res. 94, 3223–3227.

Sander, J., Wolf-Gladrow, D., Olbers, D., 1995. Numerical studies of open-ocean deep convection. J. Geophys. Res. 100, 20579–20600.

Schlosser, P., Bonisch, G., Rhein, M., Bayer, R., 1991. Reduction of Deep-water Formation in the Greenland Sea during the 1980's: Evidence from Tracer Data. Nature 251, 1054–1056.

Schott, F., Visbeck, M., Fischer, J., 1993. Observations of vertical currents and convection in the central Greenland Sea during the winter of 1988-89. J. Geophys. Res. 98, 14401–14421.

Senjyu, Y., Sudo, H., 1994. The upper portion of the Japan Sea Proper Water, its source and circulation as deduced from isopycnal analysis. Journal of Oceanography 50, 663–690.

Seung, Y., Yoon, J. H., 1995. Some features of winter convection in the Japan Sea. Journal of Oceanography 51, 61–73.

Smethie, W., Ostlund, H., Loosli, H., 1986. Ventilation of the deep Greenland and Norwegian Seas: Evidence from krypton-85, tritium, carbon-14 and argon-39. Deep-Sea Research 33, 675–703.

Spall, M., 2003. On the thermohaline circulation in flat bottom marginal seas. Journal of Marine Research 61, 1–25.

Spall, M., 2004. Boundary Currents and Watermass Transformation in Marginal Seas. J. Phys. Oceanogr. 34, 1197–1213.

Stommel, H., 1948. The westward intensification of wind-driven ocean currents. Transactions of the American Geophysical Union 29, 202–206.

Stossel, A., Yang, K., S-J, K., 2002. On the Role of Sea Ice and Convection in a Global Ocean Model. J. Phys. Oceanogr. 32, 1194–1208.

Straneo, F., Kawase, M., 1999. Comparison of Localized Convection due to Localized Forcing and to Preconditioning. J. Phys. Oceanogr. 29, 55–68.

Sverdrup, H., 1947. Wind-driven currents in a baroclinic ocean; with application to the equatorial currents of the eastern Pacific. Proc. Natl. Acad. Sci. U.S.A. 33, 318–326.

Swift, J., 1991. The Nordic Seas. Springer, Heidelberg, Ch. The Arctic Waters, pp. 129–153.

Talley, L., Lobanov, V., Ponomarev, V., Salyuk, A., Tishchenko, P., Zhabin, I., 2003. Deep convection and brine rejection in the Japan Sea. Geophysical Research Letters 30, 1159.

UN, 2007. UN Climate Change Conference in Bali. `http://unfcc.int/meetings/cop_13/items/4049.php`.

Visbeck, M., Marshall, J., Jones, H., 1996. Dynamics of isolated convective regions in the oceans. J. Phys. Oceanogr. 26, 1721–1734.

Wadhams, P., Wilkinson, J., 1999. The physical properties of sea ice in the Odden ice tongue. Deep-Sea Research 46, 1275–1300.

Wilkinson, J., 2005. Sea Ice, Convection and the Greenland Sea. PhD thesis University of Southampton.

Wilkinson, J. P., Wadhams, P., 2003. A salt flux model for salinity change through ice production in the Greenland Sea, and its relationship to winter convection. J. Geophys. Res. 108, 3147.

Wunsch, C., 2002. What is the Thermohaline Circulation? Science 298, 1179–1181.